CHEMICAL AND PHYSICAL PROPERTIES OF ATMOSPHERIC AEROSOLS (A) A CASE STUDY IN THE UNIQUE PROPERTIES OF AGRICULTURAL AEROSOLS (B) THE ROLE OF CHEMICAL COMPOSITION IN ICE NUCLEATION DURING THE ARCTIC SPRING

A Dissertation

by

SEONG-GI MOON

Submitted to the Office of Graduate Studies of
Texas A&M University
in partial fulfillment of the requirements for the degree of

DOCTOR OF PHILOSOPHY

May 2010

Major Subject: Atmospheric Sciences

CHEMICAL AND PHYSICAL PROPERTIES OF ATMOSPHERIC AEROSOLS (A) A CASE STUDY IN THE UNIQUE PROPERTIES OF AGRICULTURAL AEROSOLS (B) THE ROLE OF CHEMICAL COMPOSITION IN ICE NUCLEATION DURING THE ARCTIC SPRING

A Dissertation

by

SEONG-GI MOON

Submitted to the Office of Graduate Studies of
Texas A&M University
in partial fulfillment of the requirements for the degree of

DOCTOR OF PHILOSOPHY

Approved by:

Chair of Committee,	Sarah D. Brooks
Committee Members,	Don Collins
	Gunnar W. Schade
	William H. Marlow
Head of Department,	Kenneth P. Bowman

May 2010

Major Subject: Atmospheric Sciences

ABSTRACT

Chemical and Physical Properties of Atmospheric Aerosols
(a) A Case Study in the Unique Properties of Agricultural Aerosols
(b) The Role of Chemical Composition in Ice Nucleation during the Arctic Spring.
(May 2010)
Seong-Gi Moon, B.A., Meiji University;
M.S., West Texas A&M University
Chair of Advisory Committee: Dr. Sarah D. Brooks

This study focuses on the analysis of atmospheric particles sampled from two different field campaigns: the field study at a cattle feeding facility in the summer from 2005 to 2008 and the Indirect and Semi-Direct Aerosol Campaign (ISDAC) in 2008.

A ground site field study at a representative large cattle feeding facility in the Texas Panhandle was conducted to characterize the particle size distributions, hygroscopicity, and chemical composition of agricultural aerosols. Here, a first comprehensive dataset is reported for these physical and chemical properties of agricultural aerosols appropriate for use in a site-specific emission inventory. The emission rate and transport of the aerosols are also discussed. In addition, mixing ratios of total and gaseous ammonia were measured at the same field in 2007 and 2008. Measurements such as these provide a means to determine whether the fugitive dust emitted from a typical large feedlot represents a health concern for employees of the feeding operation and the nearby community.

Detailed chemical composition of aircraft-sampled particles collected during ISDAC was studied. Filter samples were collected under a variety of conditions in and out of mixed phase and ice clouds in the Arctic. Specifically, particles were sampled from a mixed-phase cloud during a period of observed high concentrations of ice nuclei (IN), a biomass plume, and under relatively clean ambient conditions. Composition of particles was studied on a particle-by-particle basis using several microspectroscopy techniques. Based on the elemental composition analysis, more magnesium was found in Arctic cloud residues relative to ambient air. Likewise, based on the carbon speciation analysis, high IN samples contained coated inorganics, carbonate, and black or brown carbon particles. In the samples collected during a flight through a biomass burning plume, water-soluble organic carbon was the dominant overall composition. Due to their

hygroscopic nature, these organics may preferably act as cloud condensation nuclei (CCN) rather than IN. Other ambient samples contained relatively higher fractions of organic and inorganic mixtures and less purely water-soluble organics than found in the biomass particles. The most likely source of inorganics would be sea salt. When present, sea salt may further enhance ice nucleation.

DEDICATION

This dissertation is dedicated to my family for their continued support and encouragement throughout my education.

ACKNOWLEDGEMENTS

From the formative stages of this dissertation, to the final draft, I owe an immense debt of gratitude to my supervisor, Dr. Sarah Brooks. Her sage advice, insightful criticisms, and patient encouragement aided the writing of this dissertation in innumerable ways.

I would also like to thank the members of my dissertation committee, Dr. Don Collins, Dr. Gunnar Schade, and Dr. William Marlow, for their patience, guidance, wisdom, and untiring assistance in the completion of this investigation.

For their efforts and assistance, a special thanks as well to Dr. Brent Auvermann, Rick Littleton, and Dr. Daniel Thornton. Without their help, this project would probably never have been finished.

Finally, a special thanks goes to Dr. Alexander Laskin with the Pacific Northwest National Laboratory and Dr. Mary Gilles and Dr. Ryan Moffet with the Lawrence Berkeley National Laboratory for their support and kindness. I thank them for providing assistance during the laboratory analysis for this study.

To each of the above, I extend my deepest appreciation.

TABLE OF CONTENTS

Page

CHAPTER Page

CHAPTER I

INTRODUCTION*^

This research describes aerosol chemical and physical characterization linked to their climate related properties (e.g., radiative budget). As demonstrated in this dissertation, the application of multiple complementary analytical methods is interdependent, and information obtained from one technique guides further measurements. Specific details of the real time data of the field study collected in two recent field campaigns and the sample analysis are described below.

1. A Case Study in the Unique Properties of Agricultural Aerosols

Increases in the size and number of concentrated animal feeding operations (CAFOs) have lead to an increase in public concern regarding the emission of atmospheric pollutants, including particulate matter (PM) and odor emissions. Emissions of aerosol particles from animal feeding operations has long been known to affect local air quality, visibility, and worker health (Gibb et al., 2004; Priyadarsan et al., 2005; Rule et al., 2005; Upadhyay et al., 2008; Schicker et al., 2009). Impacts of agricultural PM from livestock facilities extend through the region, through which malodorous volatile and semi-volatile compounds transported with the particles are clearly observed (Goetz et al., 2008; Occhipinti et al., 2008). State and Federal regulations strive to accurately assess the impacts of agriculture on air quality, though a lack of accurate data for PM complicates this assessment (Sweeten, 1998). Gaseous emissions from livestock have been documented as a significant regional, national, and global source of methane

---

This dissertation follows the style of Atmospheric Environment.

(CH_4), ammonia (NH_3), nitrogen oxides (NO_x), and nitrous oxide (N_2O) (NRC, 2003; Aneja et al., 2008; Denmead et al., 2008; Ro et al., 2009; Hiranuma et al., 2010). At the high concentrations of these gases measured in open-air livestock facilities, sources have been linked to odor emissions from cattle feeding operations (Hartung, 1995; Parker et al., 2005a and 2005b). To date, there is surprisingly a lack of measurements considering agricultural emissions represent a significant source of atmospheric particles. Additional measurements of agricultural aerosols are needed.

Particle size distributions are important to accurately quantify PM emissions (Wang et al., 2005). Large particles are typically dominant at the animal feeding operation facilities. For example, one study of particle size distributions from dairy farming operations was conducted in California (Nieuwenhuijsen et al., 1998). Large contributions (>80% of total mass concentration) of the very large particles (larger than 9.8 μm in diameter) to the total mass concentration in the range of 3.5 μm to 21.3 μm in diameter were observed during feeding and manure removal operation. Measurements in that study resulted in the implementation of new operational procedures, such as adding a cabin to the tractor, which resulted in a cost effective way to reduce personal exposure. In another study of particle size distributions and composition at a deep-pit swine operation in Iowa, the high abundances of supermicron particles were measured. In contrast, the population of fine fraction was very small. Specifically, the aerosol mass spectrometer measured PM_1 (particulate matter smaller than 1 μm in a diameter) as high as roughly 4 μg m^{-3}, which fractionally made up very small percentage (average roughly 6%) of the PM_{10} mass at downwind location (Martin et al., 2008).

National Ambient Air Quality Standards (NAAQS) are based on limits set by the U.S. Environmental Protection Agency (35 μg m^{-3} and 150 μg m^{-3} for 24-hour averaged $PM_{2.5}$ and PM_{10} mass concentration, respectively). Assessment of compliance with these limits presents a problem since in many cases accurate measurements are unavailable at many cattle feeding operation facility. In addition, there is clearly a need for more precise particulate measurements on higher time resolution, to capture diurnal and seasonal cycle, and response to weather conditions and precipitation.

This study of particle concentrations and size distributions presents the results of field campaign conducted in the summer of 2008 at a representative open air cattle feedlot in the Texas Panhandle. These measurements include real time observations of particle size distributions in the range of 0.01 to 25 μm in diameter and chemical characterization of particles

in the size range of PM_{10}. Also, by measuring upwind, downwind, and further downwind of the feedlot, the measurements in this study provide insight of particulate production and transport on a regional level. The measured particle size distributions at downwind location were used to estimate the emission rate of PM from single feedlot using a box model.

Importance of the study of hygroscopicity arises from the fact that particle size changes as a particle grows and dilutes at increased relative humidities. These changes also make accurate predictions of other properties, such as composition, reflective index, and aerosol extinction coefficients difficult (Hand and Kreidenweis, 2002). Previously, direct measurements of atmospheric extinction were made at a cattle feedlot, and those measurements indicate significant decreases in visibility during fugitive dust events as well as a wide variability in the reductions (Hiranuma, 2005). In that study, simultaneous measurements of the atmospheric extinction coefficient and the mass concentrations of coarse particles were made using an open-path transmissometer and Tapered Element Oscillating Microbalances (TEOMs), respectively. Two TEOMs were installed, one with a TSP inlet and one with a size-selective inlet for particulate matter (PM) with aerodynamic equivalent diameters of 10 μm or less (PM_{10}). At relative humidities (RH) less than 40%, a strong correlation between aerosol extinction and particulate mass was found. However, at high relative humidities (RH > 80%), the PM concentrations and extinction coefficient were poorly correlated, suggesting that some or all of the fugitive dust particles take up water, resulting in increased size and changes in the optical properties of the particles.

Previous hygroscopicity measurements have been conducted on numerous atmospherically relevant compounds and mixtures, including Chan and Chan (2003), Choi and Chan (2002a and 2002b), Gysel et al., (2004), Hameri and Rood, (1992), Hansson et al., (1998), Badger et al., (2006) and Brooks et al., (2002, 2003 and 2004). A number of techniques have been used to reliably measure the hygroscopicity of fine aerosol particles, for example, FTIR spectroscopy (Brooks et al.2004), electrodynamic balance (Tang and Munkelwitz, 1993) and tandem differential mobility analyzers, (Cruz and Pandis, 2000). The Environmental Scanning Electron Microscope (ESEM) technique employed here was previously used by Ebert et al. (2002) and Krueger et al. (2003). The ESEM has two specific advantages over other techniques, namely determination of the hygroscopic properties of a single particle and the advantage of studying aerosols in wide range of sizes (Ebert et al., 2002). While pertinent measurements of

water uptake as a function of RH have been conducted on humic materials (Brooks et al., 2004), any similar studies specifically on agricultural dust particles have not been performed.

Measurements of the hygroscopicity of size-selected agricultural aerosols collected from a ground site at the nominal downwind and upwind edges of a feedlot in the Texas Panhandle are reported. ESEM was used to acquire detailed images of agricultural particulates as a function of RH. The variations in hygroscopicity due to location in relation to the feedlot and time of day are discussed below.

Particle composition is also necessary for a complete understanding of PM emissions (Takahama et al., 2007; Moffet et al., 2008 and 2009). A number of studies have shown that the chemical composition of aerosol plays a key role in changing its physical properties, such as particle size and hygroscopicity (Hameri and Rood, 1992; Tang and Munkelwitz, 1993; Hansson et al., 1998; Cruz and Pandis, 2000; Brooks et al., 2002, 2003 and 2004; Choi and Chan, 2002a and 2002b; Ebert et al., 2002; Chan and Chan, 2003; Krueger et al., 2003; Gysel et al., 2004; Laskin et al., 2005a, 2005b, and 2006; Badger et al., 2006; Evelyn et al., 2009). For example, seize dependent variability in organic content measured by *in situ* aerosol mass spectrometry was observed at the preceding swine operation facility in Iowa (Martin et al., 2008). Unlike the high fraction of organic component found in submicron particles (as high as 54%), coarse size ranges (>1 μm in diameter) displayed smaller inclusion of organic carbon (20%) and a relative increase in mineral and inorganic fractions. In an airborne characterization of the aerosol downwind of a major bovine source in California, *in situ* measurements showed that organics were the dominant fraction of the total mass of collected aerosols in the plume (Sorooshian et al., 2008). The organic matter content of fugitive dust emissions from concentrated cattle operations is mainly related to the original diet and chemical conversions in the digestive tracts of cattle (Rogge et al., 2006).

Recently, a number of offline analytical techniques have been developed for the investigation of single particle composition (Takahama et al., 2007). In particular, Raman microspectroscopy (RM) has become one of the most powerful tools to study chemistry of atmospheric relevant particles on a single particle basis. To date, RM has been used to create chemical maps of single atmospheric aerosols and pollen grains (Everall, 2000a and 200b; Baldwin and Batchelder, 2001; Escribano et al., 2001; Sze et al., 2001; Sacristμn et al., 2002; Spells et al., 2003; Everall, 2004; Sadezky et al., 2005; Batonneau et al., 2006; Ivleva et al., 2007; Lee and Chan, 2007; Ivleva et al., 2007; Mansour and Hickey, 2007; Tomba and Pastor,

2007; Schulte et al., 2008). This mapping technique enables us to investigate the degree of internal mixing and multiple components in a single particle. To the best of our knowledge, this study provides the first RM measurements on agricultural aerosols. In addition, the Energy Dispersive X-ray Analyzer (EDX) was used to determine the elemental composition of single particles. To study the variation in composition with time, both RM and EDX analyses were conducted on multiple filters collected in three sampling periods; morning, afternoon, and evening. Collectively these measurements provide much needed information towards developing a better understanding of how physical and chemical properties of particulates affect local and regional air quality and visibility.

In addition to the measurements of aerosol properties, mixing ratio and atmospheric fate of ammonia (NH_3) were also investigated. Emissions of high concentrations of NH_3 from CAFOs may enhance particulate matter formation and deposition in the region (Ansari and Pandis, 1998; Aneja et al., 2000). Under typical atmospheric conditions, conversion of ammonia to the particle phase is likely to occur via the reactions between ammonia and gas phase inorganics, such as sulfuric acid or nitric acid, to form ammonium sulfate and ammonium nitrate, respectively (Denbigh, 1981; Kim and Seinfeld, 1995). However, conditions in the vicinity of the CAFO represent a highly atypical environment, in which concentrations of SO_2 and NO_x are limited with respect to stoichiometric formation of ammonium salt aerosol, and unusually high concentrations of carbon-containing particles are present. In addition, the presence of an extensive amount of organics can provide the surface for NH_3 adsorption and absorption (Siva et al., 2000; Pagans et al., 2007). The adsorption and absorption of NH_3 on organic surfaces is maximized at a moisture level of 50% to 70% (Devinny et al., 1999). Field measurements of NH_3 at agricultural sites, in particular at open-air animal feeding operation facilities, are still limited. In fact, only a few studies have been conducted at feedlots representative of the large facilities often found in the southwest United States (Faulkner and Shaw, 2008; Todd et al., 2008). Rigorous coincident measurements at the source and downwind but close to the source are required to assess the direct contribution and timescales of ammonia to particulate matter formation near the source. Extensive measurements of both gaseous and particulate ammonium species collected in and around a large feedlot are presented.

Combined together, these measurements provide much needed information towards better understanding of how physical and chemical properties of particulates affect local and regional air quality and visibility. Also, by measuring upwind, downwind, and further

downwind of the feedlot, these measurements provide initial insight into issues of particulate production and transport on a regional level.

2. The Role of Chemical Composition in Ice Nucleation during the Arctic Spring

One challenge in modeling Arctic cloud properties and their effect on global climate is to accurately understand the influence of ice nucleation on Arctic cloud formation (Curry et al., 1996). This is particularly difficult because ice nucleation parameterizations applicable to lower latitudes cannot be applied to Arctic cloud formation largely due to the unique properties of Arctic clouds (Harrington, et al., 1999; Morrison and Pinto, 2005). Specifically, springtime Arctic boundary layer clouds are characterized with the dominance of mixed-phase stratus containing both ice and liquid components caused by persistent temperature and humidity inversions and the influence of aerosols transported from lower latitudes (Barrie, 1986; Borys, 1989; Shaw, 1995; Pinto et al., 1998; Curry et al., 2000; Intrieri et al., 2002). Episodic aerosol transport from Siberia and eastern Asia to North Slope of Alaska has been reported in Rogers et al. (2001) and Prenni et al. (2009). Accurate understanding of cloud water phase is particularly important in the Arctic for the radiation balance at surface (Morrison et al., 2008). Mixed phase clouds containing high concentrations of both liquid droplets and ice crystals observed during previous Arctic campaigns, Surface Heat Budget of the Arctic Ocean (SHEBA) in spring 1998 and Measurement Program's Mixed-Phase Arctic Cloud Experiment (M-PACE) in autumn 2004. During SHEBA, liquid water was present 73% of the time based on lidar depolarization measurements (Intrieri et al., 2002). The presence of liquid water is often observed even at temperature as low as -34ºC. Likewise, mixed-phase clouds were found for 71% of time period during M-PACE field campaign (6% in liquid phase and 23% in ice phase) (McFarquhar et al., 2007).

An even bigger issue is to characterize and quantify ice nucleation activity in Arctic clouds. Ice nucleation occurs through several different freezing processes, classified either as homogeneous or heterogeneous. Homogeneous freezing of solution droplet takes place only at temperatures below ~ -38 ºC in the absence of foreign particles (Wallace and Hobbs, 2006). On the other hand, atmospheric aerosols act as an embryo of ice or ice nuclei (IN) in heterogeneous freezing mechanisms, forming ice crystals at much higher temperature than homogeneous nucleation (Mason, 1971). More specifically, atmospheric ice nucleation proceeds through

contact freezing, condensation freezing, immersion freezing, and deposition nucleation (Vali, 1985). Thus far, successful modeling of the heterogeneous ice nucleation for multiple chemical compositions has proven challenging due to its complexity (Phillips et al., 2008). Recently, several studies have shown that aerosol chemical composition plays a key role in changing heterogeneous freezing mechanisms (DeMott et al., 2009; Fornea et al., 2009, and references therein). For example, laboratory observations by DeMott et al. (1999) showed that nucleation of ice by soot occurs at -30 ºC. Another laboratory study conducted by Fornea et al. (2009) showed that freezing temperatures of atmospheric relevant humic-like substances (HULIS) vary from -6.5 to -22.2 ºC depending on compositions and freezing mechanisms, including contact and immersion. Chemical composition is especially important because *in situ* observations and off-line analysis of field collected samples identified the variability in IN composition. Mineral dust may also play an important role on influencing the ability of heterogeneous ice nucleation (Morrison and Pinto, 2005; Prenni et al., 2007). For example, an importance of dust as potential IN has been reported in another recent study by Ansmann et al. (2008). Based on the lidar observation of freezing event on Sahara dust, significant amounts of ice particles through heterogeneous glaciation were observed in cirrus cloud near the source at the temperature <-20ºC. Related to this field observation, laboratory study of heterogeneous freezing by Sahara dust was recently conducted by Connolly et al. (2009). In Connolly's study, the experiments were conducted with the aerosol interactions and dynamics in the atmosphere (AIDA) and increase in freezing efficiency was found between -24ºC and -27ºC. Upon elemental composition analysis, these particles were found to be carbon rich (78% atomic percent composition of total) followed by small fraction of silicon and calcium. These mineral dust compositions are especially important because these compositions may indicate the influence of aerosols transported from lower latitudes in Arctic case.

Several studies reported that the major components of ice nucleating carbonaceous aerosols included mineral dust, metallic materials, sulfur and silicon mixtures, and possibly ocean derived biogenic aerosols (Schnell, 1977; Chen et al., 1998; Rogers et al., 2001; DeMott et al., 2003a and 2003b; Ansmann et al., 2008; Pratt et al., 2009; Prenni et al., 2009). Rogers et al. (2001) examined elemental composition of aircraft-sampled particles in the Arctic during May 1998. In their study, aerosols which activated as IN were collected on an impactor downstream of an ice nucleation instrument, a continuous flow diffusion chamber (CFDC). Occasional peaks of IN > 40 L^{-1} were measured at processing temperature in the range from -15 ºC to -19 ºC. In

such a high IN situation, energy dispersive X-ray spectroscopy (EDX) identified large amount of sulfur, silicon, and some metals (Zn, Al, and Fe). Similar results for elemental composition were found during periods of high IN activity encountered during M-PACE study in October 2004 (Prenni et al., 2009). Despite a campaign average of IN concentration less than 1 L^{-1} during M-PACE, large spatial and temporal variation was observed. The highest measured IN concentration reached ~60 IN L^{-1} during M-PACE campaign. The most dominant composition was metallic dust transported from Asia with silicon inclusion. Thus the analysis of chemical composition of atmospheric particles and its nucleating ability is crucial step to understand how atmospheric aerosols influence ice cloud formation and overall climate change.

Depending on physical and chemical properties of aerosols, they can also serve as cloud condensation nuclei (CCN), forming water droplets by condensation (Koehler et al., 2009). In fact, previous field measurements of CCN concentration over the springtime Arctic Ocean observed relatively high levels of up to 2.5 x 10^5 L^{-1} (at 0.8% supersaturation) as compared to that in the lower latitudes (Yum and Hudson., 2001). Particle hygroscopicity and solubility are the most essential parameters in estimating a particle's ability to act as CCN (Petters and Kreidenweis, 2008; Sullivan et al., 2009). For example, experimental study conducted by Sullivan et al. (2009) showed that sufficiently soluble minerals, e.g., calcium nitrate, increase the CCN ability whereas insoluble and low hygroscopic minerals, e.g., calcium carbonate (calcite), deactivate CCN ability. For condensation of organics, changes in surface tension can influence particles nucleation ability (King et al., 2007; Engelhart et al., 2008; Brooks et al., 2009). For example, Engelhart et al. (2008) studied the activation of monoterpene derived secondary organic aerosols (SOA) formed on ammonium sulfate seeds. This study estimated the water-soluble organic carbon (WSOC) fraction in SOA and reported activation at reduced surface tension. However, in general the specific compounds contained in the water soluble fraction in aerosols which act as CCN still remains uncharacterized (Turpin et al., 2001).

For accurate understanding of Arctic clouds, it is important to properly distinguish between the roles of IN and CCN activation and define their chemical and physically properties. Ice nuclei are a limited number of select members of the total aerosol population. At the typical ambient temperatures encountered in the Arctic troposphere, only insoluble particles nucleate to the ice phase through heterogeneous freezing (Rogers et al., 2001). Insoluble components that have low CCN activity must be considered as potential source of IN. In the Sullivan study referred to above, atmospherically relevant insoluble minerals, such as calcite and calcium

sulphate, can act as IN and can be very important for heterogeneous nucleation of ice within clouds. In fact, as mentioned earlier, there are a few observations that aged mineral dust particles coupled with carbonaceous materials are observed and actually abundant in clouds. The degree of internal mixture and spatial distributions of identified constituents also must be considered for more accurate understanding of ice nucleation and IN and CCN activity threshold.

The analysis presented here focused on particles collected on the chemical properties of particles collected in mixed-phase clouds during the Indirect and Semi-Direct Aerosol Campaign (ISDAC) in the North Slope of Alaska. Arctic IN concentrations are typically lower (0.1 L^{-1} at -10 ºC and 5 L^{-1} at -20ºC) than those found at lower latitudes (Cooper et al., 1986; Rogers et al., 1998; Richardson et al., 2007). However, occasional increase of IN was observed during aforementioned SHEBA campaign as well as ISDAC described in below. Given high IN opportunity, the chemical bonding of cloud residues during high ice nucleation activity was examined. Specifically the analytical techniques here include the application of computer controlled scanning electron microscopy with an energy dispersive X-ray analyzer (CCSEM/EDX) and scanning transmission X-ray microscopy coupled with near edge X-ray absorption fine structure spectroscopy (STXM/NEXAFS). Applications of these analytical methods are independent; hence the information from one method guides subsequent measurements. Characterization of particles collected in biomass burning plume and cloud-free ambient air was also conducted. Differences between IN containing and non-IN containing aerosol populations will be also discussed.

CHAPTER II

METHODOLOGY

1. Particle Sampling and Measurement Conditions in Campaign

A. Cattle Feeding Operations Study 2005 to 2008

i. Hygroscopicity Study: In August 2005, a measurement campaign was conducted in Tulia TX, in the Texas Panhandle, where 45,000 head of cattle are housed in an open-air feedlot (2.6 km^2), "Feedlot C". Feedlot C is a representative open air Texas Cattle Feeding Association (TCFA) operation. At all TCFA facilities including Feedlot C, certain procedures are routinely conducted to minimize dust emissions, including spraying water on the surface of the pens and removal of loose manure (Sweeten, 1979). Local weather conditions at Feedlot C include large diurnal variation in temperature and relative humidity, with the relative humidity peaking in the coolest hours in morning hours (Mitchell et al, 1974). Afternoons and evenings typically have cooler temperatures, lower relative humidities, and lower wind speeds, concurrent with increased cattle activity. Major dust events occur when dry, uncompacted manure accumulates on the feedlot surface and dust is suspended by hoof action of the active cattle (Razote et al., 2006).

A low-volume cascade impactor system from PIXE, Inc. was mounted in a protective instrument housing ~2 meters above the ground at a sampling site located at the center point along the northern edge of the feedlot. This is nominally the downwind side of the feedlot. A number of complimentary measurements were underway at Feedlot C during this time, as described in Hiranuma (2005). Cascade impactor samples were also collected from a second site at the nominally upwind site of the lot. The cascade impactors were used to collect six size-resolved samples on aluminum foil filters in the sizes of <0.5 μm, 0.5 to 1 μm, 1 to 2 μm, 2 to 8 μm, 8 to 16 μm and >16 μm. Using the electron microscope, it was later observed that a number of particles on the filters were outside the specified size ranges. Several factors including turbulence, inconsistent flow rate, and irregular shape and density of agricultural dust may have contributed to the lack of distinct size cut-off points in the cascade impactor sampling (Kavouras and Koutrakis, 2001). Thus, the cascade impactors sizing was considered to be an initial sorting of the particle size. Using the electron microscope, all particles were grouped in three size ranges

(>10 μm, 2.5-10 μm and <2.5 μm diameter). Particles were further sorted by their shape as described in the next section.

A total of fifty-four size-selected filter samples were collected during three sampling periods in the morning, afternoon, and evening, from approximately 5:00-8:00, 15:00-18:00, 20:00-23:00 Central Daylight Time (CDT), respectively, on August 7, 8 and 11, 2005. The samples collected on August 7 and 8 were collected on the nominally downwind side of the feedlot, and the August 11th samples were collected on the nominally upwind side for comparison. A sampling time of approximately three hours was used for each sample. The particles collected on these days were considered to be representative of agricultural particles present in the summer in the Texas Panhandle. Relatively high levels of dust over the feedlot were visually observed on these days. Wind directions were southerly on all three days. During the collection periods, the TEOM measured 1-minute peak PM_{10} concentrations as high as ~8300 $\mu g/m^3$ on August 11.

All samples collected in the field were transported in a refrigerated cooler to Texas A&M University and stored under refrigeration until microscopy analysis could be completed at the on-campus Microscope and Imaging Center. Water uptake measurements were conducted on a total of 169 individual particles collected with the cascade impactors. In addition, EDX measurements were conducted to identify the elemental composition of the particles in the filter samples described above. A total of 208 particles collected at the feedlot were analyzed by EDX.

ii. Agricultural Ammonia Study: A number of techniques, including scrubbers, denuders, and flux chambers, have been deployed to measure concentrations of ammonia at animal feeding operations (Koziel et al., 2004; Aneja et al., 2000; Schade and Crutzen, 1995; Fitz et al., 2003). Ammonia scrubber measurements have also been performed at a variety of in-house livestock buildings of daily cows, swine, laying hens and horses (Schade and Crutzen, 1995). In this study, a simple sampling apparatus was used. It consists of paired scrubbers, one with a particulate filter upstream of the scrubber and another without (Figure 1). The filter-free sampler collects both gas-phase ammonia ($NH_3(g)$), and particle-phase ammonium (NH_4^+), which refers to in the aggregate as NH_x. Upstream of the second scrubber a glass fiber filter in a nylon housing (McMaster-Carr, model number 4795K3) removes 99.99% of particulates, leaving the gas-phase ammonia. Using the two-scrubber method, the mixing ratios of $NH_3(g)$, total NH_x, and particle-phase NH_x (total – gas) in the ambient air can be determined.

Prior to sampling, the scrubbers are rinsed twice with de-ionized Millipore water, once with 0.1 M HCl, and again with de-ionized Millipore water. The scrubbers are then filled with 10 ml of 0.1 M HCl solution for collection of ammonia species. During operation, the pump is used to vacuum the air at 3 liter per minute for 20 minutes, and the solution is drawn from the reservoir through the nozzle and forms a fine aqueous mist sprayed into the chamber. The fine droplets provide a large surface area for efficient collection of gaseous NH_3. The following reaction occurs, trapping gaseous ammonia in solution:

$$NH_3(g) + HCl(l) \rightarrow NH_4Cl(l) \qquad [1]$$

Once formed, the ammonium chloride will remain stable as long as the pH of solution remains below 2 (Schade and Crutzen, 1995). To confirm this, the ammonia concentration in a subset of the samples was measured immediately upon collection, after 24 hours, and after 72 hours, and no change in concentration was observed, within the experimental uncertainty in this study. This subset of samples included in the time tests consisted of 8 samples collected throughout the project, with 3 replicate measurements were conducted for each sample. The sampling of $NH_3(g)$ and total NH_x in the ambient air was conducted at the nominally downwind and upwind edges of Feedlot C in the summer of 2007 and 2008. This study focuses primarily on the 2008 campaign during which a third series of "far-field" samples were collected from the edge of a dirt road 3.5 km downwind of the feedyard.

For all sampling, the scrubbers were placed 1.5 m above the ground. Routine samples were collected for 20 minutes at a flow rate of 3 lpm, in the morning (~09:00 am), afternoon (~03:00 pm), and evening (~09:00 pm). All times are reported as Central Daylight Time (CDT). A total of 161 samples were collected from July 12, 2008 to July 25, 2008.

In addition to ammonia measurements, measurements of particle size distributions were collected during the project using two Grimm 1.108 Portable Aerosol Spectrometers (PAS). Since gas-phase ammonia is a potential source of new particles, it is advantageous to simultaneously measure concentrations of both ammonia and particles in order to identify correlations between the two (Aneja et al., 2000). The PAS is a laser-based aerosol spectrometer which records a particle size distribution consisting of 15 size bins from 0.3 µm to 25 µm optical diameter every six seconds (Peters et al., 2006). Two PAS instruments were used during the field campaign. Pre and post-campaign laboratory calibrations indicated that the instruments were in

agreement to within ± 3%. During the field campaigns, one PAS was continuously operated at the nominally downwind site. The second spectrometer was used to provide coincident size distribution measurements during collection of far-field ammonium samples.

Although prevailing winds at Feedlot C are southerly during the summer, there were some fluctuations in wind direction (±52°). Since these deviations translate to longer distances as moving further from the source, a plume-chasing strategy was devised to target the center of the plume for far-field sampling. A dirt road that runs nearly parallel to Feedlot C, 3.5 km away, on the downwind side was used. The area between Feedlot C and the road was an open field of recently tilled soil. The second Grimm PAS was used to survey particle size distributions along the road.

Prior to collecting each ammonia sample at the far-field site, it was attempted to determine the center of the dust plume from the CAFO at 3.5 km downwind. To do so, a series of eight PM samples was collected at prescribed far-field locations along the dirt road to roughly pinpoint the center of the plume at that moment in time. Concerning the health impact of agricultural aerosols, the analysis of total volume concentration of PM_{10} (particulate matter less than 10 µm in diameter) was primarily focused. It should be noted that volume concentration is the most direct reporting of the measurements in this study because obtaining mass concentration requires the assumption of a density. To obtain the volume concentrations of PM_{10} reported below, only the particle counts in 12 bins of optical diameters 0.3 µm to 10 µm were considered. For each bin, the number concentration was converted to a volume assuming that all particles in the bin are spheres with a diameter equal to the average diameter in that bin. The total volume in bins 1 to 12 were then summed together to obtain the total volume of $PM_{10.}$ A detailed account of the spatial and temporal variations in size distributions observed at the CAFO is available in the sections below.

After completing an initial PM_{10} survey, the point where the highest concentration of PM_{10} was measured was identified, assumed this was designated plume center for the given day, and collected NH_3 and total NH_x samples for the standard 20 minutes at 3 liter per minute, at 1.5 m above the ground. Coincident PM sampling was conducted as well. This plume-chasing procedure was repeated each time a far-field sample was collected.

Ammonia concentrations are influenced by a number of complex, interrelated variables, which include meteorological conditions, soil conditions, and the presence and concentration of aerosol particles, which could provide surfaces for ammonia adsorption. During the campaign,

both atmospheric and soil parameters were monitored. An on-site weather station was deployed on a 2 m platform at the downwind site to provide measurements of relative humidity (RH), wind direction, ambient temperature, wind speed, and rainfall, recorded every six seconds. Measurements of soil moisture content, soil temperature at the surface and 25 cm within the soil were also obtained at the downwind sample site. To check the variability of soil temperature, soil temperature was also measured at 3 additional locations, two points within the pens located nearby the downwind site and one point at the upwind site. Both the surface and subsurface measurements at all 4 sites were consistent throughout the campaign (±1.3 ºC standard deviation).

iii. Particle Size Distributions: During the summer of 2008, a measurement campaign was conducted at an open air feedlot operated by the Texas Cattle Feeding Association (TCFA) in Swisher County, TX, referred in this manuscript as Feedlot C. This feedlot, which houses 45,000 cattle in an area of one square mile is representative of the numerous large feedlots scattered throughout the U.S. southern states of Texas, Oklahoma, and New Mexico. Cattle feeding operating in this region annually market more than 7 million feed cattle, accounting for 30% of the nation's feeding cattle production.

Instruments used for particle size distribution measurement and size-resolved particle collection for RM are shown in Figure 2. The particle size distributions and samples were collected ~2 m above the ground at the nominally upwind and downwind edges of the facility (N 34º 39.5’ W101º 47.3’). A third series of "far-field" samples were also collected from the edge of a dirt road 3.5 km downwind of the feedyard. Complimentary measurements of mixing ratios of total and gaseous ammonia and atmospheric extinction of agricultural aerosols were also underway at Feedlot C during the field measurements as described in Hiranuma et al. (2008 and 2010) and Upadhyay et al. (2008).

During the field campaign, atmospheric conditions were monitored using an on-site HOBO weather station. This was deployed on a 2 m platform at the nominal downwind site to provide measurements of relative humidity, wind direction, ambient temperature, wind speed, and rainfall, recorded every six seconds. In addition, measurements of soil moisture, soil temperature at the surface and 25 cm within the soil were also obtained at the downwind sample site. As discussed below, soil moisture is a determining factor in the concentrations of atmospheric dust events. Detailed observation of daily averaged meteorological data is available in Figure 3 and discussed in below section.

iv. Particle Sampling for Raman Microspectroscopy: In the summer of 2008, PIXE Streakers were used to collect time resolved aerosol samples for offline analysis. This filter sampler was mounted in a protective instrument housing 2 m above the ground were used for continuous collection of particles at the downwind and upwind locations. The Streaker produces a continuous series of discrete samples for offline chemical composition analyses. With an air flow of one liter per minute, particles are collected in the size range of PM_{10} on 82-mm diameter aluminum filters. Sampling intervals of 15 minutes are employed for continuous daily collection at the up and downwind sites. PM_{10} samples were also collected at the far-field location while conducting the far-field PAS measurements. Due to the lack of another Streaker, far-field samples were collected with a low flow cascade impactor, which also has a nominal cut off of 10 μm diameter. Using the optical microscope, it was later observed that a number of particles on the filters were outside the specified size ranges on cascade impactor filters. Several factors including turbulence, inconsistent flow rate, and irregular shape and density of agricultural dust may have contributed to the lack of distinct size cut-off points in the cascade impactor sampling (Kavouras and Koutrakis, 2001). In fact, particle size appeared to range from ~1 to 10 μm in diameter upon an initial inspection of particles with electron microscopy. Thus, the cascade impactors sizing were considered to be an initial sorting of the particle size and particles of sizes from 1 to 10 μm were observed on both Streaker and cascade impactor filters.

Aluminum foil was used as the particle impaction surface. Prior to sampling, the foil was cleaned by rinsing with high purity isopropanol and drying at room temperature. All samples collected in the field were transported in a refrigerated cooler to Texas A&M University and stored under refrigeration until analysis by RM could be completed.

To study the variation in composition of agricultural particles with time, Raman analysis was conducted on multiple filters collected in three sampling periods; morning, afternoon, and evening, collected from 8:00 to 8:15 am, 3:00 to 3:15 pm, and 9:00 to 9:15 pm, respectively. During the field campaign in 2008, exclusively high levels of dust (hourly average PM_{10} > 10,000 μg m^{-3}) were observed at the downwind location under typical hot and dry conditions on the evening of the July 22 and 24. In addition to the regular downwind and upwind samplings, PM samples collected at far-field ~9:00 pm on these two days were also analyzed.

B. Indirect and Semi-Direct Aerosol Campaign 2008

A variety of atmospheric conditions interrelating with cloud and radiation properties may be encountered while sampling during the Arctic spring (Curry et al., 1996; Pinto et al., 1998; Curry et al., 2000; Intrieri et al., 2002). Samples were collected to study the chemical properties of particles from different representative sampling conditions over the North Slope of Alaska. Particles were collected using the Time Resolved Aerosol Collector (TRAC) on board of the Convair-580 research aircraft from the National Research Council Institute for Aerospace Research (NRC-IAR). The TRAC was deployed followed by a counterflow virtual impactor (CVI). Figure 4A shows a schematic of the CVI. CVI separates nucleated components (>5 μm D_p) from non-nucleated interstitial aerosols (<5 μm D_p) (Ogren et al., 1985). Thus, TRAC was often operated in line after a CVI to characterize the cloud residues. Both CVI samples and ambient samples were collected. For instance, cloud residues in a mixed-phase cloud were collected during the CVI was active (referred to as CVI samples) whereas both cloud residues and interstitial aerosols were collected when the CVI was not active (referred to as ambient samples). Particles were deposited directly onto the TRAC substrate that consisted of transmission electron microscope (TEM) grids with Carbon Type-B supporting films (Ted Pella, Inc., Redding, CA). The TRAC automatically switched the substrate every 5 minutes, which provided time-resolved aerosol samples. The effective cutoff size D_{50} was approximated as 0.4 μm under optimal conditions typically applied for both ground based and aircraft based samplings (Laskin et al., 2006).

While the TRAC sampler was run continuously, the chemical analysis techniques employed here are highly labor intensive. Thus it is only possible to analyze particles collected during a few chosen periods. To identify the optimal periods, a sort mechanism was first employed to choose samples representative of the range of conditions and aerosol compositions sampled. Figure 4B summarizes the classification scheme to classify sampling conditions into biomass, cloud-free, in-cloud (ambient), in-cloud (CVI), and high IN. In this scheme, cloud conditions during the flight (i.e., in-cloud or cloud-free) were first identified according to the algorithm for ISDAC developed by McFarquhar et al. (in preparation). In McFarquhar's algorithm, "in-cloud" conditions refer to either mixed-phase cloud or liquid phase clouds. Next, special cases were also identified: samples collected within a biomass burning plume and during a period of particularly high IN concentrations encountered within a mixed phase cloud.

Specifically, a biomass plume was detected by the Single Particle Laser Ablation Time-of-Flight mass spectrometer (SPLAT II). Biomass burning particles prevailed during Flight Number 25 according to the SPLAT II data (Zelenyuk et al., 2009). Thus all of the samples from Flight Number 25 are classified as collected under "biomass sampling conditions". The high IN activity period was identified by *in situ* measurements by the Texas A&M CFDC. A high concentration of IN identified by CFDC measurements indicate the presence of potential ice phase cloud (Glen and Brooks, in preparation). In this study, a minute averaged IN concentration more than 3 L^{-1} is considered as a high IN activity period compared to the mean IN concentrations of 0.3 L^{-1} when sampling on CVI. It should be noted that the TRAC impactor was deployed downstream of the CVI, but not directly downstream of the CFDC during sampling, Thus, during flights through mixed phase clouds, particles collected by the TRAC sampler include both CCN and IN, even under high IN counts.

Multiple TRAC samples were obtained in given sampling conditions. Table 1A summarizes the sample substrates used later on composition analyses and the percentage of sampling time in cloud for each sampling interval. A total of twenty five substrates were analyzed in CCSEM/EDX and STXM/NEXAFS. As can be seen in the table, clouds were present more than half of the time during the TRAC sampling.

In general, particles collected on substrates suffer from some artifacts. These artifacts include evaporation of volatile and semi-volatile species during sampling, storage, and then analysis by the applied techniques, as well as possible reactions between sampled particles and trace gases entering the impactor (Rogers et al., 2001; Hopkins et al., 2008). Artifacts like the potential reactions with the samples inside the TRAC could not be quantified. However, their possible impacts were somewhat minimized by drying particles prior to collection, which would decrease their reaction kinetics due to loss of water.

Detailed sampling conditions are summarized in Table 1B. This table primarily includes *in situ* records of ambient conditions, ice crystal concentration (>200 μm D_p), IN concentration, CCN concentration, background condensation nuclei (CN) concentrations, and associated instrument processing conditions. Unless otherwise stated, all parameters presented in this work are based on a one-minute averaged dataset. As can be seen in the table, the traces of ice crystal concentration measured by the two dimensional stereo probe (2DS, >200 μm D_p) and ambient ice super saturation (SS_{ice}) tracked together. Relatively high levels of ice crystal concentration (> 10^{-2} L^{-1}) and positive values of ambient SS_{ice} indicate the presence of ice phase components in

the cloud. Additional indication of the presence of an ice phase cloud can be inferred from the CFDC measurements. The measurements of IN concentrations were made at -17.9% to 3.6% water supersaturation (SS_w) and -21ºC to -28ºC during the TRAC sampling period. As expected, within given processing conditions, the measured IN concentration of <1.7 L^{-1} during TRAC sampling was low compared to that found in lower latitudes (Rogers et al., 1998; Richardson et al., 2007) but in good agreement with earlier studies of Arctic IN (Rogers et al., 2001; Prenni et al., 2009). During the CVI sampling period, relatively high IN concentration (8 L^{-1} at 3.5 SS_w and -22 ºC) was measured on April 29. In order to find sources and transport history of the particles, which serve as potential IN and contribute to high IN counts, flight specific backward trajectory calculations were performed using the HYSPLIT model (Draxler and Rolph, 2003). Backward trajectories calculated for 5 days prior to aircraft collection showed that such air masses were advected from north eastern Russia across the Bering Sea and also passed across continental areas of Alaska (Appendix B). Specifically, during the flights on April 26 and 29, air masses may have been influenced by both anthropogenic and biogenic emissions as the air masses passed over Fairbanks and Anchorage regions.

During the TRAC sampling, CCN concentration was continuously measured but only limited to a very low water supersaturation range (~0.1% to 0.3%). Yum and Hudson (2001) measured springtime Arctic CCN concentrations; campaign average concentrations 7.6 x 10^4 L^{-1} (in-cloud) and 2.5 x 10^5 L^{-1} (cloud-free) at 0.8% supersaturation. Their study during SHEBA applied a wide range of supersaturation and obtained CCN spectra covered two orders of magnitude (~0.02% to 1%). Within the supersaturation range of 0.1% to 0.3%, which was actually used during aerosol sampling, the data showed cloud-free conditions contains an order magnitude higher CCN concentrations compared to in-cloud conditions (Table 1B), which was similar to the observed values in Yum and Hudson (2001).

Background CN concentrations were measured using several different instruments. The passive cavity aerosol spectrometer probe (PCASP) is an airborne optical spectrometer that measures aerosol particles in the range of 0.14 to 3 μm D_p. All other CN counters, including the TSI 3775 Condensation Particle Counter (CPC), the PMS 7610 CPC, and the DMT Ultra-High Sensitivity Aerosol Spectrometer (UHSAS), were deployed at different locations with respect to the inlet system and used for different particles size ranges. Nevertheless all CN measurements are well correlated for the period studied (Table 1B). Very high ratio of CCN (at 0.8% SS_w) to CN concentration, approximately 0.65, for previous Arctic springtime campaigns has been

reported (Yum and Hudson, 2001). This CCN/CN ratio was especially high as compared to the value (0.15) obtained from another CCN measurement in the Arctic during June 1995 (Hegg et al., 1996). Increased background aerosol concentrations may have served as potential CCN. As expected, the CCN/CN ratio was as high as Yum and Hudson (2001) and CN concentrations were linearly correlated with CCN concentrations. Perhaps this high CCN to CN ratio may mean that the majority of transported aerosols from mid-latitudes in spring condensates at encountered processing supersaturation, which may deactivate the ice nucleating ability of aerosol particles (Borys, 1989). At the inversion, transported aerosols may contribute to forming typical Arctic haze (Curry et al., 1996; Curry et al., 2000; Carrió et al., 2005). Supportively, the backward trajectories indicate that air masses during biomass sampling conditions had Siberian influence, and corresponding CN and CCN measurements were obviously the highest among all sampling conditions.

2. Analytical Techniques

A. Particle Size Distributions

Aerosol size distributions were obtained using two instruments from GRIMM Technologies, Inc., a Sequential Mobility Particle Sizer (SMPS) and a Portable Aerosol Spectrometer, Model 1.108 (PAS). The SMPS consists of a Differential Mobility Analyzer (Model DMA-L) and an Ultrafine Particle Counter (Model 5.403). It records a full particle size distribution from 0.01 to 0.5 μm diameter by scanning the whole size range in 39 size bins approximately every 7 minutes. The SMPS determines particle size by measuring the electrical mobility diameter, of which a sampled particle has the same migration velocity in a constant electrical field as a sphere. A diffusion dryer was placed in-line, ensuring particles were dry upon entry to the SMPS to maintain relative humidity below 5% (Nessler et al., 2003). To confirm drying capacity of this arrangement, the relative humidity was measured in-line after 24 hours, and no change in the relative humidity was observed. The laser-based PAS sizes coarse particles in the range of from 0.3 to 25 μm optical diameter. This PAS instrument records a full 15 bin coarse mode distribution every 6 seconds. Assuming the particles are spheres, the optical diameter is equivalent to the volume equivalent diameter of the particle, thus the size distributions from the SMPS and PAS instruments can be directly combined (Peters et al., 2006).

The combined measurements of the SMPS and PAS yield a full size distribution, from 0.01 to 25 μm every 7 minutes collected at the nominally downwind site throughout the project.

As mentioned earlier, another PAS was used for the upwind and far-field measurements. The upwind measurements were collected nearly continuously with the exception of periodical interruptions during which PAS was used for brief surveys of the far-field location. The far-field measurements were conducted for ~2 hour in the afternoon (~4:00 pm local time (Central Daylight Savings) and in the evening (~10:00 pm). During the periodic far-field measurements, it was attempted to determine the center of the dust plume from the CAFO at 3.5 km downwind. To do so, a series of eight PM samples were collected at prescribed far-field locations along the dirt road to roughly pinpoint the center of the plume at that moment in time. After completing an initial PM survey, the PAS was returned to the point where the highest concentration of total PM was measured, assuming this was the plume center for the given interval, and collected PM samples for ~10 minutes. This plume-chasing procedure was repeated each time when collecting a far-field sample. The variation in the fraction of total PAS concentration (0.3 to 25 μm in diameter) transported to the far-field location is discussed in below section. It should be noted that pre and post-campaign laboratory tests confirmed that the PAS instruments were in agreement to within ± 3% throughout the campaign.

B. Hygroscopicity Analysis

Unlike standard electron microscopes which require vacuum conditions, the ESEM used in this study can be operated at higher pressures which allow the operator to introduce controlled amounts of gases, such as water vapor, to the sampling chamber. Here, the ESEM was used for two purposes. First, high-resolution images of the collected particles were obtained, allowing to qualitatively describe the shape and morphology of particles collected at the feedlot. Second, the ESEM was used to image particles to determine the hygroscopicity of particles by collecting a series of images at a controlled temperature while the relative humidity was incrementally increased.

The morphology of particles in each size range collected at the feedlot and imaged with the ESEM is now described. From each size-selected filter sample, ESEM measurements were conducted on a number of individual particles. As expected, using the low-volume cascade impactors chosen for this study resulted in filter samples sparsely covered with particles which

allowed probing individual particle characteristics. The ESEM measurements in this study were focused on individual particles which were not in contact with any others. High-resolution images of submicron particles were obtained by introducing and controlling the amount of water vapor in the Electro Scan Model E-3 ESEM equipped with a temperature- controlled sample stage.

Upon initial inspection of the dry particle images obtained with the ESEM, several distinct particle shapes were repeatedly observed on filter samples of all sizes. Nearly all particles in all sizes were broadly classified into one of three distinct shapes as follows: (A) smooth, rounded particles, (B) rough-surfaced, amorphous single particles, or (C) agglomerations of multiple amorphous particles. Representative images of particles of these types, referred to here as Type A, B, and C, respectively, are shown in Figure 5. Of all the particles randomly selected and imaged, the majority of particles was classified as Type B (roughly 82%) while significantly fewer were identified as Type A (~7%) and Type C (~11%). At smaller sizes (less than 2.5 μm diameter), the population was weighted most heavily toward the rough-textured Type B particles. This is the case for the samples collected at both the downwind and upwind sampling sites.

Due to the consistent recurrence of particles which fit into these three distinct categories, the hygroscopic measurements were conducted on particles in each shape group to determine whether morphology could be used as an indication of composition and thereby hygroscopic properties. Some compounds, specifically salts, do not take up water until a characteristic relative humidity, the deliquescence relative humidity (DRH) is reached. At the DRH, aerosol particles spontaneously take up water to become solution droplets. To test the capability of using ESEM for water uptake studies, the ESEM was first used to determine the DRH of salts with well-characterized DRHs, including sodium chloride, ammonium sulfate, and sodium sulfate. The average diameter of the salt particles used in this study was ~20 μm.

Experiments were conducted at a temperature of 15 °C. The measurements were conducted at 15 °C since stability and accuracy in temperature, relative humidity, and imaging are optimized at this temperature. At this temperature, the pressure in the sample chamber can be changed by small increments of 0.1 torr corresponding to small RH changes (0.7% to 0.8%). Samples are initially held for half an hour in the ESEM chamber at 2.5% RH to insure that the particles are initially dry. Next, the RH is incrementally increased by introducing a controlled amount of water vapor to the ESEM observation cell and waiting one to three minutes at a

constant temperature of 15 °C prior to collecting an image. The RH was incrementally increased from 7.9% to 96% in each experiment. In a typical experiment, the total number of RH steps is 50 (Table 2). Smaller increases in RH step (0.7% to 0.8 %) were used above 64% to identify the water uptake behavior and deliquescent RH as accurately as possible. It is not feasible to collect satisfactory ESEM images below 7.9% RH, because the amount of water vapor is not sufficient enough to carry backscattered electrons to the ESEM detector. While conducting measurements above 96% RH would be useful, it is not possible using this technique since pressure and temperature in the sample chamber become unstable and difficult to control at relative humidities above this point.

Here, the DRH is defined as the point at which the change in hygroscopic growth factor, D/Do, is the largest over an incremental change in RH. For each type of salt particle, six to nine experiments were conducted. The water uptake behavior for NaCl crystals with dry diameters of ~20 µm, and for a ~10 µm diameter fugitive dust particle are shown in Figure 6A and 6B, respectively. For the sodium chloride, no abrupt water uptake was observed at RH < 73% (Figure 6A III). Spontaneous water uptake and droplet formation were observed immediately after the relative humidity was increased from 73% to 74% RH (Figure 6A IV). In contrast, it can be seen that the agricultural particle does not exhibit a distinct deliquescence point, but rather exhibits small increases in size as water is gradually taken up over the range of RHs shown here.

The increases in particle diameter as a function of relative humidity are typically represented by plotting the hygroscopic growth factor, D/D_o, defined as the ratio of the particle's diameter at a certain RH by the initial dry particle diameter. In Figure 7, D/D_o is shown for each of the salts in this study. The y-axis error bars indicate the standard error in the measurements. The x-axis error bars represent experimental uncertainty in the relative humidity measurements, as described below.

The relative humidity in the ESEM chamber can be altered in a controllable fashion by incrementally increasing or decreasing the pressure in the chamber and directly cooling or heating the sample stage. This is described by the Clausius-Clapeyron equation in the form shown below:

$$RH(T) = \frac{P}{P_s \times exp\left(\frac{L_v}{R_v} \times \left(\frac{1}{273} - \frac{1}{T}\right)\right)} \quad [2]$$

RH(T): relative humidity at given temperature (%)

P: vapor pressure in the ESEM chamber (torr)

P_s: saturation vapor pressure at 273 K (= 4.58 torr)

L_v: latent heat of vaporization of water at 273 K (2.5 x 10^6 J K kg^{-1})

R_v: gas constant (461.5 J kg^{-1})

Thus, the experimental uncertainties associated with the DRH measurements can be calculated using accuracy of pressure control unit and cooling stage. To calculate uncertainty involved in the relative humidity measurement, all instrumental uncertainties were first converted to percent relative uncertainties. Instrumental accuracy of pressure control unit is within ±0.01 torr at given pressure, and calibration accuracy of temperature controller is computed as ±0.91 °C (CN9000A series operator's manual). The relative humidity inside the ESEM chamber was controlled by altering pressure (i.e., amount of water vapor) at constant temperature (15 °C) in all experiments so that uncertainties in the pressure measurement vary with pressure (±0.08% to 1%) whereas percent relative uncertainties in temperature measurement are uniform throughout the experiment (±6.08%). Then, the error of relative humidity was calculated as follows:

$$\%error[RH] = \sqrt{(\%error[P])^2 + (\%error[T])^2} \quad [3]$$

Finally, absolute uncertainty in relative humidity is found by multiplying the magnitude of the reported RH by relative uncertainty. Thus, uncertainty in the measurements ranges from ±0.48 to 5.72% RH.

As can be seen in the Figure 7, ammonium sulfate particles do not appreciably change in size until a relative humidity of ~79%. Upon reaching 79%, they deliquesce and abruptly increase in size. A sharp deliquescence point is also observed in the sodium sulfate data, at ~82% RH. In the case of the sodium chloride, a small amount of water is taken up at 68% RH, indicating the onset of deliquescence with full deliquescence occurring by ~72% RH. This slight range in relative humidities may be an indication that the NaCl used contained an impurity of

some kind. The initial experiments were conducted on sodium chloride obtained from Sigma-Aldrich of > 99.0% grade purity. To check for possible contamination, the NaCl experiments were reported together with NaCl from another source (Fluka, > 99.5% grade purity). Once again, water uptake was observed over a small range of relative humidities. Nevertheless, the overall results for these salts are in good agreement with previous measurements, as now been discussed.

One complication is that the previous deliquescence studies were conducted at 25 °C. Since deliquescence is a function of temperature, a direct comparison cannot be made. However, fortunately, a method has been developed by Tang and Munkelwitz (1993) to predict DRH as a function of temperature, provided that the DRH has been determined at one temperature. Using the equation below, the expected DRH at 25 °C based on the measurements at 15 °C is calculated.

$$DRH(298) = \frac{DRH(T)}{exp\left\{\frac{\Delta H_S \times \left[A \times \left(\frac{1}{T} - \frac{1}{298}\right) - B \times ln\left(\frac{T}{298}\right) - C \times (T - 298)\right]}{R}\right\}} \quad [4]$$

DRH(T) = deliquescence relative humidity at temperature T (in Kelvin)

R = universal gas constant = 1.99 cal mol^{-1} K^{-1}

ΔH_s = enthalpy of solution

A, B, C = empirical constants

The enthalpy values (ΔHs) used here, 448, 1510, and –2330 cal mol^{-1} for NaCl, $(NH_4)_2SO_4$, and Na_2SO_4, respectively, were calculated using data from a standard thermodynamic table in Wagman et al. (1965 and 1982) and were assumed to be independent of temperature. Values for A, B and C, are taken from Tang and Munkelwitz (1993) and collectively represent the relationship between solubility and temperature.

The predicted values of DRH at 25 ºC now can be compared to those of previous measurements obtained by others using ESEM and other techniques. This comparison is shown in detail in Figure 8. Again, the predictions for DRH at 25 °C are based on the deliquescence measurements at 15 °C. As can be seen from Figure 8, the predicted DRH obtained by ESEM agree within the experimental error to results measured with other techniques. However for each salt studied, deliquescence was observed at a slightly lower relative humidity than reported by

others using a variety of experimental techniques including ESEM. Possible reason for this offset of ~3% RH is that the ESEM has the advantage of a longer equilibration time (1 – 3 min) for each set of new conditions than is possible for most of other techniques (Ebert et al. 2002). To further confirm that particles have had adequate time to equilibrate at each RH, a time interval test was conducted. ESEM water uptake experiments were conducted on Na_2SO_4 particles. In this study, at each successive RH, the hygroscopic growth factor was measured at 1, 3, 5, and 10 minutes. The results showed no significant differences between hygroscopic growth factor collected at each time interval for a given RH, up to 96% RH (Figure 9). Overall, within the stated uncertainty, this technique is a reliable way to accurately determine the hygroscopic properties of aerosol particles and one of the only techniques that has a capability of obtaining such data for single particles and for particles of the large sizes of interest in this study. It also should be noted that a variety of salts incorporate water into their crystal structure upon water uptake out of the atmosphere, forming hydrates (Kelly and Wexler, 2006). For sodium sulfate, addition of ten water molecules forms sodium sulfate decahydrate, $Na_2SO_4 \cdot 10H_2O$. The number of molecules of water present in a given hydrate is fixed, providing its own unique hygroscopic properties prior to condensational growth. In the results section below, ESEM measurements on a total of 169 particles collected at the feedlot are presented and discussed.

Attempts to determine the efflorescence relative humidity, or RH at which aerosol particles lose water and recrystallize, were unsuccessful. Possible causes include hydrate formation, heterogeneous nucleation on the substrate, compaction of projection area after the cycle of hydration and dehydration, and alteration of original shape during the deliquescence/efflorescence process observed in this study (Ebert et al, 2002; Köllensberger et al., 1999). Other techniques in which the aerosol is suspended, rather than in contact with a substrate, have had more success in measuring efflorescence (Dougle et al., 1998).

C. Single Particle Chemical Composition Analysis

i. Energy Dispersive X-ray Analyzer: Microscopic imaging of individual particles from ISDAC and quantitative speciation of their elemental composition are performed using the CCSEM/EDX. In general, EDX quantifies the inelastic interaction between an electron beam and atoms in a particle (Skoog et al., 1997). Figure 10 illustrates the theory of this inelastic interaction. Particularly, when incoming electron radiation hits an atom, an inner shell electron of the atom is removed. Then an outer electron fills the inner vacancy. Since outer shell electrons have a higher energy state, the excess energy per transfer of an electron is emitted as a photon, in this case with a wavelength in the X-ray region of the electromagnetic spectrum. This inelastic interaction and associated photon energy and corresponding wavelength is very characteristic to each element, thus EDX can identify the elemental composition.

Specifically, a FEI XL30 digital field emission gun environmental scanning electron microscope was used. This specific microscope was equipped with an EDAX PV7761/54 ME EDX spectrometer and an ultrathin-window Si(Li) detector that allows X-ray detection from elements higher than beryllium. The relative atomic percentage was obtained and compared for 16 elements (C, N, O, Na, Mg, Al, Si, P, S, Cl, K, Ca, Mn, Fe, Zn, and Pb). These elements were selected based on their high abundance in the Arctic atmosphere found in previous elemental composition studies (Rogers et al., 2001; Prenni et al., 2009).

The CCSEM/EDX is equipped with the transmitted electron (TE) and backscattered electron (BSE) detector. During image processing, the TE signal is mixed with BSE signal to obtain high-quality images of the particles and stable signals over prolonged period of computer-controlled operation. Further descriptions of the CCSEM/EDX techniques employed in this study can be found elsewhere (Laskin et al., 2006, and references therein). Aerosol characterization using CCSEM/EDX has been widely applied to a variety of field collected particles from both ground sites (Laskin et al., 2005a; Hand et al., 2005; Johnson et al., 2005; Hopkins et al., 2008; Moffet et al., 2008) and research aircraft (Hopkins et al., 2007).

During microscopy operation, a working distance of 10 mm, an electron accelerating voltage of 20 keV with a beam current of 400 pA, and an irradiation time per a spectra of 10 seconds were used. Both X-ray spectra and images from the particles are recorded via the computer controlled mapping function, which automatically enables tracking spectra on a particle-by-particle basis. During the measurement, a large area of investigation (~575 μm x

~575 μm) on each substrate and the corresponding total number of active fields on each carbon coated substrate (~20 rows x ~20 columns >90% area covered) can be analyzed. A large area is ideal because spatial distribution of particles is inhomogeneous on TRAC films and CCSEM/EDX requires analysis across a wide range of deposition spots (Hopkins et al., 2008).

Quantitative speciation of elemental composition of the samples from cattle feeding operations were also performed using the manually controlled EDX. In this particular EDX, the x-ray detector measures the number of emitted x-rays as a function of their energy. Since elements have a characteristic energy, the EDX spectrum can be used to identify the quantity of elements present (Frankel and Aitken, 1970). One advantage of this EDX technique is that the measurements of weight percentage for specified elements can be obtained on a single particle basis. Though it would be ideal to collect hygroscopicity and chemical information on the exact same particles, it is not feasible because the ESEM and EDX are not available to us in a single microscope apparatus. Using a JEOL® JSM-6400 EDX with an energy dispersive x-ray detector, the 47 mm diameter cascade impactor samples were mounted on electron microprobe stubs. The following optimal operating conditions were used: a working distance of 15 mm, an electron accelerating voltage of 15 keV, a beam current of 1 nA, and an analysis time greater than sixty seconds. To minimize background noise, high magnifications was employed. Specifically $3x10^5$ times for the particles that have diameters of smaller than 2.5 μm and $1.5\ x10^5$ times for the particles that are larger than 2.5 μm in diameter are used. The penetration depth of electron beam is ~1 μm. Contribution of aluminum filter used for the study of agricultural aerosols was concerned because it could affect the measurements on a particle basis. Thus elemental composition analysis of agricultural aerosols was performed without counting aluminum. For ISDAC study, X-Ray coming from a particle was not distinguished from the substrate beneath. Particles were classified into specific particle-types based on combinations and ratios of elements other than those present in the substrate. Detailed sorting procedure is discussed in section below.

ii. Raman Microspectroscopy Analysis: The DXR Raman Microscope Apparatus (Thermo Fisher Scientific) is equipped with an Olympus BX microscope with a 50× objective (LMPlanFl), a 25 μm confocal aperture, and a CCD detector. A frequency doubled Nd:YVO_4 Diode Pumped Solid State (DPSS) laser is used for excitation at 532 nm. Spectra of the aerosol samples are recorded over the range of 50 to 3500 cm^{-1}, at a spectral resolution of ~7.5 cm^{-1}. Generally, the Raman MS used in this study quantifies the inelastic scattering between the

monochromatic laser beam light (532 nm in wavelength) and molecular bond's ro-vibrational transitions within single particles (Skoog et al., 1997). Figure 11 illustrates the theory of this inelastic scattering. Particularly, when an incoming photon beam interacts with a molecule, it can get scattered without changing its wavelength, i.e. energy (Rayleigh scattering), or it may exchange energy with distinct ro-vibrational states, either exciting ground states to higher ro-vibrational states or de-exciting populated higher energy states (Stokes Raman scattering). The difference (in energy or wavelength) between the original ro-vibrational energy state and the resulting state is very unique for several molecular bonds and functional groups, thus molecular compositions can be identified by Raman MS. Peaks in the Raman spectra of agricultural aerosols and their tentative functional group assignments are summarized in Table 3.

For the coarse mode samples analyzed here, the mapping was performed over three of 50 μm^2 areas on the impaction substrates. One hundred Raman spectra were obtained in each 50 μm^2 area, so a total of three hundred spectra were collected in each sample substrate. This mapping procedure was employed in this study by following the technique reported in a previous study of atmospheric aerosols using RM (Ivleva et al., 2007). The Raman apparatus is equipped with a motorized stage which moves automatically in the x and y directions. By moving the stage in incremental steps (5 μm) and taking a spectrum at each step, a spectral map of the sample can be created. Based on typical coverage of exposed filter samples, most spectra represent a single independent particle. However, occasionally, a few agglomerations were observed which were large enough to be detected in multiple spectra. A detailed strategy was also developed to categorize single particle data via RM. The full details of the approach are described elsewhere (Brooks et al, in preparation), and minimal details are presented here. Laser power influences the Raman spectra of various components differently, making quantitative measurements a challenge (Brooks et al, in preparation). For the purposes of this study, an excitation laser power of 8 mW and an illumination time of 10 s were chosen for all measurements.

iii. Scanning Transmission X-ray Microspectroscopy: The measurements of carbon speciation were conducted at the Advanced Light Source (ALS) at Lawrence Berkeley National Laboratory. The ALS is a third generation synchrotron light source which produces a unique flux of radiation from the IR to the hard X-ray region of the spectrum (Prigozhin et al., 1998). In particular, beam-lines 5.3.2 and 11.0.2 of the ALS are optimized for generating radiation in the soft X-ray range (10 to 1500 eV) and applied to STXM/NEXAFS. This X-ray microspectroscopy

is element specific as the X-ray absorption edges of different elements (e.g., carbon, nitrogen, oxygen, or sulfur) occur at different energies (Ade and Urquhart, 2002). Specifically, carbon K-edge features arise from electronic transitions of inner-shell (1s) electrons to unfilled molecular orbitals or ionic bonds upon the absorption of the incident photon energy in the range of between 278 and 320 eV. The geometric and electronic bonding structure of the sample are typically characterized by electron transitions to either a π^* anti-bonding orbital of the lowest unoccupied molecular orbital (LUMO) or σ^* saturated (single) covalent bonds of higher energy unoccupied molecular orbital (HUMO) (Solomon et al., 2005). The transmission efficiency associated with these electron transitions indicates the presence of carbon molecular bonds described below.

The STXM/NEXAFS measurements for carbon speciation were performed at the carbon K-absorption and potassium-L_2/L_3 edges (278 to 320 eV). Figure 12 illustrates the theory of the inelastic interaction between soft X-ray radiation and carbon containing molecules. During measurement, a focused soft X-ray beam is generated by a tunable monochromator and a zone plate connected to the STXM. This soft X-ray illuminates the sample and scans radiation energies in the range of 278 to 320 eV (Gutiérrez-Sosa et al., 1999; Rothe et al., 2000; Stöhr, 2003). During this scanning process, the transmitted X-rays are detected and converted to the dimensionless optical density (OD) based on Beer-Lambert law (Koprinarov et al., 2002). Thus the X-ray spectrum represents OD as a function of radiation energies. In these analyses, numbers of X-ray spectra are obtained in each 30 nm x 30 nm area over the entire area of individual particles, resulting in a "stack" of spectral images. In a stack, x and y represent spatial distances and z represents increasing intensities of the soft X-ray. Thus, with given x and y coordination, these spectral data are then compiled to generate a STXM map indicating spatial distribution of OD for individual particles (Moffet et al., 2009b). Hence spectra can be analyzed on a particle-by-particle basis. Similar analysis has been applied to many studies to identify local chemical bonding of the absorbing atom and fingerprint information of atmospherically relevant carbonaceous particles (Myneni, 2002; Maria et al., 2004; Hopkins et al., 2007; Takahama et al., 2007; Day et al., 2009; Moffet et al., 2009a and 2009b).

Decomposition of some of the molecular components in the particles due to the application of electron beam during EDX analysis has been reported in a previous study (Pósfai et al., 2003). Although a low-intensity electron beam was used during the EDX spectrum acquisition to avoid decomposition, "damages" on particles due to the electron beam were also repeatedly observed during EDX analysis as well as X-ray beam during STXM measurements in

this study. In addition, the observed impact on morphological decomposition of STXM may be even more severe than that of EDX. In X-ray microscopy, NEXAFS spectroscopic transitions are highly sensitive in terms of imaging and sample volumes (Ade and Urquhart, 2002). Hence all of the STXM/NEXAFS analysis (442 particles) was conducted first then the CCSEM/EDX (48,320 particles) was followed by to minimize the damage to the specimen and associated changes in chemical bonding. A test was also run. In this test, CCSEM/EDX analysis was conducted on STXM exposed portion and unexposed portion of substrate. Each area of investigation was ~575 µm x ~575 µm. EDX spectra from these two different areas were compared. The measured elemental compositions and equivalent circle diameters agreed at the 95% confidence level, indicating no statistically significant changes in morphology and chemical bonding are due to X-ray and electron beam exposure on the particles.

D. Ammonia Mixing Ratios

i. Scrubber Collection Efficiency: The scrubbers used in this study are built in-house in the Texas A&M Chemistry Glass Shop. Following the method of Schade and Crutzen, the collection efficiencies of the scrubbers was tested in the Texas A&M laboratory (Schade and Crutzen, 1995). As in the field experiments, 10 ml of 0.1 M HCl was placed in each scrubber, and samples were collected for 20 minutes at 3 liter per minute. Gas phase ammonia was generated by stirring an ammonium sulfate solution (250 ml of 0.01 M ammonium sulfate) and allowing the scrubbers to sample the ammonia gas emitted off the solution. After collection, ion chromatography was used to determine the concentration of ammonia collected.

All ion chromatography analysis was performed on a Dionex System 4000i with a Dionex IonPac CS12 cation exchange column using 18mM methanesulfonic acid as the eluent solution and 100 mM tetrabutylammonium hydroxide as the cation regeneration solution as specified by the supplier. For these measurements, 1µl of each standard solution was directly injected into the instrument. Solution blanks containing only 0.1 M HCl were also analyzed by ion chromatography to determine if there was any ammonia emanating from the tubing and filters, and none was detected.

One advantage of using ion chromatography is that sample solutions collected in the field can be analyzed directly without any pre-analysis sample preparation. However, disadvantages are that this method consumes a significant amount of eluent and regeneration

solutions, and daily replacement of these solutions is a necessity. Further, a new calibration is required each time the solutions are changed.

Qualitatively speaking, the mass of NH_3 in the sample solution can be converted to an approximate mixing ratio in the air. In the calculation below, two measured values are used, the mass of NH_3 in the solution (M_{NH3}) determined by ion chromatography (IC) or spectrophotometry and the total volume of air sampled by the scrubber (V_{Air}). Mixing ratios are calculated according to:

$$Mixing \quad Ratio \quad NH_3 \cong \frac{M_{NH_3}}{V_{Air} \times n_{Air} \times m_{NH_3}} \qquad [5]$$

where n_{Air} is the molar concentration of air molecules, which is assumed to be 0.0409 mol L^{-1} based on standard temperature and pressure, and m_{NH3} is the molecular mass of NH_3, 17 g mol^{-1}. It is noteworthy that while this is an adequate method to generate samples containing a range of mixing ratios for intercomparing two scrubbers or two analytical methods, the mixing ratio is only an estimate, and this is not an appropriate method for direct calibration.

Tests were conducted with multiple scrubbers in parallel and the experimental errors involved in the scrubber sampling, sample preparation, and chemical analysis were examined to define the total uncertainty in the NH_3 detection technique employed in this sudy. As a secondary test, each scrubber was also set up with a second scrubber in line at the output of the first scrubber. In each case, the concentration of ammonium in the second scrubber solution in series was below the experimental detection limit, indicating that the first scrubber in each case was ~ 100% efficient, within the experimental uncertainty. A test was also run in which 2 scrubbers set up in parallel, one scrubber with a filter in the sampling line and a second scrubber with no filter, were used to sample a single source of ammonia. The measured concentrations agreed (at the 95% confidence level), indicating that no ammonia is lost due to adsorption on the particulate filter.

As an additional test, the same experiment with de-ionized Millipore water as a scrubbing solution was conducted, and it was found that the trapping efficiency was reduced to < 30%. This confirmed that it was important to collect the field samples into acid solution instead of water.

ii. Spectrophotometric Determination of Ammonia: All samples collected at Feedlot C were stored in a refrigerator, and transported to the laboratory at Texas A&M University.

Concentrations of $NH_3(g)$ and total NH_x in solution samples were determined using visible spectrophotometry following a technique developed to measure ammonium concentrations in sea water (Solorzano, 1969; Parsons et al., 1984). This is the first time that this technique, modified by us, has been applied to agricultural air sampling. In this technique, NH_4^+ is complexed with phenol solution, sodium nitroprusside solution, and oxidizing solution which act as catalysts to form indophenol compound. The optical absorbance of blue indophenol color formed with NH_4^+ is measured spectrophotometrically at 640 nm. No other peak absorption was observed except the contribution from the water (~310 nm). The technique was originally developed for ocean water samples, which have a pH of 8.2. Since the reaction forming indophenol will not occur under acidic conditions, it was necessary to increase the pH of the field samples (collected and stored at a pH of <2) by adding aliquots of 1 M sodium hydroxide (NaOH). Titrations were performed to determine the concentration of NaOH required to ensure an endpoint pH of >11. It is noteworthy that the impact of changing pH on outgassing of the ammonia that had been trapped in the acid was negligible. The experiment was conducted on eight samples with three replicates for each sample. Three days after the first analysis, the NH_3 concentrations in solution were rechecked. Within the experimental uncertainty, no change in concentrations was observed (Figure 13). For another test, pH altered standards in acid were compared to standards made in deionized Millipore water and there was no significant difference in measured concentrations. After pH adjustment, the scrubber sample (2.5 ml) was mixed with 0.1 ml of 1 M phenol solution, 0.1 ml of 1 M sodium nitroprusside solution, and 0.25 ml of oxidizing agent. Phenol solution was prepared by dissolving 20 g of analytical grade phenol in 200 ml of 95% vol/vol ethyl alcohol. Sodium nitroprusside solution was made by dissolving 1.0 g of sodium nitroprusside, $Na_2[Fe(CN)_5NO].2H_2O$, in 200 ml of de-ionized water. Oxidizing solution was produced by mixing alkaline reagent and 0.75 M sodium hypochlorite solution in volumetric ratio of 4:1. Alkaline reagent was generated by dissolving 100 g of sodium citrate and 5 g of sodium hydroxide in 500 ml of de-ionized water and sodium hypochlorite (commercially available Clorox).

After 1 hour in the dark at room temperature, 1.5 ml of solution was transferred into an acrylic cuvette and the absorbance was measured at 640 nm. In these measurements the absorbance was zeroed against a blank standard of deionized Millipore water. A minor offset in the spectrophotometric data was observed possibly due to some absorption of the solution blank. This was equivalent to 0.7 µM. A daily calibration curve was generated using solutions

containing 0, 1, 30, 50, 80, and 100 μM NH_4^+ standards. For comparison, a calibration was also performed on standards made in 0.1 M HCl solution, and no significant differences in absorbance at 640 nm were observed between the HCl and water standards. Some of the samples contained NH_4^+ concentrations exceeding the upper detection limit of the spectrometer. In these cases, the NH_4^+ solutions were diluted with deionized Millipore water in a ratio of 1:20, and the measurements were repeated.

CHAPTER III

RESULTS AND DISCUSSION

1. Properties of Agricultural Aerosols and Emissions

A. Particle Size Distributions of Agricultural Aerosols

i. Aerosol Concentrations and Size Distributions: The bin sizes of the GRIMM SMPS and PAS instruments overlap in the range of 0.3 to 0.5 micron diameter. In laboratory calibration, it was observed that the GRIMM SMPS overcounts the particles in the largest five size bins (0.5 μm and higher diameters). Briefly, the DMA scans over a range of particle mobilities which are related to their size, and the resulting particle size is measured by a CPC. Thus, the SMPS operates by scanning the particle size range by incrementally decreasing the voltage in a stepwise scan. Since the lowest voltage corresponding to the smallest particles is the last step in a scan, it is directly followed by the highest voltage. If even a small fraction of tiny particles (present in high concentrations) are not properly flushed from the system, they will be included in the large particle count obtained at high voltage and may easily contribute to a major fraction of the counted large particles. This problem was confirmed by setting the voltage at one point for a longer period of time, during operating in the laboratory. Over a period of minutes, the concentration of large particle dropped to zero. Since the field sampling was conducted in the default fast scanning mode, overcounts may have occurred in bins 0.5 to 1 μm in diameter. Thus, SMPS measurement in those bins is not reported here. Fortunately, the PAS covers this size range.

Particle loss rate due to the inlet (3/8" opening diameter stainless tube and 2' diffusion dryer) was examined. This study postulated that the particle loss rate of particle diameter (D_p) >10 μm increased to >50%, while the plumbing loss rate of D_p < 0.5 μm (size range measured by the SMPS) counts for <17%. Further description of particle loss rate due to the inlet is available in Appendix C. To minimize the loss of coarse particles, the PAS was run without the inlet. It should also be noted that the PAS measurements were conducted at ambient relative humidity, while the SMPS measurements are of the dry particle sizes. The error caused by this discrepancy is calculated and considered to be negligible (<2%) since the previous measurements of

hygroscopicity of large particles from this feedlot showed that the particles typically have very low hygroscopic factor (1.03 at 75%) (Hiranuma et al., 2008). Hence, ambient measurements of coarse particles were valid.

Field observation of aerosol concentrations and their size distributions are now described. To illustrate the uniqueness of the atmospheric environment in the vicinity of a major cattle feedlot operation, here the particle volume distributions collected with the GRIMM PAS at three different sites are included: downtown Houston, in the smaller town of College Station (home to Texas A&M), and at the designated cattle feedlot on the Texas Panhandle. While these are only snapshots of the data collected from each location, they illustrate the extreme differences in size distribution present in urban (Houston), rural (College Station) and agricultural sites. The particle size distributions averaged over a 24 hours period for each site are shown in Figure 14. While the agricultural sample contains the least submicron particles, there is a very large peak in the coarse particle mode, centered at just below 10 μm in diameter. This large size mode is much larger than those observed at the urban and small town locations (Pitz et al., 2003; Geller et al., 2006; Kannosto et al., 2008; Yin and Harrison, 2008). Also, the coarse particle mode contains two orders of magnitude more particles than in the urban and rural settings. Maximum in coarse mode concentrations occurred during evenings (9:00 pm) as further discussed below.

Hourly averaged volume concentrations ($nm^3\ cm^{-3}$) of particles measured by PAS at the downwind and upwind location in the range of 0.3 to 25 μm in diameter for the campaign period are shown in Figure 15A. In addition, actual aerosol concentrations emitted from the feed lot estimated by subtracting upwind measurements from downwind ones are shown in Figure 15B. The SMPS measurements of the downwind location for campaign period are also shown. The data collected at the agricultural site demonstrated the extremely variable source strength of coarse particles from feedlots. As these two figures illustrate, the upwind concentrations are much lower, with average concentrations of $3.9 \times 10^{10}\ nm^3\ cm^{-3}$.

Particle volume distributions simultaneously measured at the upwind and downwind locations as a function of time (July 20 to 25, 2008) are shown in Figure 16. As seen in Figure 16A, a distinct diurnal cycle can be observed with maximum concentrations of 1-hr averaged total PAS counts ($10^{13}\ nm^3\ cm^{-3}$) occurring in the evenings (9:00 pm). There are two contributing factors leading to the high concentrations observed. First, it has consistently been observed that the animals at the feedlot are most active in the evenings (Auvermann, 2000). Second, the

boundary layer height is lowest at night (Baum et al., 2008). Another feature in the diurnal cycle of the hourly averaged coarse PM concentrations is the regular occurrence of a smaller but routine peak each morning (~6 x 10^{11} nm^3 cm^{-3}). This peak coincides with daily arrival of the feed truck, and distribution of grain for the morning feeding. It should be noted that there is a sudden drop in the concentration of atmospheric coarse particles following precipitation. Intense rain in a 3 hour period from 1:00 am to 4:00 am on July 15 resulted in 6.3 mm of accumulated precipitation. Intense rain showers within such a short period lead to a sudden drop in PM concentration. Clean atmospheric conditions persisted until the rain stopped and the pen surface dried out on July 18. Afterwards, the diurnal cycling of coarse particulate volume concentrations were once again observed. Unlike the downwind location, concentrations at the upwind site are dictated by background conditions, rather than emission from the lot. As can be seen in Figure 16B, diurnal variations were not observed at the upwind site. Figure 16C shows actual size-resolved emissions from the feedlot estimated by subtracting upwind measurements from downwind ones from July 18 to 25, 2008. During such period, the concentration of coarse particles (PM_{10}) derived from the feedlot was two orders of magnitude higher than that measured at the upwind site, while the feedlot derived fine particles (PM_1) account for ~32% of the total PM_1. Thus, under conditions of low relative humidity and low soil moisture (< 0.2 vol/vol soil moisture) as occurred on July 18 and later, the concentrations measured at the downwind site exceed the background conditions of the upwind by roughly two order magnitude.

It should be noted that some variation in the fine mode concentrations was observed on July 23, which may be attributed to observed grass cutting activities at the upwind location. Specifically, Figure 17 shows the average particle size distributions for the downwind and upwind location averaged over 24 hours period as well as 8:00 am, 3:00 pm, and 9:00 pm on July 23. This figure shows that irregularly observed high concentration of coarse PM at upwind may have been triggered by preceding cleaning activity: daily arrival and departure of the cattle truck, and associated feedlot activities usually happen in south side of the feedlot (upwind) during morning and afternoon hours. Thus nearly all of the aerosol volume observed downwind of the site is sourced directly from the facility and associated activities. The only exception was observed in the evening on July 12, during which northerly wind was dominant and increased hourly averaged PM concentration up to 6.1 x 10^{11} nm^3 cm^{-3} (Figure 15A), reversing the common upwind-downwind setup.

Next the relative number, surface area, and volume observed downwind of the site are presented. Hourly-averaged size, surface, and volume distributions of agricultural aerosols measured directly downwind of Feedlot C from July 22 to 24 at 8:00 am, 3:00 pm, and 9:00 pm are shown in Figure 18. Particle distributions of July 22, 23, and 24 are shown in Figure 18 A, B, and C, respectively. The areas below the curves in top, middle, and bottom panel correspond to the total aerosol number, surface, and volume, respectively. Irregular variations in the shape of the size distributions occasionally occur possibly as a result of irregular activities in and around the feedlot, such as cattle feeding, pen cleaning, transport activity related to load and unload cattle, or else site-specific practices. For example, increased number concentration of PM smaller than 0.1 μm in diameter at 3:00 pm on July 22 may reflect that dust emissions coincided with feedlot cleaning and removal of manure deposited on surface soil conducted typically in the afternoon (Figure 18A). A similar peak was observed at 3:00 pm on July 24 (Figure 18C). The number concentrations of fine particles at 8:00 am were generally high due to the cattle feeding activities routinely conducted in the morning. Another importance of agricultural aerosol distribution can be seen in surface area and volume distribution. Unlike the number distributions, coarse-mode peaks ~10 μm in diameter regularly dominate the total aerosol surface and volume, and corresponding coarse mode concentrations were routinely and significantly higher at 9:00 pm Thus surface and volume distributions of agricultural aerosols were somewhat predictable under typical conditions observed during our campaign.

Figure 19 illustrates the daily average of coarse and fine mode mass concentration measured at the downwind location as function of time. To obtain the coarse mode mass concentrations of PM_{10} (particulate matter less than 10 μm in diameter), only the particle counts in the twelve bins up to and including 10 μm diameter were considered. For each bin, the number concentration was converted to a mass assuming that a soil density is 2.65 g cm^{-3} and all particles in the bin are spheres with a diameter equal to the average diameter in that bin. At the downwind edge of the CAFO, exceptionally high total mass concentration of PM_{10} were observed, as high as ~1900 μg m^{-3} averaged over 24 hours. In fact, PM_{10} concentration exceeded the public health guidelines set by both the U.S. Environmental Protection Agency under the National Ambient Air Quality Standards (NAAQS) (150 μg m^{-3} for 24-hour average) for most of the campaign period (10 out of 15 days). With an hourly averaged PM_{10} as high as ~13,000 μg m^{-3} measured at 9:00 pm on July 25, the suppression of coarse mode particles further illustrate the uniqueness of the feedlot as a source of coarse mode particles. PM_{10} exceedance was

especially high when the wind direction was consistently from the south throughout the day and the pen surface was dried out (< 0.2 vol/vol soil moisture). As a caveat, hourly average PM_{10} measured at the downwind location exceeded NAAQS limit at all times and even upwind measurement come close during dry period (Figure 15A). Thus, more precise particulate measurements on higher time resolution is needed to capture diurnal cycle and reflect local environment. Although $PM_{2.5}$ is designated as fine particle under NAAQS, the size-bin boundary of 2.5 μm in diameter is not available in PAS. Thus the study of fine particles is primarily limited by the closest base categorization, which is PM_2 based on the first seven bins of the PAS. It should be noted that this is a lower limit compared to $PM_{2.5}$, so the adverse impact of fine fractions may be underestimated in this study. Under the given limitation, daily averages of PM_2 comply with the existing limits (35 μg m^{-3} for 24-hour averaged $PM_{2.5}$ mass concentration) with only an exception of July 23 (45 μg m^{-3}). As mentioned earlier, observed grass cutting activities may have contributed to the increase in overall daily average of the fine mode concentrations on this specific day.

ii. Far-Field Particle Size Distribution Measurements: Additional far-field measurements were conducted to gain insight into the transport of PM from the lot. Table 4 shows the wind and PM conditions during the far-field measurements on this particular occasion. Consistent wind speed (2.4 ± 0.5 m s^{-1}) and wind direction from south (149.1 ± 8.1 degree) were observed. The time for air mass to travel from the plume source to the far-field was calculated as 30 min. 30 minute averages (9:20 to 9:50 pm) of the total PAS concentration quantitatively measured at the downwind location and far-field location were 5.8 x 10^{12} nm^3 cm^{-3} and 3.5 x 10^{11} nm^3 cm^{-3}, respectively. The average far-field PAS volume concentration fraction of the PAS concentration measured at the downwind site was 8.5% for the particle size range of 0.3 to 25 μm in diameter (Table 4). Overall far-field measurements of PM_{10} showed that only up to ~20% of aerosol is consistently transported to the surface site 3.5 km away from the lot (Hiranuma et al., 2010). During evening measurements, a particle size mode at 10 to 15 μm is consistently present at the source location while it generally shifts to smaller size range (5 to 7.5 μm) at the far-field location. For example, our success in capturing the aerosol plume on July 22 evening is illustrated in Figure 20. As shown in this figure, the volume distributions in the plume drastically shifted to smaller sizes with downwind distance from the plume source. At the far-field location, a monomodal volume concentration peak was present in the range of 5 to 7.5 μm in particle diameter while volume concentration consistently peaked in 10 to 15 μm at source. These large

particles observed at the far-field location may be attributed to the feedlot. In the afternoon hours, the mean diameter of the downwind distribution was still 10 to 15 μm while the far-field mode shifted to smaller size (2 to 4 μm). In general, the decrease in concentration and mode size with downwind distance is attributable to a combination of particle settling and plume dispersion. For instance, a 10-micron particle, assuming a soil density of 2.65 g cm^{-3}, has a terminal settling velocity of ~0.8 cm s^{-1}. Depending on vertical mixing and horizontal wind speed, a large fraction of the 10-micron particles will not reach the far-field site under typical sampling conditions. Observed wind speed was higher in the afternoon than evening (Table 4), thus leading to stronger particle deposition and dispersion rates. However, unlike large particles, fine PM at far-field occasionally exceeded the fine PM measured at the source. This may be because the emission of smaller PM is affected by other locations, such as crop field. There was an open field of recently tilled soil between the CAFO and the far-field sampling site, but the field's contribution to the plume or its depletion via dry deposition are difficult to quantify from our measurements. The increase in the far-field PM fraction of the PM measured at the downwind site (> 25%) observed on July 16 could be due to the relative increase of PM emissions from the tilled field and a lower concentration of dust from the feedlot due to the rain recorded on July 15. In summary, we found that a consistently low fraction of the PAS concentration measured at the downwind site (≤ 7.5%) was observed at the far-field site under the hot and dry conditions (i.e., soil moisture <20%) experienced after July 18.

iii. Emission Rate and Aerosol Dispersion Model: By using a simple one dimensional multi-layer model and assuming steady state mass balance through the layers, the size resolved particle emission rate over Feedlot C can be determined. The domain of the 1D multi-layer model in this study consists of an array of 10 vertical cells (height i = 1-10) (Figure 21). The concentration at each layer is assumed to be horizontally homogeneous. To define the concentration at each vertical layer, the height of each layer is computed as

$$z_{(n+1)} = \frac{\Delta z_{(n)}}{2} + \frac{\Delta z_{(n+1)}}{2} + z_{(n)} \qquad [6]$$

In which z is the center of each cell above ground surface and Δz represents the thickness of each cell. The lowest level Δz height set to be 4 m (height for concentration measurement is ~2 m) and total height to be 1500 m. The layer thickness is calculated as

$$\Delta z_{(n+1)} = \Delta z_{(n)} f \qquad [7]$$

where f is the multiplication constant ($\Delta z_{(n+1)} / \Delta z_{(n)}$ ~1.76) calculated to achieve the upper boundary of the grid at top layer using the specified number of layers. The total height (upper boundary) is defined as the average of the highest boundary layer (Table 5). The horizontal dimensions of feedlot in this model are 1 km x 1 km. This is approximately the same as the actual dimensions of the feedlot, 822 meters along the south-north oriented edge by 1130 m along the east-west oriented edge.

Steady state mass concentrations at each model layer (i) for each particle size bin (j) are defined in the following governing equation:

$$\frac{\partial c_{i,j}}{\partial t} = -\frac{u_i}{\Delta x} c_{i,j} + \frac{\partial}{\partial z}\left(k_{zz} \frac{\partial c_{i,j}}{\partial z} \right) + \left(\frac{Q_{i,j} - c_{i,j} v_{i,j}}{\Delta z} \right) \delta_{i=1} \qquad [8]$$

where c is the mass concentration of agricultural aerosols in μg m^{-3}, u is the wind speed, Δx is the distance of the south-north oriented feedlot edge, v is the dry deposition velocity, Q is the mass emission rate of particles, and k_{zz} is the vertical turbulent dispersion rate constant (eddy diffusivity). A detailed description of eddy diffusivity is available in Appendix D. The use of the Kronecker delta, $\delta_{i=1}$, limits the emission and dry deposition calculation to the first cell in the model. A boundary condition of a net particle flux of zero is set based on mass conservation. All particles originate from the first layer. A single calculated value for a net particle flux due to emissions plus losses is obtained using equation 8. The steady state solution to equation 8 is found by advancing the governing equation in time until the calculated concentration at a given time step differs from the concentration calculated in the previous time step by less than 10^{-5} μg m^{-3}. In other words, the following convergence criteria must be met:

$$\left| \sum_{i=1}^{10} c_{i,j(t)} - \sum_{i=1}^{10} c_{i,j(t+\Delta t)} \right| < 10^{-5} \mu g \ \ m^{-3} \qquad [9]$$

The operator splitting method (Oran and Boris, 1987) is used to solve the governing equation (Equation 8). This is a mathematical method that decomposes complicated systems of partial differential equation into simpler sub-problems and treats them individually using specialized numerical algorithms (Yanenko, 1971). The vertical diffusion term is computed by applying the Crank-Nicolson method (Crank and Nicolson, 1947). In numerical analysis, the Crank–Nicolson method is a finite difference method used for numerically solving partial differential equations such as the heat equation. The Crank–Nicolson method is based on central difference in space, and the trapezoidal rule in time, giving second-order convergence in time. It is used here because it is implicit in time, and is numerically stable (Crank and Nicolson, 1947).

The emission rate of particles for each size bin during a given time period can be determined by comparing the predicted steady state concentration in the first layer with the observed concentration. Here the bisection method is used to find the emission rate that best reproduced the observed concentrations. The bisection method is a root-finding algorithm which repeatedly bisects an interval then selects a subinterval in which a root must lie for further processing.

Since the mean wind speed generally increases with height in at least the lower half of the planetary boundary layer, a reasonable vertical profile of wind velocity has to be estimated using the measured wind speed at 2 meters and an assumed power law wind velocity profile (Huang, 1979; Seinfeld and Pandis, 1998):

$$u_x(z) = u_x(h_r)\left(\frac{z}{h_r}\right)^{0.15} \qquad [10]$$

where $u_x(z)$ is the wind velocity at the height z, $u_x(h_r)$ is the wind velocity at reference height (h_r = 2 m). The exponential coefficient is a function of surface roughness height (z_0) and Monin-Obukhov length (L), but it is usually assumed to be constant, 0.15 (Huang, 1979). The Monin-Obukhov length is defined as the height at which the production of turbulence by both mechanical and buoyancy forces are equal (Seinfeld and Pandis, 1998). This parameter also provides a measure of the stability of the surface layer. Further description of Monin-Obukhov length is available in Appendix D.

The dry deposition velocity for size-resolved particles is computed by the approach developed by Wesely (1989). In this approach, the dry deposition velocity is calculated as a

function of the aerodynamic resistance, the quasi-laminar layer resistance, and the particle settling velocity (Appendix D). Eddy diffusivities are computed based on the measured meteorological inputs, including surface soil temperature, air temperature, and wind speed at a reference height (2 m) using Monin-Obukhov similarity theory (Garrett, 1992) and the parameterization schemes of Lamb et al. (1975) and Businger and Arya (1974) as documented in Seinfeld and Pandis (1998).

It should be noted that the time rate change of concentration due to condensation, transport between gas and aerosol phases, and secondary aerosol production from gas-phase reactions are all neglected in this analysis. These are fair assumptions because our previous work shows that agricultural aerosols are non-hygroscopic and are generally considered to be non-reactive primary pollutants (Hiranuma et al., 2008; Hiranuma and Brooks, in preparation).

Figure 22A shows the hourly averaged mass distribution of the agricultural aerosols measured at the downwind site on July 24, 2008, assuming a soil density of 2.65 g cm^{-3}. Figure 22B shows the corresponding emission rate computed for the same time scale. As can be seen in these figures, the coarse particle fraction dominates both total observed mass and calculated emission rates. The diurnal variations observed in measured aerosol concentration are also reflected in changes in the modeled emission rate. Maximum emission rates of 1hr averaged PM_{10} (>10^8 μg m^{-2} hr^{-1}) were observed in the evenings ~21:00 CDT. Minor peaks of mass flux from Feedlot C were also observed in the morning at ~7:00 am (PM_{10} ~ $2x10^7$ μg m^{-2} hr^{-1}).

As expected, the emission rate is consistent with PM concentration measured at the downwind site of the CAFO and appears to be linearly related with the concentration (correlation coefficient r = 0.9). As a limitation, however, the model used in this study assumes a steady state condition of aerosol concentration over a prolonged interval (1 hour). This may be a problem because the atmospheric boundary layer can change within a shorter period of time thereby influencing the particle concentrations. Another limitation is the estimation of the influence of boundary layer height on the measured concentration in ground level. Table 6 summarizes the conditions of PBL and particle concentrations measured at the downwind site for the time period corresponding to Figure 22. In this table, gray highlighted areas represent times when the rate change of planetary boundary layer (PBL) is larger than10% over an hour. More specifically, the time rate change of PBL (ΔPBL, %) is calculated based on hourly averaged PBL data as $\left|\frac{PBL_t - PBL_{t-1}}{PBL_t}\right|$. During these periods, we do not consider the calculated emission rates to be

reliable. Exceptionally high rate of increase in PBL (>25%) was observed at 9:00 to 10:00 am due to thermal expansion of atmosphere. Likewise, abrupt decrease in PBL was found shortly after the sunset (8:00 to 10:00 pm). Further careful analysis is needed to determine the error introduced by falsely assuming steady state conditions when the boundary layer height is, in fact, changing. Based on Table 6, we estimate that our emissions calculated are reliable during twelve hours in the day. The estimated time rate of change of the PBL was relatively small (<10%) during these times, particularly from noon to early evening. During this specific period, averaged emission rate of PM_{10} was calculated as $1.6x10^{7}$ μg m^{-2} hr^{-1}. However unfortunately, the steady state analysis is not reliable for calculating emissions during the most interesting times in the day, that is, in the evenings when the maximum ground level concentrations of particles were observed.

Emissions can be modeled for nonequilibrium conditions though this is more difficult and would require additional modeling and greater computational resources than available for this project. Alternatively, an easier solution would be to use a tracer for which changes in concentration are directly related to boundary layer height. Hypothetically, if the rate change of the boundary layer height were correlated with the rate of change in fine mode particle concentrations, it would be reasonable to use the fine mode concentrations as an indicator for identifying changes in the boundary layer height, giving a single calculated error value with respect to the effect of the boundary layer. However, as can be seen in Table 6, during the time investigated for this modeling study there is no consistent correlation between variations in fine mode and boundary layer height at the 95% confidence level.

B. Hygroscopic Properties of Agricultural Aerosols

Having shown that the ESEM technique can be accurately used to determine the hygroscopic behavior of aerosols, the results on agricultural dust particles are reported. Water uptake studies were conducted on agricultural particles in three size ranges (>10 μm, 2.5-10 μm and <2.5 μm diameter). Within each size range, experiments were conducted on particles in each shape group observed above (Type A, B and C from Figure 5). The hygroscopic growth factor (D/D_o) and DRH of 87 individual agricultural particles from downwind samples were determined using ESEM at a temperature of 15 °C. Water uptake as a function of relative humidity is plotted in Figure 23.

A fraction of the coarse-mode particle population deliquesced at approximately 80% RH and grew to twice their original dry sizes at an RH of 96%. As can be seen from Figure 23A and 20B, distinct deliquescence behavior was observed only for the smooth rounded particles (Type A) that have dry diameters (D_o) larger than 2.5 μm. The DRH of these agricultural aerosols were determined as 79.5 ± 7.0% for particles that have D_o of >10 μm and 76.3 ± 9.5% for particles that have D_o of 2.5 – 10 μm. The hygroscopic growth factors calculated at 96% RH were 1.8 ± 0.4 and 2.0 ± 0.5 for the largest and intermediate size ranges, respectively. The maximum change in growth factor resulting from an increase of 0.1 torr in pressure (corresponding to a ~0.7 % increase in RH) was 0.4 ± 0.3 for particles in both of these size ranges. The observed variability in DRH for individual particles indicates that the composition of agricultural particles is not uniform. The observed difference in hygroscopic growth factors for each size range suggests that particle size also has an influence on hygroscopicity. In the size range of < 2.5 μm diameter, Type A particles took up only a small amount of water, starting at ~70% RH and gradually increasing up to 96% RH. In all size ranges, particles in the other shapes (Type B and C) gradually took up only a small amount of water at and above 70% RH. In these cases, no abrupt change in water uptake or particle size was observed at any RH, indicating Type B and C particles do not contain significant concentrations of deliquescent materials.

To look for statistically significant trends in uptake behavior, it was first attempted to identify several parameters which quantitatively describe a particle's water uptake behavior. The "hygroscopicity parameters" chosen were the deliquescence relative humidity (for those samples with a clearly identifiable deliquescence point), the maximum increase in the hygroscopic growth factor due to an increase of ~0.7% RH, and the hygroscopic growth factor at 96% RH (the highest RH achieved in this ESEM experiments). All data collected were pooled into data subsets according to several factors: particle dry size, particle shape, sampling location, and sampling time of day. A mean value was computed for each hygroscopicity parameter for each subset. These mean values were then compared to see if any of the data subsets were statistically unique at the 95% confidence limit (Hoshmand, 1988).

Based on this analysis, it is found that Type A particles in the 2 larger sizes (>10 μm diameter and 2.5-10 μm diameter) took up a significant amount of water near 75% to 80% RH. This deliquescent behavior is statistically different (95% confidence) than the behavior of particles in the other two shape groups which took up only small amounts of water, even at high RH. For particles smaller than 2.5 μm, Type A particles took up only a small amount of water,

starting at ~50% RH and gradually increasing above 50% RH. This behavior is similar to the behavior of particles in the other shapes (Type B and C).

DRH of 82 individual agricultural particles from upwind samples were determined using ESEM at a temperature of 15 °C. Particles collected at the upwind site took up slightly more water than those at the downwind site. While qualitatively the growth curves for particles on the downwind and upwind side of the feedlot were somewhat different, it was observed that all hygroscopic parameters were statistically similar (within 95% confidence) for the nominally upwind and downwind sampling locations. This suggests that samples collected on the nominally upwind edge have similar compositions on these days, perhaps due to horizontal mixing of feedlot dust. Likewise, samples collected during morning, afternoon and evening all exhibited similar behavior (within 95% confidence), suggesting that no notable changes in composition occur throughout the day. This implies that changes in overall concentrations and changes in relative humidity throughout the day may be responsible for changes in visibility as observed by the transmissometry measurements.

As shown in Figure 24, the results were compared to the water uptake behavior of some common components of atmospheric aerosols, including ammonium sulfate and humic materials, in a further effort to identify the possible composition of the aerosols. For these purposes, ammonium sulfate was chosen as a representative of the major component of background sulfate aerosol. Humic materials (e.g., Pahokee Peat Reference humic acid and Suwannee River fulvic acid) were chosen due to a number of studies that suggest a large fraction of organic aerosol present in the atmosphere can be classified as humic materials and due to the likelihood that the agricultural dust would contain large amounts of decaying organic matter, such as humic-like materials (Ghio et al., 1996). Interestingly, the water uptake pattern exhibited by Type B and C is very similar to the behavior of particles containing the humic materials (Brooks et al., 2004) (Figure 24). These data may suggest that particles in Shape Groups B and C collected at the feedlot may contain significant fractions of soil or humic-like materials.

C. Composition of Agricultural Aerosols and Relationship with Morphology

i. Elemental Composition of Fugitive Dust Particles: Manually Controlled EDX was used to determine the elemental composition of particles in three groups described above. In this study, particles in each size range (i.e., >10, 2.5-10 and <2.5 μm), 208 in total, were analyzed by

EDX. The averaged relative weight percentage of each element was measured for particles in three different size ranges (i.e., >10, 2.5-10, and <2.5 μm) and the shape types (Type A, B, and C from Figure 5) in this study.

EDX measurements showed that particles of all types in this study are composed predominantly of carbon. The carbon content is especially large in the non-hygroscopic particles (which included particles of Types B and C in the larger sizes and all three particle types in the < 2.5 μm diameter range). The following ten elements; N, O, Na, Mg, Si, P, S, Cl, K, and Ca were also detected in lower concentrations in particles of all types and sizes. Uncertainty in the reported percentages is within ± 3% to 5% for each element studied. The high carbon concentrations were consistent with previous findings. For example, Rogge et al. (2006) stated that the organic matter content of fugitive dust emissions from concentrated cattle operations is mainly related to the original diet and its chemical conversions in the digestive tracts of cattle. Weingartner et al. (1997) stated that the carbon particles are formed by aggregation, and some agglomeration occurs, forming branched chains which may lead to the irregular structure which recurs in Type C particles (Figure 5).

Analysis was performed to determine whether observed variations in the elemental compositions were statistically significant with respect to the morphological features. The relative weight percentage of eleven elements (C, N, O, Na, Mg, Si, P, S, Cl, K, and Ca) was compared. On average, Type A particles in all sizes contained a higher weight percentage potassium (19.0 ± 13.2%) than the both Type B and C particles. A possible source of the potassium may be the inorganic mineral additives included in cattle diets (Buchanan et al., 1996). No significant differences between particles of Type B and C were determined in any of the three sizes. This is expected since Type C is likely composed of agglomerations of single Type B particles. Other than potassium, EDX analysis did not yield any other information on composition differences of particles in the different shape groups.

ii. Characterization of Chemical Compositions by Raman: Composition of the particles has been observed on single particle basis using RM. Since RM is a high resolution but time consuming technique, only a total of 10 samples were analyzed. These samples include the upwind, downwind, and far-field samples collected in the evening on July 22 and 24. Complementary samplings in morning and afternoon were conducted at the downwind location to examine time variation in composition.

As can be seen in Figure 25A, a Raman spectrum was collected at each of the point grid on the microscope map. Multiple particles were collected and imaged in this sample. Next spectra were sorted and major peaks were identified. For example, the Raman spectra of three particles are shown in Figure 25B. Each of these particles in this sample (I, II and III) have different major components. Particle I and II are mainly composed of calcium nitrate ($Ca(NO_3)_2$) and calcium carbonate ($CaCO_3$), respectively. Unlike these, the major components of particle III are organic compounds. The broad peak at ~1500 cm^{-1} indicates the presence of amorphous carbon (Sadezky et al., 2005). Further, the Raman spectra indicate that the particles were internally mixed. For example, the spatial distribution of inorganics in all particles is mapped in Figure 26. Maps of the integrated area of individual peaks, $CaCO_3$, $Ca(NO_3)_2$, and amorphous carbon are shown in Figure 26 A, B, and C, respectively. For instance, Particle II shows up in the first two spectral maps, but not the third which indicates that the particle contained $Ca(NO_3)_2$ and $CaCO_3$, and did not contain any amorphous carbon. In contrast, Particle III is predominantly composed of amorphous carbon.

A total of 3000 spectra were analyzed for particles collected at the downwind, upwind, and far-field location in 2008. The results are summarized in Table 7. The total number of spectra recorded per investigated filter ranged from 47 to 237 depending on sampling time and location. All peaks >50 counts per second were considered to be major components. Next, spectra were sorted into several groups based on their major components. Four categories were used to classify all the 993 spectra based on similar spectral features. Other than the four major categories described below, a peak at the Raman shift, ~100 cm^{-1}, was occasionally observed. This peak is the contribution of lattice vibration in crystals (Bougeard et al., 1977).

The qualitative classification of spectra types is now described. “Organics” type classified in Table 7 includes the complex combination of characteristic Raman bands contributed from fatty acids (e.g., stearic acid) and specific organic chemical bonds. The “inorganics” include $Ca(NO_3)_2$, sodium nitrate ($NaNO_3$), and$CaCO_3$. These appeared to be a minor component (< 5% of recorded spectra). Next, any combination of inorganic peaks and organics was grouped as “inorganic dominant complex” type. Consistently low fraction of these particles (<3% of recorded spectra) was observed at each sample. Lastly, the most dominant type of spectra were categorized in “soil/soot dominant complex”. Particles in this category were characterized by the presence of amorphous carbon that coincides with broad spectra from 1050 to 1620 cm^{-1}. Quantitative characterization of carbonaceous materials within the range of the

first-order Raman bands of 1050 to 1620 cm^{-1} is described elsewhere (Sadezky et al., 2005; Ivleva et al., 2007).

Figure 27 shows representative Raman spectra of highly internally mixed particles. For example, representative Raman spectra of an inorganic dominant complex and a soil/soot dominant complex are shown in Figures 27A and 27B, respectively.

Table 8 shows detailed chemical components identified in our major inorganic categories and soil/soot dominant complex from the representative sample. A high percentage of the particles as high as 23% containing inorganic dominant complex and inorganics are found in samples from the upwind and downwind location in the afternoon and evening on July 22. For example, total inorganics from the sample collected at the upwind location on July 22 evening are shown in Table 8A. In contrast, consistently small percentage of these was observed in all samples collected on July 24 (up to 12%). Among all the mean spectral data subsets on July 22, the contributions of $Ca(NO_3)_2$ at 1050 cm^{-1} were especially high at the upwind location in the evening (9%). A possible source of inorganics may include salt component of cattle diet distributed in feedyard during feeding activity and soil-derived minerals (Buchanan et al., 1996; Ocsay et al., 2006). $Ca(NO_3)_2$ is an important component of atmospheric aerosols because it is hygroscopic compared to non-hygroscopic $CaCO_3$ and calcium sulfate ($CaSO_4$) (Gustafsson et al., 2005; Liu et al., 2008; Sullivan et al., 2009). Minor fraction of other salts ($(NH_4)_2SO_4$, Na_2SO_4, NH_4NO_3, $NaNO_3$) and mineral dust constituents ($NaHCO_3$ and Na_2CO_3) identified in this study are also hygroscopic (Ansari and Pandis, 1999; Zweifel et al., 2001), but overall contribution to particle hygroscopicity is small due to large content of less hygroscopic organics (Hiranuma et al., 2008). The strong prevalence of organic material in particles at Feedlot C is an unusual atmospheric aerosol composition scenario. In comparison, particle composition in rural areas is typically dominated by ammonium sulfate and ammonium nitrate, though areas closer to urban centers contain increased levels of organic materials according to nationwide IMPROVE network measurements (Malm et al., 2004). It should be noted that some salts, such as potassium chloride and sodium chloride have no fundamental Raman active mode (Batonneau et al., 2006). These salts are rich in feeding materials and actually have been identified in our previous study of elemental composition analysis of agricultural aerosols from the same lot (Hiranuma et al., 2008).

Overall, the fraction of soil/soot dominant complex and organics was consistently the most prevalent composition in analyzed samples, accounts for at least 75% of the total spectra

(Table 7). These organic compounds may be attributed to a combination of wide variety of sources, such as cattle, organic components of diet, dry manure on the corral surface, dust from dirt roads. Interestingly, organic particles containing fatty acids were abundant at the downwind location in the morning of July 22. Although it is difficult to specify the exact source of these, observed location- and time specific feedyard activities, such as loading and unloading of outgoing and incoming cattle and diet milling, may have contributed to this increase in population of fatty acids.

For the soil/soot dominant complex categories, inorganic inclusions represent a small percentage of the total particles. Quantitatively this accounts overall average 14% in analyzed samples. One exception to this was found at the downwind location in the evening of July 22, accounting for 51%. In general, as can be seen in Table 8B, a highly complex mixture of inorganic compounds can be found as a part of soil/soot dominant particles.

As stated above, all data reported thus far was collected with an excitation laser intensity of 8 mW. Unfortunately, the variation of Raman band with the laser excitation energy is also reported elsewhere (Escribano et al., 2001). For comparison, spectra at lower intensities (1 mW and 4 mW) were also collected to look for any variations. For example, certain organics such the amorphous and graphitic carbon peaks fluoresce significantly with laser power. For example, it was found that some of atmospheric relevant organic substances, such as polycyclic aromatic hydrocarbons (e.g., pyrene and anthracene) and humic-like substances (e.g., Pahokee Peat Soil II from the International Humic Substance Society), are only detectable below 80 mJ (i.e., 8 mW x 10 sec) of laser intensity. In our samples, terpenoids, such as beta-carotene, were found only in particles collected at the far-field location on July 24 ~9:00 pm at lower laser intensity (1 and 4 mW). It is noteworthy that source of terpenoid may be derived from an open field of recently tilled soil that was between the CAFO and the far-field sampling site as it was found only at the far-field location. Possible decomposition of beta-carotene would explain the disappearance of the peak at 8 mW (Schulte et al., 2008).

Figure 28 illustrates the intensity variation on average fractions of composition categories. For our major organic categories observed, a linear increase of fraction of organics (5% to 39%) per increase in laser intensity was found, while reciprocal relation was found between soil/soot dominant complex fraction and laser intensity (90% to 53%). Measurement uncertainties (standard deviation) on 8 mW were calculated using data of lower intensities. Average fractions of each component (inorganics, inorganic dominant complex, organics, and

soil/soot dominant complex) identified on given filters were 4 ± 0.3, 3 ± 1, 39 ± 17, and 53 ± 18%, respectively. The linear increase in organics fraction may imply that organics identified are Raman active at higher range of laser intensity and the increase in detected organics population may have influenced the relative fraction of other compounds as well as measurement uncertainties among different intensities. Further discussion on the spectral curve-fitting and associated quantitative inter-comparison of applied intensities is available in Appendix E.

D. Atmospheric Ammonia Mixing Ratio at a Cattle Feeding Facility

i. Comparison between NH_3 Measurement Methods: A series of laboratory samples generated by collecting gas from the headspace over solutions containing ammonium ions in concentrations of 20-120 μM were analyzed by both ion chromatography and visible spectrophotometry. Under standard conditions without any dilutions, this translates to atmospheric mixing ratios concentrations of ~80-490 ppbv under operating condition used in the field. The results are shown in Figure 29. The uncertainty in measurements by ion chromatography and visible spectrophotometry are ± 10% and ± 18%, respectively. Within these uncertainties, the measurements by both methods agree over the full range of concentrations. It should be noted that additional measurements at lower concentration (e.g., 1μM) may be needed for complete understanding of comparison between two techniques. Overall, the new spectrophotometry method (with a detection limit of 1 μM) employed here is an inexpensive, rapid, and accurate technique for this application. All samples collected in the field as described below were analyzed by spectrophotometry.

ii. Field Measurements: Measurements of atmospheric and soil conditions sampled throughout the 2008 campaign are shown in Figure 3. Routine samples were collected for 20 minutes at a flow rate of 3 lpm, in the morning (~09:00 am), afternoon (~03:00 pm), and evening (~09:00 pm). The wind direction was consistently southerly, with the exception of July 12, 2008. As Figure 3 illustrates, the average wind speed was 3.5 ± 1.3 m s^{-1}, and never exceeded 6.3 m sec^{-1} during the project. The average ambient temperature was 25 ± 5 ºC. Although the overall variation in temperature was small, the range of relative humidities encountered varied greatly (average 58 ± 20% RH).

During the sampling campaign, one extended period of rainy conditions occurred from July 13 to 16. In the field, a rain gauge recorded 1.0, 9.4, 10.3, and 2.0 mm of rainfall on July

13^{th}, 14^{th}, 15^{th}, and 16^{th}, respectively. During the rainy period, the soil moisture content rose to 0.2 vol/vol wet basis (Figure 3), which is considered fully saturated, based on the porosity of soil (Lawrence and Hornberger, 2007). The soil remained saturated until 3 days after the rain ended. As illustrated by the PM measurements below, saturated soil conditions are coincident with clean atmospheric conditions, and dusty conditions occur only when the soil moisture has dried out to below 0.2 vol/vol. Throughout the campaign, a diurnal cycling of the air and surface soil temperatures was observed (Figure 3). In addition, a routine peak of subsurface soil temperature at the evening was observed under dry conditions.

A time series of the total NH_x and gas-phase NH_3 concentrations (20-min averages unless otherwise stated) observed at the downwind site during 2008 is shown in Figure 30A. For comparison, the concentrations of PM_{10} measured by the Grimm PAS at the same location during that time are shown in Figure 30B. The mixing ratios of ammonia species were higher at the downwind site, with a campaign average total NH_x of 1562 ppbv and NH_3(g) of 1465 ppbv at the downwind site compared to 194 ppbv and 133 ppbv at the upwind site. At the downwind site, a maximum total NH_x mixing ratio of as 2947 ppbv was observed on July 16^{th}. This was after a day of rain, which moistened the soil and may have allowed for enhanced microbial activity. Only one downwind sample was collected in which the concentration was in the same range as the upwind samples. This was on July 13^{th}, which was an unusual day since the wind was from the north. In general, the NH_x concentration was highly variable throughout the project, and did not follow a clear diurnal cycle. Due to the large number of variables contributing to the concentration of ammonia observed, it is not possible to attribute the observed variability to a single parameter during this time period. For example, Todd et al. noted that ground-level concentrations of NH_3 observed at cattle feedlots depend strongly on the Monin-Obukhov stability length, which widely varies throughout the day (Todd et al., 2008).

As seen in Figure 30B, the concentrations of PM_{10} at the feedlot have a distinct diurnal cycle, with exceedingly high maximum concentrations, relative to PM_{10} concentrations in other urban and rural environments (Yin and Harrison, 2008). Maximum concentrations of 1-hr averaged PM_{10} ($>2.5x10^{12}$ nm^3 cm^{-3}) occurred in the evenings. These peaks are coincident with increases in cattle activity, increased boundary-layer stability, and daily minima in the moisture content of the corral surfaces (Auvermann, 2000; Upadhyay et al., 2008). Additional contributing factors to increased dust concentrations are moisture content of the corral surfaces and changes in the relative temperatures of the air and soil surface. Each evening, the air is

cooled to below the temperature of the soil. This evening temperature gradient may enhance the upward flux of dust and ammonia from the surface. While this is consistent with the diurnal behavior observed in the aerosol concentrations, no corresponding trend is observed in ammonia concentrations.

A summary of NH_3(g) and total NH_x samples collected in the morning (~09:00 am), afternoon (~03:00 pm), and evening (~09:00 pm) is shown in Figure 31. One result illustrated by Figure 31 is that the ambient NH_3 at the feedyard is almost exclusively in gas phase. In some samples, the concentration of gaseous NH_3 measured were the same as the total NH_x mixing ratios, within the uncertainty of the measurements (± 18%), indicating no detectable NH_x at all in the condensed or particle phase. Further evidence that the ammonia remains in the gas phase under the conditions encountered at Feedlot C can be found in the previous work (Hiranuma et al., 2008). In concurrent work, elemental analysis of the particles collected at Feedlot C was conducted and it was found that agricultural aerosols at Feedlot C contain large amounts of carbon but only small amounts of nitrogen-containing species (Hiranuma et al., 2008). At the relative humidities encountered during this measurement campaign (usually <75%), the particles have not undergone significant deliquescence (Hiranuma et al., 2008), which is consistent with the limited conversion of ammonia to the condensed phase (Pagans et al., 2007). The dominance of organic material in particles at Feedlot C is an unusual scenario. According to nationwide IMPROVE network measurements, particle composition in rural areas is typically dominated by ammonium sulfate and ammonium nitrate, though areas closer to urban centers contain increased levels of organic materials (Malm et al., 2004).

For comparison, the ammonia measurements collected in 2007 using the identical method are shown in Figure 31B. In 2007, with total of 34 samples, an average of 1114 ppbv and 33 ppbv NH_x was observed at the downwind and upwind sites, respectively. These values are much lower than the average NH_x mixing ratios reported for 2008, 1562 ppbv (downwind) and 194 ppbv (upwind). The observed differences are most likely due to scavenging during the more frequent rain showers during the 2007 campaign. In 2007, it rained 10 out of 25 sampling days, amounting to 40.6 mm of rain during the campaign. The average temperature in 2007, 26 ±3 ºC, was similar to the average for 2008, 25 ±5 ºC. In comparison, Koziel reported much lower concentrations of gas phase NH_3 with an hourly average of 712 ppbv observed at the same site during the Spring of 2003 (Koziel et al., 2004). However, since the time scales differ by a factor of three between these measurements and the measurements in this study, the results are not

strictly comparable. Additional measurements are needed to assess the seasonal variability of ammonia emissions.

iii. Far-Field Sampling of Ammonia and Particulates: Additional far-field measurements were conducted ~3.5 km downwind from the feedyard to gain insight into the early stages of ammonia fate and transport from the lot. As described above, a series of eight measurements of PM concentrations were conducted along the farfield road in order to identify the location of the aerosol plume from the feedlot. The success in capturing the aerosol plume is illustrated in Figure 32A. In this figure, far-field PM_{10} concentrations are plotted against PM_{10} concentrations coincidentally measured at the downwind edge of the feedlot. With the average far-field PM fraction of the coarse PM measured at the downwind site as 8.5%, a well correlation coefficient ($r = 0.9$) was found. This proves successful capturing and consistent sampling of the remnants of the PM plume, at ~3.5 km downwind. In addition, the far-field PM concentrations were less that 20% of the concentrations at the downwind edge of the CAFO (Figure 33). The decrease in concentration with downwind distance is attributable to a combination of particle settling and plume dispersion. Depending on vertical mixing, a large fraction of the 10-micron particles will not reach the far-field site under typical sampling conditions. Overall, the PM measurements indicate successful choices of far field sampling site and capture of the plume from the CAFO.

Without any loss by chemical reactions, or addition of ammonia from fresh sources, the ammonia sampled at the farfield site would be expected to be correlated with the downwind measurements. However, a much weaker correlation was found between ammonia concentration at the edge of the lot and further downwind ($r \leq 0.5$) as shown in Figure 32B. At 3.5 km, the concentrations of ammonia were more variable, ranging from ~0.1% to 23% of the downwind concentrations. The average far-field mixing ratio at this site was 180 ppbv for total NH_x and 162 ppbv for $NH_3(g)$. These average values match the average mixing ratios at the upwind site, at the 95% confidence level, though less variability was observed at the upwind location. It is noteworthy that an open field of recently tilled soil was between the CAFO and the far-field sampling site, but the field's contribution to the ammonia plume or its depletion via dry deposition cannot be quantified from the measurements. Interestingly, at 3.5 km downwind, the ammonia species are still predominantly in the gas phase.

As can be seen in Figure 33A, changes in ammonia concentrations over 3.5 km distance did not parallel the changes in PM concentrations well, and one could not be used as a tracer for the other in this particular study. However, a significant correlation ($r \sim 0.7$) was present during

the dry period, which coincided with <0.2 vol/vol soil moisture content after the evening of July 18 (Figure 33B). The poor covariance arises from the fact that the PM deposits faster, especially due to its significant settling velocity, than NHx. Specifically, based on these measurements, agricultural ammonia is almost exclusively in the gas phase near the source under the hot and dry conditions experienced at Feedlot C. It appears that the emission and dispersion of ammonia is less predictable than that of aerosols before the dry period (Figure 32B). More measurements are needed to quantitatively understand the high variability in observed ammonia concentrations. Ammonia mixing ratios depend on both conditions in the soil, where microbial activity is driven by soil temperature, moisture, and pH, and in the air, where the conversion of gas-phase ammonia to the particulate phase depends on air temperature, humidity, precipitation, and the presence and composition of preexisting particles.

2. Role of Chemistry in Ice and Cloud Nucleation

A. Single Particle Elemental Composition Analysis

A total of twenty five substrates were analyzed on a particle-by-particle basis by CCSEM/EDX. These substrates consist of 12 CVI samples and 13 ambient samples (Table 1A). At the analysis rate of ~700 particles per hour, a total of 48,320 particles deposited onto carbon coated copper transmission electron microscopy grids were analyzed. Figure 34 shows an example of particle distributions analyzed by SEM for CVI and ambient sample substrate with a magnification of 7000x. As seen from the images, the density of particles deposited on the TRAC substrate is variable. Only large cloud residues (>5 μm in diameter) are directed onto TEM grid support films during CVI sampling whereas both interstitial particles and cloud droplet residues are collected during ambient sampling, resulting in higher density of particles. As expected, aerosol coverage on TRAC samples is roughly consistent with *in situ* aerosol measurements made by other ISDAC participating groups. Likewise, higher CN concentrations are measured during ambient sampling than CVI period (Table 1B). The mean particle density, which is the fraction of particle number to investigated area, of the ambient samples was roughly 2.1×10^{-2} μm^{-2}. This value was an order magnitude higher than the mean particle density of CVI samples.

Elemental compositions were studied based on five major compositional groups: CNO, CNOSSi, NaMg, AlSiCa, and other. Once all the measurements were done, spectra were manually redistributed and qualitatively classified into these five groups based on chemical similarity. The qualitative classification of spectra types is now described. Figure 35A illustrates the classification scheme. The first group, namely "CNO" group, includes particles which contain carbon, nitrogen and oxygen in any combination. Oxygenated carbonaceous particles are ubiquitous and major components of submicron aerosol particles in the troposphere (Middlebrook et al., 1998; Day et al., 2009). Besides these major components, particles may also contain variable minor amounts of oceanic origin sulfur and silicon. If so, they are categorized as the "CNOSSi" group. With minor amounts of silicon containing species (e.g., kaolinite, montmorillonite), these particles typically appear as the organic particles with attached or internally mixed with soluble sulfate component (Zuberi et al., 2002; Hung et al., 2003; Hopkins et al., 2008). The inclusion of these soluble components is relatively important because the hygroscopic properties of carbonaceous aerosol largely depend on the fraction of soluble inorganic particles (Semeniuk et al., 2007; Day et al., 2009). The "NaMg" group is salt containing particles representatives. For pure NaCl, the stoichiometric atomic percentage of K α energy from Na and Cl is 1:1 (Laskin et al., 2006). Finally, the "AlSiCa" group represents mineral containing particles. All remaining particles are assigned to one, nonspecific group of the "other" particles.

Figure 35B shows the results of CCSEM/EDX analysis based on the preceding classification scheme. In general, elemental compositions of the ambient samples were all similar. In specific, relative fraction of CNOSSi group appears dominant in all the ambient samples, suggesting the presence of soluble sulfates containing carbonaceous particles. Though there was a little more variability in composition types observed in the in-cloud ambient samples, the difference was not statistically significant at the 95% confidence level.

In contrast, smaller contribution from CNOSSi group was found in CVI samples. One important result illustrated by Figure 35B is that the substantial fraction of salt containing particles labeled as NaMg can be found in the high IN subset. Historically, sea water and sea salt are considered as a possible source of IN (Schnell, 1977; Rosinski et al., 1986 and 1987). The backward trajectories also showed evidence that air masses sampled in this specific period (i.e., Flight Number 34) traveled near the ocean surface and ascended to the aircraft altitude (Appendix B). Hence oceanic sources may have contributed to the sodium and magnesium

enrichment in particles, thereby possibly enhancing nucleation ability to ice phase. Unlike other three groups, "AlSiCa" and "other" appeared to be minor types. Relative contributions of the AlSiCa particles normally remain at ~1% to 7% level and largely the same throughout the entire samples (Figure 35B).

For more insightful comparison, a mean value of each compositional group for each subset of sampling conditions was computed and compositional variability was analyzed. The results are shown in Figure 36. As can be seen, the average CNO fraction was calculated as 27% for biomass samples, 15% for the cloud-free samples, 11% for the in-cloud (ambient) samples, 39% for the in-cloud (CVI) samples , and 39% for the samples collected during high IN conditions (Figure 36A). These mean values were compared to see if any of the data subsets are statistically unique at certain confidence limit. The results of statistical analysis showed that the data subsets collected during CVI period contain higher fraction of CNO compositional group compared to the ambient samples at the 75% confidence limit. Likewise, the average CNOSSi fraction is calculated as 58% for the biomass samples, 65% for the cloud-free samples, 65% for the in-cloud (ambient) samples, 36% for the in-cloud (CVI) samples, and 15% for the high IN samples (Figure 36B). Associated mean comparisons show that the data subsets collected during ambient contain a higher fraction of CNOSSi compositional group than CVI-ON samples at the 85% confidence limit. It should be noted that the dominance of carbon (>90%) in particles at each substrate is typical. Mean fraction of carbon in CNO and CNOSSi is computed as 96% of the total number of atoms and 93%, respectively. Thus combined with preceding CCN measurements (Table 1B), the result suggested that even with small inclusion of sulfur and silicon, particles in CNOSSi group can act as an efficient CCN. Sulfur and silicon containing particles may also act as potential IN. In fact, as mentioned earlier, previous studies of the Arctic aerosol composition showed that large amount of sulfur and silicon containing carbonaceous compounds were found in IN during both the Arctic spring and autumn (Rogers et al., 2001; Prenni et al., 2009). However there must be other compositions in combination with CNOSSi that trigger ice nucleation. The relative fraction of NaMg in high IN samples (42%) is statistically unique at the 85% confidence level as compared to other subsets ranging from 6% to 19% (Figure 36C). It should be noted that large variability observed in the in-cloud (CVI) subset may mean the variability in the amount of oceanic derived salts that potentially act as efficient IN. For the same reason given earlier, the back trajectory analysis showed that the aircraft flew

through an air mass that had ascended from the sea level (Appendix B). Subset average of the "other" fraction ranges from 1% to 7%.

Figure 37 shows elemental ratios of magnesium to sodium for salt containing particles in all twenty five samples. The dominance of sodium in particles at each substrate was typical but magnesium content occasionally reached > 10% only in CVI samples. Magnesium fraction was especially high in the high IN activity period. Previous X-ray elemental composition study conducted by Rosinski et al. (1986) observed occasional increase in magnesium in ice-forming nuclei (> 1 μm D_p) collected over the Pacific Ocean off the coast of New Zealand. Oceanic sources are likely to have a spatial and seasonal dependence, related to variations in biogenic activity. Mineral dust may be another potential source of magnesium. For example, the presence of substantial amounts of magnesium containing mineral dust and sea salt in the form of cirrus ice residue were observed in lower latitudes by *in situ* aerosol mass spectrometry during a dust transport event from the Sahara to midlatitudes (Cziczo et al., 2004). Thus one unique contribution of this study to the understanding of ice nucleation is that the particles containing magnesium that are potentially of sea spray and mineral origin were abundant in high IN samples, and may play an important role in ice phase cloud formation. In addition, the analysis suggests that even little inclusions of magnesium salts may facilitate IN activation. The dominance of carbon (>70%) in salt bearing particles is typical and largely the same over the entire period. Previous studies also showed that nearly all aerosol particles consist of mixed particles containing salts from the ocean water attached to an organic matrix (Rosinski et al., 1986 and 1987). In addition, a relatively large population of particles in the "other" group was found in the ambient samples compared to CVI samples, indicating that this analysis may be missing the identity of some essential nuclei (Figure 36D).

Figure 38 illustrates chemically resolved particle size distributions determined from the CCSEM/EDX data combined for twenty five analyzed samples. The size distribution in this figure indicates a monomodal mean size of CNO, CNOSSi, NaMg, AlSiCa, and other as 0.34, 0.44, 0.47, 0.43, and 0.44 μm, respectively. The mean size of CNO particles (0.34 μm) is statistically smaller at the 95% confidence level as compared to other composition categories (0.43 to 0.47 μm). Although no statistical difference is observed, mean size of salt containing particles are larger than others. Another TRAC-CCSEM/EDX study reported the mode diameter of residual sea salt particles in the CVI samples collected at the ground site located in Point Reyes National Seashore, ~1 km from the coast, were larger (D_p ~0.8 μm) than sulfur rich

particles (D_p = 0.4 to 0.5 μm) (Hopkins et al., 2008). Thus particle size influences chemistry; therefore a particle's ability to nucleate as IN. As a caveat, it is noteworthy that particles that have D_p < 0.3 μm were not counted for a particle-by-particle basis analysis.

One consideration is that the size distributions measured in CCSEM/EDX are not directly comparable to that measured in STXM/NEXAFS. In particular, mean particle diameter measured in CCSEM/EDX (0.4 μm) was smaller than that in STXM/NEXAFS (0.5 μm). The main factors contributing to this discrepancy are the difference in total number of particles analyzed in each technique and corresponding analysis process. As mentioned earlier, CCSEM/EDX was automated computer controlled technique. Two order magnitude higher number of particles was analyzed in CCSEM/EDX. Also because small particles can form due to impaction on substrate, analysis is restricted to particles larger than a size of 0.3 μm in diameter. In contrast, STXM/NEXAFS was manually controlled inspection basis so no strict cut-off size was employed, but the STXM/NEXAFS analysis is highly labor intensive. Thus it was only possible to analyze fewer particles than CCSEM/EDX. Each technique has both advantages and disadvantages in terms of particle size measurements. The CCSEM/EDX provides statistically relevant knowledge about morphology and size because of its high analysis rate and imaging capability.

B. Analysis of NEXAFS Absorption Spectra

To obtain chemical bonding information, complementary analysis of single particles using STXM/NEXAFS was conducted. A total of seven samples from the ISDAC were surveyed using STXM/NEXAFS and are reported here (Table 1A). A total of 442 particles from ISDAC were analyzed by STXM. As an example, several independent particles collected in high IN sampling condition were given in Figure 39A. For illustration purposes, the NEXAFS spectra of two particles are shown in Figure 39B. In addition to characteristic absorption of the C 1s → $\pi^*_{R(C^*=O)OH}$ transition for COOH groups identified at 288.5 eV in both particles, each of the particles (I and II) had different major components. In particular, a spectrum of particle I had significant contribution from carbonate (CO_3) at 290.4 eV while a spectra of both particle I and II display characteristic absorption of sp^2 hybridized carbon-carbon double bonds at 285.1 eV. All other identified functional groups described the different spectral features of the carbon edge and allowed for additional physical insight to be gained from the NEXAFS spectra.

Table 9 summarizes the mean characteristic absorption of NEXAFS spectra that incorporates individual particles in multiple sampling conditions. This table provides chemical bonding information (electronic transition and functionality) as well as corresponding position of peaks relative to the applied energy in the range of 278 to 320 eV (i.e., carbon K-edge). As can be seen in the table, relatively smaller inclusion of total carbon (i.e., edge step peak area) were found in CVI samples compared to the ambient samples, inferring the abundance of non-carbon species, such as sea salts and mineral salts. More important information was found in the fractions of carbon-carbon sp^2 bonds and carbonate. The abundance of sp^2 hybridized C=C bonds, characterized by the large peak at 285 eV, has been considered an indication of the presence of black carbon (soot) or brown carbon (soil or humic-like substances) (Hopkins et al., 2007). Likewise, any presence of characteristic absorption of the K 1s $\rightarrow \pi^*_{C^*O3}$ transition identified at 290.4 eV is indicative of the presence of carbonate. Interestingly these two peaks were preferably found in high IN samples. Statistical treatment of the dataset using a mean comparison supportively showed that the black or brown carbon and carbonate fractions are statistically significant in CVI samples, especially during the high IN activity period. Thus the findings in this study may add convincing evidence of ice nucleation by black or brown carbon that has been hypothesized from some controlled laboratory studies (DeMott et al., 1999 and 2009; Koehler et al., 2009). Identification of carbonate particles collected during the high IN activity period is a unique aspect of this study. Though there is a seasonal dependence related to variations in phytoplankton's activity, carbonate ions are present at some level in aerosols collected above in the Arctic Ocean throughout the year (Bates et al., 2009). Other local sources of carbonate include soils minerals and freshwater streams in the Arctic (Keller et al., 2007). Thus, in addition to the previously found constituents that possibly contribute to ice nucleation, carbonate may also play an important role in heterogeneous ice nucleation.

The degree of internal mixing state in individual particles was studied by spatially mapping the chemical phases: organic carbon (OC), black or brown carbon (BBC), inorganic species (IO), and carbonates (CO_3). The qualitative classification of these chemical phases is now described. The OC phase indicates a large contribution from the C 1s $\rightarrow \pi^*_{R(C^*=O)OH}$ transition for COOH (carboxylic) groups identified at 288.5 eV and minor contributions from nitrogen containing organics, sulfur containing organics, and carbon-carbon sp^2 bonds (C=C) at 285 eV (Moffet et al., 2009a). Carbon-carbon sp^2 bonds (C=C) rich particle regions itself are indicated as BBC, which could be black carbon (soot) or brown carbon (soil or humic-like

substances). IO phase can be indicated as the fraction of pre absorption edge optical depth (OD_{pre}) occurring between 278 and 280 eV in NEXAFS spectrum to post absorption edge optical depth (OD_{post}) at 320 eV (Moffet et al., 2009b). IO can be quantified as OD_{pre}/OD_{post} because the OD_{pre} is proportional to the number of non-carbon atoms and OD_{post} is proportional to the total carbon (Henke et al., 1993). From the fact that there were not much mineral elements (Al, Si, and Ca) or metallic elements (Mn, Fe, Zn, and Pb) found in the sampled particles, the increase in inorganic fraction may attribute to the increase in salt particles (sodium and magnesium) and secondary formed sulfate particles. The increase in these inorganic fractions has been reported in the marine boundary layer of lower latitudes (Hopkins et al., 2008). Any presence of characteristic absorption of the K 1s $\rightarrow \pi^*_{C*O3}$ transition for carbonate functional group identified at 290.4 eV is indicated as carbonate.

For example, Figure 40 shows spatial distributions of identified phases in representative particles collected during high IN activity period. Degree of internal mixture state is also visually inferred from this figure. For instance, the particle including carbonate with organic carbon (i.e., carboxylic) coating around inorganic core is found in particle I (Figure 40) and associated STXM spectra (Figure 39B), but not in particle II. In addition, both Particle I and II does contain black or brown carbon.

Once all chemical phase mappings on a particle-by-particle basis were done, particles were manually resorted into several major groups based upon the chemical phase present within individual particles. Eight major groups used in this study include: (1) OC, (2) OC IO, (3) OC BBC, (4) OC IO BCC, (5) OC CO3, (6) OC IO CO3, (7) OC BBC CO3, and (8) OC IO BBC CO3. Then population of each group was counted with respect to sampling conditions. The results are shown in Figure 41. As illustrated in this figure, the fraction of homogeneous OC particles (green) is much greater in biomass (72%) than other sampling conditions (10% to 42%). This increase in homogeneous OC particles may be related to the high fraction of water-soluble sulfur containing organics evidently supported by the CCSEM/EDX analysis (Figure 35B). Some atmospheric relevant carboxylic acids are also known to be hygroscopic. Peng et al. (2001) studied the hygroscopicity of low molecular weight dicarboxylic acids using an electrodynamic balance and found that some acids (malonic acid, gultaric acid, citric acid, malic acid, and tartaric acid) showed hygroscopic growth factor 1.3 to 1.5 at 90% relative humidity. Thus combined with the fact that OC phase includes a large contribution from carboxylic group, these water-soluble organics may have nucleated as CCN and undergone condensational growth.

There was not much difference between other two ambient samples. The difference observed between homogeneous OC dominant biomass samples and other two ambient conditions is the increase in the fraction of OC IO mixtures. OC IO fraction in biomass is 8% while samples from other two conditions indicate >45%. Slightly greater inclusion of inorganic elements in these samples compared to biomass samples can be inferred from preceding elemental composition analysis (Figure 35B). Most likely source of inorganic would be sea salt particles and secondary formed sulfate particles. These compositions may further contribute to enhance a particle's ability to nucleate as CCN.

In general, CVI samples are characterized with the variability in chemical phases and the increase in the fraction of non-homogeneous mixed-particles. The particle structure of organic carbon (i.e., carboxylic) coating around inorganic core is commonly found for nearly all particles observed in CVI samples. Small inclusion of other chemical phase was also characteristic. Specifically, the increase in carbonate containing particles (OC CO3, OC IO CO3, OC BBC CO3, and OC IO BBC CO3) is a very unique feature of CVI samples (Figure 41). For instance, more than 29% of particles collected during CVI contain carbonate, while the ambient samples indicate <13% carbonate inclusion. Additional details of the CVI samples can be gained by comparing in-cloud (CVI) and high IN. As expected, carbonate and BBC were preferentially observed in high IN samples. The increase in black or brown carbon containing particles (32%) as well as higher order mixtures is characteristic to the samples collected in the high IN sampling condition. Consistent with the STXM/NEXAFS spectral analyses described earlier (Table 9), the analysis of spatially mapped chemical phases also showed that the particles collected in high IN activity period was rich in inorganics, black or brown carbon, and carbonates.

Figure 42 illustrates chemically resolved particle size distribution obtained from STXM/NEXAFS. The average size of the carbonate and black or brown carbon containing particles with higher order mixtures (e.g., OC IO BBC CO3 fraction) computed as 1 μm in diameter is bigger than non-carbonate containing particles (0.4 to 0.6 μm in diameter). At the 95% confidence level, particles with inorganics, carbonate, and black or brown carbon are statistically larger than other types. Samples analyzed during the high IN samples contained large fraction of sodium and magnesium containing particles. The mean size of salt (sodium and magnesium) containing particles appeared to be larger than others as mentioned in elemental composition analysis. In general, particle size and chemistry are the most important essential factors influencing a particle's ability to act as heterogeneous nuclei (DeMott et al., 1994). For

example, according to the *in situ* measurements reported by Cziczo et al. (2004), large particles (>0.75 μm in D_p) coincided with a high fraction of ice residue, containing a mixture of sea salt and mineral dust whereas smaller particles are of soluble interstitial components, such as sulfates and nitrates. This interrelationship between composition and size was also found in laboratory studies that focused on the nucleation of ice from mineral dust coated by thick layers of aqueous sulfate species (Zuberi et al., 2002; Hung et al., 2003). In the case of this study, the STXM/NEXAFS data suggest the high abundance of inorganics, carbonate, and black or brown carbon in internally mixed particle can affect the ice nucleation properties of aerosols in Arctic and therefore influence their role as IN. However, the results in this study cannot determine whether the fundamental reason for the increase in IN activity was due to the physical or chemical properties.

CHAPTER IV

SUMMARY AND CONCLUSIONS

1. A Case Study in the Unique Properties of Agricultural Aerosols

Particulate matter emissions have impacts on air quality and human health as well as radiative properties and climate. While efforts have been made to characterize urban anthropogenic aerosol emissions, similar efforts are seriously lacking in agricultural settings. This study represents the most comprehensive onsite measurement campaign of the chemical and physical properties of aerosols at a representative CAFO in the Texas Panhandle. As our results indicate, aerosols at the feedlot are unique in size, concentration, composition, and diurnal cycle from those emitted in other urban and rural locations. Thus fundamental assumptions of aerosol properties must be revised when evaluating feedlots as local and regional emissions.

Two instruments, a GRIMM SMPS and a GRIMM PAS Model 1.108 were used simultaneously to measure size distributions over the broad range of 0.01 to 25 microns diameter. Extremely high atmospheric loadings of hourly averaged PM were measured by PAS, up to 10^{13} nm^3 cm^{-3} in volume and roughly 13,000 $\mu g\ m^{-3}$ in mass. Two major factors that contributed to the high concentrations routinely observed at evening included an increase in cattle activity and decreased boundary layer height. Between 7:00 and 8:00 am each morning, lesser peaks of up to 1.9×10^{12} nm^3 cm^{-3} in volume and roughly 5000 $\mu g\ m^{-3}$ in mass (hourly averaged) were observed during coincident daily distribution of grain to the lot during feeding activity.

Size distribution measurements showed that coarse particulates, of 10 μm in diameter and greater, dominated the particulate volume concentrations. Strikingly, the coarse particle mode routinely observed at the feedlot contains two orders of magnitude more particles than typical urban and rural measurements. With a daily averaged PM_{10} as high as ~1900 $\mu g\ m^{-3}$, the National Ambient Air Quality Standard for PM_{10} was consistently exceeded for the daily average limit of 150 $\mu g\ m^{-3}$. In contrast, concentrations of submicron particles observed at the feedlot are similar to average urban concentrations. Our measured PM_2 mostly complied with the $PM_{2.5}$ standard during our two weeks sampling period of continuous observations. Only exception was on July 23. Grass mowing activity conducted in the lot on this specific day possibly contributed

to the increase in fine particle concentrations. The observed particle distributions directly downwind of the feedyard were similar in shape and mode locations (10 μm in diameter and greater for volume or mass) as those reported by Martin et al. (2008) and Schneider et al. (2001) for a swine facility. Thus the high concentrations and preceding diurnal cycle of coarse mode particles evidently suggest that the open-air cattle feedlot is a unique source of coarse mode particles, deteriorating local air quality (Upadhyay et al., 2008) and potentially onsite worker health (Priyadarsan et al., 2005).

Our far-field measurements of size-resolved PM concentration showed that ground level concentrations at a distance of 3.5 km away from the lot was typically 8.5% of concentration at the downwind edge of the facility. During evening dust peaks, a particle size mode was observed to be in the range of 10 to 15 μm in diameter at the source location whereas it generally shifted to smaller size range (5 to 7.5 μm) as it reached the far-field location. Main factors that cause such decrease in the size of transported particle include particle deposition and dispersion.

In addition, the emission rate of agricultural aerosols was estimated using the particle size distribution measurements from the downwind site in 2008. The box model analysis was conducted by assuming steady state for mass concentrations. The results of the box model analysis showed that hourly averaged PM_{10} emission rate reached $>10^8$ μg m^{-2} hr^{-1} in the evenings and ~ $2x10^7$ μg m^{-2} hr^{-1} during morning peak hours. However, this result must be used with caution because steady state mass concentration may be invalid for half of the day, especially during the time period when a significant change in PBL height is observed. Larger than 25% rate change of PBL was observed both in morning (9:00 to 10:00 am) and evening (8:00 to 10:00 pm). On the other hand, the time rate of change of PBL depth was relatively small (<10%) during daytime , particularly from noon to early evening. We estimate that our emissions calculated are reliable during these six hours. During this specific period, averaged emission rate of PM_{10} was calculated as $1.6x10^7$ μg m^{-2} hr^{-1}. As a future study, emissions for non-equilibrium conditions and quantification of the effect of the boundary layer must be invoked for obtaining insights into agricultural aerosol emission and its relation with diurnal variation and meteorological conditions. Horizontal turbulent dispersion also must be invoked relative to vertical dispersion and horizontal advection. Finally, coagulation is another important process that can influence both particle concentration and size distribution. Thus coagulation must be incorporated in the box model.

The study of hygroscopicity was conducted in an effort to characterize the morphological, hygroscopic, and chemical properties of agricultural aerosols and to attempt to identify any correlations between these properties. Size-selected aerosol sampling was conducted on a large cattle feedlot near Tulia, TX. A cascade impactor aerosol sampler was employed at both the downwind and upwind edges of Feedlot C.

In each of the size ranges (i.e., >10, 2.5-10, and <2.5 μm), high resolution images of the particles were obtained with ESEM. The shapes of nearly all particles collected could be described by one of three shape types: (A) smooth, rounded particles, (B) amorphous particles, or (C) agglomerations of multiple amorphous particles. Overall, the corresponding number percentage for each shape group were roughly 7% for Type A, 82 % for B, and 11% for C.

The water uptake behavior of size-selected agricultural aerosol was observed by ESEM as a function of relative humidity. In the size ranges of 2.5 to 10 μm diameter and > 10 μm diameter, aerosols of Type A had deliquescence points of 75% to 80% and increased to hygroscopic growth factors of 2 at RH 96%, while particles in Type B and C exhibited low water uptake over the full range of relative humidities studied (up to 96% RH). At sizes less than 2.5 μm diameter, particles of all shaped exhibited low water uptake.

Any statistically significant differences in hygroscopicity of particles collected at the nominally downwind and upwind edges of Feedlot C were not observed. Hygroscopic parameters considered in this analysis include the deliquescence relative humidity (for those samples with a distinct deliquescence point), the maximum increase in the hygroscopic growth factor due to a 0.1 torr increase in pressure corresponding to a 0.7% to 0.8% increase in RH, and the hygroscopic growth factor at 96% RH (the highest RH achieved in this ESEM experiments). Likewise, samples collected during morning, afternoon and evening had similar hygroscopicity.

Here it was observed that a percentage of the coarse agricultural particles readily take up water, while particles at the lower end of this range (< 2.5 μm) do not. The results in this study suggest that the changes in light scattering and visibility in the vicinity of cattle feedlots may be driven, in part, by water uptake and increased size of coarse particles as a function of changes in relative humidity. Water uptake by the extremely high concentrations of coarse particles at the feedlot contributed to the increase in light attenuation and degradation of visibility causing the poor correlation between PM concentrations and extinction coefficient at high relative humidities (RH > 80%). This is interesting since under most atmospheric conditions, it is the fine, rather than coarse, particle fraction that drives changes in visibility. It is noteworthy that the

water uptake measurements by ESEM cannot be performed on particles at very small sizes (<1 μm). At low RH, measurements of total PM are strongly correlated with total extinction (Hiranuma, 2005). However, as one would expect based on the results presented here, at higher RH, this correlation is weakened. Further studies will include simultaneous measurements of mass concentration, extinction coefficient and hygroscopicity. The hygroscopicity data could be used to develop an RH-dependent correlation factor to account for changes in particle size and light scattering ability. RH-adjusted particulate mass concentrations could then be used as an accurate proxy for aerosol extinction over a broader range of RHs.

In addition to physical measurements, the offline measurements of single particle compositions were performed using RM. The composition of particles at the feedlot was mainly composed of organic compounds. The major component of aerosols at the feedlot was soot or soil material in 53 ± 18% of the particles analyzed. Particles containing other smaller organics comprised an additional 39 ± 17% of the total particle population. The remaining particles contained either strictly inorganics or mixtures of inorganics and organics. The presence of abundant calcium was often associated with soil-derived particles (Krivacsy and Molnar, 1998; Ocsay et al., 2006).

Substantial amount of fatty acids observed at the downwind location in the morning of July 22 may have been contributed from cattle transport and onsite diet milling. Another interesting feature of organic composition was found in soil/soot dominant particles. High fraction of organic-inorganic mixture (51% of total population of the sample) was found in the sample collected at the downwind location in the evening of July 22, possibly derived from corral and pen surface during routine evening dust.

In addition, elemental analysis of the particles showed that the largest fraction of chemical composition of agricultural aerosols was carbon (>75%). Also, Type A particles in the size range of > 10 μm and 2.5 – 10 μm contain significant amount of potassium (~19%). This indicates that potassium may enhance the hygroscopicity of agricultural aerosols. Schönherr and Luber (2001) reported that salts of potassium deliquesce over a wide range of relative humidities (KCl 86%, K_2CO_3 44%, KNO_3 95%, and KH_2PO_4 97%). To further explore the relationship between hygroscopicity and chemical composition, future studies of chemical composition analysis are needed. For example, Raman microscopy, can be used to obtain more detailed chemical information on a particle by particle basis.

During the summers of 2007 and 2008, total and gaseous ammonia were collected at the nominally downwind and upwind edges of Feedlot C, as well as ~3.5 km farther downwind of the lot. Off-line analysis of field samples to determine NH_3 mixing ratios was performed using a new spectrophotometric method. Comparisons showed that results from this method and standard ion chromatography agreed very well. The new spectrophotometry approach provides an excellent alternative to ion chromatography, and is faster, easier, and less expensive than chromatography.

At the downwind edge of the CAFO, exceptionally high mixing ratios of total NH_x were observed, as high as ~2900 ppbv averaged over 20 minutes. At this site, mixing ratios of at least 1000 ppbv of NH_3 were observed under both dusty and relatively dust-free conditions. The mixing ratios observed at the upwind location were an order of magnitude lower ($\leq$ 200 ppbv). It is noteworthy that while the concentrations observed at the downwind site of this ~45,000 head cattle feeding operation comply with the existing limits set by the U.S. National Institute of Occupational Health and Safety (< 35 ppm averaged over 15 minutes), the daily peaks exceed the worker-exposure guideline set by both the U.S. Environmental Protection Agency (141 ppb) and the U.S. Department of Health and Human Services (1.7 ppm for acute exposure of 1-14 days and 0.3 ppm for chronic exposure) (Wathes et al., 2003). Conditions in the atmosphere and in the soil were also measured to explore how these influence ammonia concentrations. Regression between ammonia mixing ratio and single meteorological parameter was examined in the way that ammonia data subset (both total NHx and NH_3(g)) were plotted against the simultaneously collected meteorological and soil parameters over same time period. No statistical correlation was observed. Elucidation of dependence on these parameters may be possible but will require measurements over a longer period of time and consideration of the combined influences of multiple variables to fully explain the complex variability observed in concentrations of gaseous and total ammonia species.

In addition, far-field measurements of PM_{10} showed that only up to ~20% of aerosol is consistently transported to the surface site at a distance of 3.5 km away from the lot. The ammonia concentrations at the far-field site were also significantly and variably lower than at the edge of the lot, ranging 0.1 to >20% of the concentrations at the downwind edge of the facility, with average concentrations comparable to the upwind site. One unique contribution of this study to the understanding of agricultural ammonia is that ammonia emitted from the cattle feeding activities was almost exclusively in the gas phase, even in the presence of extensive

particle loadings. Under conditions typically occurring elsewhere in the atmosphere, this would be unlikely. However, based on the predominately organic composition and low hygroscopicity of particulates at Feedlot C, it is inferred that the moisture content of PM during the 2008 project was rarely high enough for significant adsorption and absorption of NH_3 to occur (Hiranuma et al., 2008). Overall, this study provides a better understanding of ammonia emissions from an open-air animal feeding operation.

In conclusion, this study includes important measurements on the chemical and physical aspects of agricultural aerosols and the health concern they poise for local workers and others in the region. Our analysis of particle size distribution and composition showed that agricultural aerosol represents a complex mixture, both in terms of size and chemical composition, and it largely contains less hygroscopic salts in particles with a small inclusion of potentially water soluble constituents. In terms of health concern, acute exposure to very high concentrations of agricultural PM_{10} during feedyard operation may contribute to cardiovascular diseases and complications (Schicker et al., 2009). Thus at the feedlot, precautions, such as wearing certified inhalation protection, should be taken to avoid over exposure during peak times in the evenings. While local levels are a health concern for individuals working at the facility, the coarse particles observed are likely to experience rapid deposition, resulting in minimal transport and little or no regional scale impacts.

2. The Role of Chemical Composition in Ice Nucleation during the Arctic Spring

Detailed chemical characterization of aircraft-sampled particles from cloud residues and interstitial aerosols collected during ISDAC in 2008 was investigated to understand the possible connection between chemistry and nucleating ability. In particular, this study focused on the microspectroscopic analysis of individual particles sampled from mixed-phase Arctic stratus clouds off the coast of Barrow, Alaska. In addition, chemical characterization of particles collected during cloud-free conditions and biomass burning plume were performed for comparison.

CCSEM/EDX analysis suggests that submicron particles containing magnesium that may originate in sea spray, surface soil, or freshwater stream are present in the aerosol populations during high ice nucleation activity, suggesting that these magnesium containing particles play an important role in IN activation in Arctic clouds. At the ambient water

supersaturation and ice super saturation encountered during the high IN sampling period, the particles containing salts (i.e., sodium and magnesium) coupled with insoluble organic species can act as effective heterogeneous ice nucleation. Observed ice crystal concentrations during the high IN activity period were three order magnitude higher than cloud-free conditions. Elemental composition of biomass and other ambient samples were generally similar and characterized with a mixture of sulfur and silicon containing carbonaceous particles. Possible source of sulfur and silicon include chemically aged sea salt, secondary formed sulfate particles, and transported mineral aerosols from mid-latitudes (Hopkins et al., 2008; Prenni et al., 2009).. Overall, comparison between CVI samples and ambient samples suggest that that interstitial aerosols are likely to consist of substantial fraction of soluble sulfur and silicon containing carbonaceous particles while cloud residues contains relatively less amount of these particles, possibly deactivating particles' ability to condensate.

Chemical bonding of carbonaceous particles is studied by STXM/NEXAFS. Degree of internal mixture and spatial distributions of identified constituents were also examined. In biomass samples, the fraction of homogeneous organic carbon is dominant, accounting for 72% of the total population of interstitial aerosols and cloud droplet residuals. This high abundance of homogeneous organic carbon particles was consistent with the high fraction of water-soluble sulfur containing organics identified in the CCSEM/EDX analysis. Particles containing hygroscopic, or at least semi-hygroscopic, carboxylic functionality were also included in the homogeneous organic carbon. In the samples collected during flight through a biomass burning plume, carboxylic and sulfuric acids were the dominant overall composition. Due to their hygroscopic nature, these organics may preferably act as CCN rather than IN. Other ambient samples contained relatively higher fractions of organic and inorganic mixtures and less purely water-soluble organics than found in the biomass particles. The most likely source of inorganic would be sea salt. When present, magnesium salt may further enhance a particle’s ability to nucleate to the liquid phase. As compared to the ambient samples, CVI samples were generally characterized with their variability in chemical constituents and the increase in the fraction of non-homogeneous mixed-particles. Specifically, abundance of carbonate and black or brown carbon found in internally mixed particles collected during high IN activity period may affect the ice nucleation properties of aerosols in Arctic and therefore influence their role as IN. These well known non-hygroscopic components may deactivate a particle’s ability to condensate and act as

compensatory IN. The qualitative analysis suggests that even little inclusion of carbonate and/or black or brown carbon may have significant impact on the IN activation.

In addition, chemically resolved particle size distribution was obtained from both CCSEM/EDX and STXM/NEXAFS. In elemental composition analysis, mean size of sodium and magnesium containing particles (roughly 0.5 μm in dimater) appears to be larger than mean diameter (roughly 0.4 μm). Similar observation is reported from mid-latitude samples (Hopkins et al., 2008). One unique result was obtained during STXM/NEXFAS analysis. In chemical bonding analysis, particles with carbonate and black or brown carbon (roughly 1 μm in diameter) are statistically larger than mean diameter (roughly 0.5 μm). Carbonate and black or brown carbon containing particles appear to be higher order mixtures with inorganic and organic species. Based on the fact that high IN samples contain large fraction of sodium and magnesium containing particles, inorganic found in high IN samples may consist of a lot of sea salt and mineral derived magnesium rather than secondary formed sulfate particles. These salt inclusion is especially important because sea water has been considered as a possible source of IN as mentioned earlier (Schnell, 1977; Rosinski et al., 1986 and 1987). In general, particle size and chemistry are the most essential factors influencing a particle's ability to act as heterogeneous nuclei (DeMott et al., 1994). In the case of this study, the STXM/NEXAFS data suggests the high abundance of inorganics, carbonate, and black or brown carbon in internally mixed particle can affect the ice nucleation properties of aerosols in Arctic and therefore influence their role as IN. However, this study cannot determine whether the fundamental reason for the increase in IN activity is due to the physical or chemical properties.

In conclusion, on the basis of elemental composition, substantial amount of submicron particles containing magnesium was preferentially found in Arctic mixed-phase cloud during high IN activity. Likewise, based on chemical bonding information, high IN samples contained coated inorganics, carbonate and black or brown carbon particles. These particles may be transported into the polar region and deposited onto the ice pack. Thus IN involving process may enhance ice nucleation and absorption of solar radiation in Arctic.

REFERENCES

Ade, H. and Urquhart, S.G. 2002. NEXAFS spectroscopy and microscopy of natural and synthetic polymers. In Sham, T.K. eds. Chemical Applications of Synchrotron Radiation, pp. 48. World Scientific Publishing Co. Ltd. Singapore.

Aneja, V. P., Chauhan, J.P., and Walker, J.T. 2000. Characterization of atmospheric ammonia emissions from swine waste storage and treatment lagoons. Journal of Geophysical Research, 105(11), 535-545.

Aneja, V.P., Arya, S.P., Kim, D.-S, Rumsey, I.C., Arkinson, H.L., Semunegus, H., Bajwa, K.S., Dickey, D.A., Stefanski, L.A., Todd, L., Mottus, K., Robarge, W.P., and Williams, C.M. 2008. Characterizing ammonia emissions from swine farms in eastern North Carolina: Part 1-conventional lagoon and spray technology for waste treatment. Journal of the Air & Waste Management Association, 58(9), 1130-1144.

Ansari, A.S. and Pandis, S.N. 1998. Response of inorganic PM to precursor concentrations. Environmental Science Technology, *32*(18), 2706-2714.

Ansari, A. S. and Pandis, S. N. 1999. Prediction of multicomponent inorganic atmospheric aerosol behavior. Atmospheric Environment, 33 (5), 745-757.

Ansmann, A., Tesche, M., Althausen, D., Müller, D., Seifert, P., Freudenthaler, V., Heese, B., Wiegner, M., Pisani, G., Knippertz, P., and Dubovik, O. 2008. Influence of Saharan dust on cloud glaciation in southern Morocco during the Saharan Mineral Dust Experiment. Journal of Geophysical Research, 113, D04210, doi:10.1029/2007JD008785.

Auvermann, B. W. 2000. Lesson 42: Controlling dust and odor from open lots. In Koelsch, R. et al., eds. Livestock and Poultry Environmental Stewardship (LPES) National Curriculum, pp. 26. Midwest Plan Service, Ames, IA.

Badger, C. L., Griffiths, P. T., George, I., Abbatt, J. P. D., and Cox, R. A. 2006. Phase transitions and hygroscopic growth of aerosol particles containing humic acid and mixtures of humic acid and ammonium sulphate. Atmospheric Chemistry and Physics, 6, 755-768.

Baldwin, K.J. and Batchelder, D.N. 2001. Confocal Raman micrspectroscopy through a planar interface. Applied Spectroscopy, 55, 517-524.

Barrie, L.A. 1986. Arctic air-pollution - An overview of current knowledge. Atmospheric Environment, 20, 643-663.

Bates, N.R., Mathis, J.T., and Cooper, L.W. 2009. Ocean acidification and biologically induced seasonality of carbonate mineral saturation states in the western Arctic Ocean. Journal of Geophysical Research, 114, C11007, doi:10.1029/2008JC004862.

Batonneau, Y., Sobanska, S., Laureyns, J., and Bremard, C. 2006. Confocal microprobe Raman imaging of urban tropospheric aerosol particles. Environmental Science & Technology, 40 1300-1306.

Baum, K.A., Ham, J.M., Brunsell, N.A., and Coyne, P.I. 2008. Surface boundary layer of cattle feedlots: implications for air emission measurement. Agricultural and Forest Meteorology, 148, 1882-1893.

Borys, R.D., 1989. Studies of ice nucleation by Arctic aerosol on AGASP-II. Journal of Atmospheric Chemistry, 9, 169-185.

Bougeard, D., Lautié, and Novak, A. 1977. Single crystal Raman spectra and lattice vibrations of purine. Journal of Raman Spectroscopy, 6, 80-83.

Brooks, S. D., Wise, M. E., Cushing, M., and Tolbert, M. A. 2002. Deliquescence behavior of organic/ammonium sulfate aerosol. Geophyiscal Research Letters, 29, 23.

Brooks, S. D., Garland, R. M., Wise, M. E., Prenni, A. J., Cushing, M., Hewitt, E., and Tolbert, M. A. 2003. Phase changes in internally mixed maleic acid/ammonium sulfate aerosols. Journal of Geophysical Research, 108(D15), 23-1.

Brooks, S. D., DeMott, P. J., and Kreidenweis, S. M., 2004. Water uptake by particles containing humic materials and mixtures of humic materials with ammonium sulfate. Atmospheric Environment, 38, 1859-1868.

Brooks, S.D., Gonzales, M., and Farias. R. 2009. Using surface tension measurements to understand how pollution can influence cloud formation, fog, and precipitation. Journal of Chemical Education, 86 (7), 838-841.

Buchanan, J.S., Berger, L.L., Ferrell, C, Fox, D.G., Galyean, M, Hutcheson, D.P., Klopfenstein, T.J., and Spears, J. 1996. Nutrient requirements of beef cattle: Subcommittee on Beef Cattle Nutrition, Committee on Animal Nutrition, Board on Agriculture, National Research Council. National Academy Press. Washington DC.

Businger, J.A., and Ayra, S.P.S. 1974. Height of the mixed layer in the stably stratified planetary boundary layer. Advances in Geophysics., 18A, 73-92.

Carrió, G.G., Jiang, H., and Cotton, W.R. 2005. Impact of aerosol intrusions on Arctic boundary layer clouds. Part II: Sea ice melting rates. Journal of the Atmospheric Sciences, 62, 3094-3105.

Chan, M. N. and Chan, C. K. 2003. Hygroscopic properties of two model humic-like substances and their mixtures with inorganics of atmospheric importance. Environmental Science and Technology, 37 (22), 5109-5115.

Chen, Y., Kreidenweis, S.M., McInnes, L.M., Rogers, D.C., and DeMott, P.J. 1998. Single particle analyses of ice nucleating particles in the upper troposphere and lower stratosphere. Geophysical Research Letters, 25, 1391-1394.

Choi, M. Y., and Chan, C. K. 2002a. Continuous measurements of the water activity of aqueous droplets of water-soluble organic compounds. Journal of Physical Chemistry A, 106, 4566-4572.

Choi, M. Y. and Chan, C. K. 2002b. The effects of organic species on the hygroscopic behaviors of inorganic aerosols. Environmental Science & Technology, 36, 2422-2428.

Connolly, P.J., Möhler, O., Field, P.R., Saathoff, H., Burgess, R., Choularton, T., and Gallagher. M. 2009. Studies of heterogeneous freezing by three different desert dust samples. Atmospheric Chemistry and Physics, 9, 2805-2824.

Cooper, W.A., 1986. Ice initiation in natural clouds. Precipitation enhancement-A scientific challenge, Meteorological Monographs, 21, 29-32.

Crank J. and Nicolson, P. 1947. A practical method for numerical evaluation of solutions of partial differential equations of the heat=conduction type. Mathematical Proceedings of the Cambridge Philosophical Society. 43, 50-67.

Cruz, C.N. and Pandis, S.D. 2000. Deliquescence and hygroscopic growth of mixed inorganic-organic atmospheric aerosol. Environmental Science and Technology, 34, 4313-4319.

Curry, J.A., W. B. Rossow, D. Randall, and J. L. Schramm, 1996. Overview of Arctic cloud and radiation characteristics. Journal of Climate, 9, 1731-1764.

Curry, J.A., Hobbs, P.V., King, M.D., Randall, D.A., Minnis, P., Isaac, G.A., Pinto, J.O., Uttal, T., Bucholtz, A., Cripe, D.G., Gerber, H., Fairall, C.W., Garrett, T.J., Hudson, J., Intrieri, J.M., Jakob, C., Jensen, T., Lawson, P., Marcotte, D., Nguyen, L., Pilewskie, P., Rangno, A., Rogers, D.C., Strawbridge, K.B., Valero, F.P.J., Williams, A.G., and Wylie, D. 2000. FIRE Arctic Clouds Experiment, Bulletin of the American Meteorological Society, 81, 5-29.

Cziczo, D. J., DeMott, P. J., Brooks, S. D., Prenni, A. J., Thomson, D. S., et al., 2004. Observations of organic species and atmospheric ice formation, Geophysical Research Letters, *31*, L12116.

Day, D.A., Takahama, S., Gilardoni, S., and Russell, L. M. 2009. Organic composition of single and submicron particles in different regions of western North America and the eastern Pacific during INTEX-B 2006. Atmospheric Chemistry and Physics, 9, 5433-5446.

DeMott, P. J., Meyers, M.P., and Cotton, W.R. 1994. Parameterization and impact of ice initiation processes relevant to numerical-model simulations of cirrus clouds, Journal of Atmospheric Sciences, 51, 77-90.

DeMott, P. J., Chen, Y., Kreidenweis, S.M., Rogers, D.C., and Eli Sherman, D. 1999. Ice formation by black carbon particles. Geophysical Research Letters, 26, 2429-2432.

DeMott, P. J., Cziczo, D.J., Prenni, A.J., Murphy, D.M., Kreidenweis, S.M., Thomson, D.S., Borys, R., and Rogers, D.C. 2003a. Measurements of the concentration and composition of nuclei for cirrus formation. Proceedings of the National Academy of Sciences USA, 100, 14655-14660.

DeMott, P. J., Sassen, K., Poellot, M.R., Baumgardner, D., Rogers, D.C., Brooks, S.D., Prenni, A.J., and Kreidenweis, S.M. 2003b: African dust aerosols as atmospheric ice nuclei. Geophysical Research Letters, 30, 1732, doi:10.1029/2003GL017410.

DeMott, P.J., Petters, M.D., Prenni, A.J., Carrico, C.M., Kreidenweis, S.M., Collett Jr., J.L., and Moosmüller, H. 2009. Ice nucleation behavior of biomass combustion particles at cirrus temperatures. Journal of Geophysical Research, 114, D16205, doi:10.1029/2009JD012036.

Denbigh, K. 1981. The Principles of Chemical Equilibrium, 4th ed. Cambridge University Press. Cambridge, UK.

Denmead, O. T., Chen, D., Griffith, D. W. T., Loh, Z. M., Bai, M., and Naylor, T. 2008. Emissions of the indirect greenhouse gases NH_3 and NOx from Australian beef cattle feedlots. Australian Journal of Experimental Agriculture, 48, 213-218.

Devinny, J.S., Deshusses, M.A., and Webster, T.S. 1999. Biofiltration for Air Pollution Control. Lewis Publishers. Boca Raton, FL.

Dougle, P.G., Veefkind, J.P., and ten Brink, H.M. 1998. Crystallization of mixtures of ammonium nitrate, ammonium sulphate and soot. Journal of Aerosol Science, 29(3), 375-386.

Draxler, R. R., and Rolph, G.D. 2003. HYSPLIT (Hybrid Single-Particle Lagrangian Integrated Trajectory) model, Air Resour. Lab., NOAA, Silver Spring, MD (Available at http://www.arl.noaa.gov/ready/hysplit4.html).

Ebert, M., Inerle-Hof, M., and Weinbruch, S. 2002. Environmental scanning electron microscopy as a new technique to determine the hygroscopic behavior of individual aerosol particles. Atmospheric Environment, 36, 5909-5916.

Engelhart, G.J., Asa-Awuku, A., Nenes, A., and Pandis, S.N. 2008. CCN activity and droplet growth kinetics of fresh and aged monoterpene secondary organic aerosol. Atmospheric Chemistry and Physics, 8, 3937-3949.

Escribano, R., Sloan, J.J., Siddique, N., Sze, N., and Dudev, T. 2001. Raman spectroscopy of carbon-containing particles. Vibrational Spectroscopy, 26 179-186.

Evelyn J.F., Martin, S.T., and Buseck P.R. 2009. Deliquescence and efflorescence of potassium salts relevant to biomass-burning aerosol particles. Aerosol Science and Technology, 43, 799-807.

Everall, N.J. 2000a. Modeling and measuring the effect of refraction on the depth resolution of confocal Raman microscopy. Applied Spectroscopy, 54, 773-782.

Everall, N.J. 2000b. Confocal Raman microscopy: why the depth resolution and spatial accuracy can be much worse than you think. Applied Spectroscopy, 54, 1515-1520.

Everall, N.J. 2004. Depth Profiling with Confocal Raman Microscopy, Part II. Spectroscopy, 19, Circle 16-27.

Faulkner, W.B. and Shaw, B.W. 2008. Review of ammonia emission factors for United States animal agriculture. Atmospheric Environment, 42, 6567-6574.

Fitz, D.R., Pisano, J.T., Malkina, I.L., Goorahoo, D., and Krauter, C.F. 2003. A passive flux denuder for evaluating emissions of ammonia at a dairy farm. Journal of the Air & Waste Management Association, 53(8), 937-945.

Fornea, A. P., Brooks, S. D., Dooley, J. B., Saha, A., 2009. Heterogeneous freezing of ice on atmospheric aerosols containing ash, soot, and soil. Journal of Geophysical Research, 114, D13201.

Frankel, R.S. and Aitken, D.W. 1970. Energy dispersive x-ray emission spectroscopy. Applied Spectroscopy, 24(6), 557-566.

Garrett, J. R., 1992. The atmospheric boundary layer. Cambridge University Press. Cambridge, UK.

Geller, M., Biswas, S., and Sioutas, C. 2006. Determination of particle effective density in urban environments with a differential mobility analyzer and aerosol particle mass analyzer. Aerosol Science and Technology, 40, 709-723.

Ghio, A.J., Stonehuerner, J, Pritchard, R.J., Piantadosi, C.A., Quigley, D.R., Dreher, K.L., and Costa, D.L. 1996. Humic-like substances in air pollution particulates correlate with concentrations of transition metals and oxidant generation. Inhalation Toxicology, 8 (5), 479-494.

Gibbs, S.G., Green, C.F., Tarwater, P.M., and Scarpino, P.V. 2004. Airborne antibiotic resistant and nonresistant bacteria and fungi recovered from two swine herd confined animal feeding operations. Journal of Occupational and Environmental Hygine, 1(11), 699-706.

Goetz, S., Aneja, V.P., and Zhang, Y.2008. Measurement, analysis, and modeling of fine particulate matter in eastern north Carolina. Journal of the Air & Waste Management Association, 58(9), 1208-1214.

Gustafsson, R.J., Orlov, A., Badger, C.L., Griffiths, P.T., Cox, R.A., and Lambert, R.M. 2005. A comprehensive evaluation of water uptake on atmospherically relevant mineral surfaces: DRIFT spectroscopy, thermogravimetric analysis and aerosol growth measurements. Atmospheric Chemistry and Physics Discussions, 5, 7191-7210.

Gutiérrez-Sosa, A., J.F. Walsh, R. Lindsay, P.L. Wincott, and G. Thornton. 1999. Carbonate co-adsorption geometry on TiO2 (110) 1X1-Na. Surface Science, 433–435, 538-542.

Gysel, M., Weingartner, E., Nyeki, S., Paulsen, D., Baltensperger, U., Galambos, I., and Kiss, G. 2004. Hygroscopic properties of water-soluble matter and humic-like organics in atmospheric fine aerosol. Atmospheric Chemistry and Physics, 4, 35-50.

Hameri, K. and Rood, E. A. M. 1992. Hygroscopic properties of a NaCl aerosol coated with organic compounds. Journal of Aerosol Science, 23, 437-440.

Hand, J. L. and S. M. Kreidenweis. 2002. A new method for retrieving particle refractive index and effective density from aerosol size distribution data. Aerosol Science and Technology, 36, 1012-1026.

Hand, J. L., Malm, W. C., Laskin, A., Day, D., Lee, T., Wang, C., Carrico, C., Carrillo, J., Cowin, J. P., Collett Jr., J., and Iedema, M. J., 2005. Optical, physical and chemical properties of tar balls observed during the Yosemite Aerosol Characterization Study. Journal of Geophysical Research-Atmosphere, 110, D21210.

Hansson, H. C., Rood, M. J., Koloutsou-Vakakis, S., Hameri, K., Orsini, D., and Wiedensohler, A. 1998. NaCl aerosol particle hygroscopicity dependence on mixing with organic compounds. Journal of Atmospheric Chemistry, 31 (3), 321-346.

Harrington, J. Y., Reisin, T., Cotton, W.R., and Kreidenweis, S.M. 1999. Cloud resolving simulations of Arctic stratus - Part II: Transition-season clouds. Atmospheric Research, 51, 45-75.

Hartung, J. 1995. Gas and particulate-emissions from livestock housing. Deutsche Tierarztliche Wochenschrift, 102(7), 283-288.

Hegg, D.A., Hobbs, P.V., Gasso, S., Nance, J.D., and Rangno, A.L. 1996. Aerosol measurements in the Arctic relevant to direct and indirect radiative forcing. Journal of Geophysical Research, 101, 23,349-23,363.

Henke, B.L., Gullikson, E.M., and Davis, J. C. 1993. X-ray interactions: photoabsorption, scattering, transmission, and reflection at E=50-30000 eV, Z=1-92. Atomic Data and Nuclear Data Tables, 54, 181.

Hiranuma, N. 2005. Open-path transmissometry to determine atmospheric extinction efficiency associated with feedyard dust. Thesis, West Texas A&M University, Canyon, TX.

Hiranuma, N., Brooks, S.D., Auvermann, B.W., and Littleton, R. 2008. Using environmental scanning electron microscopy to determine the hygroscopic properties of agricultural aerosols. Atmospheric Environment, 42(9), 1983-1994.

Hiranuma, N., Brooks, S.D., Thornton, D.C.O., and Auvermann, B.W. 2010. Atmospheric ammonia mixing ratios at an open-air cattle feeding facility. Journal of Air & Waste Management Association, 60, 210-218.

Hopkins, R. J., Tivanski, A. V., Marten, B. D., and Gilles, M. K. 2007. Chemical bonding and structure of black carbon reference materials and individual carbonaceous atmospheric aerosols. Journal of Aerosol Sciences, 38, 573-591.

Hopkins, R. J., Desyaterik, Y., Tivanski, A. V., Zaveri, R. A., Berkowitz, C. M., Tyliszczak, T., Gilles, M.K., and Laskin, A. 2008. Chemical speciation of sulfur in marine cloud droplets and particles: Analysis of individual particles from the marine boundary layer over the California current. Journal of Geophysical Research-Atmosphere, 113, D04209.

Hoshmand, A.R. 1988. Statistical methods for environmental and agricultural sciences. CRC Press, Boca Raton, FL.

Huang, C.H. 1979. Theory of dispersion in turbulent air flow. Atmospheric Environment, 13, 453-463.

Hung, H.-M., Malinowski, A., and Martin, S.T. 2003. Kinetics of heterogeneous ice nucleation on the surfaces of mineral dust cores inserted into aqueous ammonium sulfate particles. Journal of Physical Chemistry A, 107, 1296-1306.

Intrieri, J. M., Shupe, M.D., Uttal, T., and McCarty, B.J. 2002. An annual cycle of Arctic cloud characteristics observed by radar and lidar at SHEBA. Journal of Geophysical Research, 107, 8030, doi:10.1029/2000JC000423.

Ivleva, N.P., McKeon, U., Niessner, R., and Pöschl, U. 2007. Raman microspectroscopic analysis of size-resolved atmospheric aerosol particle samples collected with an ELPI: Soot, humic-like substances, and inorganic compounds. Aerosol Science and Technology, 41, 655-671.

Johnson, K. S., Zuberi, B., Molina, L. T., Molina, M. J., Iedema, M. J., Cowin, J. P., Gaspar, D. J., Wang, C., and Laskin, A.. 2005, Processing of soot in an urban environment: case study from the Mexico City metropolitan area. Atmospheric Chemistry and Physics, 5, 3033-3043.

Kannosto, J., Virtanen, A., Lemmetty, M., Mäkelä, J.M., Keskinen, J., Junninen, H., Hussein, T., Aalto, P., and Kulmala, M. 2008. Mode resolved density of atmospheric aerosol particles. Atmospheric Chemistry and Physics, 8, 5327-5337.

Kavouras, I.G. and Koutrakis, P. 2001. Use of polyurethane foam as the impaction substrate/collection medium in conventional inertial impactors. Aerosol Sci. Technol. 34, 46-56.

Keller, K., Blum, J.D., and Kling, G.W. 2007. Geochemistry of soils and streams on surfaces of varying ages in Arctic Alaska. Arctic, Antarctic and Alpine Research, 39 (1), 84-98.

Kelly, J.T. and Wexler, A.S. 2006. Water uptake by aerosol: water activity in supersaturated potassium solutions and deliquescence as a function of temperature, Atmospheric Environment, 40 (24), 4450-4468

Kim, Y.P. and Seinfeld, J.H. 1995. Atmospheric gas–aerosol equilibrium: III. Thermodynamics of crustal elements Ca^{2+}, K^{+}, and Mg^{2+}. Aerosol Science Technology, 22, 93-110.

King, S.M., Rosenoern, T., Shilling, J.E., Chen, Q., and Martin, S.T. Cloud condensation nucleus activity of secondary organic aerosol particles mixed with sulfate. Geophysical Research Letters, 34, L24806, doi:10.1029/2007GL030390, 2007.

Koehler, K.A., DeMott, P.J., Kreidenweis, S.M., Popovicheva, O.B., Petters, M.D., Carrico, C.M., Kireeva, E.D., Khokhlova, T.D., and Shonija, N.K. 2009. Cloud condensation nuclei and ice nucleation activity of hydrophobic and hydrophilic soot particles. Physical Chemistry Chemical Physics, 11, 7906-7920.

Köllensberger, G., Friedbacher, G., Kotzick, R., Niessner, R. and Grasserbauer, M. 1999. In-situ atomic force microscopy investigation of aerosols exposed to different humidities. Fresenius Journal of Analytical Chemistry, 364, 296-304.

Koprinarov, I., A. Hitchcock, C. McCrory, and R. Childs. 2002. Quantitative mapping of structured polymeric systems using singular value decomposition analysis of soft x-ray images. Journal of Physical Chemistry B. 106. 5358-5364.

Koziel, J.A., Baek, B-H., Spinhirne, J.P., and Parker, D.B. 2004. Ambient ammonia and hydrogen sulfide concentrations at a beef cattle feedlot in Texas. In Proc. ASAE/ESAE Annual International Meeting. Ottawa, Ontario, Canada: ASAE. Paper 044112.

Krivacsy, Z. and Molnar, A.1998. Size distributions of ions in atmospheric aerosols. Atmospheric Research, 46(3), 279-291.

Krueger, B. J., Grassian, V.H., Laskin, A., and Cowin, J. P. 2003. The transformation of solid atmospheric particles into liquid droplets through heterogeneous chemistry: Laboratory insights into the processing of calcium containing mineral dust aerosol in the tropo-sphere. Geophysical Research Letter, 30, 48.

Lamb, R.G., Chen, W.H., and Seinfeld, J.H. 1975. Numerico-empirical analysis of atmospheric diffusion theories, Journal of the Atmospheric Sciences, 32, 1794-1807.

Laskin, A., Wietsma, T.W., Krueger, B.J., and Grassian, V.H., 2005a. Heterogeneous chemistry of individual mineral dust particles with nitric acid: a combined CCSEM/EDX, ESEM, and ICPMS study. Journal of Geophysical Research-Atmospheres, 110, D10.

Laskin, A., Iedema, M. J., Ichkovich, A., Graber, E. R., Taraniuk, I., and Rudich, Y., 2005b. Direct Observation of Completely Processed Calcium Carbonate Particles in Polluted Atmospheric Environment. Faraday Discussions, 130, 453-468.

Laskin, A., Cowin, J. P., and Iedema, M. J. 2006. Analysis of individual environmental particles using modern methods of electron microscopy and X-ray microanalysis. Journal of Electron Spectroscopy and Related Phenomena, *150*, 260-274.

Lawrence, J. E. and Hornberger, G. M. 2007. Soil moisture variability across climate zones. Geophysical Research Letters, 34, L20402.

Lee, A.K.Y. and Chan, C.K. 2007. Single particle Raman spectroscopy for investigating atmospheric heterogeneous reactions of organic aerosols. Atmospheric Environment, 41, 4611-4621.

Liu, Y.J., Zhu, T., Zhao, D.F., and Zhang, Z.F. 2008. Investigation of the hygroscopic properties of Ca(NO3)2 and internally mixed $Ca(NO_3)_2/CaCO_3$ particles by micro-Raman spectrometry. Atmospheric Chemistry and Physics, 8, 7205-7215.

Malm, W.C., Schichtel, B.A., Pitchford, M.L., Ashbaugh, L.L., and Eldred, R.A. 2004. Spatial and monthly trends in speciated fine particle concentration in the United States. Journal of Geophysical Research, 109, D03306.1-D03306.22.

Maria, S.F., Russell, L.M., Gilles, M.K., and Myneni, S.C.B. 2004. Organic aerosol growth mechanisms and their climate-forcing implications. Science, 306, 1921-1924.

Mansour, H.M. and Hickey, A.J. 2007. Raman characterization and chemical imaging of biocolloidal self-assemblies, drug delivery systems, and pulmonary inhalation aerosols: a review. AAPS PharmSciTech, 8 (4) E99.

Martin, R.S., Silva, P.J., Moore, K., Erupe, M., and Doshi, V.S. 2008. Particle composition and size distributions in and around a deep-pit swine operation, Ames, IA. Journal of Atmospheric Chemistry, 59, 135-150.

Mason, B.J. 1971. The physics of clouds, Oxford Univeristy Press, Oxford, UK.

McFarquhar, G.M., Zhang, G., Poellot, M.R., Kok, G.L., McCoy, R., Tooman, T., Fridlind, A., Heymsfield, A.J. 2007. Ice properties of single-layer stratocumulus during the mixed-phase Arctic cloud experiment: 1. observations. Journal of Geophysical Research, 112, D24201.

Middlebrook, A. M., Murphy, D. M., and Thomson, D. S. 1998. Observations of organic material in individual marine particles at Cape Grim during the First Aerosol Characterization Experiment (ACE 1), Journal of Geophysical Research, 103, 16475-16483.

Mitchell, D. W., Jacquot, L. L., and Chance, R. B. 1974. Soil survey of Swisher County, Texas. United States Department of Agriculture, Soil Conservation Service in Cooperation with Texas Agricultural Experiment Station, Washington DC.

Moffet, R.C., Desyaterik, Y., Hopkins, R.J., Tivanski, A.V., Gilles, M.K., Shutthanandan, V., Molina, L.T., Gonzalez, R. A., Johnson, K.S., Molina, M.J., Laskin, A., and Prather, K. A., 2008. Characterization of aerosols containing Zn, Pb, and Cl from an industrial region of Mexico City. Environmental Science and Technology, 42, 7091-7097.

Moffet, R. C. Henn, T.R., Tivanski, A.V., Hopkins, R. J., Desyaterik, Y., Kilcoyne, A.L.D., Tyliszczak, T. Fast, J., Barnard, J., Shutthandan, V., Cliff, S.S., Perry, K.D., Laskin, A., and Gilles, M.K. 2009a. Microscopic characterization of carbonaceous aerosol particle aging in the outflow from Mexico City. Atmospheric Chemistry and Physics, 9, 16993-17033.

Moffet, R.C., Henn, T., Laskin, A., and Gilles, M.K. 2009b. Automated assay of internally mixed individual particles using X-ray spectromicroscopy maps. Submitted to Analytical Chemistry.

Morrison, H., and Pinto, J.O. 2005. Mesoscale modeling of springtime Arctic mixed-phase stratiform clouds using a new two-moment bulk microphysics scheme. Journal of Atmospheric Sciences, 62, 3683–3704.

Morrison, H., Pinto, J.O., Curry, J.A., and McFarquhar, G.M. 2008. Sensitivity of modeled arctic mixed-phase stratocumulus to cloud condensation and ice nuclei over regionally varying surface conditions. Journal of Geophysical Research, 113, D05203, doi:10.1029/2007JD008729.

Myneni, S. C. B. 2002. Soft X-ray spectroscopy and spectromicroscopy studies of organic molecules in the environment. In Fenter, P. et al., eds. Applications of synchrotron radiation in low-temperature geochemistry and environmental sciences, pp. 579. Mineralogical Society of America, Washington DC.

National Research Council (NRC), 2003. Air emissions from animal feeding operations: current knowledge, future needs. Ad Hoc Committee on Air Emissions from Animal Feeding Operations, Committee on Animal Nutrition, NRC.

Nessler, R., Bukowiecki, N., Henning, S., Weingartner, E., Calpini, B., and Baltensperger, U. 2003. Simultaneous dry and ambient measurements of aerosol size distributions at Jungfraujoch. Tellus, 55B, 808-819.

Nieuwenhuijsen, M.J., Kruize, H., and Schenker, M.B. 1998. Exposure to dust and its particle size distribution in California agriculture. American Industrial Hygiene Association, 59 (1), 34-38.

Occhipinti, C., Aneja, V.P., Showers, W., and Niyogi, D. 2008. Back-trajectory analysis and source-receptor relationships: particulate matter and nitrogen isotopic composition in rainwater. Journal of the Air & Waste Management Association, 58(9), 1215-1222.

Ocsay, R., Salma, I., Wang, W., and Maenhaut, W. 2006. Characterization and diurnal variation of size-resolved inorganic water-soluble ions at a rural background site. Journal of Environmental Monitoring, 8, 300-306.

Ogren, J. A., Heintzenberg, J., and Charlson, R.J. 1985. In-situ sampling of clouds with a droplet to aerosol converter. Geophysical Research Letters, 12, 121-124.

Oran, E.S., and Boris, J.P. 1987. Numerical simulation of reactive flow. Elsevier, New York.

Pagans, E., Font, X., and Sánchez, A. 2007. Adsorption, absorption, and biological degradation of ammonia in different biofilter organic media. Biotechnology and Bioengineering, 97 (3), 515-525.

Parker, D.B., Rhoades, M.B., Schuster, G.L., Koziel, J.A., and Perschbacher-Buser, Z.L. 2005a. Odor characterization at open-lot beef cattle feedyards using triangular forced-choice olfactometry. Transactions of the ASAE., 48(4), 1527-1535.

Parker, D.B., Pandrangi, S., Greene, L.W., Almas, L.K., Cole, N.A., Rhoades, A.B., and Koziel, J.A. 2005b. Rate and frequency of urease inhibitor application for minimizing ammonia emissions from beef cattle feedyards. Transactions of the ASAE., 48(2), 787-793.

Parsons, T.R., Maita, Y., and Lalli, G.M. 1984. A Manual of Chemical and Biological Methods for Seawater Analysis. Pergamon Press. Oxford, UK.

Peng, C., Chan, M., and Chan, C. 2001. The hygroscopic properties of dicarboxylic and multifunctional acids: Measurements and UNIFAC predictions. Environmental Science & Technology, 35, 4495-4501.

Peters, T. M., Ott, D., and O'Shaughnessy, P. T. 2006. Comparison of the Grimm 1.108 and 1.109 portable aerosol spectrometer to the TSI 3321 aerodynamic particle sizer for dry particles. Annals of Occupational Hygiene, 50(8), 843-850.

Petters, M. D. and Kreidenweis, S. M. 2008. A single parameter representation of hygroscopic growth and cloud condensation nucleus activity – Part 2: Including solubility. Atmospheric Chemistry and Physics, 8, 6273-6279.

Phillips, V.T.J., DeMott, P.J., and Andronache, C. 2008. An empirical parameterization of heterogeneous ice nucleation for multiple chemical species of aerosol. Journal of Atmospheric Sciences, 65, 2757-2783.

Pinto, J. O., 1998. Autumnal mixed-phase cloudy boundary layers in the Arctic. Journal of Atmospheric Sciences, 55, 2016-2038.

Pitz, M., Cyrys, J., Karg, E., Wiedensohler, A., Wichmann, E.-H., and Heinrich, J. 2003. Variability of apparent particle density of an urban aerosol. Environmental Science and Technology, 37, 4336-4342

Pósfai, M., Simonics, R., Li, J., Hobbs, P.V., and Buseck, P.R. 2003. Individual aerosol particles from biomass burning in southern Africa: 1. Compositions and size distributions of carbonaceous particles, Journal of Geophysical Research, 108, Art. 8483.

Pratt, K.A., DeMott, P.J., French, J.R., Wang, Z., Westphal, D.L., Heymsfield, A.J., Twohy, C.H., Prenni, A.J., , and Prather, K.A. 2009. In situ detection of biological particles in cloud ice-crystals. Nature Geoscience Letter, 2, 398-401. DOI: 10.1038/NGEO521.

Prenni, A.J., Harrington, J.Y., Tjernström, M., DeMott, P.J., Avramov, A., Long, C.N., Kreidenweis, S.M., Olsson, P.Q., and Verlinde, J. 2007. Can ice-nucleating aerosols affect arctic seasonal climate? Bulletin of the American Meteorological Society, 88, 541-550.

Prenni, A.J., DeMott, P.J., Rogers, D.C., Kreidenweis, S.M., McFarquhar, G.M., Zhang, G., and Poellot, M.R. 2009. Ice nuclei characteristics from M-PACE and their relation to ice formation in clouds. Tellus, 61B, 436-448.

Prigozhin, G.Y., Woo, J., Gregory, J.A., Loomis, A.H., Bautz, M.W., Ricker, G.R., Kraft, S. 1998. X-ray absorption near edge structure in the quantum efficiency of x-ray charge-coupled devices. Optical Engineering, 37(10) 2848-2854.

Priyadarsan, S., Annamalai, K., Sweeten, J.M., Holtzapple, M.T., and Mukhtar, S. 2005. Co-gasification of blended coal with feedlot and chicken litter biomass. Proceedings of the Combustion Institute, 30, 2973-2980.

Razote, E.B., Maghirang, R.G., Predicala, B.Z., Murphy, J.P., Auvermann, B.W., Harner, J.P., and Hargrove, W.L. 2006. Laboratory evaluation of the dust-emission potential of cattle feedlot surfaces. Transactions of the ASAE, 49 (4), 1117-1124.

Richardson, M. S., DeMott, P. J., Kreidenweis, S. M., Cziczo, D. J., Dunlea, E. J. and co-authors. 2007. Measurements of heterogeneous ice nuclei in the western United States in springtime and their relation to aerosol characteristics. Journal of Geophysical Research, 112, D02209.

Ro, K.S., Johnson, M.H., Varma, R.M., Hashmonay, R.A., and Hunt, P. 2009. Measurement of greenhouse gas emissions from agricultural sites using open-path optical remote sensing method. Journal of Environmental Science and Health Part A, 44(10), 1011-1018.

Rogers, D. C., DeMott, P. J., Kreidenweis, S. M. and Chen, Y. L. 1998. Measurements of ice nucleating aerosols during SUCCESS. Geophysical Research Letters, 25, 1383-1386.

Rogers, D. C., and DeMott, P.J., and Kreidenweis, S.M. 2001. Airborne measurements of icenucleating aerosol particles in the Arctic spring. Journal of Geophysical Research, 106, 15053-15063.

Rogge, W.F., Medeiros, P.M. and Simoneit, B.R.T. 2006. Organic maker compounds for surface soil and fugitive dust from open lot dairies and cattle feedlots. Atmospheric Environment, 40, 27-49.

Rosinski, J., Haagenson, P.L., Nagamoto, C.T., and Pmúngo, F. 1986. Ice forming nuclei of maritime origin, Journal of Aerosol Science, 17, 23-46.

Rosinski, J., Haagenson, P.L., Nagamoto, C.T., and Pmúngo, F. 1987. Nature of ice-formingn uclei in marinea ir masses. Journal of Aerosol Science, 18, 291-309.

Rothe, J., M.A. Denecke, and K. Dardenne. 2000. Soft x-ray spectromicroscopy investigation of the interaction of aquatic humic acid and clay colloids. Journal of Colloid and Interface Science, 231, 91-97.

Rule, A.M., Chapin, A.R., McCarthy, S.A., Gibson, K.E., Schwab, K.J., and Buckley, T.J. 2005. Assessment of an aerosol treatment to improve air quality in a swine concentrated animal feeding operation (CAFO). Environmental Science and Technology, 39 (24), 9649-9655.

Sacristun, J., Reinecke, H., Mijangos, C., Spells, S., and Yarwood, J. 2002. Surface modification of polystyrene films. Depth profiling and mapping by Raman microscopy. Macromolecular Chemistry and Physics, 203, 678-685.

Sadezky, A., Muckenhuber, H., Grothe, H., Niessner, R., and Pöschl, U. 2005. Raman microspectroscopy of soot and related carbonaceous materials: Spectral analysis and structural information. Carbon, 43 1731-1742.

Schade, G.W. and Crutzen, P.J. 1995. Emission of aliphatic amines from animal husbandry and their reactions: potential source of N_2O and HCN. Journal of Atmospheric Chemistry, 22, 319-346.

Schicker, B., Kuhn, M., Fehr, R., Asmis, L.M., Karagiannidis, C., and Reinhart, W.H. 2009. Particulate matter inhalation during hay storing activity induces systemic inflammation and platelet aggregation. European Journal of Applied Physiology, 105, 771-778.

Schneider, F.E., Engelhardt, T., and Wieser, P.H. 2001. Characterization of aerosol particles from animal husbandry with single particle analytical techniques. Paper 01-4010, presented at 2001 American Society of Agricultural Engineers, Sacramento, CA, July30–August 1, 2001. ASAE, St. Joseph, MI.

Schnell, R.C. 1977. Ice nuclei in seawater, fog water and marine air off the coast of Nova Scotia: Summer 1975. Journal of Atmospheric Sciences, 34, 1299-1305.

Schönherr, J, Luber, M. 2001. Cuticular penetration of potassium salts: effects of humidity, anions and temperature. Plant and Soil. 236, 117-122.

Schulte, F., Lingott, J., Panne, U., and Kneipp, J. 2008. Chemical Characterization and Classification of Pollen. Analytical Chemistry, 80 9551-9556.

Seinfeld, J.H. and Pandis, S.N., 1998. Atmospheric Chemistry and Physics. Wiley, New York.

Semeniuk, T. A., Wise, M. E., Martin, S. T., Russell, L. M., and Buseck, P. R. 2007. Hygroscopic behavior of aerosol particles from biomass fires using environmental transmission electron microscopy. Journal of Atmospheric Chemistry. 56, 259-273.

Shaw, G.E. 1995. The arctic haze phenomenon. Bulletin of the American Meteorological Society, 76, 2403-2413.

Siva, K.B., Aminuddin, H., Husni, M.H.A., Manas, A.R. 2000. Ammonia volatilization from urea as affected by humic substances derived from palm oil mill effluent (POME) and tropical peat. Tropical Agriculture, 77(1), 13-20.

Skoog, D.A., Holler, F.J., and Nieman, T.A. 1997. Principles of instrumental analysis. 5th ed. Thomson Learning , London, UK.

Solomon, D., Lehmann, J., Kinyangi, J., Liang, B., and Schäfer, T. 2005. Carbon K-edge NEXAFS and FTIR-ATR spectroscopic investigation of organic carbon speciation in soils. Soil Science Society of America Journal, 69, 107-119.

Solorzano, L. 1969. Determination of ammonia in natural waters by the phenolhypochlorite method. Limnology and Oceanography, 14, 799-801.

Sorooshian, A., Murphy, S.M., Hersey, S., Gates, H., Padro, L.T., Nenes, A., Brechtel, F.J., Jonsson, H., Flagan, R.C., and Seinfeld, J.H. 2008. Comprehensive airborne characterization of aerosol from a major bovine source. Atmospheric Chemistry and Physics, 8, 5489-5520.

Stöhr, J. 2003. NEXAFS Spectroscopy, 1st ed., Springer-Verlag, Berlin, Heidelberg.

Spells, S.J., Reinecke, H., Sacristán, J., Yarwood, J., and Mijangos, C. 2003. Depth profiling of polymer films by confocal Raman spectroscopy. Macromolecular Symposia, 203, 147-154.

Sullivan, R.C., Moore, M.J.K., Petters, M.D., Kreidenweis, S.M., Roberts, G.C., and Prather, K.A. 2009. Effect of chemical mixing state on the hygroscopicity and cloud nucleation properties of calcium mineral dust particles. Atmospheric Chemistry and Physics Discussions, 9, 2609-2644.

Sweeten, J. M. 1979. Water works for dust control. Feedlot Mgmt. 20(6), 28-31.

Sweeten, J.M., Parnell, C.B. JR., Shaw, B.W., and Auvermann, B.W. 1998. Particle size distribution of cattle feedlot dust emission. Transactions of the ASAE, 41(5), 1477-1481.

Sze, S.K., Siddique, N., Sloan, J.J., and Escribano, R. 2001. Raman spectroscopic characterization of carbonaceous aerosols. Atmospheric Environment, 35, 561-568.

Takahama, S., Gilardoni, S., Russell, L. M., and Kilcoyne, A. L. D. 2007. Classification of multiple types of organic carbon composition in atmospheric particles by scanning transmission Xray microscopy analysis, Atmospheric Environment, 41, 9435-9451.

Tang, I.N. and Munkelwitz, H.R. 1993. Composition and temperature dependence of the deliquescence properties of hygroscopic aerosols. Atmospheric Environment, 27A, 467-473.

Todd, R.W., Cole, N.A., Clark, N., Flesch, T.K., Harper, L.A., and Baek, B.H. 2008. Ammonia emissions from a beef cattle feedyard on the southern High Plains. Atmospheric Environment, 42(28), 6797-6805.

Tomba, J.P. and Pastor, J.M. 2007. Confocal Raman microspectroscopy with dry objectives: A depth profiling study on polymer films. Vibrational Spectroscopy, 44 62-68.

Turpin, B. J. and Lim, H.-J. 2001. Species contributions to $PM_{2.5}$ mass concentrations: revisiting common assumptions for estimating organic mass, Aerosol Science & Technology, 35, 602-610.

Upadhyay, J., B.W. Auvermann, A.N. Paila and N. Hiranuma. 2008. Open-path transmissometry to determining the atmospheric extinction efficiency of feedyard dust. Transactions of the ASABE., 51(4), 1433-1441.

Vali, G. 1985. Nucleation terminology. Journal of Aerosol Science, 16, 575-576.

Wagman, D.D. Evans, W.H., Halow, I., Parker, V.B., Bailey, S.M., and Schumm, R.H. 1965. Selected values of chemical thermodynamic properties. National Bureau of Standards. Washington, DC.

Wagman, D.D., Evans, W.H., Parker, V.B., Schumm, R.H., Halow, I., Bailey, S.M., Churney, K.L., and Nuttall, R.L. 1982. The NBC tables of chemical thermodynamic properties. Journal of Physical and Chemical Reference Data. 11, Supplement No. 2.

Wallace, J.M. and Hobbs, P.V. 2006. Atmospheric science: an introductory survey, 2nd ed., pp. 483, Academic, San Diego, CA.

Wang, X.L., Sato, T., Xing, B.S., Tamamura, S., and Tao, S. 2005. Source identification, size distribution and indicator screening of airborne trace metals in Kanazawa, Japan. Journal of Aerosol Science. 36(2) 197-210.

Wathes, C.M., Demmers, T.G.M., and Xin, H. 2003. Ammonia concentrations and emissions in livestock production facilities: guidelines and limits in the USA and UK. In Proc. ASAE Annual International Meeting. Las Vegas, NV: ASAE. Paper 034112.

Weingartner, E., Burtescher, H. and Baltensperger, U. 1997. Hygroscopic properties of carbon and diesel soot particles. Atmospheric Environment, 31, 2311-2327.

Wesley, M.L. 1989. Parameterizations of surface resistance to gaseous dry deposition in regional scale, numerical models. Atmospheric Environment, 23, 1293-1304.

Yanenko, N.N. 1971. The Method of Fractional Steps. Springer-Verlag, New York.

Yin, J.X. and Harrison, R.M. 2008. Pragmatic mass closure study for $PM_{1.0}$, $PM_{2.5}$ and PM_{10} at roadside, urban background and rural sites. Atmospheric Environment, 42(5), 980-988.

Yum, S.S., and Hudson, J.G. 2001. Vertical distributions of cloud condensation nuclei spectra over the springtime Arctic Ocean. Journal of Geophysical Research, 106, 15045-15052.

Zelenyuk, A., Imre, D., Liu, P., Macdonald, A.M., and Leaitch, R. 2009. The properties of individual aerosol particles sampled over north slope of Alaska during ISDAC. Presented in Atmospheric Science Program (ASP) Science Team Meeting, Santa Fe, NM, February 25-27, 2009. (http://www.asp.bnl.gov/ASP_ST_mtg_pres_2009/Zelenyuk_ASP.pdf).

Zuberi, B., Bertram, A.K., Cassa, C.A., Molina, L.T., and Molina, M.J. 2002. Heterogeneous nucleation of ice in (NH4)2SO4-H2O particles with mineral dust immersions, Geophysical Research Letters, 29(10), 1504, doi:10.1029/2001GL014289.

Zweifel, H., Maier, R.D., Schiller, M. 2001. Plastics additives handbook 6th ed. Hanser, München, Germany.

APPENDIX A

Table 1A. Sample substrates used in CCSEM/EDX and STXM/NEXAFS analyses. Sample ID reads flight number - substrate number (e.g., F25-S20).

Sampling Condition	ISDAC Flight #	Date	TRAC Start Time, UTC	Sample ID	In-Cloud Time, %
Biomass	25	4/19/2008	9:36 pm	F25-S16	0
	25	4/19/2008	9:42 pm	F25-S17	20
	25	4/19/2008	9:47 pm	F25-S18	0
	25	4/19/2008	9:52 pm	F25-S19	0
	25	4/19/2008	9:57 pm	*F25-S20	0
	25	4/19/2008	10:07 pm	F25-S22	0
Clound-Free (ambient)	30	4/26/2008	8:15 pm	*F30-S6	0
	31	4/27/2008	1:54 am	F31-S72	0
	31	4/27/2008	1:59 am	F31-S73	0
In-Clound (ambient)	31	4/27/2008	1:49 am	F31-S71	10
	31	4/27/2008	2:15 am	F31-S76	100
	31	4/27/2008	2:20 am	*F31-S77	100
	31	4/27/2008	2:35 am	F31-S80	100
In-Cloud (CVI)	30	4/26/2008	9:22 pm	*F30-S19	100
	31	4/27/2008	1:03 am	*F31-S62	100
	31	4/27/2008	1:08 am	F31-S63	100
	31	4/27/2008	1:18 am	F31-S65	100
	31	4/27/2008	1:23 am	F31-S66	100
	31	4/27/2008	1:28 am	F31-S67	100
	31	4/27/2008	1:39 am	F31-S69	100
	34	4/29/2008	2:17 am	F34-S64	67
	34	4/29/2008	2:23 am	F34-S65	70
	34	4/29/2008	2:38 am	F34-S68	83
High IN	34	4/29/2008	2:28 am	*F34-S66	30
	34	4/29/2008	2:33 am	*F34-S67	60

*Used for STXM

Table 1B. Sampling conditions during TRAC sampling. Mean based on a minute averaged data is shown.

	Ambient Conditions			Ice Crystal (>200 μm D_p)
Sampling Condition	Air Temp., °C	SS_{water}, %	SS_{ice}, %	2DS Ice Crystal Conc., $x10^{-4}$ L^{-1}
Biomass (ambient)	-13.2	-51.1	-45.7	1.1
Cloud-Free (ambient)	-21.1	-22.6	-6.6	0.1
In-Cloud (ambient)	-13.0	-2.4	10.9	40.7
In-Cloud (CVI)	-11.7	-4.6	7.1	145.7
High IN (CVI)	-10.7	-9.9	0.1	220.2

	IN			
Sampling Condition	Aerosol Temp., °C	SS_{water}, %	SS_{ice}, %	CFDC *IN Conc., L^{-1}
Biomass (ambient)	-21.6	-5.3	18.0	0.1
Cloud-Free (ambient)	-27.4	0.4	31.5	0.6
In-Cloud (ambient)	-21.6	-4.2	19.3	1.7
In-Cloud (CVI)	-20.8	-5.5	16.5	0.2
High IN (CVI)	-21.8	2.4	26.9	1.0

	CCN			
Sampling Condition	SS_{water}(A), %	SS_{water}(B), %	CCN(A) Conc., $x10^5$ L^{-1}	CCN(B) Conc., $x10^5$ L^{-1}
Biomass (ambient)	0.32	0.26	4.3	4.9
Cloud-Free (ambient)	0.15	0.14	2.2	1.5
In-Cloud (ambient)	0.19	0.24	1.4	1.4
In-Cloud (CVI)	0.19	0.22	0.3	0.3
High IN (CVI)	0.18	0.19	0.4	0.3

	CN			
Sampling Condition	PCASP, $x10^5$ L^{-1}	PMS7610, $x10^5$ L^{-1}	TSI3775, $x10^5$ L^{-1}	UHSAS Toal, $x10^5$ L^{-1}
Biomass (ambient)	5.9	2.5	6.1	4.7
Cloud-Free (ambient)	2.6	1.0	2.3	1.8
In-Cloud (ambient)	1.5	0.9	2.4	1.6
In-Cloud (CVI)	1.1	0.3	3.0	0.7
High IN (CVI)	1.3	0.4	3.9	3.1

*High IN Activity: 8 IN L^{-1} and 3 IN L^{-1} were measured on April 29 at 2:29 and 2:36 UTC, respectively

Table 2. The total number of RH steps (50 per experiment) employed in the ESEM study. This is the measurement at 15 ºC.

Pressure, torr	RH, %
1	7.9
1.9	15.1
2.6	20.6
3.2	25.4
3.8	30.1
4.5	35.7
5.1	40.4
5.7	45.2
6.4	50.8
7	55.5
7.7	61.1
8.3	65.8
8.4	66.6
8.5	67.4
8.6	68.2
8.7	69
8.8	69.8
8.9	70.6
9	71.4
9.1	72.2
9.2	73
9.3	73.8
9.4	74.5
9.5	75.3
9.6	76.1

Pressure, torr	RH, %
9.7	76.9
9.8	77.7
9.9	78.5
10	79.3
10.1	80.1
10.2	80.9
10.3	81.7
10.4	82.5
10.5	83.3
10.6	84.1
10.7	84.9
10.8	85.7
10.9	86.4
11	87.2
11.1	88
11.2	88.8
11.3	89.6
11.4	90.4
11.5	91.2
11.6	92
11.7	92.8
11.8	93.6
11.9	94.4
12	95.2
12.1	96

Table 3. Raman frequencies observed in spectra of agricultural aerosols and their tentative assignments to the classes of molecules and/or vibrational modes.

Raman Shift, cm-1	Tentative Assignment [a,b,c]
Chemical bonding of Organics (<525/>2700 cm^{-1})	
178 cm^{-1}	symmetric CI_4 stretches
160 to 200 cm^{-1}	skeletal deformation of aliphatic nitriles
267 cm^{-1}	symmetric CBr_4 stretch in solution
335 to 355 cm^{-1}	skeletal deformation of monoalkyl acetylenes
150 to 425 cm^{-1}	chain expansion of n-alkanes
437 cm^{-1}	symmetric CI_3 stretch of CHI_3 (in solution)
459 cm^{-1}	symmetric CCl_4 stretch
483 cm^{-1}	symmetric CI_2 stretch
484 to 475 cm^{-1}	skeletal deformation of dialkyl diacetylenes
485 to 495 cm^{-1}	CI stretch of secondary/tertiary iodoalkanes
480 to 510 cm^{-1}	SS stretches of dialkyl trisulfides
500 to 510 cm^{-1}	CI stretch of primary iodoalkanes
523 cm^{-1}	CI stretches from CH_3I
510 to 525 cm^{-1}	SS stretch of dialkyl disulfides
1200	disordered graphitic lattice (A_{1g} symmetry), polyenes, or ionic impurities
1350	disordered graphitic lattice (A_{1g} symmetry)
1500	amorphous carbon, black or brown carbon
1580	ideal graphitic lattice (E_{2g}-symmetry)
1620	disordered graphitic lattice (E_{2g}-symmetry)
2700 to 2850 cm^{-1}	CHO group vibration of aliphatic aldehydes
2849 to 2969 cm^{-1}	symmetric/antisymmetric stretches of n-alkanes ($-CH_2$/$-CH_3$)
2986 to 2974 cm^{-1}	symmetric NH_3^+ stretch of aqueous alkyl ammonium chlorides
2980 to 2990 cm^{-1}	symmetric $=CH_2$ stretches of $C=CH_2$ derivatives
3026 cm^{-1}	symmetric $=CH_2$ stretches of ethylene (gas)
3000 to 3040 cm^{-1}	CH stretch of C=CHR derivatives
3057 cm^{-1}	aromatic CH stretch of alkyl benzenes
3062 cm^{-1}	CH stretch of benzene
3070 to 3095 cm^{-1}	antisymmetric $=CH_2$ stretch of $C=CH_2$ derivatives
3000 to 3100 cm^{-1}	aromatic CH stretch of benzene derivatives
3020 to 3100 cm^{-1}	CH_2 stretches of cyclopropane
3103 cm^{-1}	antisymmetric $=CH_2$ stretch of ethylene (gas)
3154 to 3175 cm^{-1}	bonded NH stretch of pyrazoles
3145 to 3190 cm^{-1}	bonded symmetric NH_2 stretch of primary amides
3290 to 3310 cm^{-1}	bonded NH stretch of secondary amides
3250 to 3300 cm^{-1}	bonded symmetric NH_2 stretch of primary amines
3300 to 3350 cm^{-1}	$\equiv$CH stretch of alkyl acetylenes
3325 to 3355 cm^{-1}	bonded antisymmetric NH_2 stretch of primary amines
3374 cm^{-1}	CH stretch of acetylene (gas)
3340 to 3380 cm^{-1}	bonded OH stretch of aliphatic alcohols
3330 to 3400 cm^{-1}	bonded antisymmetrc NH_2 stretch of primary amines

Raman Shift, cm-1	Tentative Assignment [a,b,c]
Inorganics (Major Peak)	
976 cm^{-1}	ammonium sulfate ($(NH_4)_2SO_4$)
994 cm^{-1}	sodium sulfate (Na_2SO_4)
1006 cm^{-1}	calcium sulfate ($CaSO_4$)
1044 cm^{-1}	ammonium nitrate (NH_4NO_3)
1046 cm^{-1}	bi-sodium carbonate ($NaHCO_3$)
1050 cm^{-1}	calcium nitrate ($Ca(NO_3)_2$)
1069 cm^{-1}	sodium nitrate ($NaNO_3$)
1080 cm^{-1}	sodium carbonate (Na_2CO_3)
1088 cm^{-1}	calcium carbonate ($CaCO_3$)
Inorganics (Minor Peaks)	
452/615/2263/3122 cm^{-1}	$(NH_4)_2SO_4$
450/621/1102-1153 cm^{-1}	Na_2SO_4
414/493/619/700/1134 cm^{-1}	$CaSO_4$
140-172/715/832/1385/1768/ 2399/3023-3133 cm^{-1}	NH_4NO_3
112-207/686/1269/1433 cm^{-1}	$NaHCO_3$
187/725/1386 cm^{-1}	$NaNO_3$
187/699/1062 cm^{-1}	Na_2CO_3
280/712 cm^{-1}	$CaCO_3$

[a,b] Organic chemical bond on the basis of Dollish et al. (1974) and Ivleva et al. (2007)
[c] For identification of Raman spectra (band wavenumbers and relative intensities) of inorganics, the resolved spectra are compared with commercially available spectral libraries (Thermo Scientific, Nicolet Instruments, Marcel Dekker Inc.).

Table 4. Hourly averaged wind properties data ± standard deviation from mean during far-field particle size distributions measurements are shown. Total PAS concentration (0.3 to 25 μm D_p) measured at downwind and far-field as well as its ratio are also shown.

Sample Date & Time	Wind Speed, m/s	Wind Direction, degree	Downwind, $x10^{11}$ nm^3 cm^{-3}	Far-Field, $x10^{11}$ nm^3 cm^{-3}	Far-Field/Downwind PAS Concentration Ratio, %
7/14 9:00 pm	2.2 ± 0.3	155.7 ± 6.1	34.1	1.1	3.2
7/16 5:00 pm	5.3 ± 0.7	167.2 ± 9.8	0.8	0.3	34.7
7/16 9:00 pm	2.7 ± 0.4	131.2 ± 3.9	0.7	0.2	25.7
7/18 4:00 pm	5.9 ± 1.3	175.9 ± 12.8	3.7	0.2	5.9
7/18 9:00 pm	2.6 ± 0.5	123.8 ± 7.5	39.2	1.4	3.5
7/20 4:00 pm	5.2 ± 1.4	155.7 ± 22.0	5.1	0.4	7.5
7/20 9:00 pm	2.3 ± 0.4	128.7 ± 6.8	102.0	1.6	1.6
7/22 4:00 pm	5.0 ± 1.3	142.2 ± 19.6	7.9	0.1	1.6
7/22 9:00 pm	2.4 ± 0.5	149.1 ± 8.1	58.1	3.5	6.0
7/24 4:00 pm	4.0 ± 1.2	145.9 ± 28.4	6.3	0.04	0.6
7/24 9:00 pm	3.3 ± 0.7	144.3 ± 9.6	70.4	2.2	3.2

Table 5. Height of 10 layer in the empirical box model in this study

Cell Number	Layer Thickness (dz), m	Mid-point (z), m
1	4.0	2.0
2	7.0	7.5
3	12.4	17.2
4	21.8	34.4
5	38.4	64.5
6	67.7	117.5
7	119.2	211.0
8	209.8	375.4
9	369.4	665.0
10	650.3	1174.8

Note: upper boundary is 1500 m.

Table 6. Conditions of PBL and particle concentrations used to compute hourly emission rates on July 24, 2008: hourly time rate change of PBL, total SMPS mass concentration, PM_1 mass concentration measure by PAS, calculated PM_1 emission rate, and PM_{10} emission rate. Both SMPS and PAS measurements were collected at the downwind site. Gray highlighted area represents ΔPBL >10%.

Date and Time, CDT	ΔPBL, m	ΔPBL, %	ΔSMPS, $\mu g/m^3$	ΔPM_1, $\mu g/m^3$	PM_1 emission rate, $x10^5$ $\mu g/m^2$	PM_{10} emission rate, $x10^6$ $\mu g/m^2$
7/24/2008 0:00	-27.3	10.7	0.2	-0.5	5.2	8.8
7/24/2008 1:00	-23.7	10.2	-0.2	1.7	3.4	9.0
7/24/2008 2:00	-25.5	12.3	-1.7	-2.8	3.7	6.1
7/24/2008 3:00	-15.3	8.0	-0.7	-0.9	4.4	6.0
7/24/2008 4:00	19.5	9.2	-5.2	-7.8	3.9	4.1
7/24/2008 5:00	31.6	13.0	-3.4	-5.0	2.9	6.0
7/24/2008 6:00	24.6	9.2	0.4	-0.3	2.6	12.8
7/24/2008 7:00	38.0	12.4	-0.3	0.3	3.1	20.1
7/24/2008 8:00	54.1	15.0	-1.7	-2.2	3.9	17.3
7/24/2008 9:00	131.3	26.8	0.5	-0.7	4.4	14.0
7/24/2008 10:00	1569.2	76.2	0.5	1.5	4.4	17.6
7/24/2008 11:00	325.3	13.6	0.1	-0.6	3.9	15.4
7/24/2008 12:00	250.5	9.5	0.0	0.1	3.5	11.2
7/24/2008 13:00	69.6	2.6	-0.3	-0.1	3.9	10.9
7/24/2008 14:00	93.4	3.3	1.5	1.2	3.9	12.4
7/24/2008 15:00	97.3	3.4	-1.2	-1.1	4.1	13.0
7/24/2008 16:00	63.1	2.1	-1.1	-0.5	3.7	12.2
7/24/2008 17:00	64.1	2.1	1.0	0.6	3.8	10.3
7/24/2008 18:00	-122.0	4.2	0.3	0.8	4.4	18.2
7/24/2008 19:00	-122.0	4.4	0.5	1.5	4.6	35.3
7/24/2008 20:00	-1161.8	71.8	-0.3	3.9	5.1	73.1
7/24/2008 21:00	-356.0	28.2	-0.7	6.6	5.3	127.1
7/24/2008 22:00	-589.2	87.6	-1.7	-9.2	2.9	68.9
7/24/2008 23:00	-55.3	9.0	-0.4	-1.3	2.5	15.3
7/25/2008 0:00	-35.8	6.2	2.1	0.6	3.6	44.4

Table 7. Time-resolved chemical composition of agricultural aerosols at 8mW of laser intensity used in Raman microspectroscopy: investigated area, number of particle deposition spots investigated; number of Raman spectra recorded; ratio of the number of all spectra with signals characteristic for each component ± standard errors from averaging over different particle deposition spots.

Date	July 22	July 22	July 22	July 22	July 22
Location	Downwind	Downwind	Downwind	Upwind	Far-Field
Time	Morning	Aftrenoon	Evening	Evening	Evening
Investigated Spots	3	3	3	3	3
Recorded spectra	237	50	103	86	107
Characteric spectra, %	99.1 ± 0.1	100	100	100	98.0 ± 0.3
High fluorescence, %	0.9 ± 0.1	0	0	0	2.2 ± 0.4
Inorganics, %	0.5 ± 0.1	12.2 ± 0.8	6.8 ± 0.6	14.6 ± 1.5	2.9 ± 0.5
Inorganic Dominant Complex, %	1.6 ± 0.1	0	7.6 ± 0.8	8.6 ± 0.7	0.0 ± 0.0
Inorganic + Inorganic(s), %	0	0	4.6 ± 0.5	1.3 ± 0.2	0
Inorganic(s) + Organics, %	1.6 ± 0.1	0	3.1 ± 0.3	7.3 ± 0.7	0
Organics, %	36.5 ± 1.3	32.5 ± 2.3	16.5 ± 0.8	52.4 ± 2.0	49.5 ± 2.8
Organics <525 cm^{-1} >2700 cm^{-1}, %	8.8 ± 0.5	32.5 ± 2.3	10.2 ± 1.0	47.6 ± 1.9	47.4 ± 2.6
Fatty Acid [R-C(=O)OH], %	27.8 ± 1.7	0	6.4 ± 0.4	4.8 ± 0.9	2.1 ± 0.2
Soil/Soot Dominant Complex, %	60.6 ± 1.4	55.3 ± 2.0	69.0 ± 0.7	24.5 ± 0.4	45.5 ± 3.4
Soil/Soot, %	21.5 ± 1.9	31.5 ± 2.3	12.1 ± 0.4	1.2 ± 0.2	27.2 ± 2.2
Soil/Soot + Inorganic(s), %	3.6 ± 0.4	2.4 ± 0.6	24.6 ± 0.9	10.7 ± 0.6	8.3 ± 0.9
Soil/Soot + Organics, %	31.6 ± 1.7	14.1 ± 0.3	6.4 ± 0.3	2.2 ± 0.2	9.2 ± 0.8
Soil/Soot + Inorganic(s) + Organics, %	3.8 ± 0.1	7.4 ± 1.1	25.9 ± 1.1	10.4 ± 0.4	0.7 ± 0.1

Date	July 24	July 24	July 24	July 24	July 24
Location	Downwind	Downwind	Downwind	Upwind	Far-Field
Time	Morning	Aftrenoon	Evening	Evening	Evening
Investigated Spots	3	3	3	3	3
Recorded spectra	127	77	108	47	51
Characteric spectra, %	100	98.9 ± 0.2	100	100	100
High fluorescence, %	0	1.1 ± 0.2	0	0	0
Inorganics, %	2.0 ± 0.3	0	0	5.2 ± 0.7	0
Inorganic Dominant Complex, %	1.4 ± 0.1	0	0	6.5 ± 0.8	3.3 ± 0.8
Inorganic + Inorganic(s), %	0.7 ± 0.1	0	0	2.8 ± 0.7	0
Inorganic(s) + Organics, %	0.7 ± 0.1	0	0	3.7 ± 0.7	3.3 ± 0.8
Organics, %	30.5 ± 2.0	70.5 ± 0.7	56.3 ± 0.8	34.3 ± 3.3	13.3 ± 1.6
Organics <525 cm^{-1} >2700 cm^{-1}, %	28.4 ± 1.8	68.6 ± 0.7	56.3 ± 0.8	34.3 ± 3.3	6.7 ± 1.6
Fatty Acid [R-C(=O)OH], %	2.1 ± 0.2	1.9 ± 0.4	0	0	6.7 ± 1.6
Soil/Soot Dominant Complex, %	66.1 ± 1.8	28.4 ± 0.5	43.7 ± 0.8	54.0 ± 2.8	83.3 ± 2.1
Soil/Soot, %	35.1 ± 0.9	17.3 ± 0.6	19.8 ± 0.9	16.5 ± 2.2	43.1 ± 3.8
Soil/Soot + Inorganic(s), %	11.4 ± 0.9	1.1 ± 0.2	1.8 ± 0.2	6.8 ± 1.3	6.7 ± 1.1
Soil/Soot + Organics, %	17.9 ± 0.5	8.9 ± 0.8	19.3 ± 0.2	19.1 ± 1.5	33.5 ± 1.2
Soil/Soot + Inorganic(s) + Organics, %	1.7 ± 0.2	1.1 ± 0.2	2.9 ± 0.2	11.6 ± 1.5	0

Table 8. Chemical composition of (A) total inorganics on the sample collected at upwind location on July 22 evening and (B) soil/soot dominant complex on the sample collected at downwind location on July 22 evening.

A

Component(s)	Population ± Standard Error, %
Inrorganics	14.6 ± 1.5
$Ca(NO_3)_2$ (1050 cm^{-1})	8.9 ± 1.3
$NaNO_3$ (1069 cm^{-1})	4.6 ± 0.4
$CaCO_3$ (1088 cm^{-1})	1.0 ± 0.2
Inrganic Dominant Complex	8.6 ± 0.7
$CaSO_4 + Ca(NO_3)_2$	1.3 ± 0.2
$Ca(NO_3)_2$ + Other Organics	3.6 ± 0.4
$Ca(NO_3)_2 + NaNO_3$ + Oher Organics	1.3 ± 0.2
$Ca(NO_3)_2 + CaCO_3$ + Other Organics	2.4 ± 0.4

B

Component(s)	Population ± Standard Error, %
Soil/Soot Dominant Complex	69.0 ± 0.7
Soil/Soot	12.1 ± 0.4
Soil/Soot + Other Organics	6.4 ± 0.3
Soil/Soot + $(NH_4)_2SO_4 + CaSO_4$ + Other Organics	1.1 ± 0.2
Soil/Soot + $CaSO_4$	1.9 ± 0.2
Soil/Soot + $CaSO_4$ + Other Organics	1.1 ± 0.2
Soil/Soot + $CaSO_4 + Ca(NO_3)_2$	0.8 ± 0.1
Soil/Soot + $CaSO_4 + Ca(NO_3)_2 + NaNO_3$ + Other Organics	0.8 ± 0.1
Soil/Soot + $CaSO_4 + Ca(NO_3)_2 + CaCO_3$	1.1 ± 0.2
Soil/Soot + $NH_4NO_3 + Ca(NO_3)_2$	1.1 ± 0.2
Soil/Soot + $NaHCO_3$ + Other Organics	0.8 ± 0.1
Soil/Soot + $NaHCO_3 + NaNO_3$ + Other Organics	0.8 ± 0.1
Soil/Soot + $Ca(NO_3)_2 + NaNO_3$	4.2 ± 0.5
Soil/Soot + $Ca(NO_3)_2 + NaNO_3$ + Other Organics	10.5 ± 0.8
Soil/Soot + $Ca(NO_3)_2 + NaNO_3 + CaCO_3$	2.3 ± 0.4
Soil/Soot + $Ca(NO_3)_2 + NaNO_3 + CaCO_3$ + Other Organics	0.8 ± 0.1
Soil/Soot + $Ca(NO_3)_2 + CaCO_3$	1.1 ± 0.2
Soil/Soot + $Ca(NO_3)_2 + CaCO_3$ + Other Organics	1.1 ± 0.2
Soil/Soot + $NaNO_3$	10.9 ± 0.5
Soil/Soot + $NaNO_3$ + Other Organics	7.9 ± 0.5
Soil/Soot + $CaCO_3$	1.1 ± 0.2
Soil/Soot + $CaCO_3$ + Other Organics	1.1 ± 0.2

Table 9. Peak areas (OD eV per particle) given by deconvolution of the average single particle carbon K-edge spectrum ± standard error for each sampling condition. The standard error was estimated by the sample standard deviation divided by the square root of the recorded spectra per a sample. Chemical bonding information are referred from Moffet e al. (2009a), and references therein.

Energy (eV)	Transition	Functionallity	Biomass	Cloud-Free(ambient)	In-Cloud (ambient)	In-Cloud (CVI)	High IN
285.1	1s → π*	C*=C	0.17 ± 0.01	0.19 ± 0.02	0.17 ± 0.01	0.17 ± 0.02	0.23 ± 0.02
286.5	K 1s → π* or K 1s →	R(C*=O)R or C*OH	0.19 ± 0.01	0.30 ± 0.04	0.12 ± 0.01	0.19 ± 0.02	0.28 ± 0.02
287.7	K 1s → C-H*	C*H, C*H2, C*H3	0.54 ± 0.01	0.23 ± 0.01	0.57 ± 0.02	0.26 ± 0.03	0.34 ± 0.02
288.5	K 1s → π*	R(C*=O)OH	0.81 ± 0.01	1.00 ± 0.04	0.85 ± 0.02	0.60 ± 0.04	0.75 ± 0.02
289.5	K 1s → 3pσ*	OC*H2	0.91 ± 0.01	0.63 ± 0.03	0.94 ± 0.03	0.43 ± 0.04	0.56 ± 0.02
290.4	K 1s → π*	C*O3	0.10 ± 0.01	0.13 ± 0.02	0.16 ± 0.02	0.11 ± 0.02	0.17 ± 0.02
297.1, 299.7	L2 2p1/2→ L3 2p3/2→	K*	0.10 ± 0.01	0.21 ± 0.03	0.07 ± 0.01	0.13 ± 0.01	0.07 ± 0.01
292.2	K 1s → σ*	C*-C, C*-O	1.48 ± 0.05	1.72 ± 0.12	1.40 ± 0.09	0.99 ± 0.13	1.18 ± 0.06
300	1s → σ*	C*=C, C*=O	1.45 ± 0.06	2.07 ± 0.14	0.94 ± 0.09	1.70 ± 0.13	1.87 ± 0.07
294.5	Edge step	Total Carbon	19.32 ± 0.16	12.20 ± 0.65	17.15 ± 0.52	8.02 ± 0.77	12.18 ± 0.56

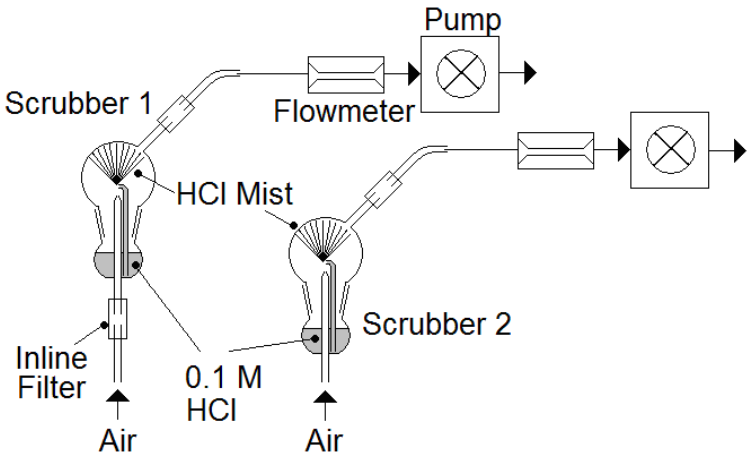

Figure 1. Experimental design for ammonia sampling. Scrubbers 1 and 2 are used to collect NH_3(g) and total NH_x, respectively.

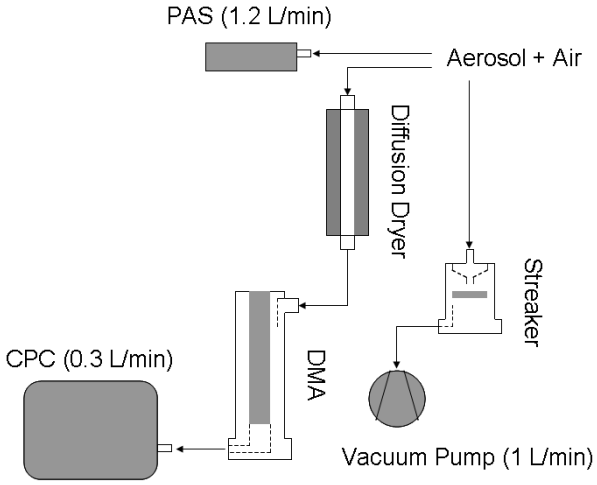

Figure 2. Schematics of instruments for the measurement of *in situ* particle size distributions (GRIMM Sequential Mobility Particle Sizer (SMPS) and Portable Aerosol Spectrometer (PAS)] and particle collection (PIXE Streaker).

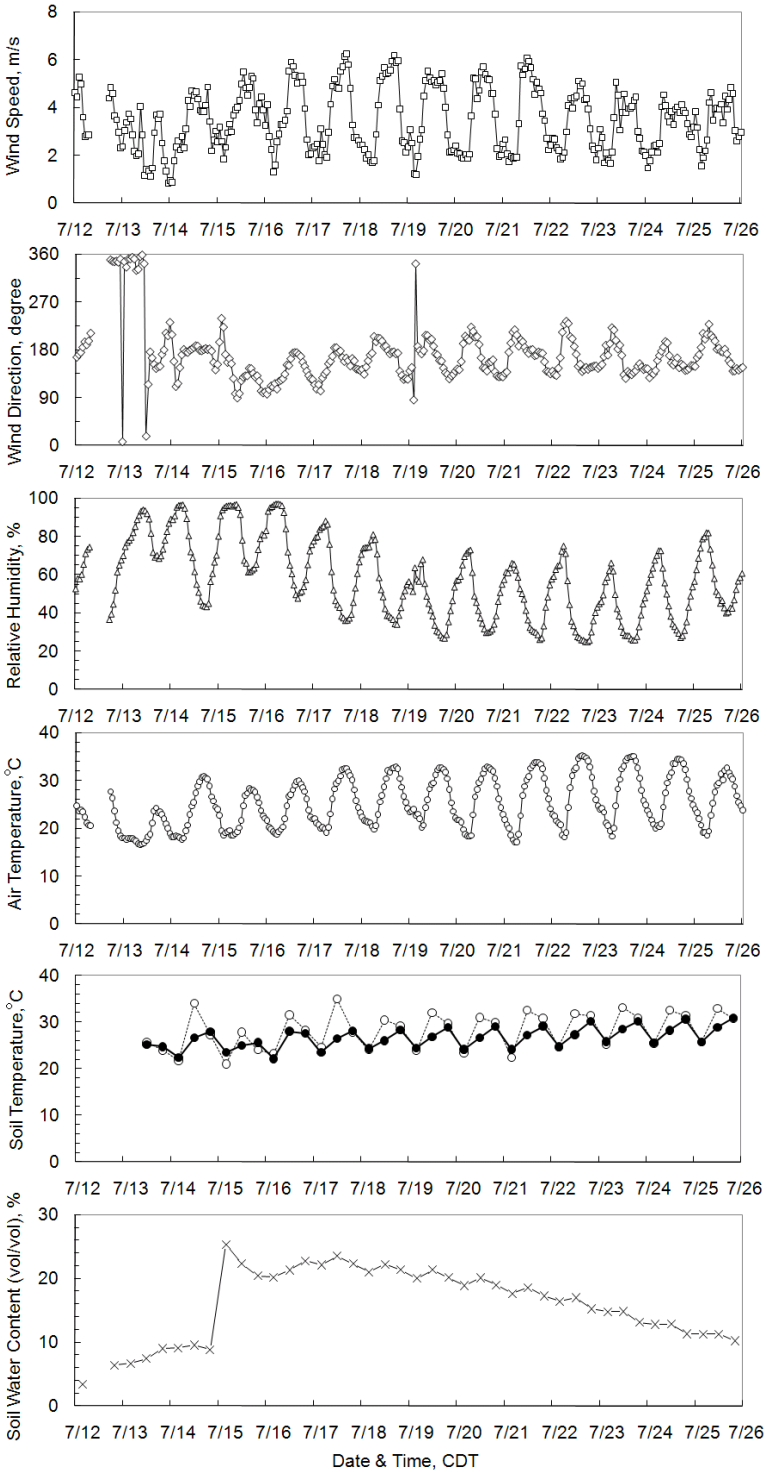

Figure 3. Hourly time-averaged meteorological data is shown including wind speed, wind direction, relative humidity, and air temperature. Measurements of soil temperature at a depth of 5 cm (open circles), soil temperature at a depth of 25 cm (solid circles), and soil water content at a depth of 25 cm (crosses) are also shown (Adapted from Hiranuma et al., 2010).

A

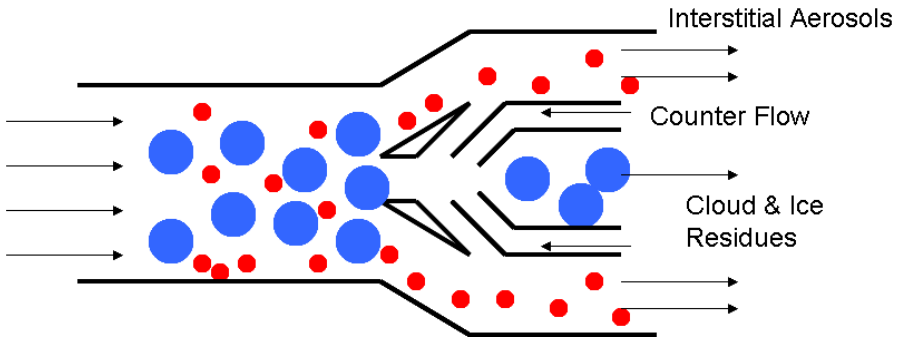

B

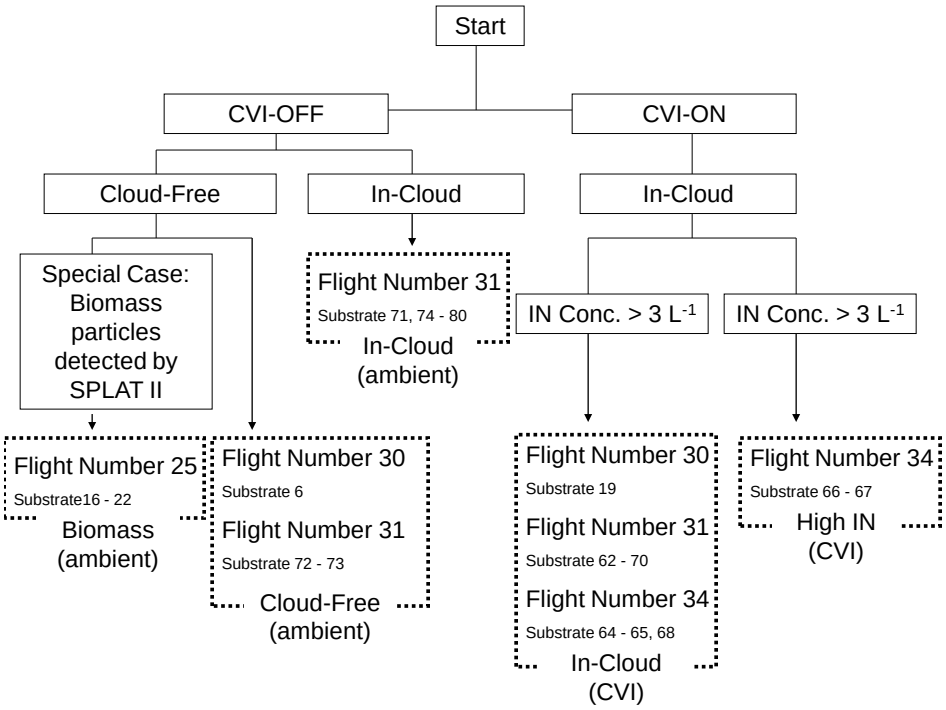

Figure 4 (A) Particle separation by a counterflow virtual impactor and (B) Algorithms used to identify the five defined sampling conditions [i.e., biomass, cloud-free, in-cloud (ambient), in-cloud (CVI), and high IN] for twenty five TRAC samples (i.e., Table 1A). Special case includes biomass indication by SPLAT II and high IN activity indication by CFDC.

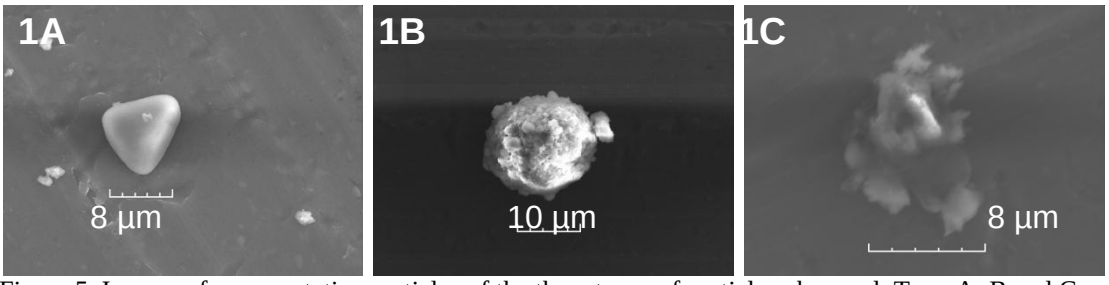

Figure 5. Images of representative particles of the three types of particles observed: Type A, B and C are shown in 5A, 5B, and 5C, respectively.

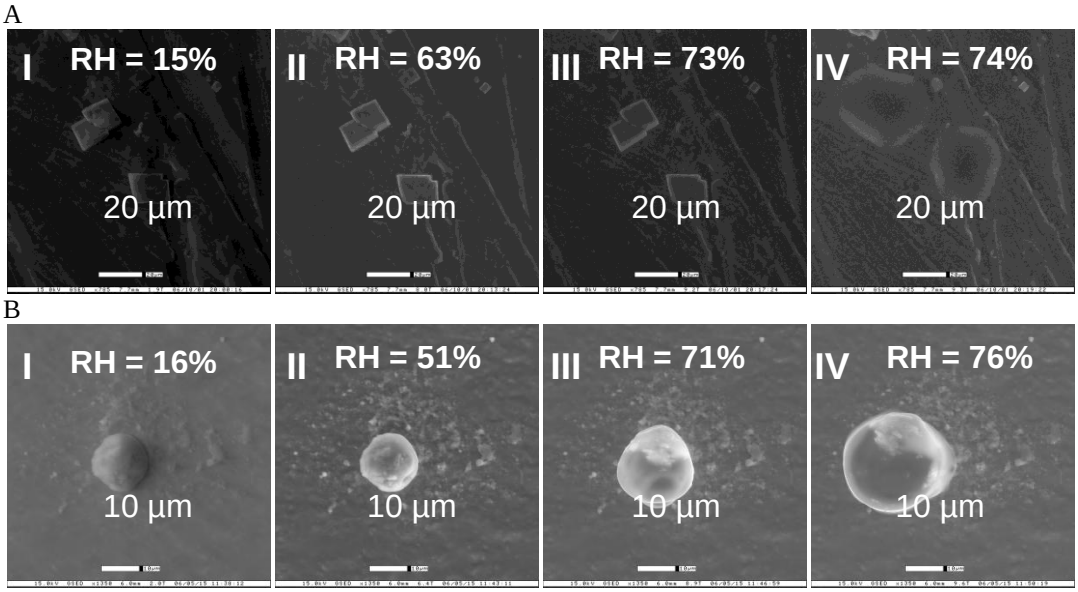

Figure 6. ESEM images obtained during water uptake experiments. Particles in A are sodium chloride crystals (~20 µm diameter), and in B are from an agricultural sample (~10µm diameter).

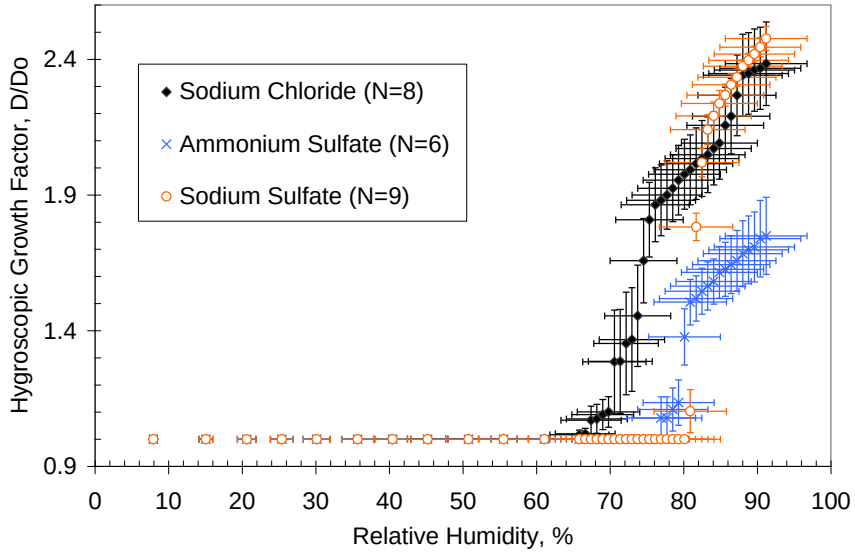

Figure 7. Hygroscopic growth factor as a function of relative humidity for sodium chloride, ammonium sulfate and sodium sulfate is shown as solid diamonds, crosses, and open circle, respectively.

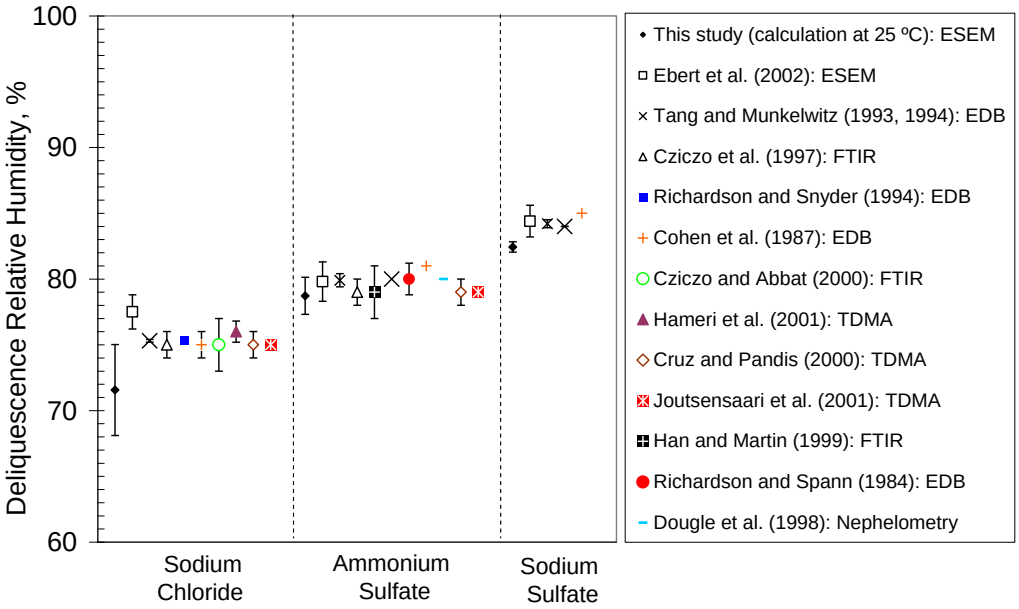

Figure 8. Summary of the deliquescent relative humidities of well known salts by various techniques.

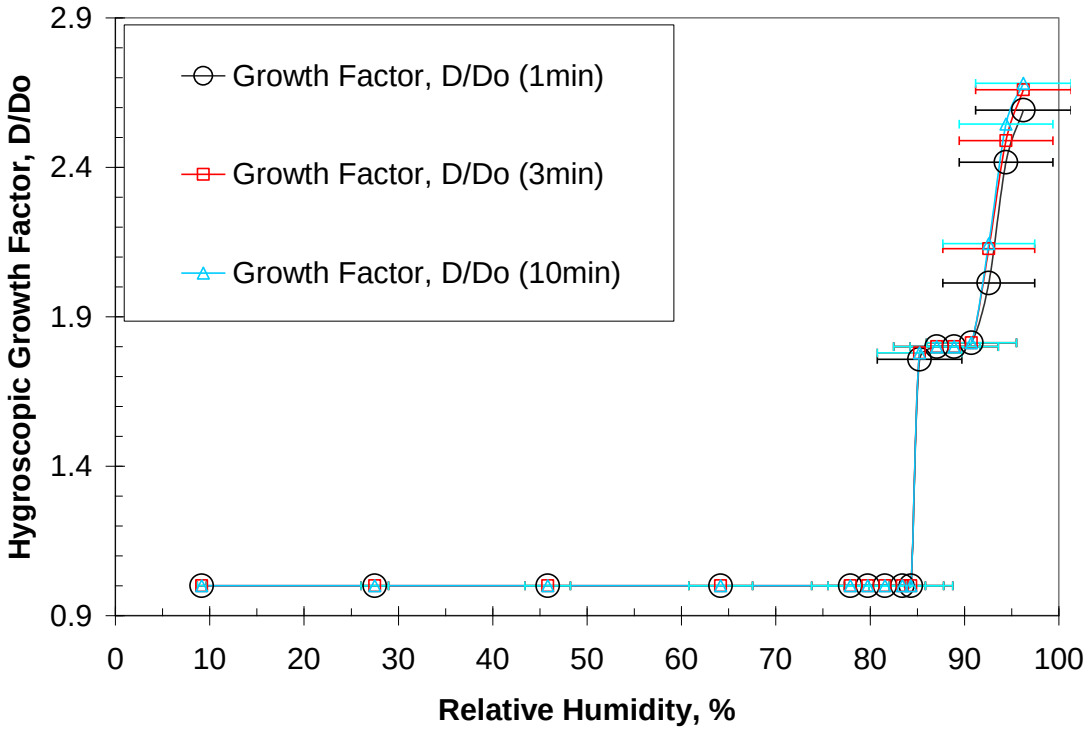

Figure 9. Time Scale of ESEM water uptake experiments.

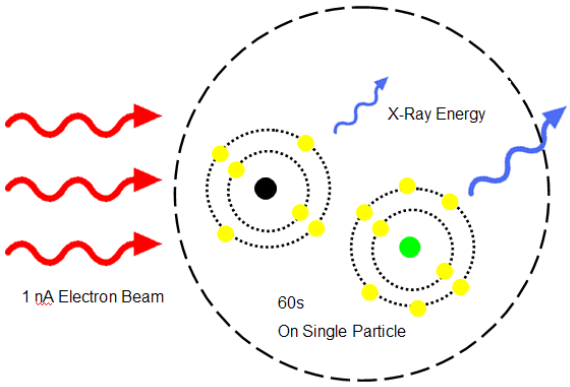

Figure 10. Concept of EDX's inelastic interaction. Electrons are distributed around nucleus of carbon (black) and oxygen (green) in single particle.

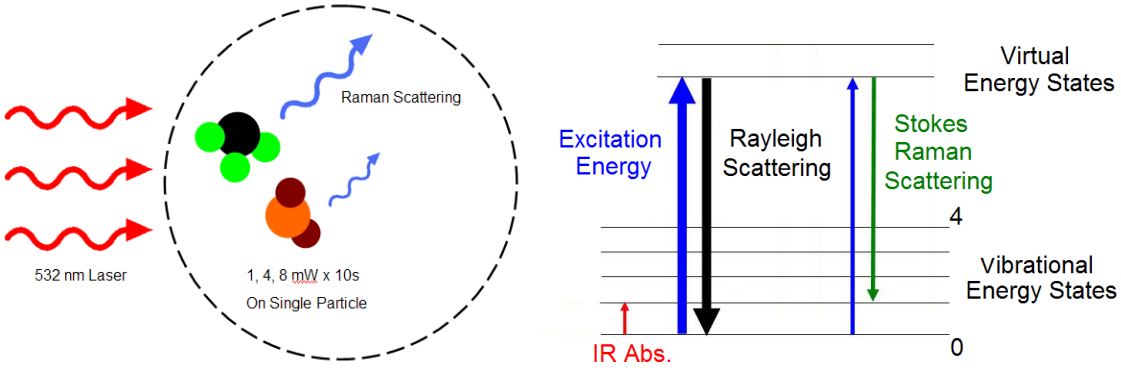

Figure 11. Concept of Raman MS's inelastic scattering.

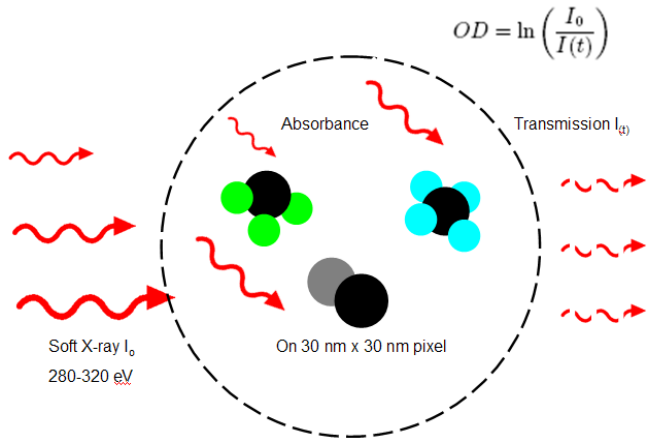

Figure 12. Concept of Raman STXM/NEXAFS's inelastic interaction. Table 9 provides chemical bonding information (electronic transition and functionality) as well as corresponding position of peaks relative to the applied energy in the range of 278 to 320 eV.

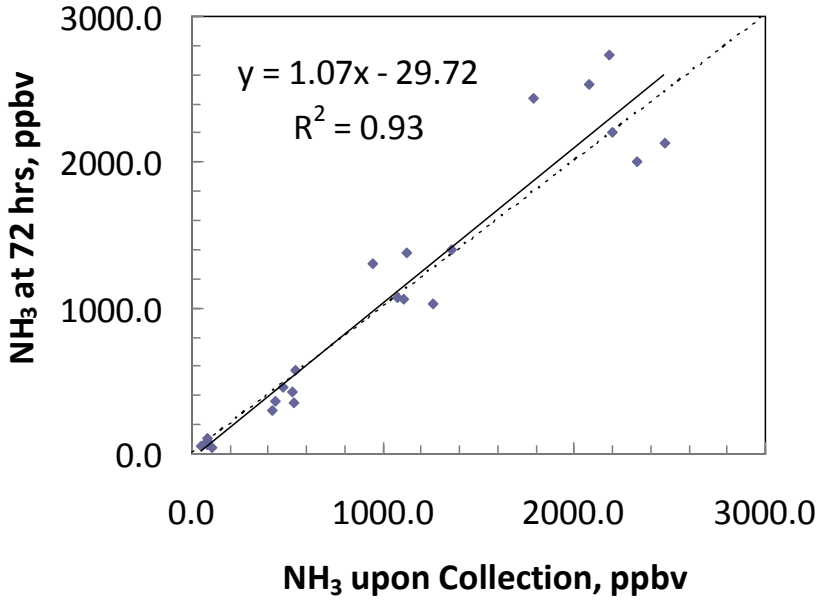

Figure 13. The stability of ammonia in pH altered samples.

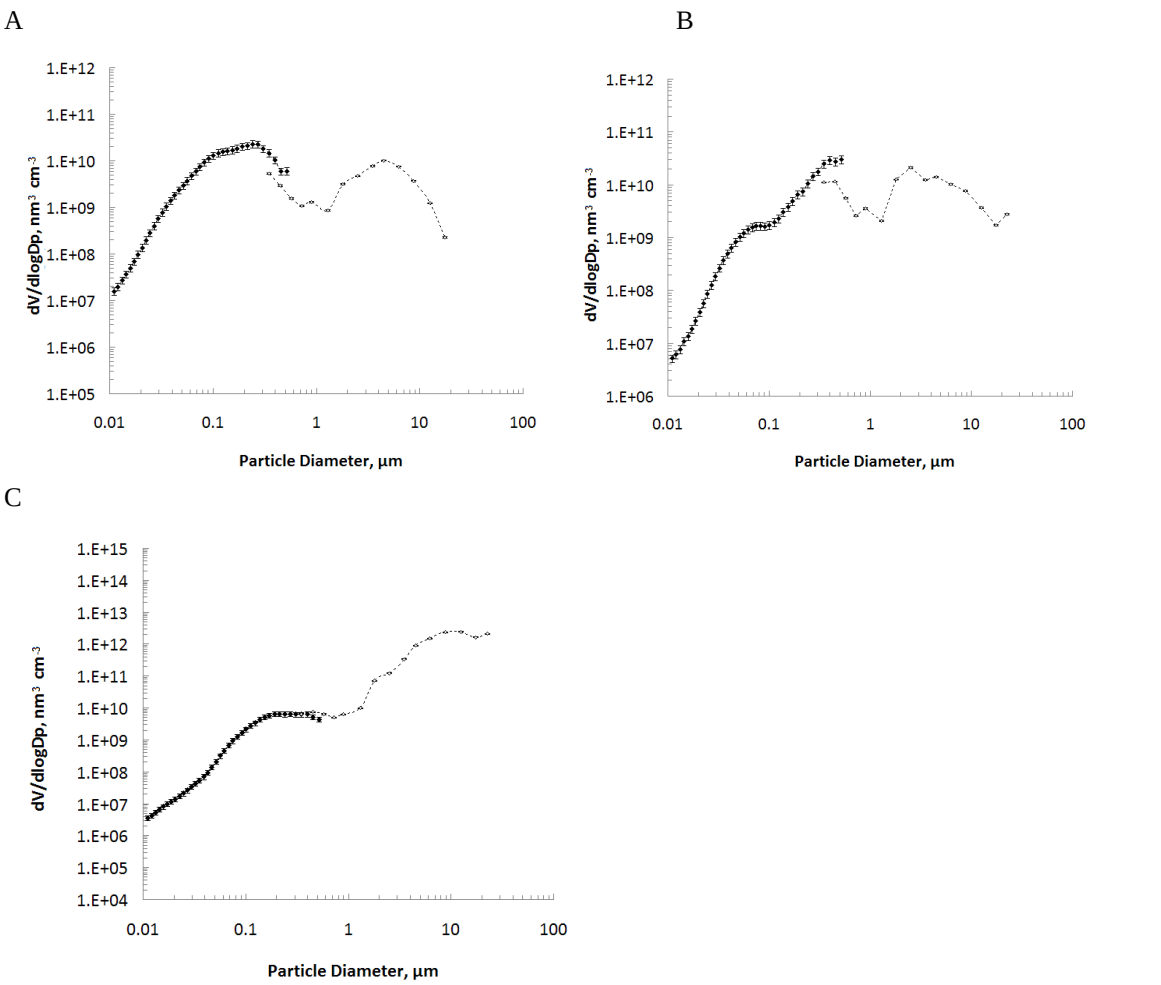

Figure 14. Measured 24 hour averaged particle volume distribution in (A) Houston on September 26th 2006, (B) College Station on June 16th 2006, and (C) Tulia on July 24th 2008. Solid data points were measured by SMPS (0.01 to 0.5 µm) and open data points were measured by PAS (0.3 to 25 µm). Error bars represent the inlet loss rate of the SMPS (± 17%) and the measurement accuracy of the PAS (± 3%).

A

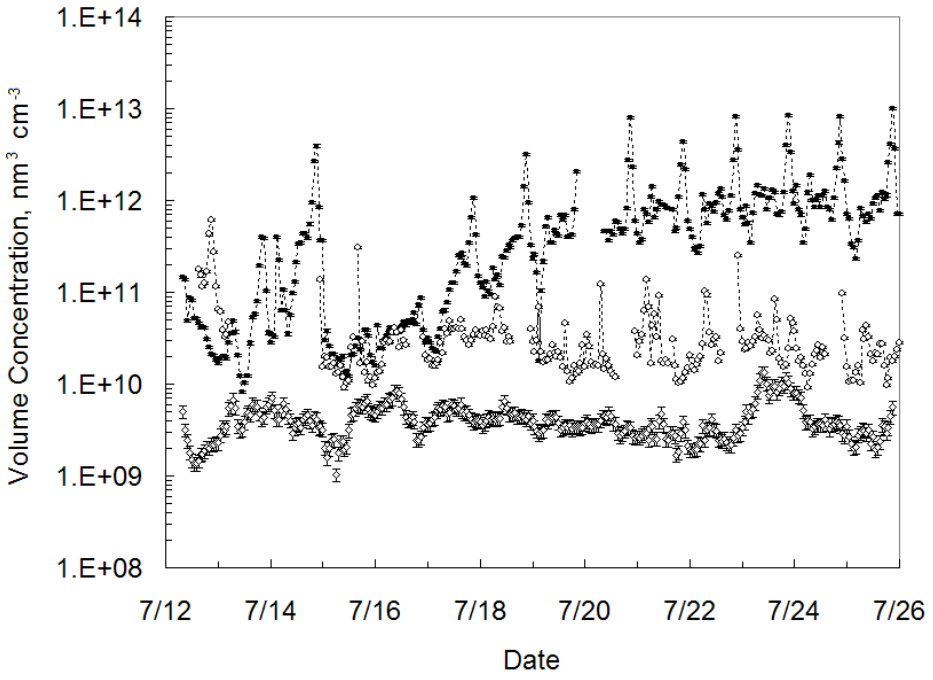

B

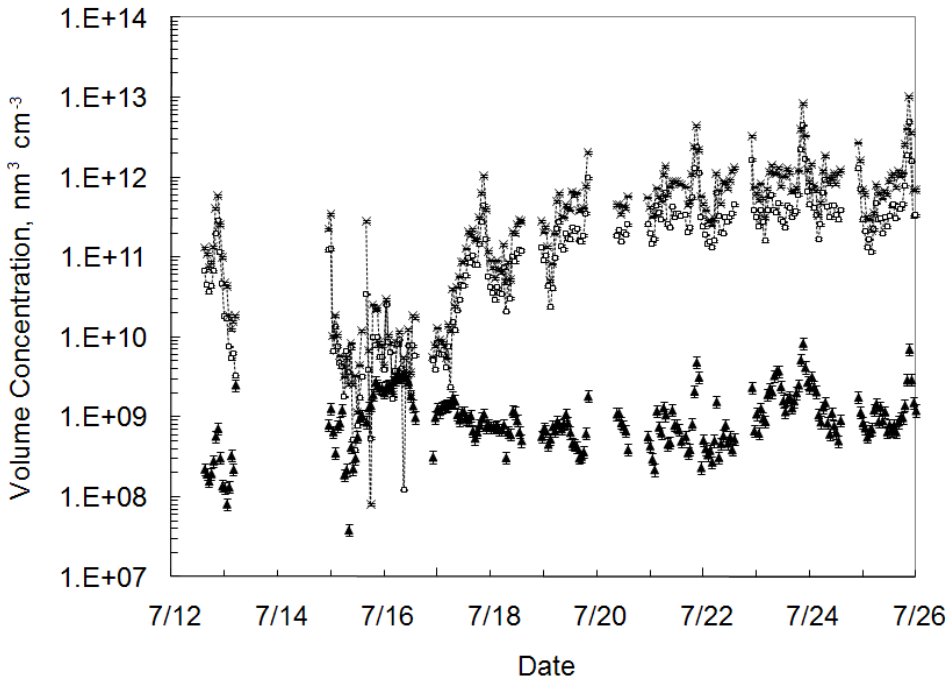

Figure 15. (A) Hourly averaged volume concentrations of PM measured by PAS at the downwind (solid squares) location, upwind (open circles) location, and total SMPS counts at downwind (open diamond) location and (B) actual emissions from the feedlot for total PAS (cross), PAS PM_{10} (open square), and PAS PM_1 (solid triangle) estimated by subtracting upwind measurements from downwind ones. Error bars represent the inlet loss rate of the SMPS (± 17%) and the measurement accuracy of the PAS (± 3%). Note that multiplying 2.65 x 10^{-9} (assuming soil density of 2.65 g cm^{-3}) to volume concentration (nm^3 cm^{-3}) results in mass concentration in the unit of μg m^{-3}.

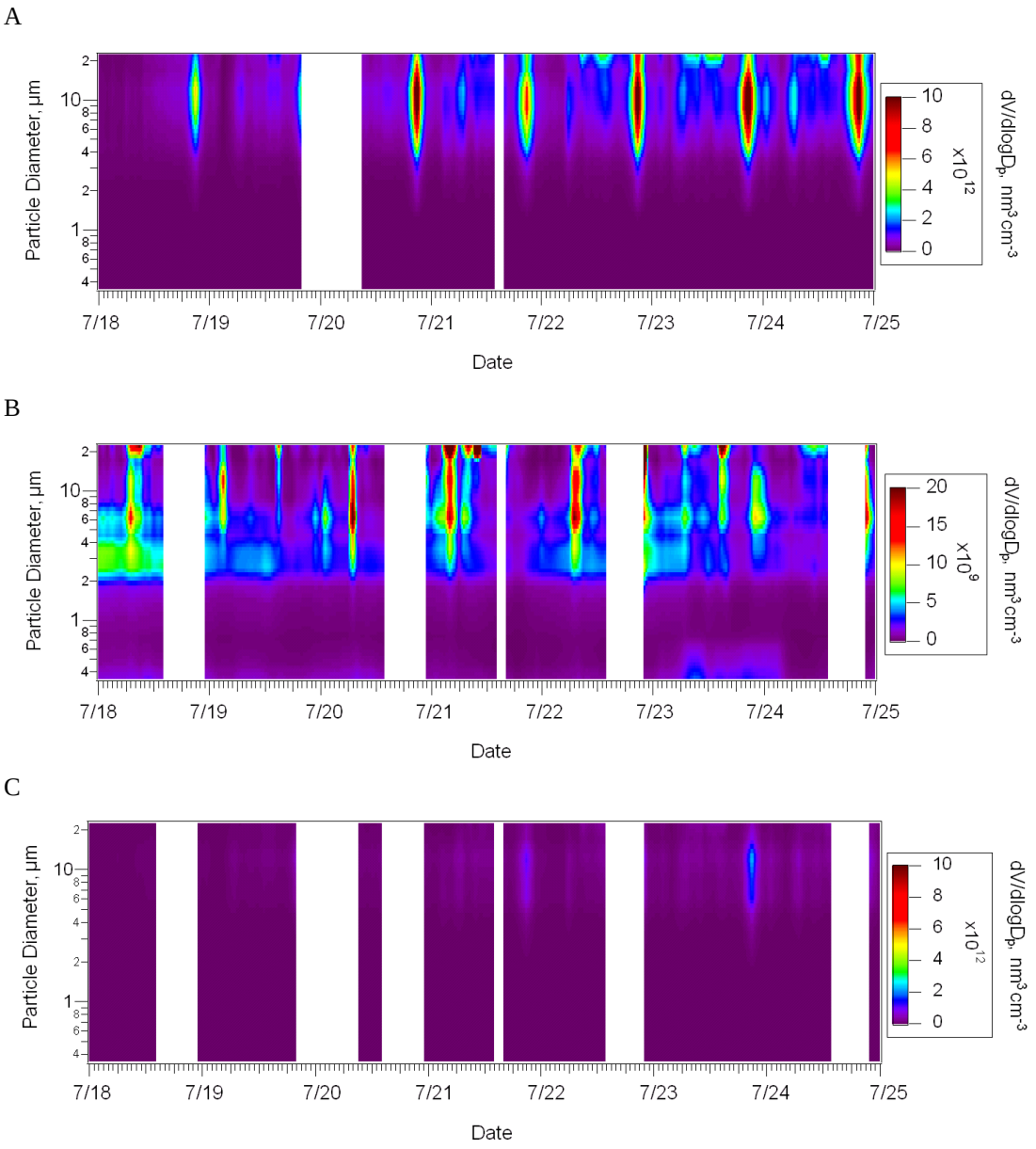

Figure 16. Hourly averaged aerosol volume distributions of (A) downwind, (B) upwind, and (C) subtraction of upwind measurements from downwind ones from July 18 to 25, 2008. Particle size distributions were measured by PAS (0.3 to 25 µm).

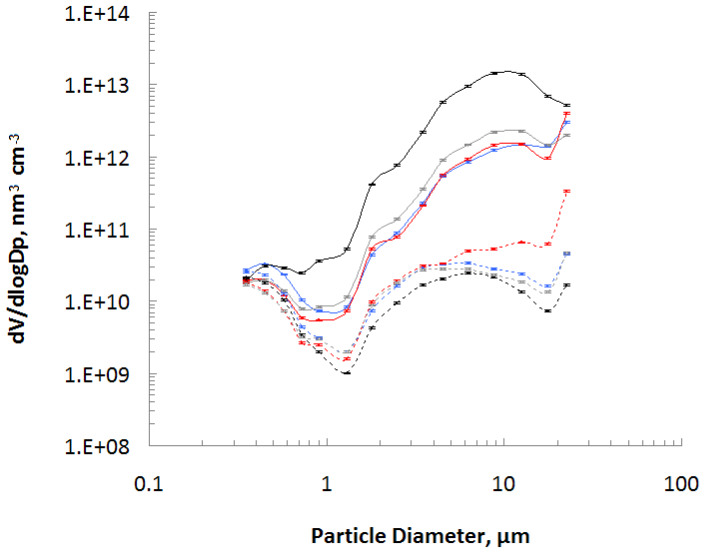

Figure 17. Measured agricultural aerosol volume distributions at 8:00 am (blue), 3:00 pm (red), and 9:00 pm (black) in downwind location (solid) and upwind location (dashed) on July 23rd 2008. Gray data points represent 24 hour averaged size distributions. Both particle size distributions were measured by PAS (0.3 to 25 µm). Error bars represent the measurement accuracy of the PAS (± 3%).

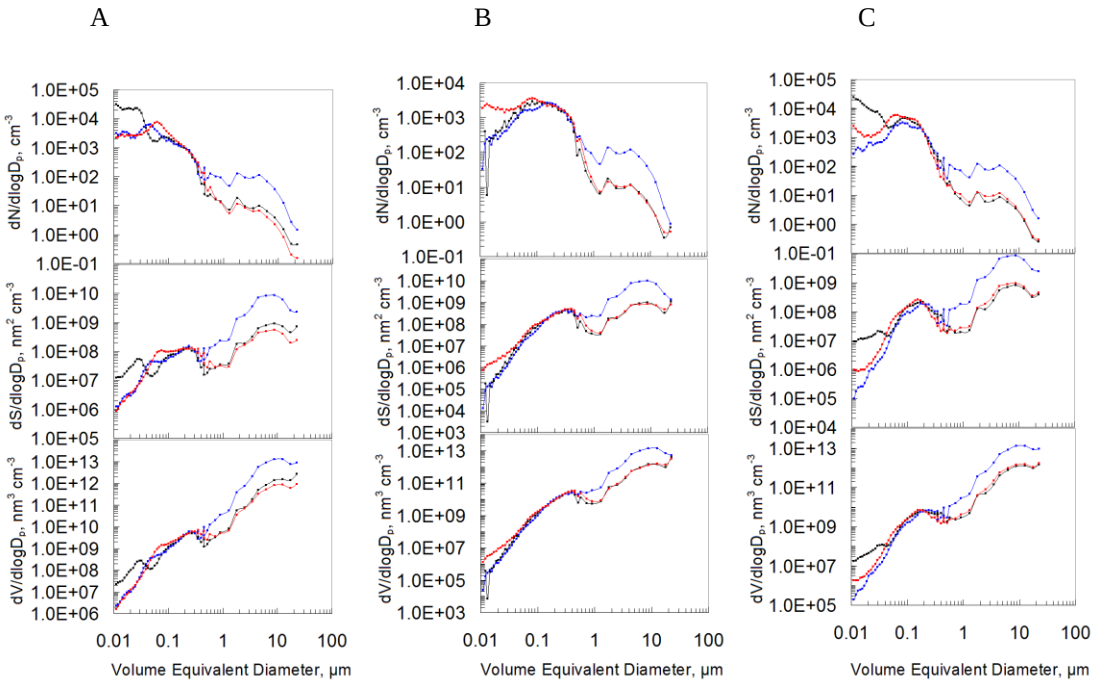

Figure 18. Hourly averaged agricultural aerosol number, surface, and volume distributions as a function of log D_p measured at the downwind site. Distributions are plotted at selected time 8:00 am (red), 3:00 pm (black), and 9:00 pm (blue) on (A) July 22, (B) July 23, (C) July 24.

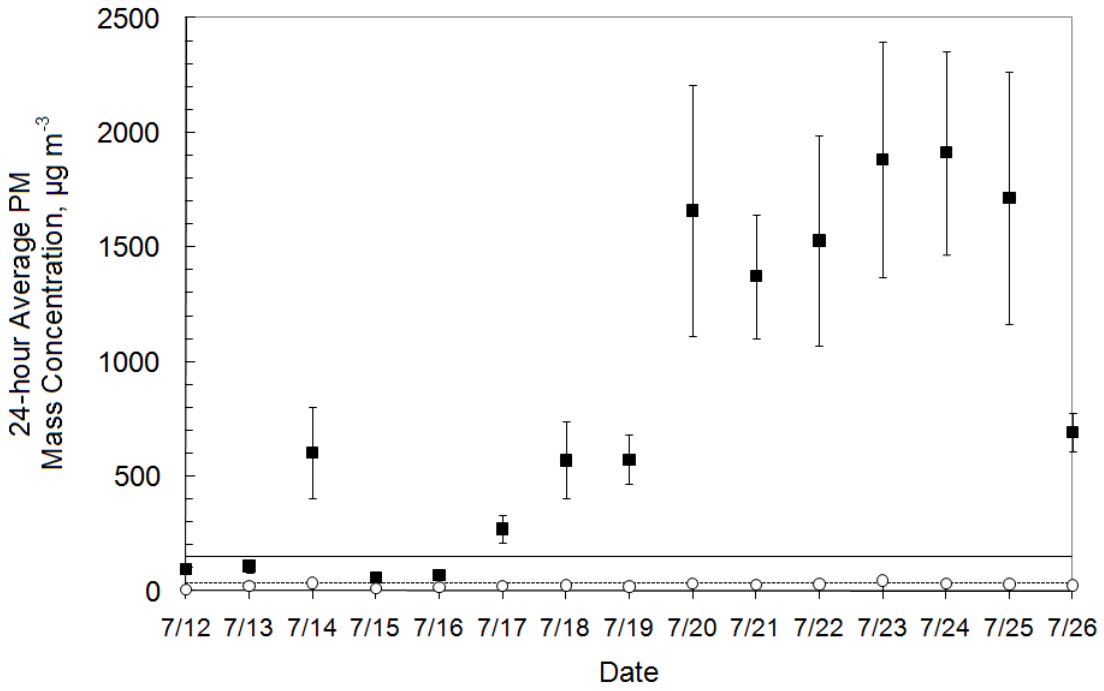

Figure 19. Daily average of PM_{10} (solid square) and $PM_{2.0}$ (open circle) mass concentration measured at the downwind location as function of time. Solid and dashed lines represent the public health standard under the NAAQS (150 µg m^{-3} for PM_{10} and 35 µg m^{-3} for $PM_{2.5}$, respectively). Error bar represents the standard deviation of the mean measured concentration over 24 hour period.

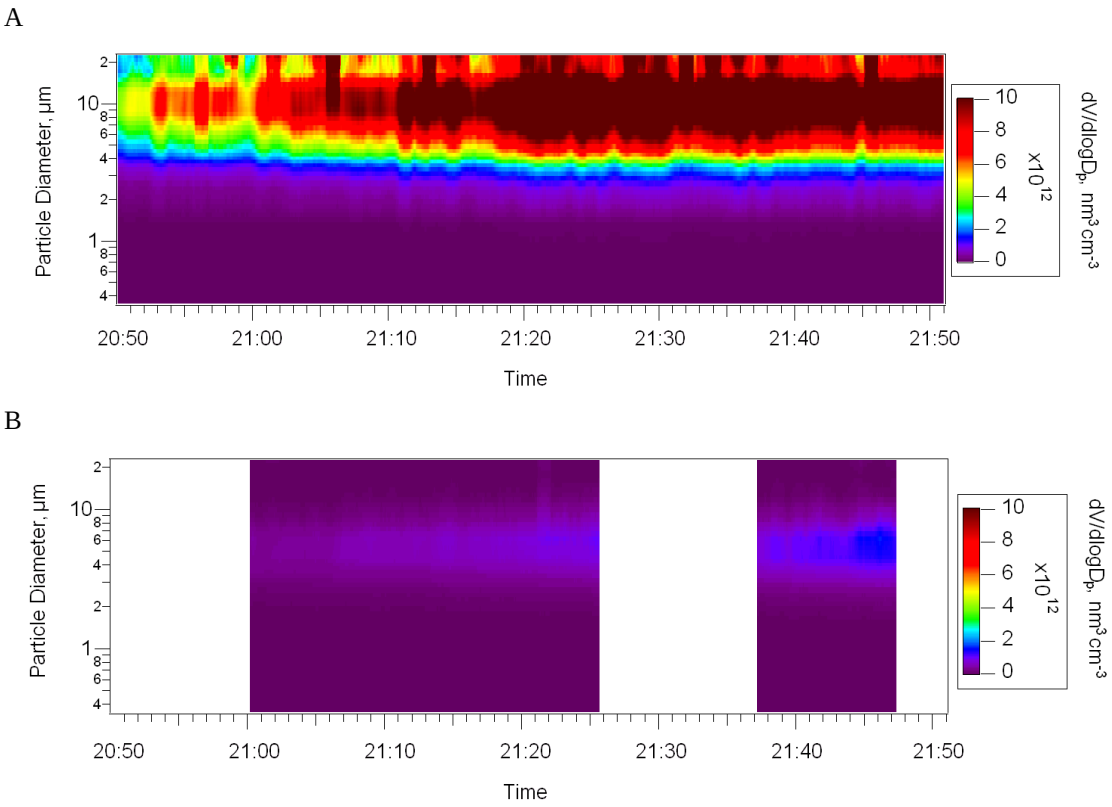

Figure 20. Measured agricultural aerosol volume distributions in (A) downwind location and (B) far-field location on July 22, 2008. Both particle size distributions were measured by PAS (0.3 to 25 µm).

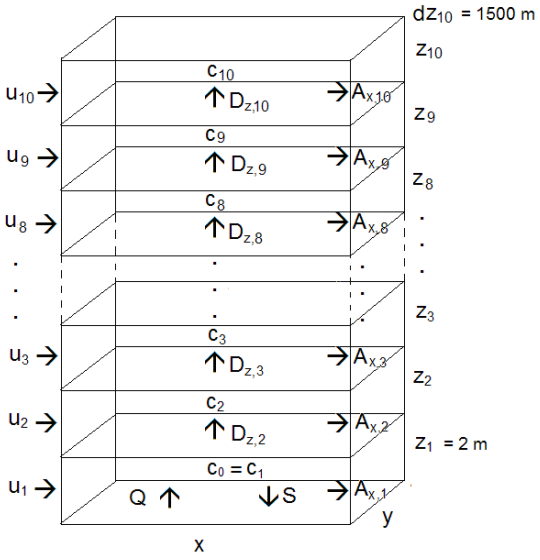

Figure 21. Schematic depiction of a one-dimensional column model. u_i is the wind speed with the wind assumed to have a constant direction at layer i. Q represents the mass emission flux, S the dry depotion flux, A_x the horizontal advection term, and D_z the vertical diffusion flux. Height representation is approximately log scaled.

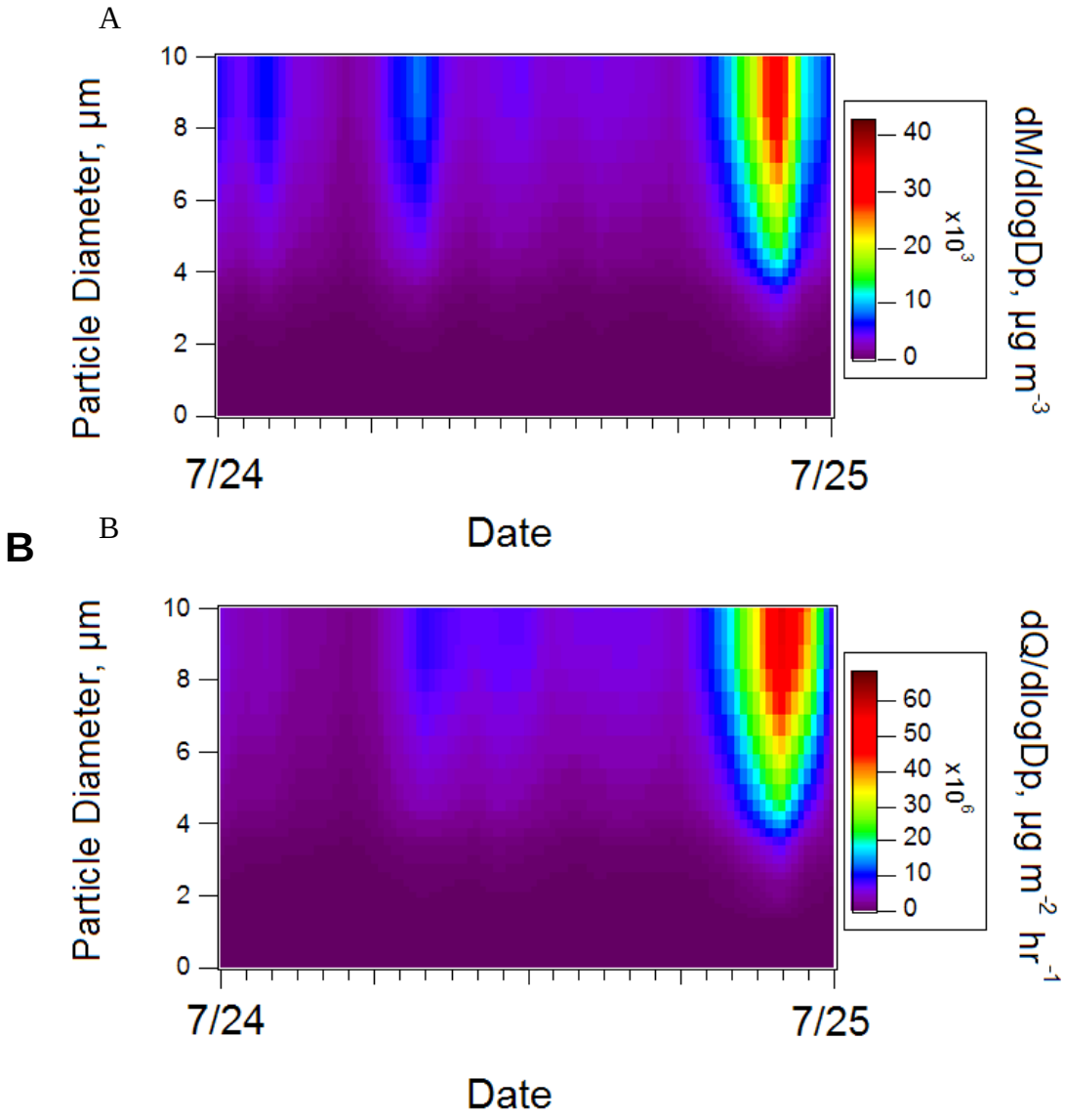

Figure 22. Hourly averaged (A) mass concentration and (B) emission rate of size-resolved agricultural particles as a function of time measured in 2008.

A

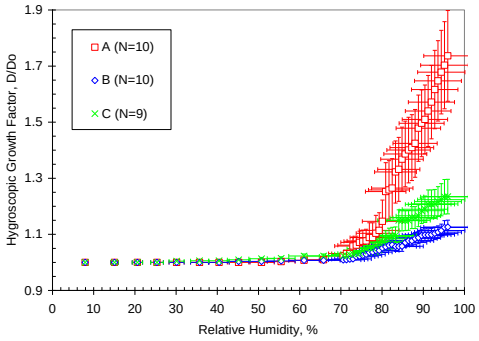

B

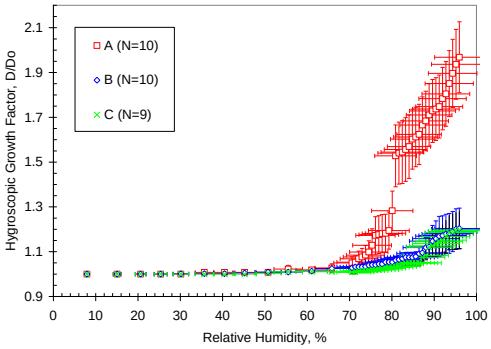

C

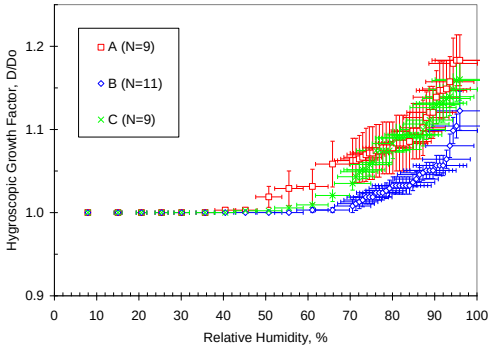

Figure 23. Hygroscopic growth factor as a function of relative humidity for particles collected at the downwind edge of the feedlot in size range >10 µm, 2.5-10 µm, and <2.5 µm are shown in A, B, and C, respectively.

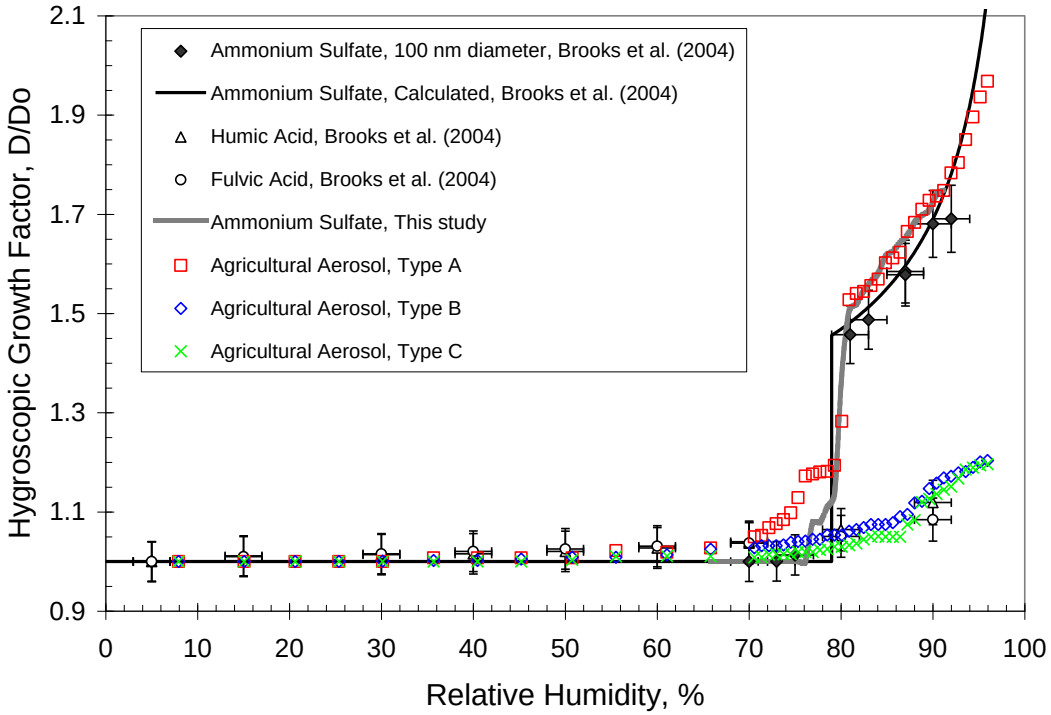

Figure 24. Hygroscopic growth factor for particles collected during this study and known compositions: Agricultural aerosol data is for downwind in size range of 2.5-10µm.

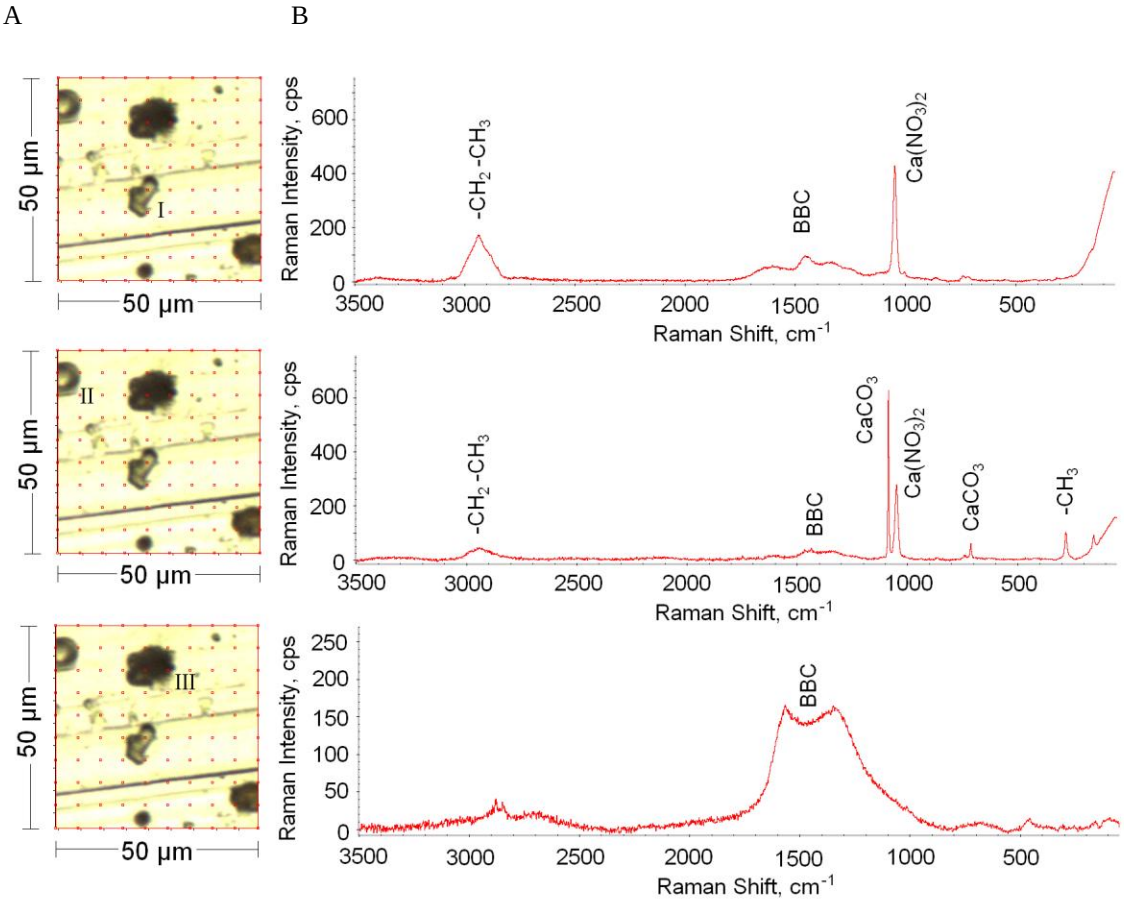

Figure 25 (A) Microscopic image of particles derived from upwind location collected on July 22 at ~9:00 pm (B) Raman spectra of agricultural particle I, II, and III (i.e., Fig. 25A) in spectral range of 50 to 3500 cm^{-1}: (I) $Ca(NO_3)_2$ at 1050 cm^{-1}, (II) $CaCO_3$ at 1085 cm^{-1}, and (III) amorphous carbon with broad spectra ~1500 (1050-1620) cm^{-1}. Other identified peaks (≥ 50 cps) represent (I) lattice vibrations in crystals at ~100 cm^{-1}, and soil/soot dominant complex at ~1500 and 2940 cm^{-1} (II) $Ca(NO_3)_2$ at 1050 cm^{-1}, minor peaks of $CaCO_3$ at 281 and 712 cm^{-1}, and soil/soot dominant complex at 155, ~1500, and 2944 cm^{-1}.

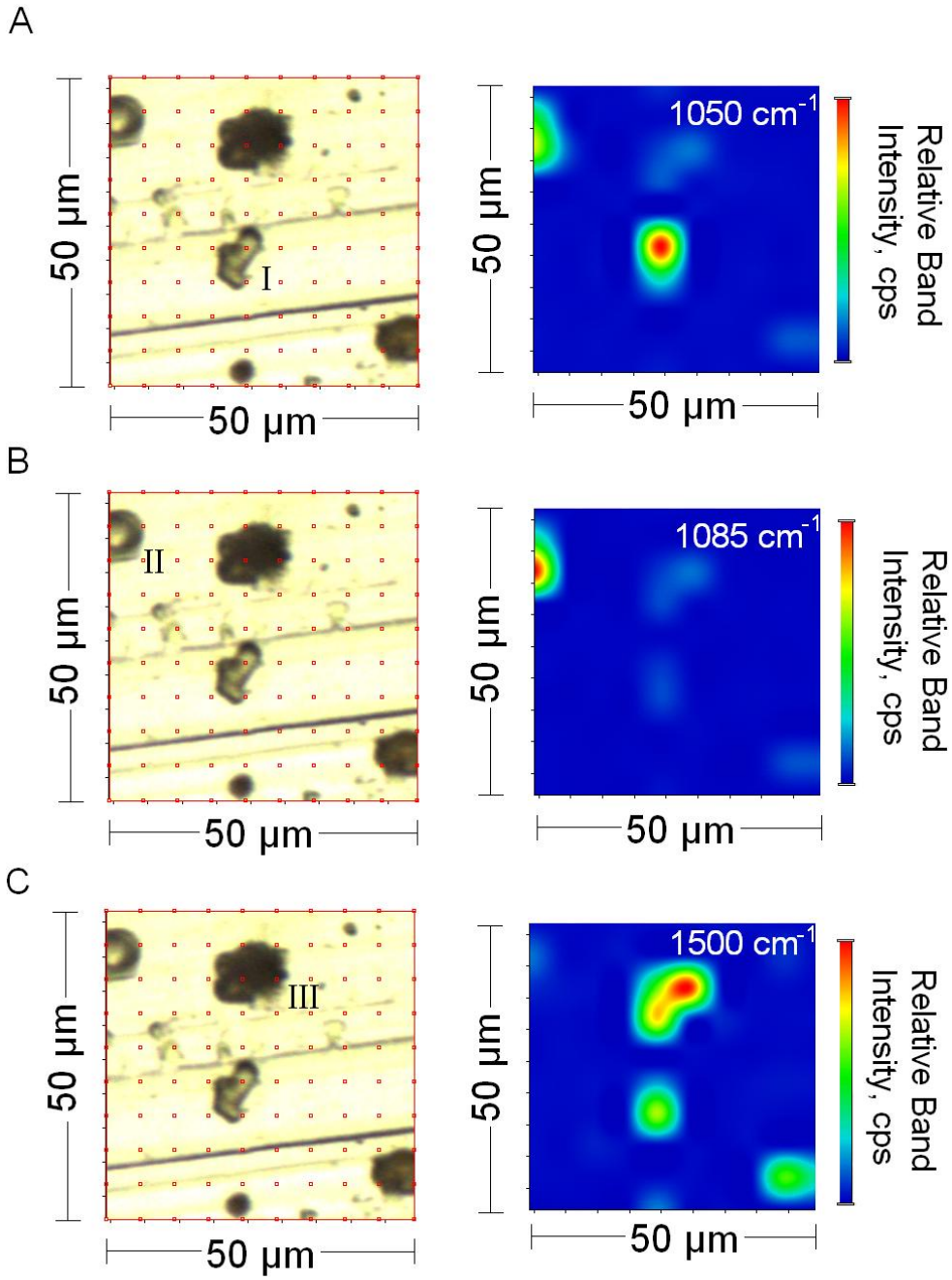

Figure 26. Chemical maps of selected molecular groups in agricultural aerosols at different Raman band position, (A) 1050 cm^{-1}: $Ca(NO_3)_2$, (B) 1085 cm^{-1}: $CaCO_3$, and (C) 1500 cm^{-1}: amorphous carbon (i.e., I, II, and III from Fig 25A and 25B). Mapping experiment was conducted on particles collected on July 22, 2008 at ~9:00 pm in upwind location with a laser power of 8mW.

A

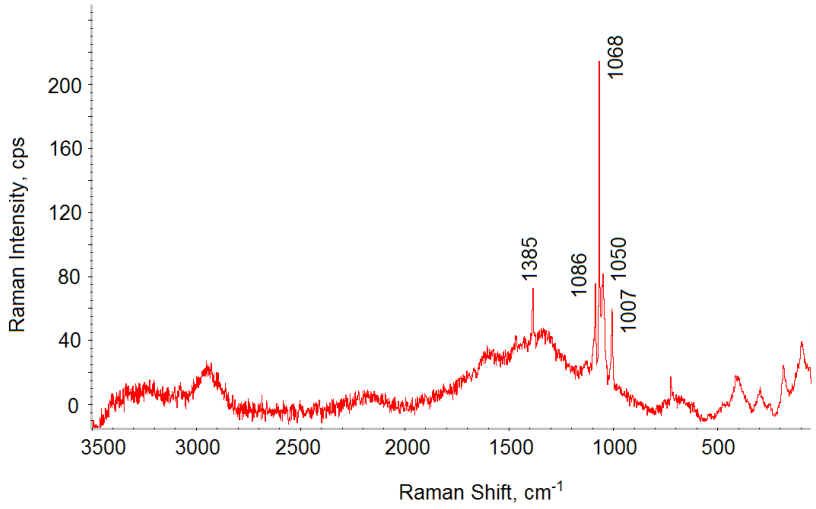

B

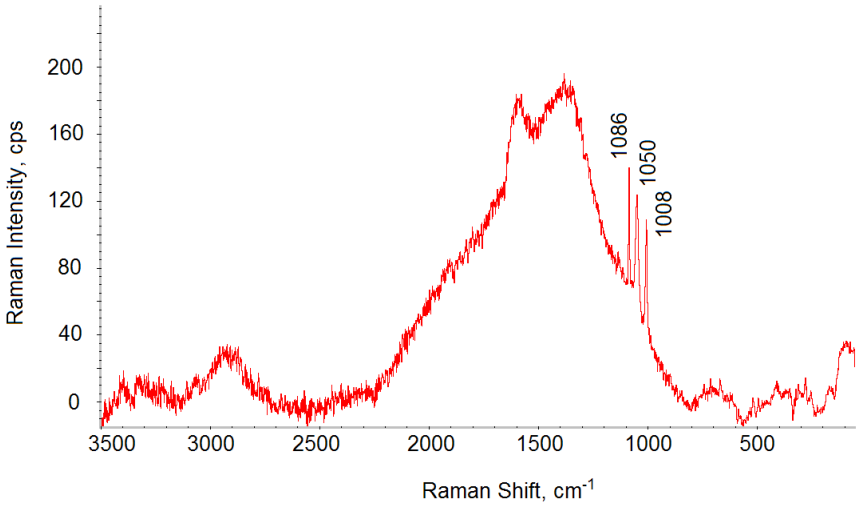

Figure 27. Qualitative classification of spectra types: (A) inorganic dominant complex, (B) soil/soot dominant complex. Threshold is ≥50 cps. For these particular spectra, (A) 1007 $CaSO_4$; 1050 $Ca(NO_3)_2$; 1068/1385 $NaNO_3$; 1086 $CaCO_3$, (B) 1008 $CaSO_4$; 1050 $Ca(NO_3)_2$; 1086 $CaCO_3$; ~1500 HULIS bands. Both spectra are measured at 8mW on sample collected at downwind location in the evening on July 22.

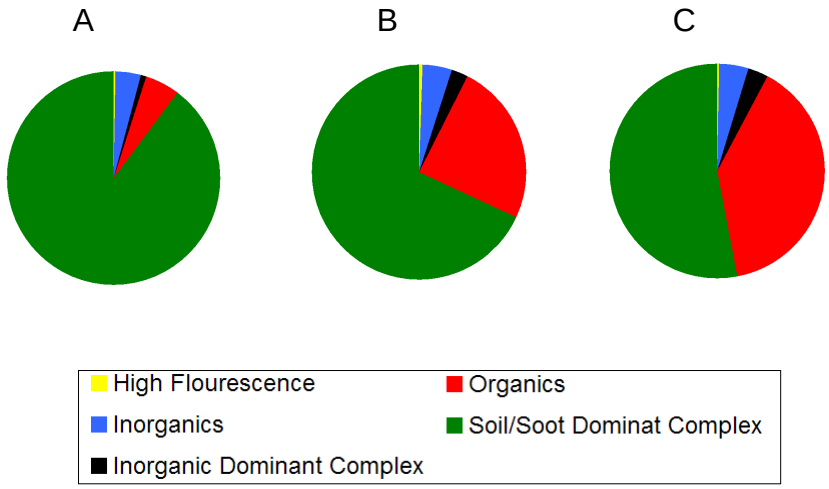

Figure 28. Average fractions of composition categories identified by Raman microspectrometry analyses for samples collected on July 22 and 24, 2008 with the laser excitation energy at (A) 1mW, (B) 4mW, and (C) 8mW.

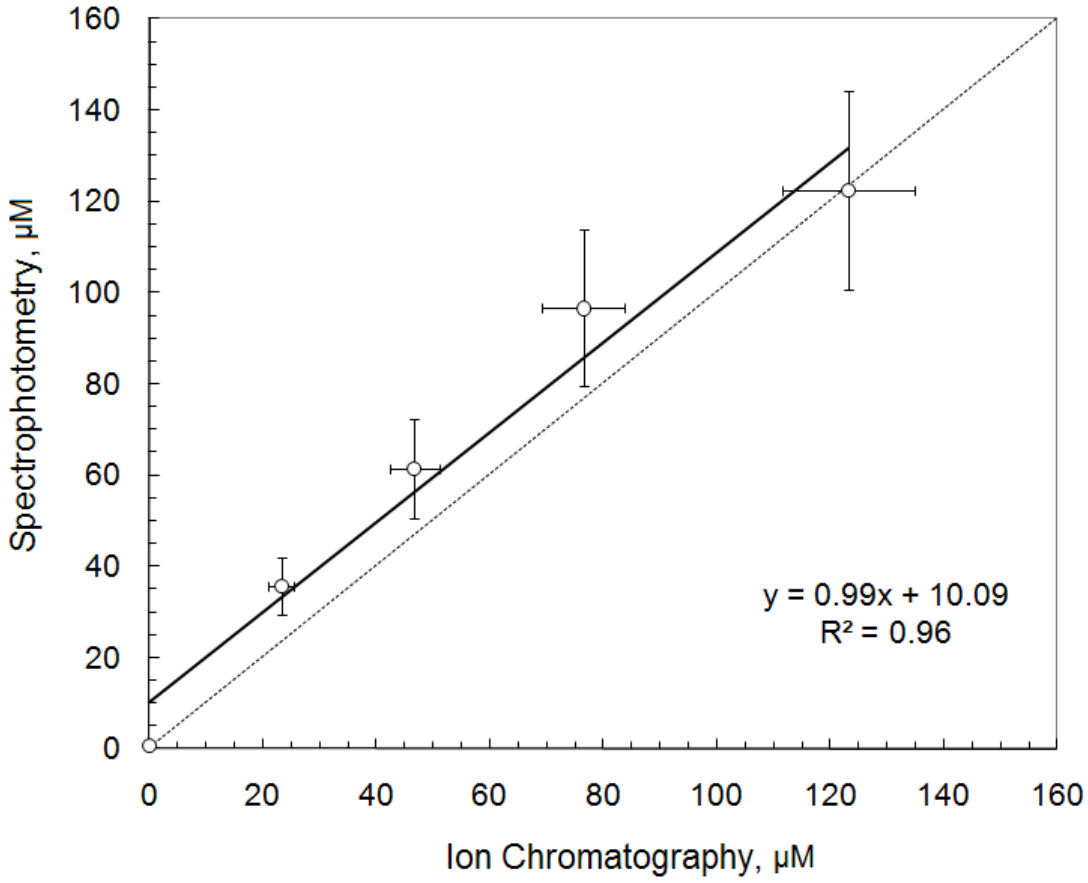

Figure 29. Comparison between ion chromatography and visible spectrophotometry measurements for solutions of known concentrations of ammonium.

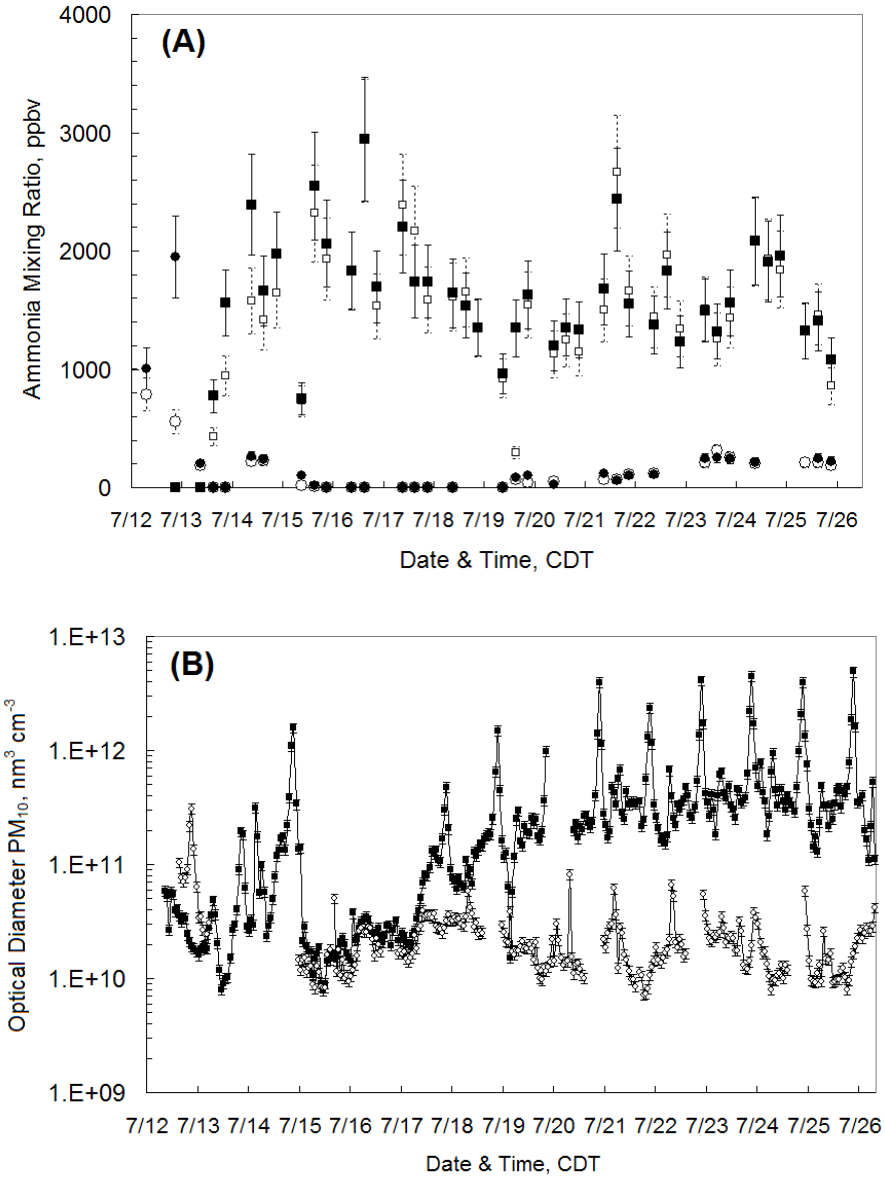

Figure 30. (A) Mixing ratios of total NH_x at the downwind and upwind sites are shown as solid squares and solid circles, respectively. Mixing ratios of gas phase ammonia at the downwind sites are shown as open squares and open circles, respectively. Error bars represent the experimental uncertainty of the spectrophotometric technique (± experimental error) and (B) Volume concentrations (20-minute averages) of PM_{10} at the downwind (solid squares) and upwind sites (open circles). Error bars represent the inlet loss rate of the aerosol spectrometer (± 10% inlet loss rate).

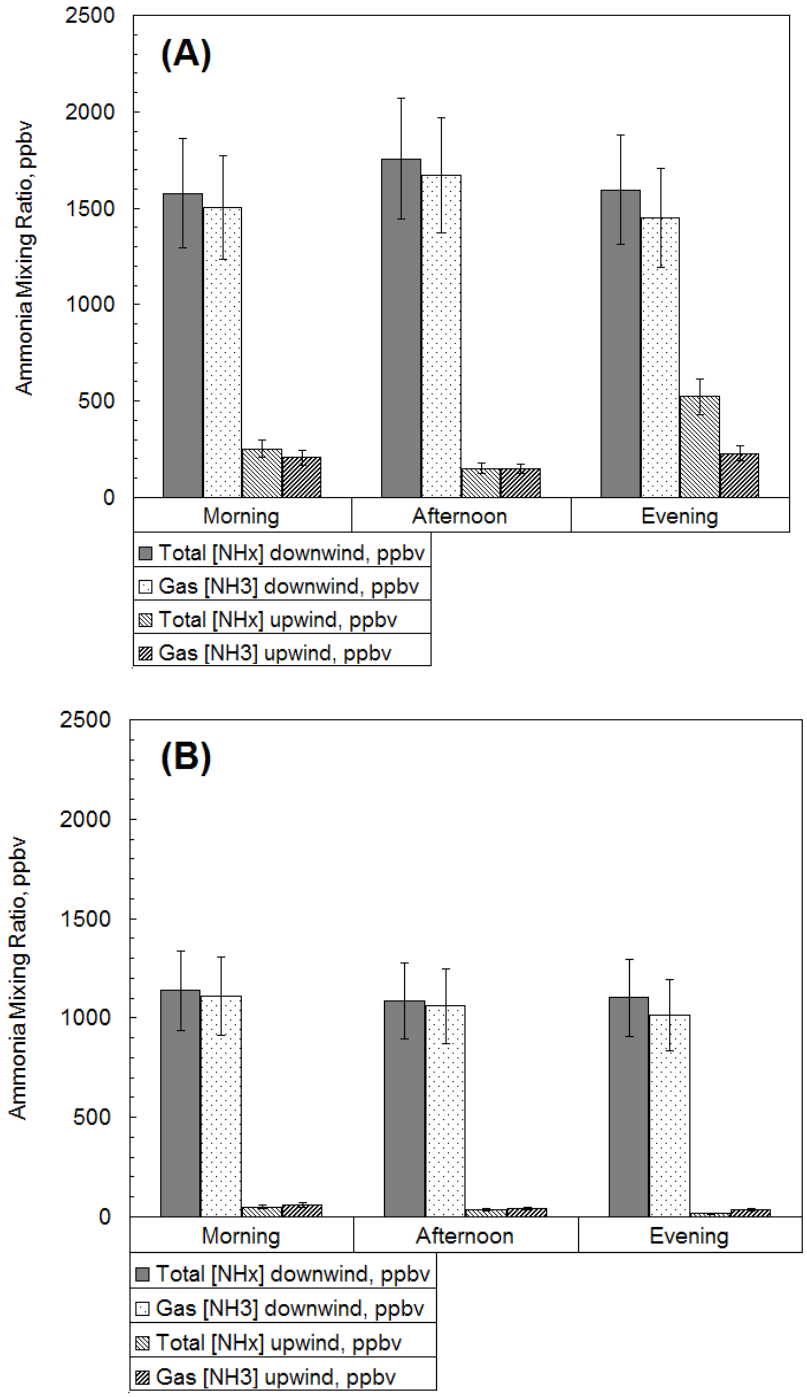

Figure 31. Average ammonia concentrations measured in 2008 and 2007 are shown in A and B, respectively.

A

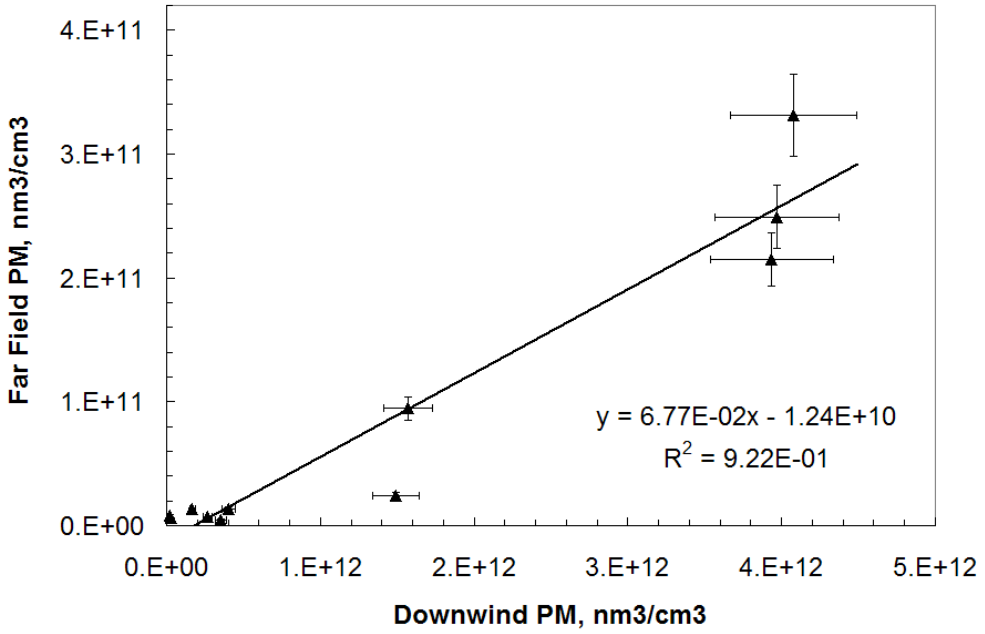

B

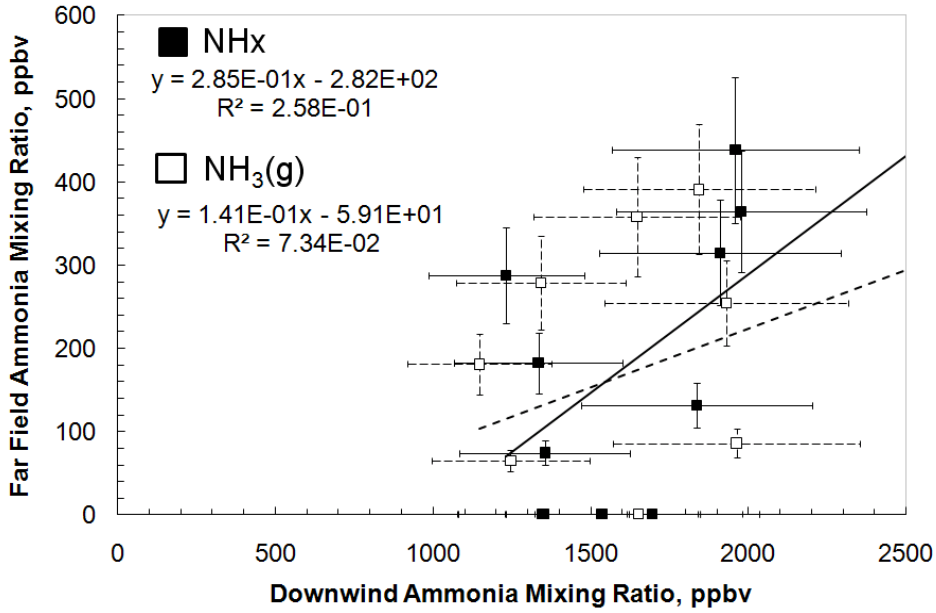

Figure 32. Correlation between 20-minute time-averaged concentrations of (A) PM_{10} and (B) NHx and NH_3(g) measured at the downwind and far-field locations.

A

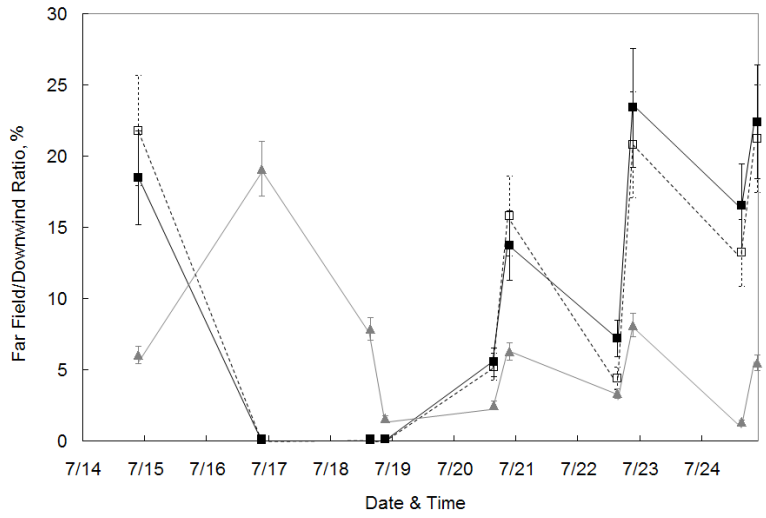

B

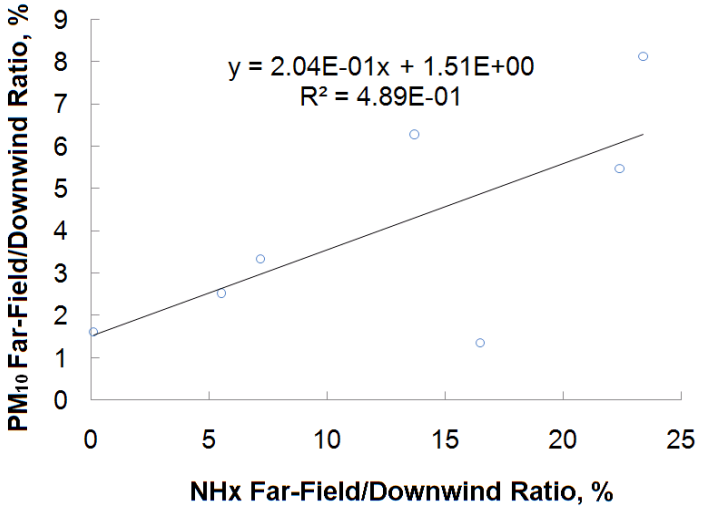

Figure 33. (A) Ratios of concentrations measured at the far-field (~3.5 km downwind) site compared to those measured at the downwind edge of the feedlot for PM_{10} (solid triangles), total NH_x (solid squares), and gas phase ammonia (open squares). Lines connecting the data points are included in guide the eye. (B) Regression analysis between PM_{10} and NHx far-field/downwind ratio for the dry period after July 18.

CVI Ambient

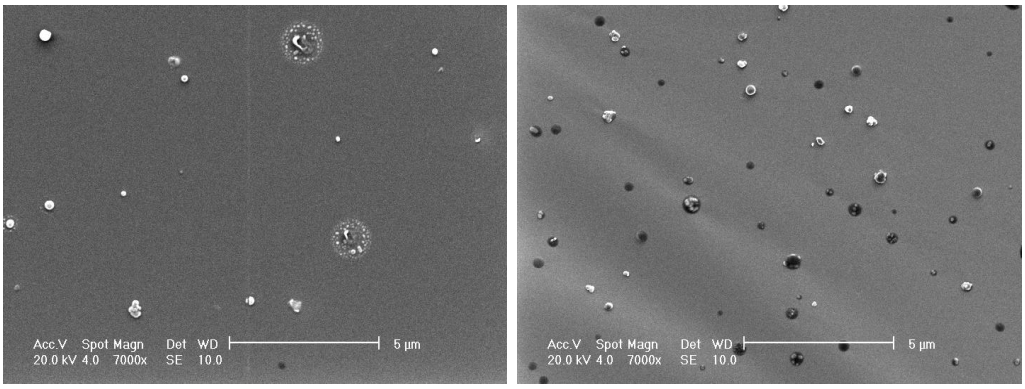

Figure 34. SEM images of two samples collected from the CVI (left: F30-S19) and ambient (right: F30-S06) sampling periods during the flight number 30 on April 26, 2008. Magnified fields of view (7000x) show representative particles from the central areas of samples.

A

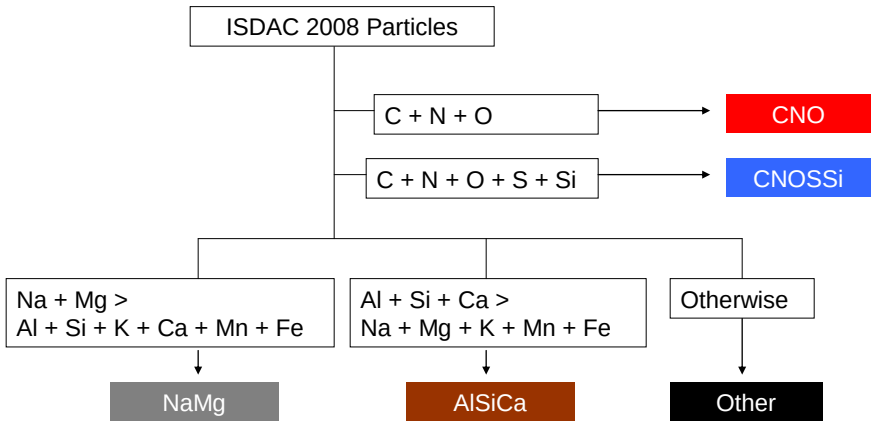

B

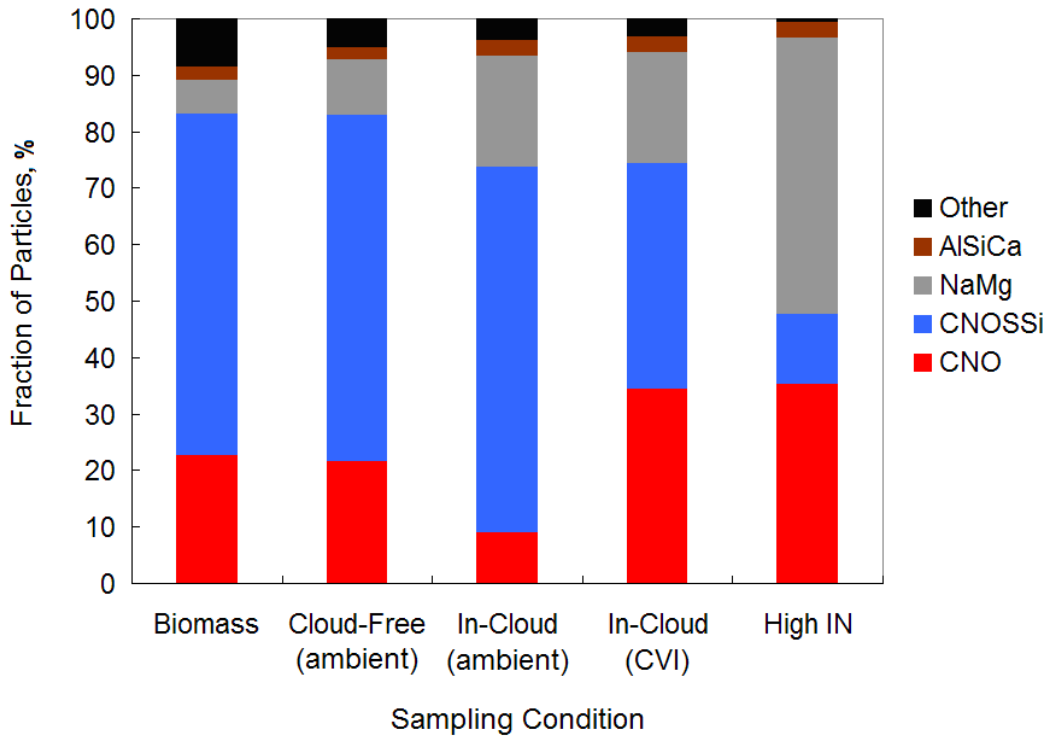

Figure 35. (A) Classification scheme to define particle type applied to the CCSEM/EDX analysis (B) Stacked column chart diagram of particle groups in samples.

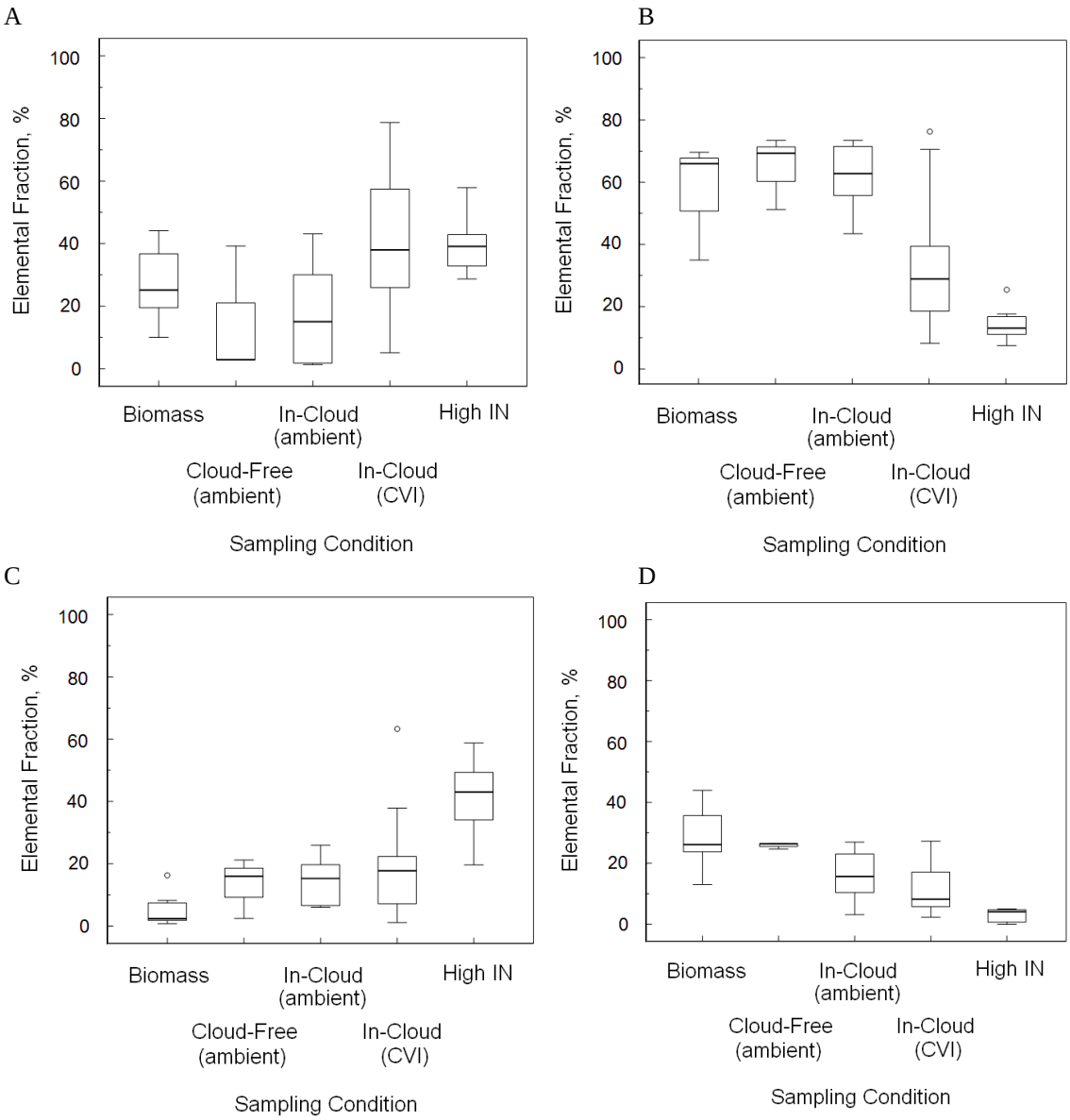

Figure 36. Sampling condition-basis elemental fraction of (A) CNO, (B) CNOSSi, (C) NaMg, and (D) other. Boxes encompass the 25th and 75th percentile of the data, lines within boxes represent the median value, and whiskers span 1.5 times the interquartile range. Circles represent data points that lie outside of this range.

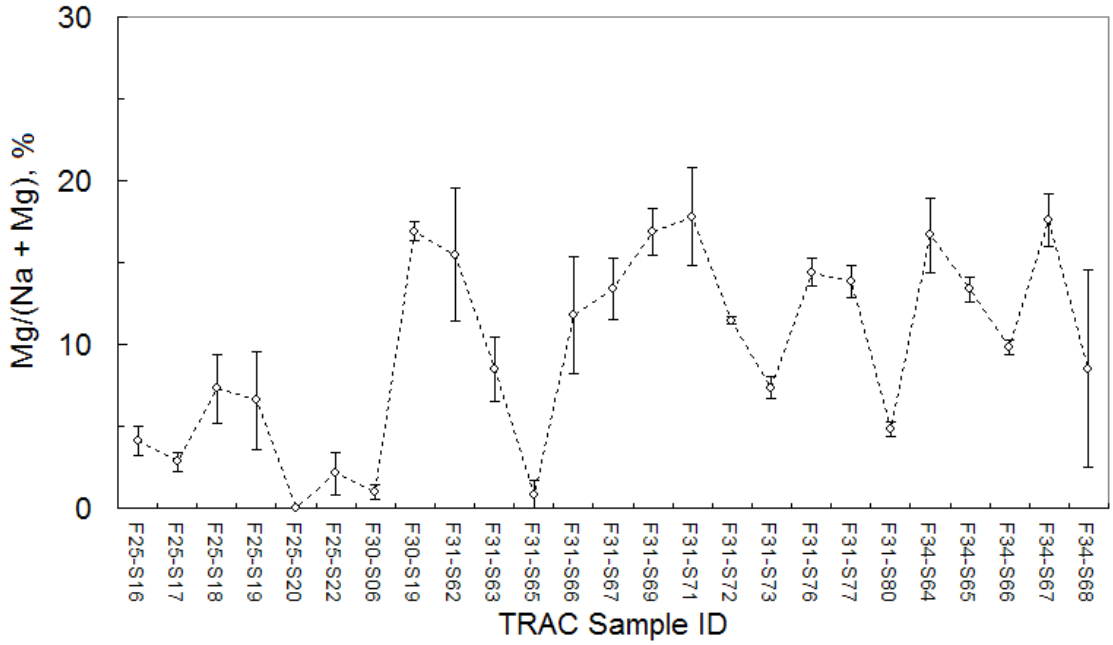

Figure 37. Elemental ratios of Mg/(Na + Mg) measured by CCSEM/EDX analysis. X-axis reads TRAC sample ID (i.e., Table 1A). F30-S19, F31-S62 to -S67, F34-S64 to -S67 were CVI samples. Error bars represent standard error from mean. Lines connecting the data points are included in guide the eye.

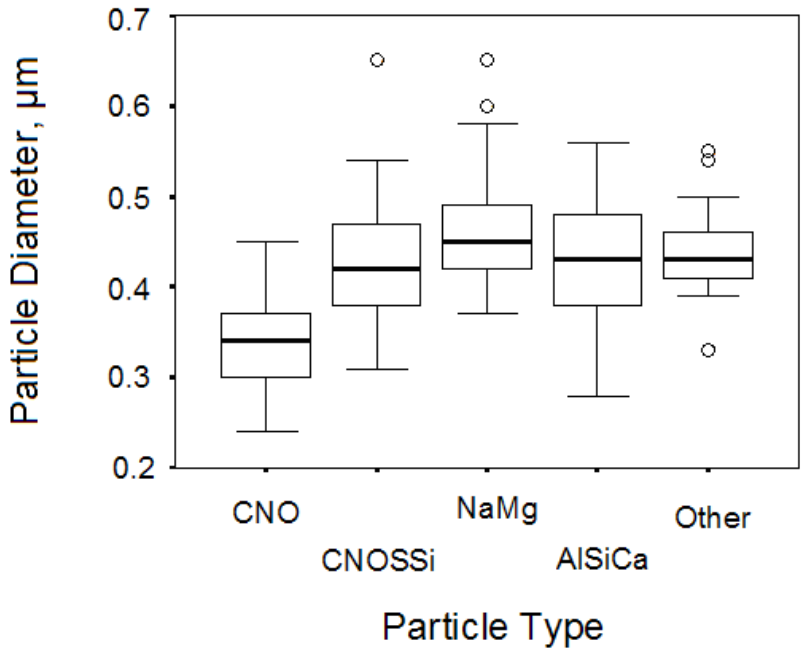

Figure 38. Chemically resolved size distribution box plots inferred from the CCSEM/EDX data sets. X-axis represents CCSEM/EDX particle type. All twenty five analyzed samples are combined.

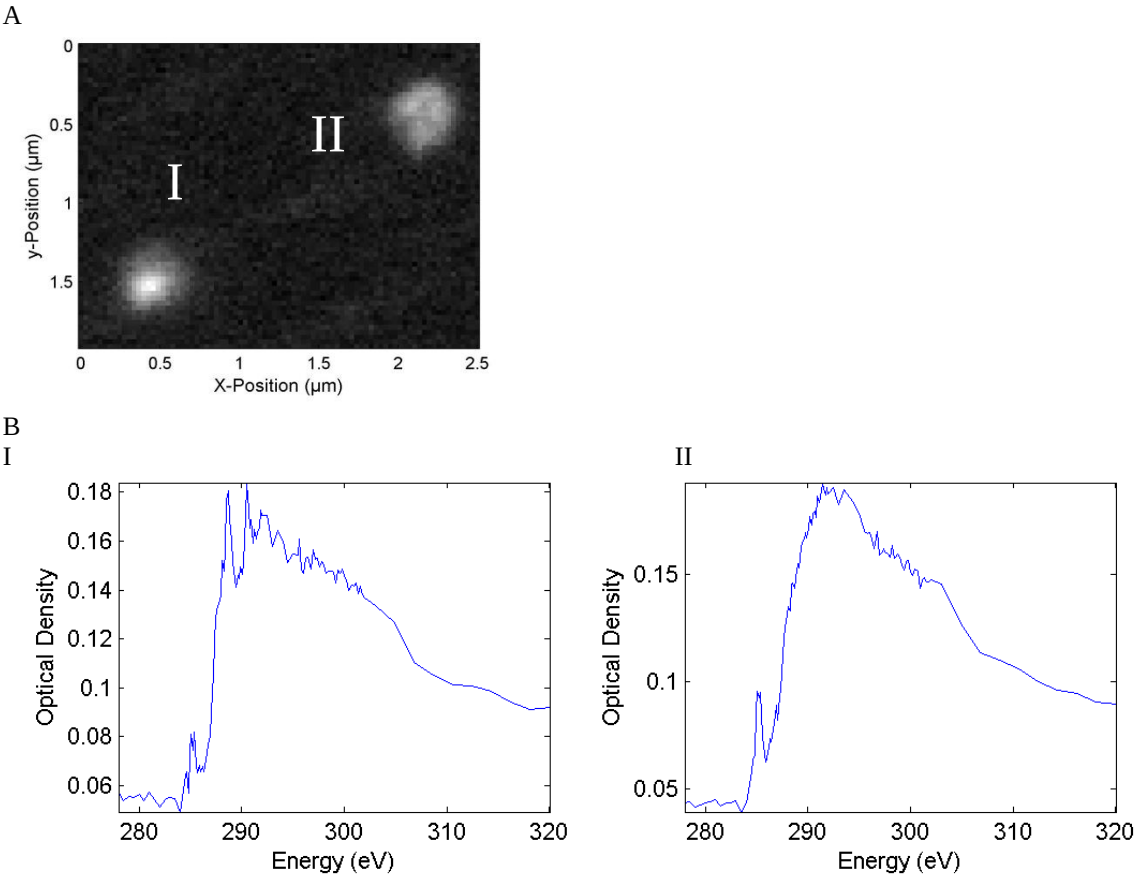

Figure 39 (A) Microscopic image of particles derived from high IN period collected on F34-S67. (B) STXM spectra of aircraft collected particle I and II (i.e., Fig. 39A) in spectral range of 278 to 320 eV: Paricle I contains CO_3 at 290.4 eV and both Particle I and II contain sp^2 hybridized carbon-carbon double bonds at 285.1 eV. Characteristic absorption of the C 1s → $\pi^*_{R(C^*=O)OH}$ transition for COOH groups was identified at 288.5 eV in both particles.

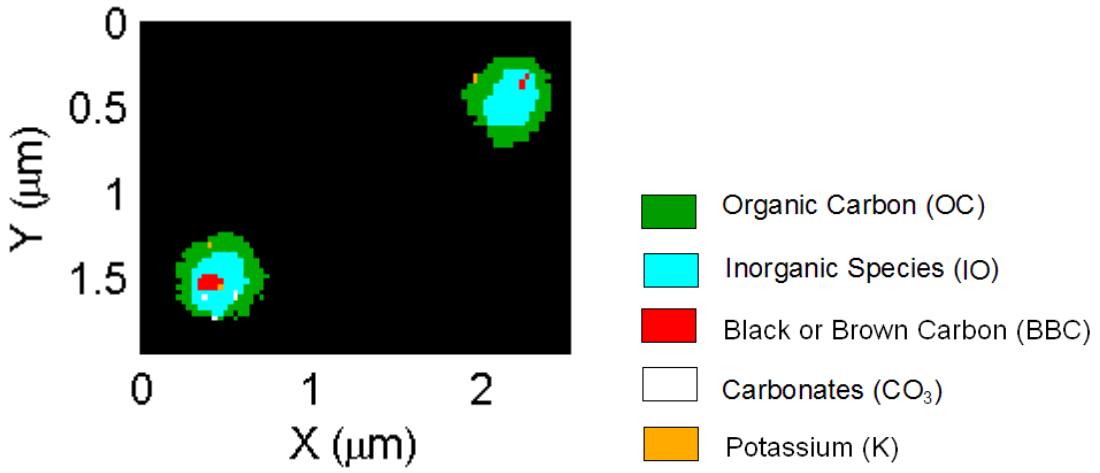

Figure 40. Scanning X-ray micrograph showing particles color coded carbon speciation (i.e., Fig. 39A and 39B).

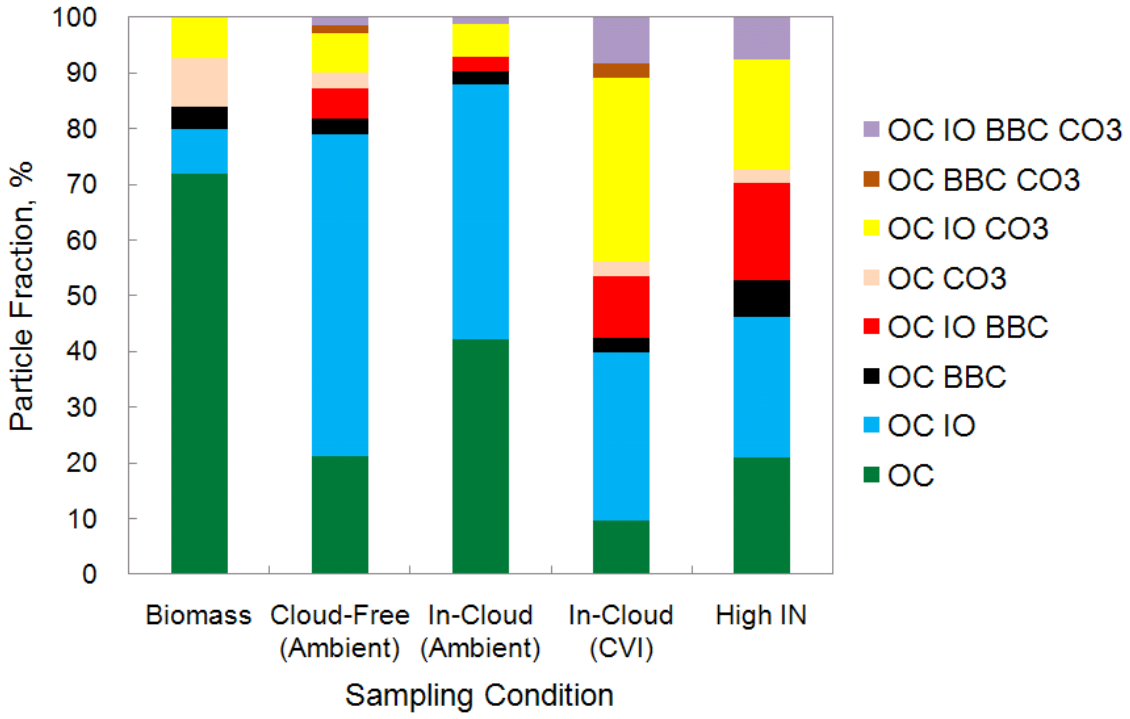

Figure 41. Stacked column chart diagram of particle groups in the samples analyzed by the STXM/NEXAFS.

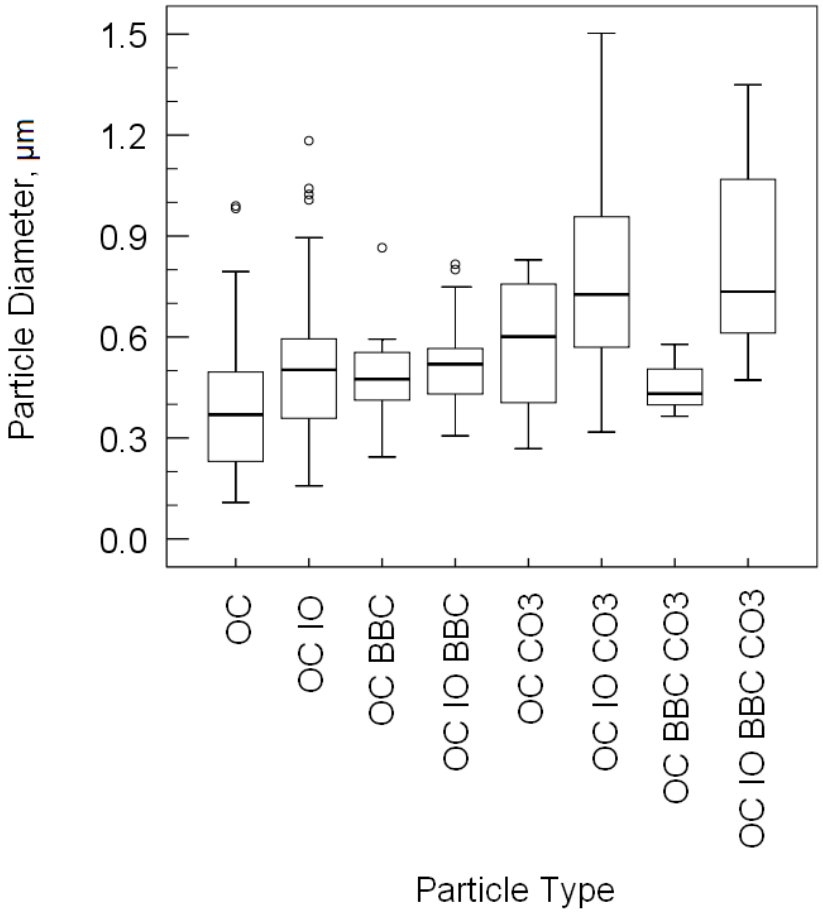

Figure 42. Chemically resolved size distribution box plots inferred from the STXM/NEXAFS data sets. X-axis represents STXM/NEXAFS particle type. All 442 analyzed samples are combined.

APPENDIX B

Summary of flight conditions during ISDAC 2008

ISDAC Flight Number	Flight Duration				*Flight Location		
	Date	TRAC Start Time, UTC	TRAC End Time, UTC	Number of TRAC Samples Used (Sample ID)	Altitude, m	Latitude, degree	Longitude, degree
F25 (CVI-OFF)	4/19/2008	21:36:54	22:12:49	6 (S16-21; S22)	2693.2 ± 1885.4	71.200 ± 0.268	-155.254 ± 0.436
F30 (CVI-OFF)	4/26/2008	20:15:34	20:20:41	1 (S06)	5755.1 ± 354.2	70.595 ± 0.034	-150.957 ± 0.115
F30 (CVI-ON)	4/26/2008	21:22:19	21:27:26	1 (S19)	503.5 ± 172.0	71.203 ± 0.032	-151.496 ± 0.167
F31 (CVI-ON)	4/27/2008	1:03:11	1:48:51	6 (S62-63; S65-67; S69)	584.8 ± 202.8	72.460 ± 0.107	-155.445 ± 0.661
F31 (CVI-OFF)	4/27/2008	1:48:52	2:40:53	6 (S71-73; S76-77; S80)	711.1 ± 309.1	72.582 ± 0.103	-156.274 ± 0.743
F34 (CVI-ON)	4/29/2008	2:17:56	2:43:38	5 (S64-68)	1193.2 ± 717.5	71.407 ± 0.209	-156.332 ± 0.499

*Flight location data represent mean ± one standard deviation.

Backward-trajectory for studied flights

Flight Number 25

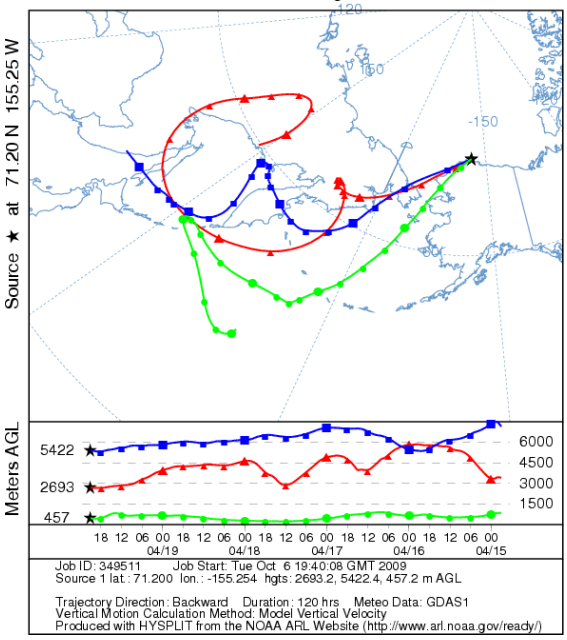

Flight Number 30 (CVI-OFF)

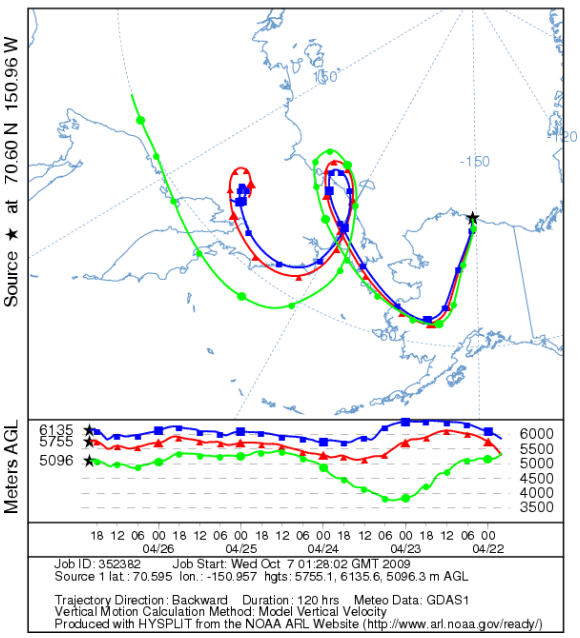

Flight Number 30 (CVI-ON)

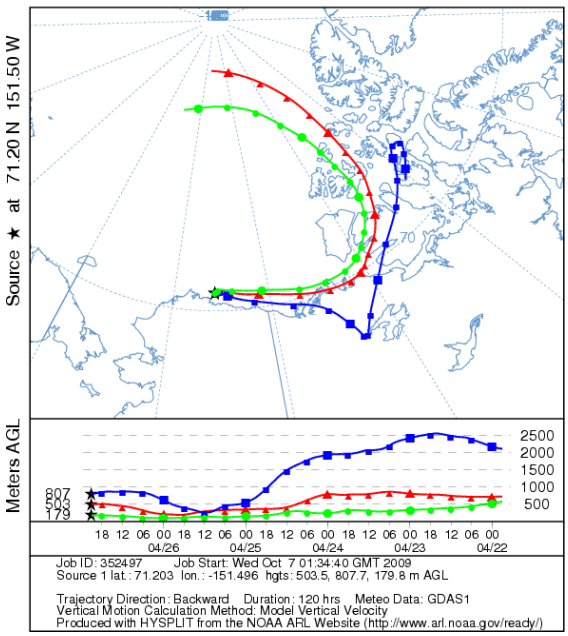

Flight Number 31 (CVI-ON)

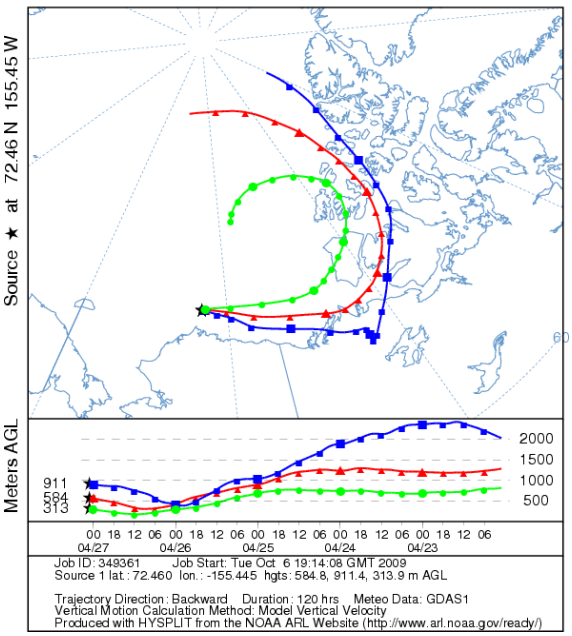

Flight Number 31 (CVI-OFF)

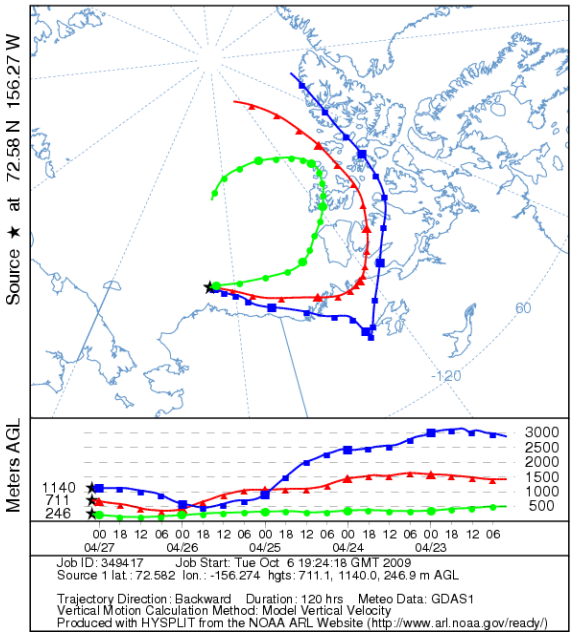

Flight Number 34

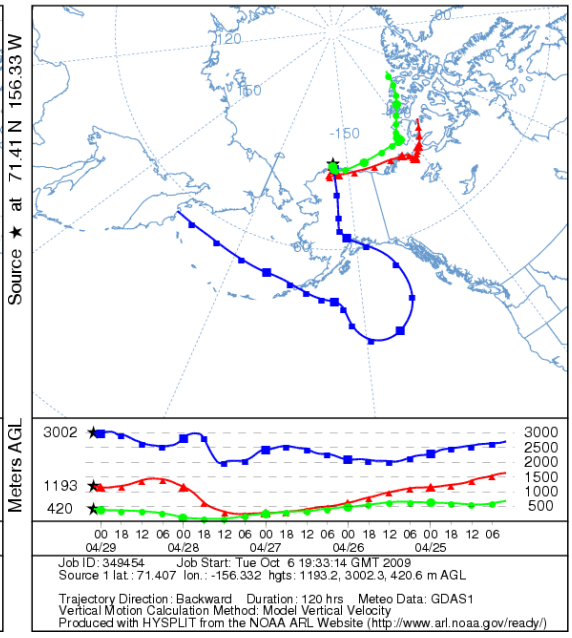

Spatio-Temporal Map - Air Temperature, °C

Flight Number 25

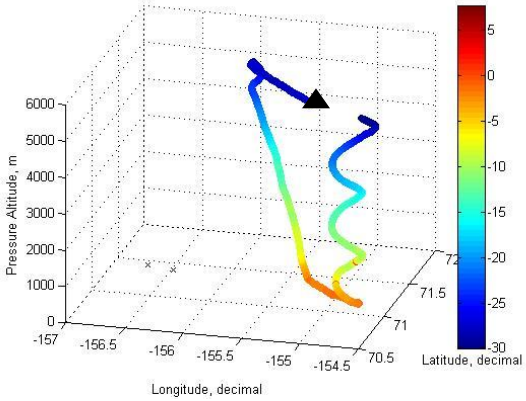

Flight Number 30 (CVI-OFF)

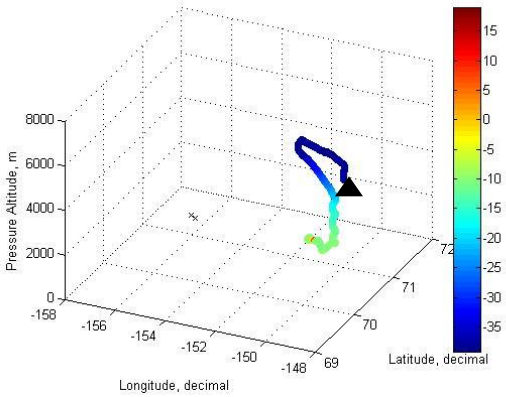

Flight Number 30 (CVI-ON)

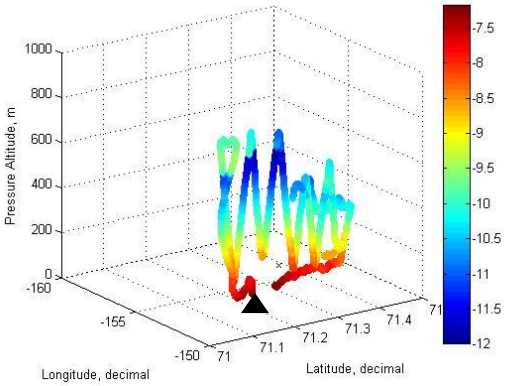

Flight Number 31 (CVI-ON)

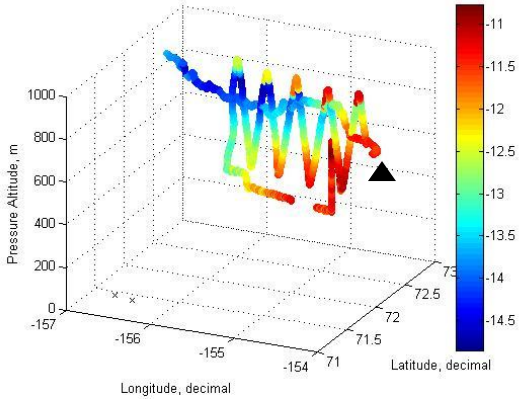

Flight Number 31 (CVI-OFF)

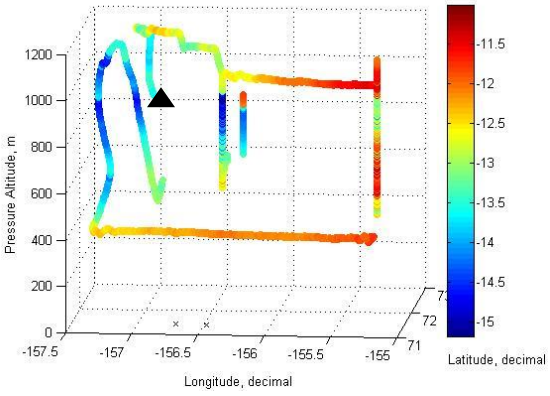

Flight Number 34

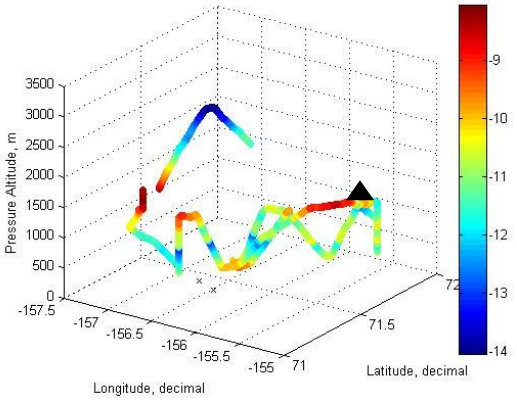

Note: Triangle represents TRAC start time and crosses represent Barrow, Alaska (lat. 71.429 – long. 156.715) and Point Barrow (lat. 71.389 – long. 156.479).

Spatio-Temporal Map - Total Water Content, g m^{-3}

Flight Number 25

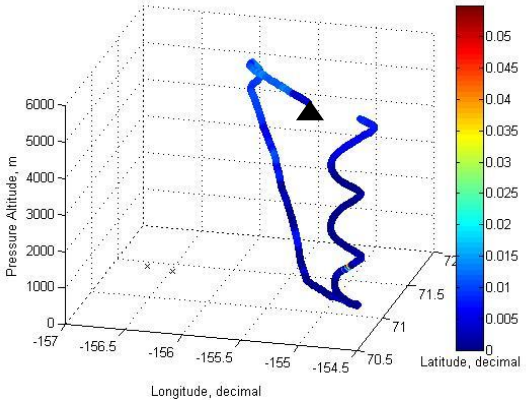

Flight Number 30 (CVI-OFF)

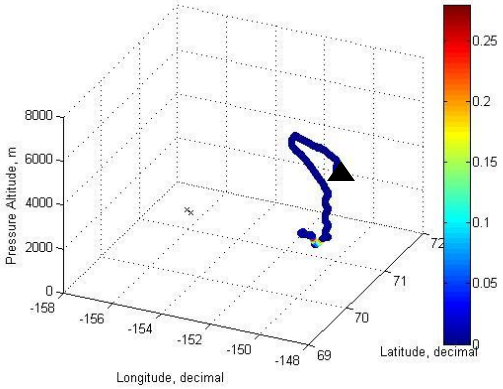

Flight Number 30 (CVI-ON)

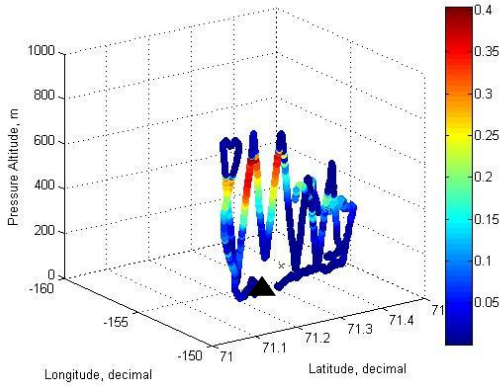

Flight Number 31 (CVI-ON)

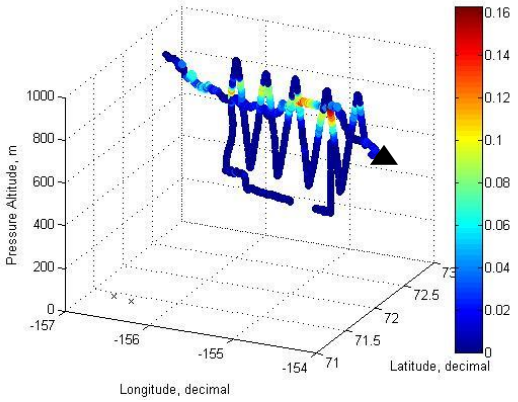

Flight Number 31 (CVI-OFF)

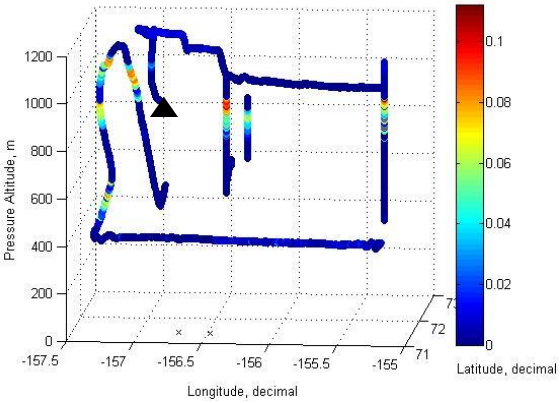

Flight Number 34

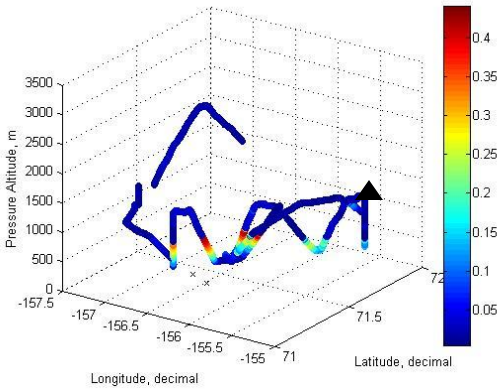

Note: Triangle represents TRAC start time and crosses represent Barrow, Alaska (lat. 71.429 – long. 156.715) and Point Barrow (lat. 71.389 – long. 156.479).

Spatio-Temporal Map - Ice Supersaturation, %

Flight Number 25

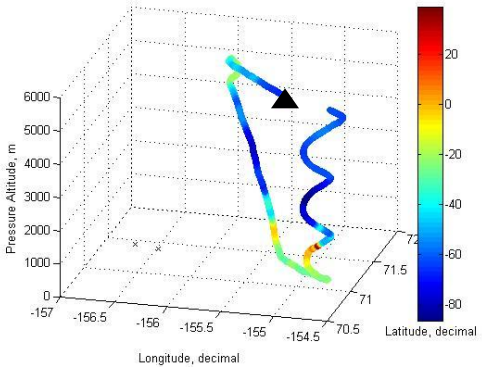

Flight Number 30 (CVI-OFF)

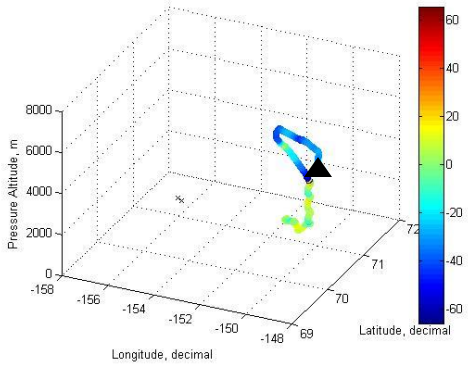

Flight Number 30 (CVI-ON)

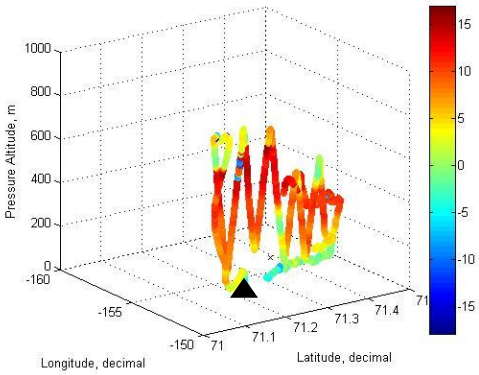

Flight Number 31 (CVI-ON)

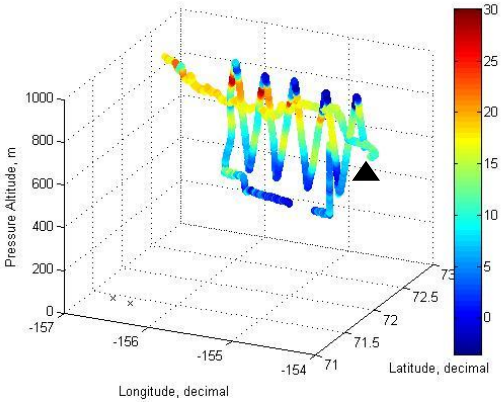

Flight Number 31 (CVI-OFF)

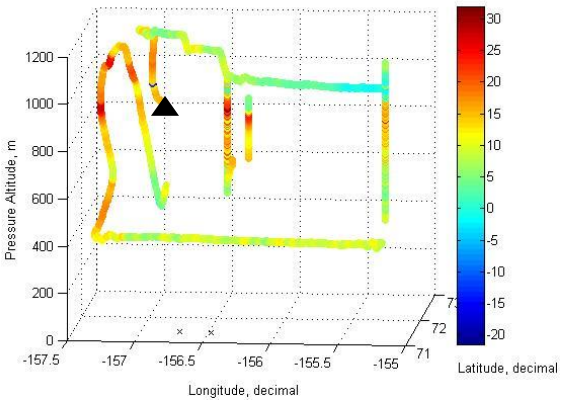

Flight Number 34

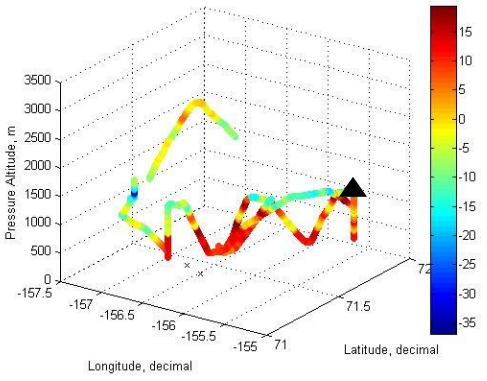

Note: Triangle represents TRAC start time and crosses represent Barrow, Alaska (lat. 71.429 – long. 156.715) and Point Barrow (lat. 71.389 – long. 156.479).

APPENDIX C

The Loss Rate of Perma Pure PD-Series™ Dryer for Low Air Flow Application

The Perma Pure PD-Series™ dryer (2' length, 2.18 mm OD, 20 tube Nafion dryer) was tested for its particle loss rate under low air flow condition (1.5 liter per minute) both in the lab and field. The Grimm Sequential Mobility Particle Sizer and Counter (SMPS+C) and Grimm 1.1.08 Portable Aerosol Spectrometer (PAS) measurements were used in tandem to observe the aerosol concentrations both with and without the permapure dryer (PPD) in line, in order to determine the particle loss rate as a function of particle size for the overall size range of 50 nm to 20 µm diameter.

SMPS+C measures real-time ultrafine aerosol size distribution measurements in the range of 10 nm – 1 µm. The Grimm SMPS consists of a Differential Mobility Analyzer (DMA) and Condensation Particle Counter (CPC). The DMA operates by classifying particles based on their electrical mobility and resultant particle concentrations are measured by the CPC every 7 minutes for overall size range (Rodrigue et al., 2007).The Grimm PAS is an optical particle counter that measures particle number concentration in 15 channels from 0.3 µm to 20 µm. With a resolution of 1 count/liter, this instrument is capable of operating in dusty environments, up to 100 mg/m^3 (Peters et al., 2006).

The responses of these instruments with the PPD in the line were compared with the responses without the perapure dryer for seven sizes of monodisperse solid aerosols composed of PSLs in the lab and a polydisperse aerosol composed of feedyard dust in the field. To calculate particle losses as a function of size, the particle concentration obtained with the PPD in line has been subtracted from the concentration observed without the PPD for each particle size.

Lab Measurement Method

During the lab experiments, monodisperse particles with a known composition and size were generated using the TSI atomizer (Model 3076) with PolyStyrene Latex (PSL) sphere standards from Duke Scientific. Seven different size of PSLs used for this lab study include 50 nm, 150 nm, 240 nm, 500 nm, 700 nm, 1000 nm, and 3000 nm. In laboratory measurements, the SMPS+C was used to determine the particle loss rate for 56.4 – 692.1 nm particles, and PAS was used for 450 – 2500 nm range. Figure 1 shows the lab experimental setup with the PPD in a line. The atomizer generates polydispersse particles in concentrrations of ~10^6 particles/cm^3 (10^8 particles/sec). The generated particles were sent through the diffusion dryers and counted by both the SMPS+C and the PAS. Two of 1' long ATI diffusion dryers (Model 250) and 2' homemade diffusion dryer were placed in a line for initial drying.

In order to have clean and dry counter flow for the PPD, the laboratory gas dryer from W. A. Hammond DRIERITE Co. LTD was attached to the purge line. A counter flow of ~1.7 lpm was controlled by an NPT orifice. This experiment was conducted with the total air flow of 1.5 lpm (0.3 lpm for SMPS+C and 1.2 lpm for PAS). While the focus of this report is on particle losses, it is noteworthy the drying capacity of this particular arrangement produced a RH below 1% for at least 48 hours of continuous operation.

Field Measurement Techniques

Particle loss rate due to the inlet and dryer were also investigated during field measurements. An on-site loss test was conducted at the beef cattle feedyard in Tulia, TX using the Grimm PAS. Sampling cycle of PAS was 1 minute. This field was chosen because of the wide variety of particle sizes, including high concentrations of coarse particles are typically emitted from the yard into the atmosphere. The measurements were made in the afternoon of June 13, 2007, 13:30 - 16:50 PM and June 15, 2007 12:50 – 17:50, when the dust concentration was predicted to be stable and air was calm.

As depicted in the Figure 2, all system components including an inlet, dryers, and concentration monitors were housed inside a research trailer. Figure 3 shows the on-site configuration of both with PPD and without PPD case.

Three different measurements were made; particle loss rate with (1) diffusion dryer + 3' stainless inlet (3/8' OD) [blue color coded], (2) no inlet at the roof of trailer [yellow], and (3) diffusion dryer + PPD + 3' stainless inlet (3/8' OD) [red]. As can be seen in the Figure 4, the measurement duration was 50 minutes in June 13, 2007 measurements, for each measurement; 13:30 - 14:20 PM, 15:00 - 15:50 PM, and 16:00 - 16:50 PM, respectively. The same procedure was implemented in June 15, 2007. The averaged number concentration for each bin size (i.e., PAS channels) were computed by averaging 50 minute of measurement for each measurement, and the fraction of the number concentration with the PPD over that without the PPD was calculated to see the transmission rate of the PPD. The transmission rate values in percentage were subtracted from 100% to find the actual loss rate.

Results

As shown in Figure 5, the lab loss rate was plotted on the y-axis as a function of corresponding instrument size on the x-axis, and regression curve was computed using seven different data points (i.e., size and corresponding loss rate). In laboratory measurements, SMPS+C was used to determine the paricle loss rate for 56.4 – 692.1 nm particles (circle points), and PAS was used for 450 - 2500 nm range (square points). The values in overlap range (between 450 and 692.1 nm) were averaged to have one regression curve for the measurements by two different instruments. The results indicate that the particle losses are not significant at most of measured particle sizes. A notable exception to this is that a loss rate of 2500 nm particles was > 25%, possibly due to the increase in the gravitational force with increased size of the particle.

Now the result of field measurement is discussed. The advantage of doing the on-site measurement is the availability of large particles (>3 μm), which are difficult to generate in the lab. One disadvantage of the on-site data is that the particle generation rate is unpredictable, meaning it highly depends on the meteorological conditions (e.g., wind speed, wind direction, etc). Therefore, having negative values for loss rate at some sizes is the nature of this experiment even though it is physically unrealistic. Since the primary interests were in the loss rate of large size particles (>1 μm), only PAS was used for the field measurement.

As shown in the Figure 6, the loss rate of PPD is plotted on the y-axis as a function of PAS bin size on the x-axis. Raw data is plotted with dots. Logarithmic regression curve (a) and quadratic poly-nominal regression curve (b) for the loss rate of PPD are also shown in the figures. The result shows that the on-site loss test data agrees with lab loss test. In both tests, the loss rates of ~2500 nm particles are ~25%. The loss rate becomes apparent (~40%) if the size of the particle is larger than 3500 nm.

Figure 7 shows the particle loss rate with only diffusion dryer (without the PPD) in the inlet line. As can be seen from the figures, particle loss rate is not as significant as the case of having PPD in a line for the range up to 12.5 µm; however, the loss rate appears to become significant > 12.5 µm. In addition, the combined particle loss rate of both lab and field measurement depicted in one graph is available in the appendix. The combined graph features the loss rate over the full scale size range (50 to 20000 nm) for both PPD and diffusion dryer.

Conclusion

The loss rate of the Perma Pure dryer for low air flow case was studied. Overall results are shown in Figure 8. Both lab and field studies were conducted with 1.5 lpm of air flow. The Grimm SMPS+C and PAS were used to measure the size distribution and corresponding size resolved concentration of monodispersed particles generated by atomizer. Overall size range of particles analyzed in the lab was 56.4 nm – 2500 nm. For the field measurement, only PAS was used because only the loss rate of large size of particles (> 1 µm) was concerned. With lab and field results, it was found that the loss rate of particles larger than 2.5 µm become significant. The loss rate becomes >25% for the particle that has a dimameter ~2.5 µm and >40% for the particle is larger than 3500 nm. This loss rate becomes too large for this PPD to be useful in air quality field measurements on particles of greater than 2.5 micron diameter. Therefore the application of PPD may be limited for he study of gas or particulate matters with aerodynamic equivalent diameters of 2.5 µm or less ($PM_{2.5}$).

References

Rodrigue, Jason., Ranjan, M., Hopke, P. K., and Dhaniyala, S. 2007. Performance Comparison of Scanning Electrical Mobility Spectrometers. *Aerosol Science and Technology*. 41: 360-368.

Peters, T. M., Ott, D., and O'Shaughnessy, P. T. 2006. Comparison of the Grimm 1.108 and 1.109 Portable Aerosol Spectrometer to the TSI 3321 Aerodynamic Particle Sizer for Dry Particles. *Annals of Occupational Hygiene.* 50(8): 843-850.

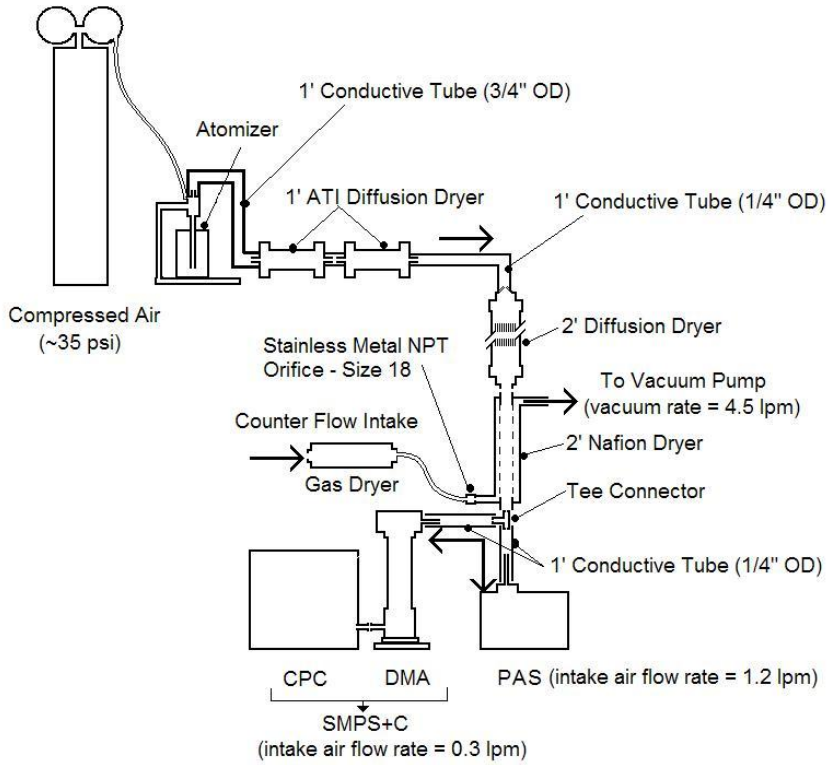

Figure 1. Lab experimental setup for diffusion dryer and permapure dryer in a line.

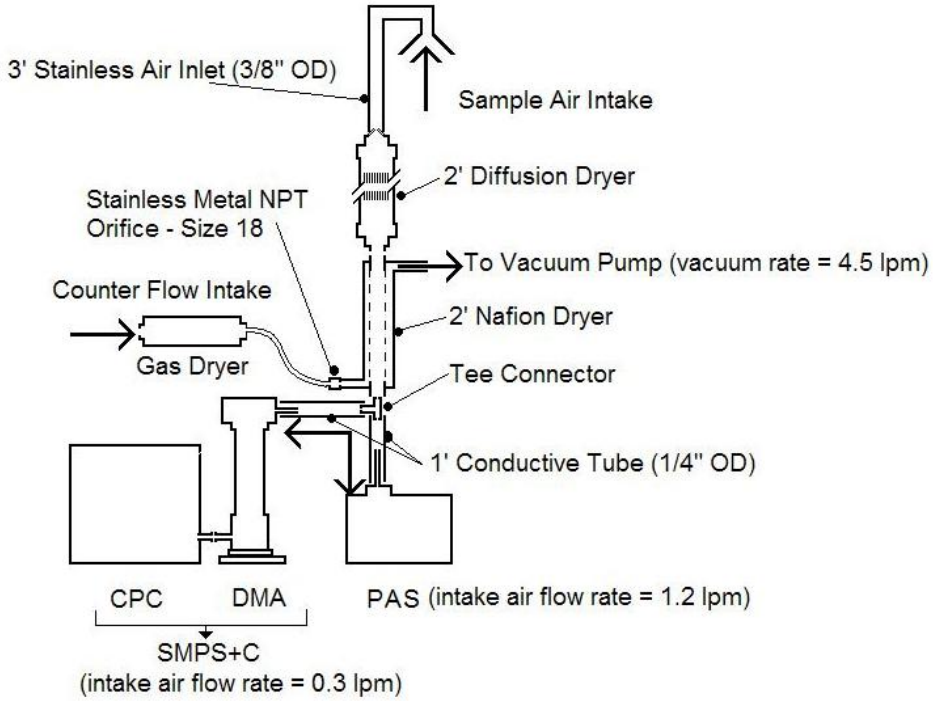

Figure 2. Field experimental setup for diffusion dryer and permapure dryer in a line.

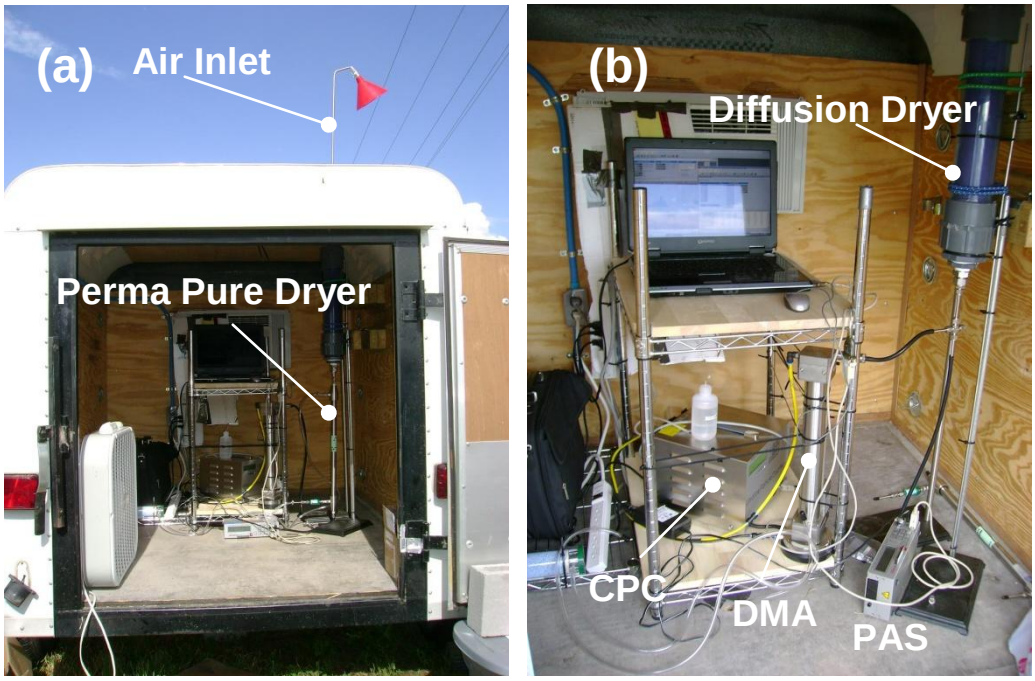

Figure 3. (a) On-site configuration with permapure dryer in a line; (b) On-site setup without permapure dryer.

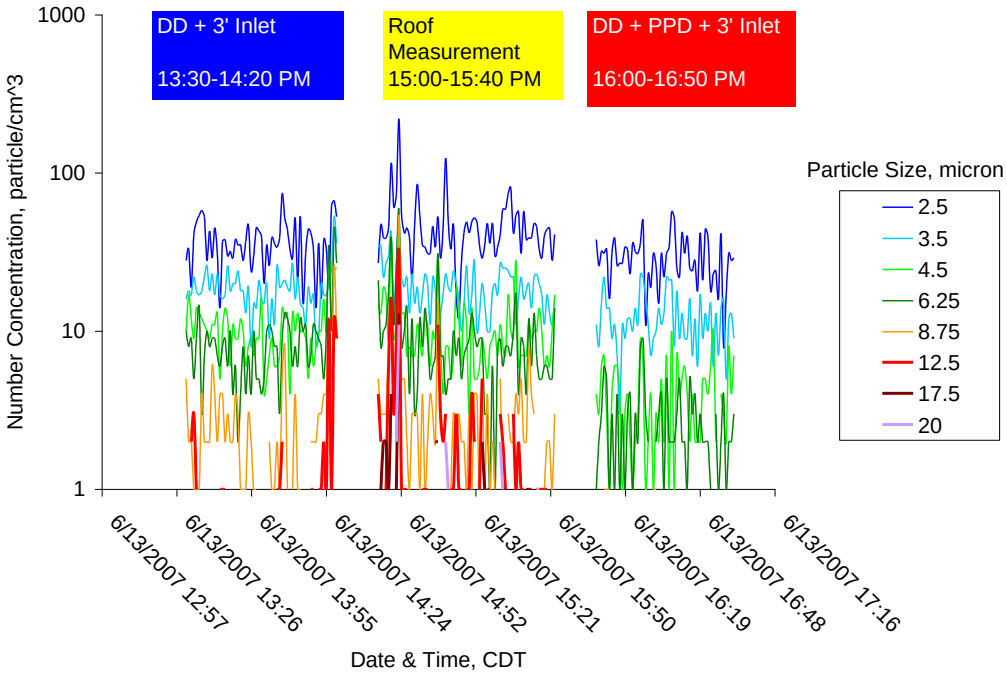

Figure 4. Number concnetration of agricultural particles as a function of time for three different inlet (graph notation: DD = Diffusion dryer; PPD = Perma Pure Dryer).

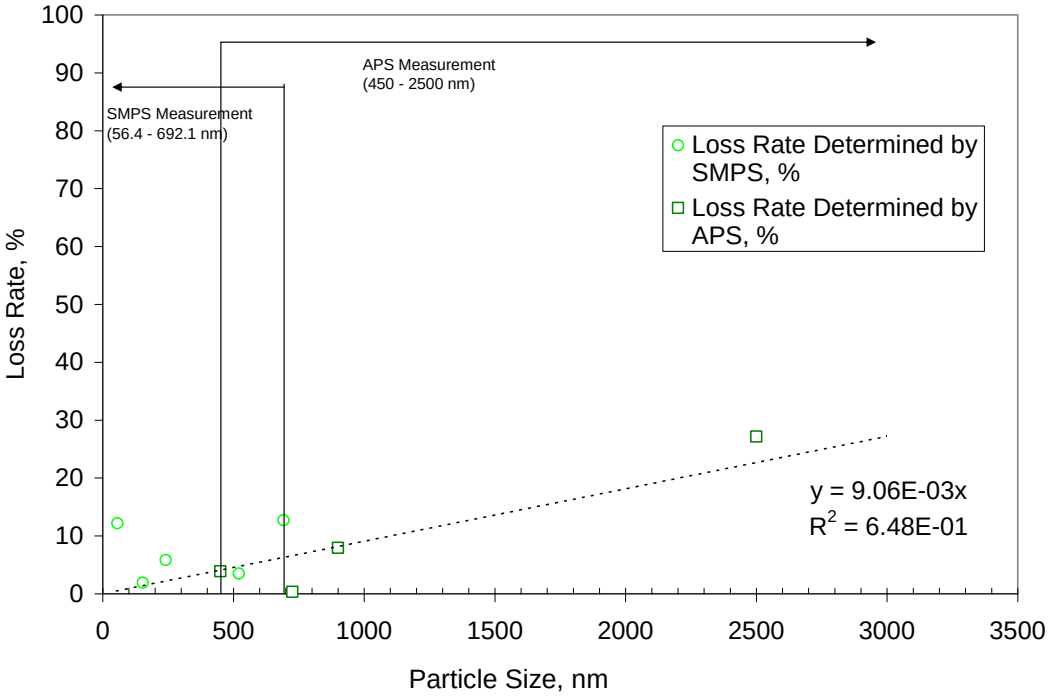

Figure 5. Lab loss rate of Perma Pure dryer for 56.4 to 2500 nm range.

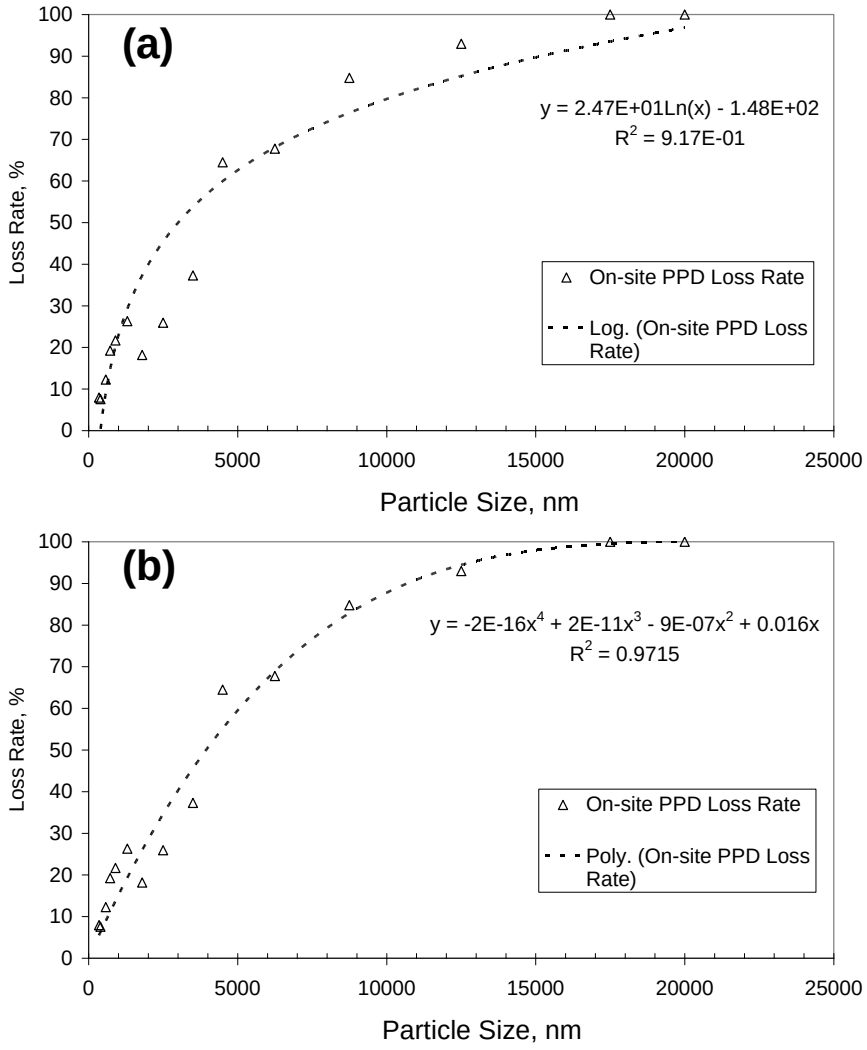

Figure 6. On-site loss rate of Perma Pure dryer for 350 to 20000 nm range; (a) Loss rate with logarithmic regression curve, (b) Loss rate with quadratic poly-nominal regression curve.

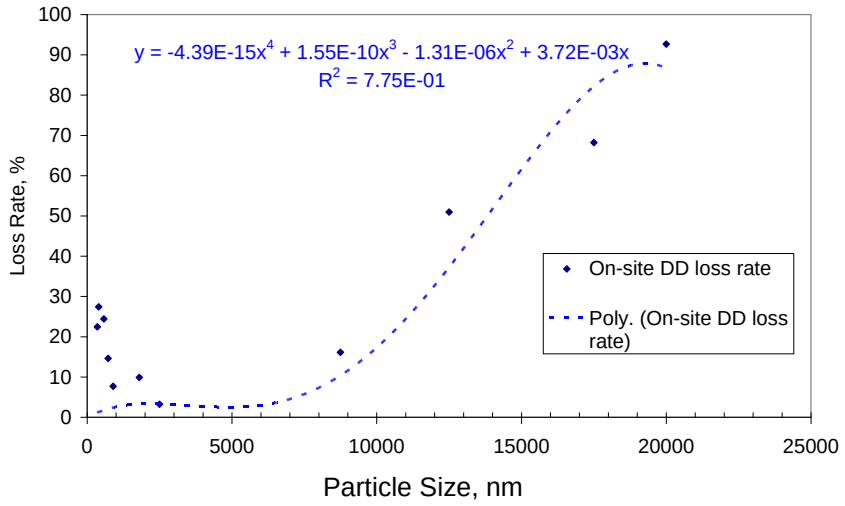

Figure 7. On-site loss rate without Perma Pure dryer in the inlet line. DD means diffusion dryer.

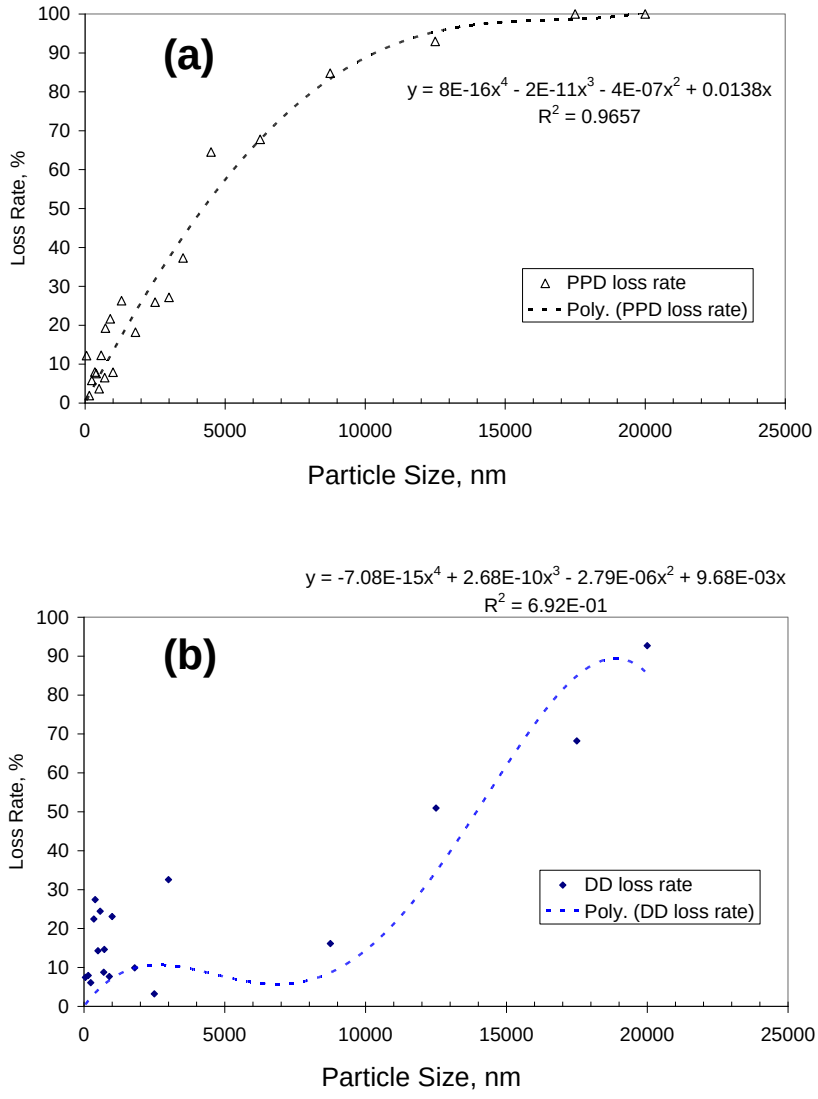

Figure 8. Lab and field combined loss rate of Perma Pure dryer for 50 to 20000 nm range; (a) Loss rate of Perma Pure dryer, (b) Loss rate of diffusion dryer (graph notation: DD = Diffusion dryer; PPD = Perma Pure Dryer).

APPENDIX D

1. Monin-Obukhov Length

The Monin-Obukhov length (L) is the height at which the production of turbulence by mechanical and buoyancy forces is equal (Seinfeld and Pandis, 1998). More importantly, this parameter provides a measure of the stability of the surface layer. The Monin-Obukhov length (in meters) is given by

$$L = -\frac{\rho \hat{c}_p T_0 u_*^3}{\kappa g \bar{q}_z} \qquad [A1]$$

where ρ is the air density, $\hat{c}_p$ is the heat capacity of air, T_0 is the standard temperature, u_* is the frictional velocity, κ is he von Karman constant (typically ~0.35), g is the acceleration of gravity, and $\bar{q}_z$ is the vertical mean turbulent flux (eddy flux), which is the mean rate of transfer of a conservative property through a surface by vertical turbulent eddies. For an approximately neutral stability condition, L is large positive number. As stability increases, the L decreases. For very stable conditions, L approaches zero. When L is negative, it typically represents unstable atmospheric conditions. Only exception is L becomes lower than -10^5 m. A very large negative L is considered again as a neutral condition (Monin and Obukhov, 1954). It should be noted that neutral means neither stable nor unstable atmospheric stability condition.

2. Eddy diffusivity

The Eulerian solution of atmospheric transport of a species i (neglecting reaction) must satisfy the continuity equation (Seinfeld and Pandis, 1998), thus the time rate of change of the concentration of species ci can be expressed as the summation of advection, diffusion, and emission/removal (Lin and Hildemann, 1997)

$$\frac{\partial c_i}{\partial t} + \frac{\partial}{\partial x_j}(u_j c_i) = D_i \frac{\partial^2 c_i}{\partial x_j \partial x_j} + S_i(\vec{x}, t) \qquad i = 1,2,...N \qquad [A2]$$

where u_j is the jth component of the velocity, D_i is the molecular diffusivity of species i, $S(\vec{x}, t)$ is the rate of addition of species i at location $x = (x_1, x_2, x_3)$ and time t.

The turbulent dispersion rate constant (eddy diffusivity) is now described. Turbulence can be expressed as a contribution from a stochastic fluctuating component of u_j (velocity) and c_i (concentration), for instance,

$$u_j = \overline{u_j} + u_j' \qquad [A3]$$

$$c_i = \overline{c_i} + c_i' \qquad \text{[A4]}$$

Where $\overline{u}_j$ and $\overline{c}_i$ are the deterministic mean components and u_j' and c_i' represent stochastic components.

Substituting equation A3 and A4 into equation A2, we get

$$\frac{\partial \overline{c_i}}{\partial t} + \frac{\partial}{\partial x_j}(\overline{u_j}\,\overline{c_i}) = D_i \frac{\partial^2 \overline{c_i}}{\partial x_j \partial x_j} + \frac{\partial}{\partial x_j}(u_j' c_i') + S(\vec{x},t)$$

[A5]

Introducing "eddy diffusivity" (k_{jk}), the turbulent fluxes ($\overline{uj'ci'}$) can be related to the concentration $\overline{c}$.

$$(u_j' c_i') = -k_{jk} \frac{\partial \overline{c}}{\partial x_k}$$

$$= -k_{j1} \frac{\partial \overline{c}}{\partial x} - k_{j2} \frac{\partial \overline{c}}{\partial y} - k_{j3} \frac{\partial \overline{c}}{\partial z} \qquad \text{j=1,2,3} \qquad \text{[A6]}$$

Here eddy diffusivity is defined as:

$$k_{ij} = \begin{pmatrix} k_{11} & k_{12} & k_{13} \\ k_{21} & k_{22} & k_{23} \\ k_{31} & k_{32} & k_{33} \end{pmatrix} \approx k_{11} \quad k_{22} \quad k_{33} \qquad (k_{ij} = 0 \text{ when } i \neq j) \qquad \text{[A7]}$$

Including eddy diffusivity in the equation A5 leads to:

$$\frac{\partial \overline{c_i}}{\partial t} + \frac{\partial}{\partial x_j}(\overline{u_j}\,\overline{c_i}) = D_i \frac{\partial^2 \overline{c_i}}{\partial x_j \partial x_j} + \frac{\partial}{\partial x_j}\left(k_{jj} \frac{\partial \overline{c}}{\partial x_j}\right) + S(\vec{x},t) \qquad \text{[A8]}$$

The analytical solution to the time rate change of concentration at an instantaneous source is

$$\frac{\partial \overline{c}}{\partial t} + \overline{u} \frac{\partial \overline{c}}{\partial x} = k_{xx} \frac{\partial^2 c}{\partial x^2} + k_{yy} \frac{\partial^2 c}{\partial y^2} + k_{zz} \frac{\partial^2 c}{\partial z^2} \qquad \text{[A9]}$$

in which the rate of addition of particles (S) is incorporated with the boundary condition at initial time below.

$$c(x,y,z,t) = 0$$
$$c(x,y,z,0) = S\delta(x)\delta(y)\delta(z) \qquad \text{[A10]}$$

It should be noted that this particular study assumed steady state for the time rate change of aerosol concentration ($\frac{\partial \bar{c}}{\partial t} = 0$). Thus final solution of atmospheric transport including considerations of turbulence is

$$c(x,y,z,t) = \frac{S}{8(\pi t)^{3/2}(k_{xx}k_{yy}k_{zz})^{1/2}} \exp\left(-\frac{(x-\bar{u}t)^2}{4k_{xx}t} - \frac{y^2}{4k_{yy}t} - \frac{z^2}{4k_{zz}t}\right) \qquad \text{[A11]}$$

In this study, horizontal turbulent dispersion (k_{xx} and k_{yy}) is neglected. Further details regarding the vertical diffusion coefficient, k_{zz}, are described in next section.

3. Vertical Diffusion Coefficient, k_{zz}

In this study, the flux is assumed to be nondivergent in the surface layer and maximum vertical extent is 10% of PBL, in which wind direction does not change significantly with height (Figure A1). Under these conditions, the vertical diffusion coefficient, k_{zz}, according to Lin and Hildemann (1996) can be expressed as

$$k_{zz} = \frac{\kappa u_* z}{\phi\left(\frac{z}{L}\right)} \qquad \phi\left(\frac{z}{L}\right) = \begin{cases} 1 + 4.7\frac{z}{L} & \frac{z}{L} > 0 \quad stable \\ 1 & \frac{z}{L} = 0 \quad neutral \\ \left(1 - 15\frac{z}{L}\right)^{-1/2} & \frac{z}{L} < 0 \quad unstable \end{cases} \qquad \text{[A12]}$$

where κ is the Von Kármán constant, (typically ~0.4), which is a dimensionless constant describing the logarithmic velocity profile of a turbulent fluid flow near a boundary with a no-slip condition (Deleonibus and Simpson, 1989), u_* is the friction velocity, which is a measurement of the surface shear stress, L is the Monin-Obukov stability length. Further computation of k_{zz} in the entire Ekman layer is described in Seinfeld and Pandis (1998).

4. Dry Deposition Velocity

Dry deposition velocity, v_d, for particles can be calculated using the following governing equation (Wesley, 1989):

$$v_d = \frac{1}{r_a + r_b + r_a r_b v_s} + v_s \quad [A13]$$

in which, r_a is the aerodynamic resistance, r_b is the quasi-laminar layer resistance, and v_s is the particle settling velocity. Each resistance term and settling velocity are explained separately in below.

In this study, the flux is assumed to be nondivergent in the surface layer and maximum vertical extent is 10% of PBL, in which wind direction does not change significantly with height (Figure A1). Under this condition, r_a, is

$$r_a = \frac{1}{\kappa u*}\left[\ln\left(\frac{z}{z_0}\right) + 4.7(\zeta - \zeta_0)\right] \quad [A14]$$

where κ is the von Karman constant ~0.4, u* is the friction velocity, z is the top of constant-flux layer, z_0 is the roughness length [0.041 m (Baum et al., 2008)], ζ is the dimensionless height scale, which can be expressed as the fraction of z to the Monin-Obukhov length (L) (=z/L), and ζ_0 is another dimensionless height scale (= z_0/L).

Next, the quasi-laminar layer resistance for particles is given by

$$r_b = \frac{1}{u_*(Sc^{-2/3} + 10^{-3/St})} \quad [A15]$$

S_c is the Schmidt number, $S_c = \upsilon/D$, where υ is the kinetic viscosity of air (1.5×10^{-5} m^2 s^{-1}) and D is the Brownian diffusivity of the particles. For example, Figure A2 shows the aerosol diffusion coefficient in air at 30ºC as a function of particle diameter. As can be seen in the figure, the particle diffusion coefficient decreases with the increase in particle diameter. The Stokes number can be written as $St = v_s u_*^2/g\upsilon$.

Finally, the gravitational settling velocity, v_s, is given by Stokes Law,

$$v_s = \frac{\rho_p D_p^2 g C_c}{18\mu} \quad [A16]$$

where ρ_p is the density of the particle (2.65 g/cm^3 in this study using soil density), D_p the particle diameter, g the gravitational acceleration (9.81 m s^{-2}), μ the viscosity of air (1.78×10^{-5} kg m^{-1} s^{-1}), and C_c the slip correction factor.

Figure A3 shows the resulting dry deposition velocity for agricultural aerosols as a function of particle size. Dry deposition velocity was computed for stable atmospheric condition. There is a linear relation between deposition velocity and particle diameter, and influence of z on $v_{d,i}$ is almost negligible for supermicron size particles(so also on $c_{i(t)}$) (Figure A3 (A)). Influence of atmospheric condition (neutral) on dry deposition velocity is illustrated in Figure A3 (B).

Figure A4A and A4B show the dry deposition rate and emission rate at far-field location for fine fraction (PM_1) and coarse fraction (PM_{10}) of agricultural aerosols based on the data in 2008. Dry deposition rate was calculated by multiplying measured mass concentration (μg m^{-3}), estimated dry deposition velocity at z = 20 m (m s^{-1}), and travel time (s) for air mass to reach 3.5 km distance (i.e., far-field) from the research feedlot. As expected, larger particles had much higher (~4 order magnitude higher) deposition rate than fine particles. As can also be seen from these figures, dry deposition can be an important particle removal process as it accounted for roughly 37% of the modeled emissions at the far-field location (from subtraction of dry deposition rate from modeled emission rate). Deposition rate may be especially high during the evening hours when atmospheric loadings of coarse particles are abundant. For example, at an atmospheric loading of 1 mg m^{-3} of particles larger than 5 μm D_p, a deposition velocity of 5 cm s^{-1}, and assuming a mixing depth of 50 m near the surface, only 0.16 mg m^{-3} (84% loss) would be observed after 30 min, and more than 97% would be lost after one hour (from c(t) = c(t=0) * exp(-dv/BLdepth*t)) (Herner et al., 2006). Observed wind speeds during the evening hours were lower than during the day, contributing to longer transport times of agricultural aerosols to the far-field site. In contrast, the dry deposition rate of the fine fraction (<1 μm D_p) was very small. Specifically, the estimated average far-field dry deposition fraction of the particle emission at the downwind site was <1% for all times. Thus, these particles are transported on a regional level and may cause regional scale impacts while, as depicted in Figure 20, nearly all larger particles were gone by the time the air reached the far-field location.

References

Baum, K.A., Ham, J.M., Brunsell, N.A., and Coyne, P.I. 2008. Surface boundary layer of cattle feedlots: implications for air emission measurement. *Agricultural and Forest Meteorology*, 148, 1882-1893.

DeLeonibus, P.S. and Simpson, L.S. 1989. Observations of the von Karman constant over open-ocean waves. *Oceanic Engineering, IEEE Journal of*, 14(3), 248-253.

Herner, J.D., Ying, Q., Aw, J., Gao, O. Chang, D.P.Y., and Kleeman, M.J. 2006. Dominant mechanisms that shape the airborne particle size and composition in central california. *Aerosol Science and Technology*, 40, 827-844.

Lin, J.S., and Hildemann, L.M. 1996. Analytical solutions of the atmospheric diffusion equation with multiple sources and height-dependent wind speed and eddy diffusivities, *Atmospheric Environment*, 30, 239-254.

Lin, J.S., and Hildemann, L.M. 1997. A generalized mathematical scheme to analytically solve the atmospheric diffusion equation with dry deposition, *Atmospheric Environment*, 31, 59-72.

Monin, A.S. and Obukhov, A.M. 1954. Basic turbulent mixing laws in the atmospheric surface layer, *Tr. Geofiz. Inst. Akad. Nauk SSSR*, 24, 163-187.

Seinfeld, J.H. and Pandis, S.N., 1998. *Atmospheric Chemistry and Physics.* Wiley, New York.

Wesley, M.L. (1989) Parameterizations of surface resistance to gaseous dry deposition in regional scale, numerical models. *Atmospheric Environment*, 23, 1293-1304.

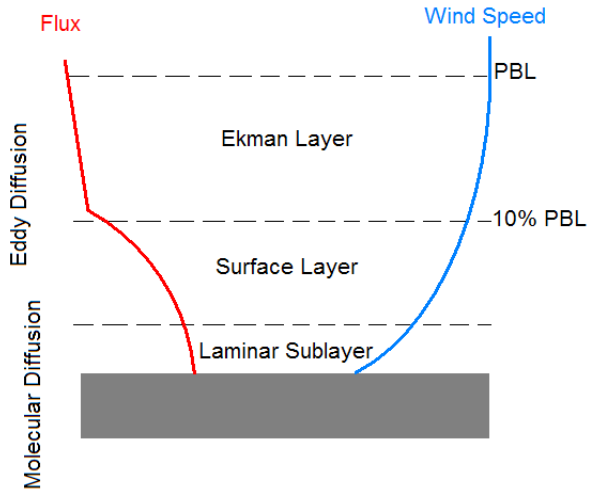

Figure A1. Schematic illustration of atmospheric layers. Molecular diffusion is dominant between ground surface and displacement and roughness height. Eddy diffusion is assumed to be predominant within 10% of PBL.

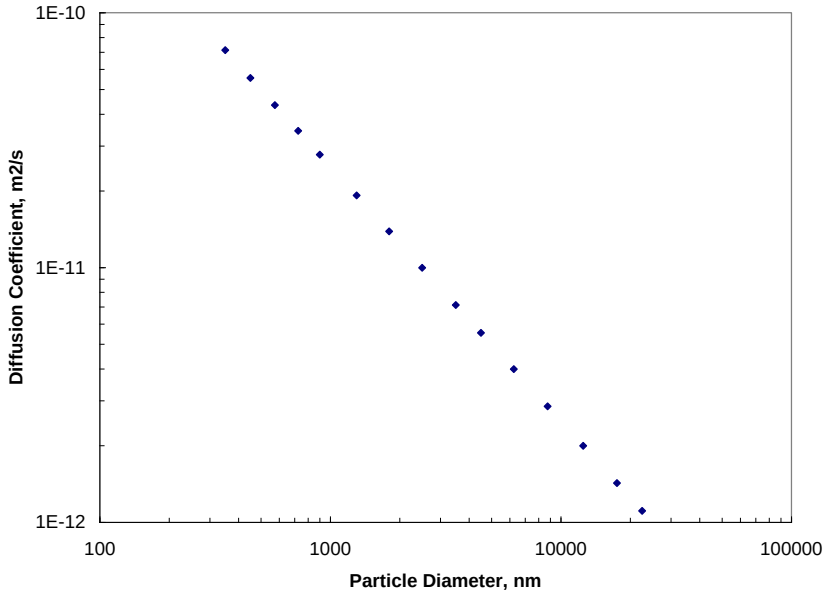

Figure A2. Aerosol diffusion coefficient in air at 30ºC as a function of diameter (0.3 to 25 micron range)

A

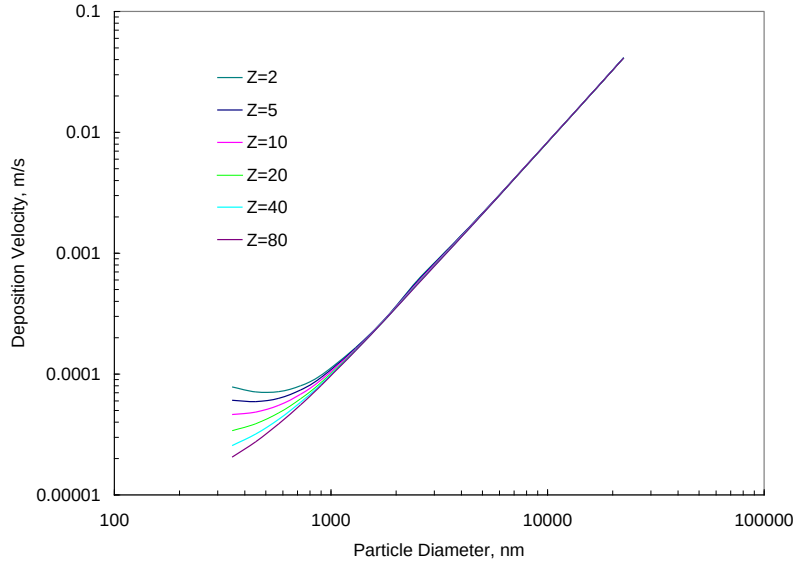

B

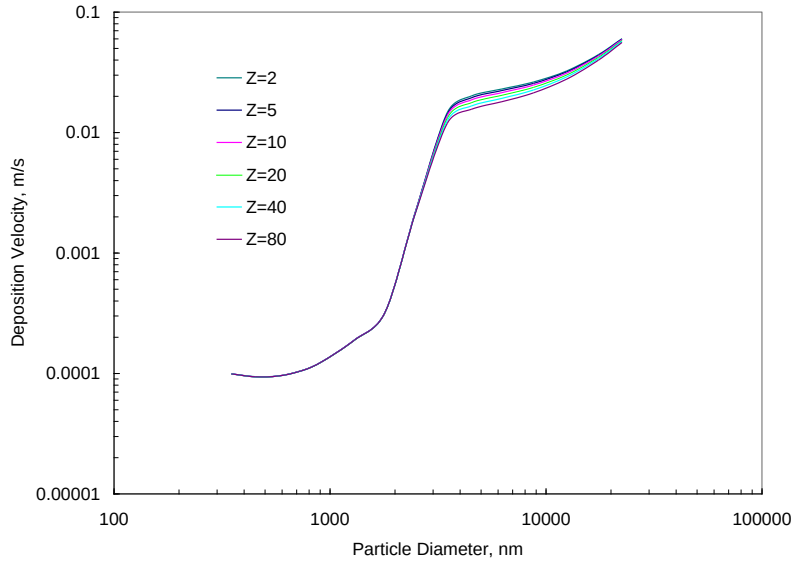

Figure A3 (A) Particle dry deposition velocity of agricultural aerosols (0.3 to 25 micron range) and (B) Particle dry deposition velocity of agricultural aerosol in the case of neutral atmospheric stability (ζ=0)

A

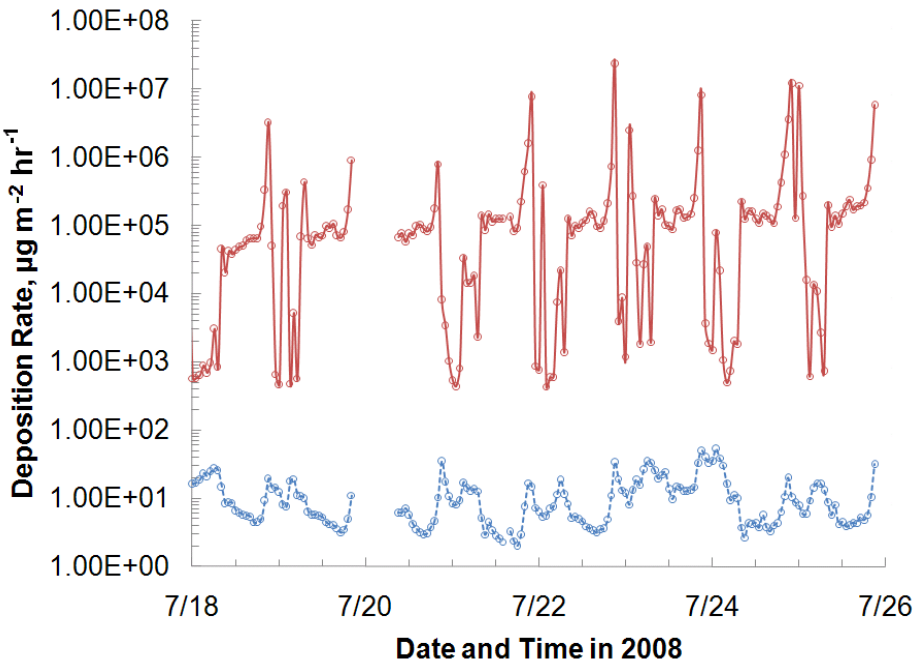

B

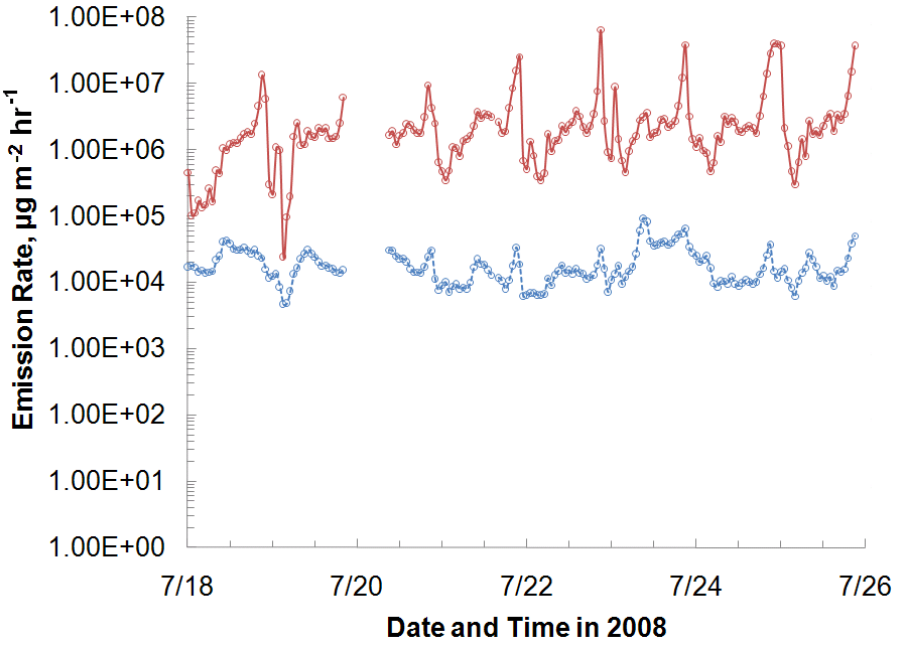

Figure A4. (A) Particle dry deposition rate at the far-field location and (B) modeled emission rate of PM_1 (blue) and PM_{10} (red) in 0.3 to 25 micron range using equation 8 (p. 40).

APPENDIX E

Spectral Curve-Fitting and Associated Quantitative Inter-comparison of Applied Intensities

1. Curve-Fit

The investigation of single-particle morphology and composition using Raman microscopy has been reported to correlate shape and chemistry (Sadezky et al., 2005). In this study, Raman microspectroscopy has been employed to explore the molecular-basis chemical composition on atmospheric aerosols. In recent studies, Raman microspectroscopy and associated chemical mapping techniques have been applied for the quantitative analysis of soot, humic-like substances (HULIS) and inorganic compounds in size resolved samples of air particulate matter collected with an electrical low pressure impactor (Ivleva et al., 2007).

In addition to qualitative classification of Raman spectra, quantitative characterization of carbonaceous materials can be performed according to a method similar to that described by Sadezky et al. (2005) and Ivleva et al. (2007). In these studies, a combination of four Lorentzian peaks and a Gaussian peak with full width at half maximum (FWHM) were fitted at each of the peak locations in the spectral range between 800 and 2000 cm^{-1}, namely G or "Graphite" peak centered at about 1580 cm^{-1} and D or "Defect" peaks at 1350, 1620, 1500, and 1200 cm^{-1} (D_1 – D_4, respectively). The Lorentzian curve-fits were used for G, D_1, D_2, and D_4 bands and the Gaussian fit was used for D_3 band. Detailed definition of each band is given in elsewhere (Ivleva et al., 2007). Quantification of each band enables us to understand difference in vibration modes of crystalline and molecular structures in the sample materials. Further parameterization of band intensity ratio provides information about the abundance of the graphitic component in carbonaceous materials. Specifically, Ivleva et al. (2007) showed that both the bandwidth and the relative intensity of D bands (I_D/I_G) of humic acid were higher than those of soot (i.e., standard diesel soot). The correlation between the increase in ratio of apparent elemental carbon to total carbon content (EC_a/TC) and decrease of the relative intensity of D bands was also described using parameters, such as I_{D1}/I_G, I_{D2}/I_G, $I_{D1}/(I_G+I_{D1}+I_{D2})$, and $I_{D3}/(I_G+I_{D2}+I_{D3})$. In our study here, particles collected at feedyard C as well as four reference materials for soot and HULIS have been investigated to define structural properties of carbonaceous particles. Graphite, soot generated by burning propane in our laboratory, Fluka standard Humic Acid, and well-characterized Pahokee Peat Soil II, and Leonardite, obtained from the International Humic Substance Society (IHSS), is used as a surrogate for aerosols composed of HULIS.

Figure 1 shows characteristic Raman spectra of the reference materials for HULIS (Graphite, Fluka standard Humic Acid, Pahokee Peat Soil II, and Leonardite). They all show pronounced peaks at ~1350 cm-1 (D peaks) and ~1580 cm-1 (G peak), but the D and G peaks exhibit greatly varying relative intensities and widths. Table 1 summarizes spectral parameters for the first-order Raman bands of agricultural particle samples and related reference humic materials (λ_0 = 532 nm). For comparison with earlier studies (Sadezky et al., 2005), we have also parameterized I_{D1}/I_G, I_{D2}/I_G, I_{D3}/I_G, $I_{D1}/(I_G+I_{D1}+I_{D2})$, and $I_{D3}/(I_G+I_{D2}+I_{D3})$. As can be seen in Figure 2, our observations differ somewhat from those of (Ivleva et al., 2007). Specifically, we found that the D_1 band width exhibits a non-linear correlation with the $I_{D1}/(I_G+I_{D1}+I_{D2})$. Comparison between graphite and other reference HULIS shows a increase of I_{D3}/I_G with decreasing EC_a/TC, which reflects a increase of the amorphous organic carbon fraction (highly disordered material) and decrease of graphitic structure (highly ordered material). Thus the increase in D_1 FWHM

represents an increase of structural disorder. This result may indicate that Raman microscopy may serve as an efficient tool for the characterization of soot and related carbonaceous materials and the degree of graphitic structural order.

2. Intensity Comparison

To quantify the effect of applying intensities on Raman spectra, we first employ prescribed curve-fitting procedure to find spectral area over the specific Raman shift range. For example, Figure 3 shows Raman spectra at three different intensities [i.e., 1 (red), 4 (purple), and 8 mW (green)]. These spectra were from samples collected in the evening of 24 July, 2008 sampled at downwind location in west Texas. For empirical purposes, we focus on soil/soot complex region (1050-1620 cm^{-1}) and organics bands region (2700-3100 cm^{-1}). Curve fitting analyses are conducted with 5 bands (i.e., Sadezky et al., 2005) in 1050 to 1620 cm^{-1} region and 5 bands (all Lorentzian function) in 2700 to 3100 cm^{-1} region at each intensity.

Table 2 summarizes the results of curve-fitting and spectral area comparison upon applied intensities. As seen in the table, the increase rate in spectral area of organics is a order magnitude higher than that of soil/soot. This evidently indicates that organics we identified are Raman active at higher range of laser intensity and suppression of organics may have influenced the relative fraction of soil/soot compounds.

References

Ivleva, N.P., McKeon, U., Niessner, R., and Pöschl, U. 2007. Raman microspectroscopic analysis of size-resolved atmospheric aerosol particle samples collected with an ELPI: Soot, humic-like substances, and inorganic compounds. *Aerosol Science and Technology*, 41, 655-671.

Sadezky, A., Muckenhuber, H., Grothe, H., Niessner, R., and Pöschl, U. 2005. Raman microspectroscopy of soot and related carbonaceous materials: Spectral analysis and structural information. *Carbon*, 43 1731-1742.

Table 1. Spectral parameters for the first-order Raman bands of agricultural particle samples, urban samples collected in downtown Houston, and related reference humic materials (λ_0 = 532 nm): number of analyzed spectra (n), band position (Raman Shift, cm^{-1}), full width at half maximum (FWHM, cm^{-1}), peak intensity ratios relative to the G band (arithmetic mean values ± standard errors).

Band	Parameter	07-24-08 Morning DW Agricultural Aerosols	07-22-08 Evening DW Agricultural Aerosols	3-21-09 Morning Rush Hou Houston	Graphite	Soot	Leonardite	Peat	Fluka Humic Acid
	n	3	5	3	5	5	5	5	5
G	Position	1537.4 ± 4.5	1548.4 ± 3.7	1585.6 ± 3.2	1578.6 ± 0.8	1571.0 ± 1.3	1589.5 ± 0.6	1541.7 ± 11.3	1562.2 ± 4.8
	FWHM	151.3 ± 16.0	174.6 ± 16.6	70.3 ± 2.4	27.9 ± 1.6	54.8 ± 2.4	89.0 ± 1.1	180.2 ± 41.2	90.1 ± 5.9
D1	Position	1342.9 ± 3.9	1349.0 ± 2.1	1348.7 ± 1.0	1345.0 ± 0.3	1344.6 ± 0.7	1370.8 ± 0.4	1326.5 ± 11.8	1345.7 ± 0.8
	FWHM	255.9 ± 24.0	288.4 ± 3.5	174.4 ± 10.0	40.1 ± 1.0	200.1 ± 2.0	313.9 ± 3.8	271.4 ± 5.0	255.4 ± 15.6
	I_{D1}/I_G	3.4 ± 0.8	2.9 ± 0.5	3.7 ± 0.2	1.0 ± 0.1	12.8 ± 1.3	4.2 ± 0.2	3.3 ± 1.3	9.9 ± 1.3
	$I_{D1}/(I_G+I_{D1}+I_{D2})$	0.7 ± 0.1	0.7 ± 0.0	0.7 ± 0.0	0.5 ± 0.0	0.8 ± 0.0	0.8 ± 0.0	0.6 ± 0.1	0.8 ± 0.0
D2	Position	1593.1 ± 2.5	1597.4 ± 1.7	1610.3 ± 2.1	1616.8 ± 1.0	1599.0 ± 0.9	1615.8 ± 0.9	1593.8 ± 3.3	1596.6 ± 1.9
	FWHM	81.3 ± 3.5	67.9 ± 3.6	55.3 ± 3.3	26.1 ± 2.1	61.1 ± 0.3	44.7 ± 2.9	74.9 ± 4.9	73.5 ± 8.5
	I_{D2}/I_G	0.6 ± 0.1	0.2 ± 0.1	0.5 ± 0.1	0.2 ± 0.0	1.7 ± 0.2	0.1 ± 0.0	0.4 ± 0.1	1.4 ± 0.4
D3	Position	1475.5 ± 29.5	1492.0 ± 21.0	1526.4 ± 4.0	1490.1 ± 6.1	1538.1 ± 2.0	1547.4 ± 0.3	1435.1 ± 30.6	1515.1 ± 6.8
	FWHM	324.9 ± 122.2	217.0 ± 93.7	166.5 ± 3.3	64.0 ± 18.0	173.0 ± 1.5	91.0 ± 1.8	145.4 ± 20.1	176.3 ± 8.6
	I_{D3}/I_G	0.7 ± 0.3	0.3 ± 0.2	0.7 ± 0.0	0.1 ± 0.0	3.0 ± 0.3	0.2 ± 0.0	0.4 ± 0.2	1.6 ± 0.4
	$I_{D3}/(I_G+I_{D3}+I_{D2})$	0.3 ± 0.1	0.2 ± 0.1	0.3 ± 0.0	0.1 ± 0.0	0.5 ± 0.0	0.2 ± 0.0	0.2 ± 0.1	0.4 ± 0.0
D4	Position	1119.2 ± 18.3	1118.7 ± 5.0	1183.0 ± 5.7	1290.5 ± 21.8	1177.5 ± 4.0	1100.8 ± 3.0	1096.4 ± 7.9	1153.9 ± 20.0
	FWHM	319.6 ± 19.0	275.2 ± 13.1	275.5 ± 12.3	224.6 ± 28.1	216.8 ± 21.0	235.5 ± 6.9	212.9 ± 21.9	242.4 ± 27.3

Table 2. Curve-fitting and spectral area comparison.

	Soil/Soot 1100-1600 cm^{-1}	Organics 2700-3100 cm^{-1}
A_{1mW}	27043.8	2760.1
A_{4mW}	58552.4	4530.9
A_{8mW}	92017.1	83675.9
$\frac{A_{4mW}}{A_{1mW}}$	2.2	1.6
$\frac{A_{8mW}}{A_{1mW}}$	3.4	30.3
$\frac{A_{8mW}}{A_{4mW}}$	1.6	18.5

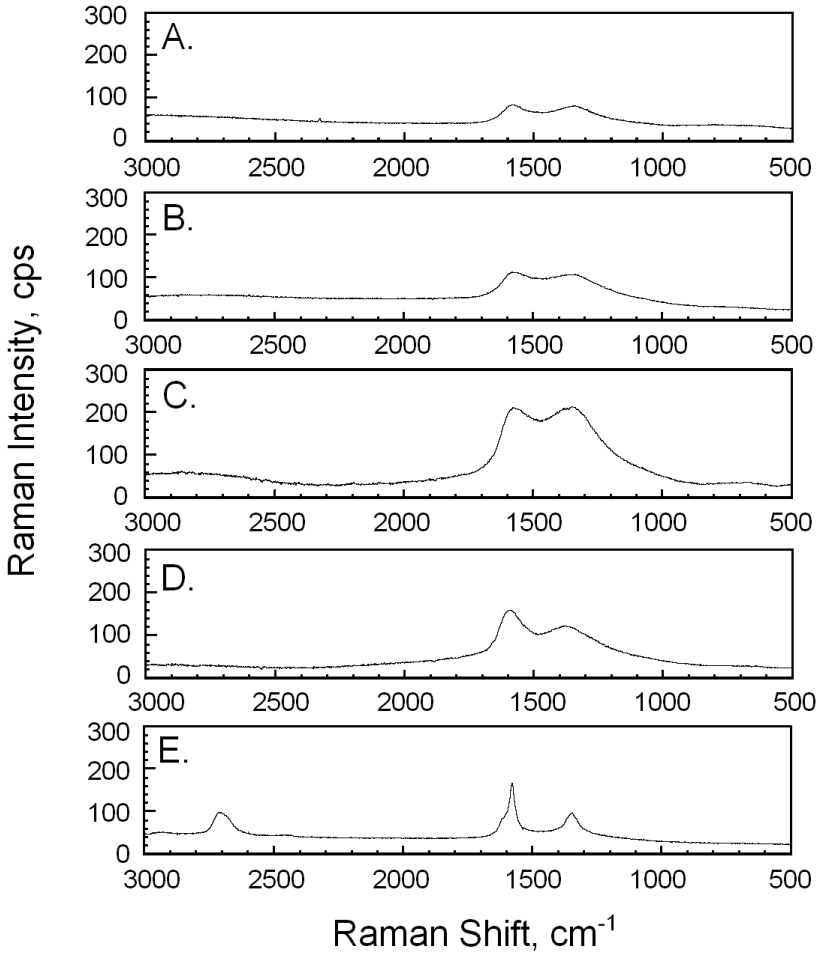

Figure 1. Raman spectra (λ_0 = 532 nm) of different reference carbonaceous HULIS materials: (A) soot generated by burning propane in our laboratory (B) Fluka humic acid (C) peat humic acid (D) leonardite humic acids (E) graphite.

A

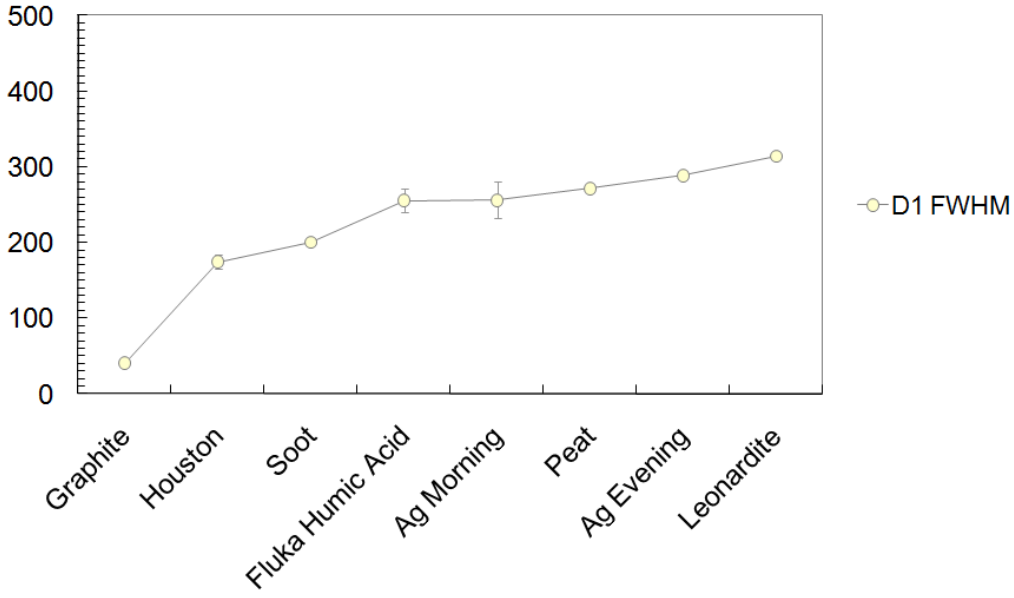

B

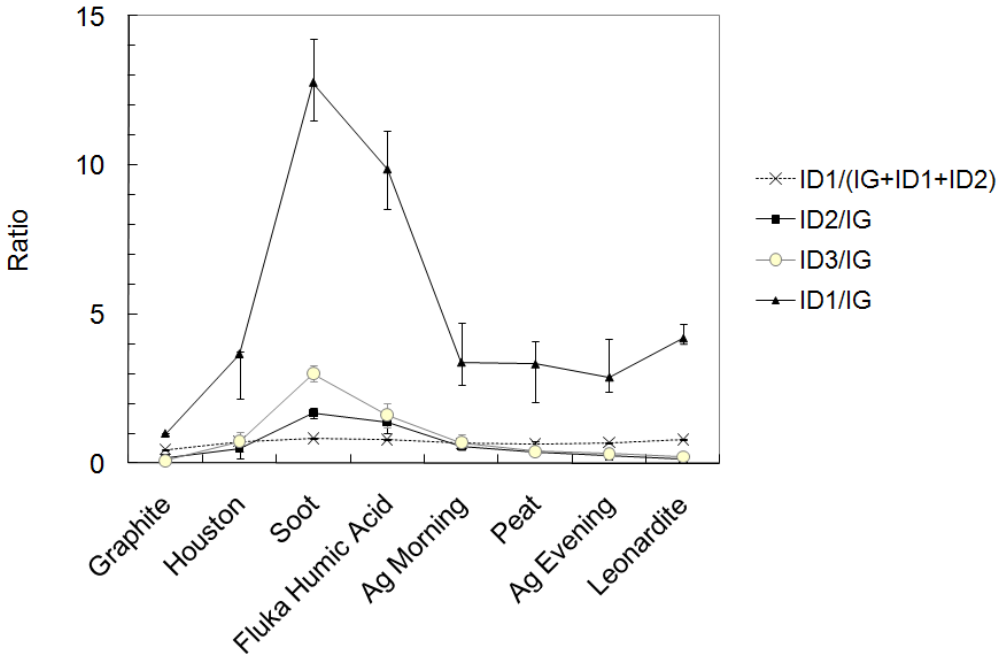

Figure 2. (A) Full widths at half maximum (FWHM) of D_1 band and (B) $I_{D1}/(I_G+I_{D1}+I_{D2})$, I_{D2}/ I_G, I_{D3}/ I_G, and I_{D1}/ I_G of samples and reference materials for soot and humic-like substances (mean values ± standard errors).

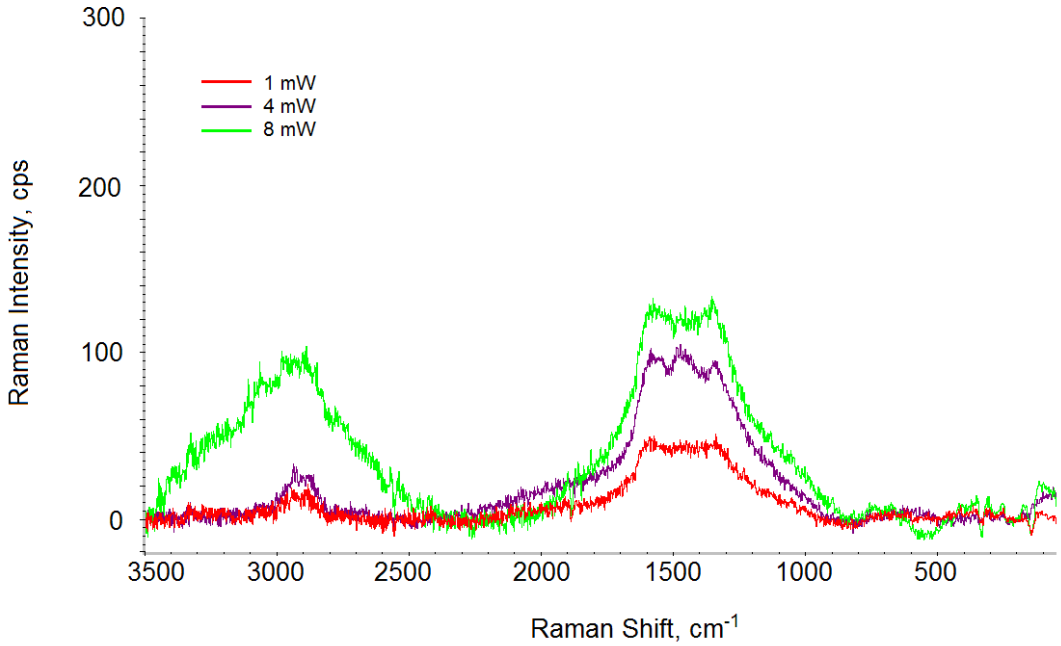

Figure 3. Raman spectra at three different intensities [i.e., 1 (red), 4 (purple), and 8 mW (green)]. These spectra were from samples collected in the evening of 24 July, 2008 sampled at downwind location.

VITA

Name:	Seong-Gi Moon (a.k.a., Naruki Hiranuma)
Address:	1204 Eller O&M Bldg. MS 3150 Department of Atmospheric Sciences College Station, TX 77843-3150
Email Address:	naruki.hiranuma@pnl.gov naruki10@yahoo.com
Education:	B.A., Economics, Meiji University, 2000 M.S., Environmental Sciences, West Texas A&M University, 2005 Ph.D., Atmospheric Sciences, Texas A&M University, 2010